EXPLORING UNIQUE OPTICAL PROPERTIES OF UPCONVERSION NANOCRYSTALS TOWARDS A NEW LIBRARY OF MOLECULAR PROBES

By

Jiangbo Zhao

Supervisors:

A/Prof. Dayong Jin, Prof. James A. Piper

Prof. Ewa M. Goldys, A/Prof. Judith M. Dawes

In accordance with the requirements for completion of a

Doctorate of Philosophy at Macquarie University

January 2014

To parents and sisters

To Yang Liu

Except where acknowledged in the customary manner, the material presented in this thesis is, to the best of my knowledge, original and has not been submitted in whole or in part for a degree in any university or institution other than Macquarie University.

Jiangbo Zhao

Acknowledgements

I sincerely acknowledge the group of people I have met over the past 4 years at Macquarie University. Their brilliant minds and radical openness encouraged me to spend a lovely and fruitful period on the way to earn my PhD degree. I feel lucky to make a journey on the right research topic, but also I am very pleased to have so many exciting moments and wonderful experiences with the people I know here. It significantly promoted my professional and personal advancements which I do not expect at the beginning of PhD study.

I truly thank my PhD supervisors Dayong Jin, Jim Piper, Ewa Goldys, and Judith Dawes. Since I am one of the first two students to receive the PhD training at the newborn Advanced Cytometry Labs managed by Dr. Jin, I have accessed invaluable chances to learn skills by observing him how to lead, manage and grow the lab, build up the network and translate into collaborations. I appreciate that Dr. Jin is open to share the philosophy and experiences of tackling difficulties and creating opportunities in a variety of contexts. I have been excited by his strong self-motivation, strategic design, persistence and optimism. I am greatly inspired by Prof. Piper's curiosity in science and insight on the project. In particular, I am pressed for his orientation to pursue practical applications by commercializing scientific output to make an impact on people's lives. I am also grateful to gain the supervision from experienced and skilled scientists, Prof. Goldys and A/Prof. Dawes. I am ensured on the right track to the PhD project due to their continued patience and unwavering approach to the research exploration. All experiences working with supervisors are shaping me as an independent and a critical thinking researcher, and their emphasis on "the power of focusing" keeps working in my career.

I acknowledge our group members and lab colleagues. I am proud that our lab is a place full of the atmosphere of sharing and support. I would like to thank Dr. Yiqing Lu, who set up the purpose-designed scanning microscope and contributed to lifetime decoding techniques in this thesis. I had thoroughly enjoyable experience with Mr. Jie Lu and Ms.

Lixin Zhang. I cherish interactions with Dr. Run Zhang, Mr. Yujia Liu, Mr. Xianlin Zheng, and Mr. Deming Liu. Benefits of working with these lovely friends cannot be expressed by finite words.

I am indebted to my collaborators or colleagues, at Macquarie University (Dr. Wei Deng, Dr. Christopher McRae, Dr. Anwar Sunna, Dr. Zhen Song, Ms. Debra Birch, and Mr. Russell Field), at University of California, Riverside (Prof. Yadong Yin and Dr. Zhenda Lu) and at University of Adelaide (Prof. Tanya Monro and Dr. Erik Schartner). Their brilliance and skills have added a great value to my research results. I could not have achieved successes in such a smooth way without the help and support from them.

I have the pleasure of doing Australian Footy with players at Macquarie University, attending Taekwondo class with Master Ron Claassens, and spending many leisure hours with friends at Sydney. The life during my PhD would not have been so colourful without you.

I present special acknowledgements to my parents and sisters. Your love helped me over the downtime. I would never have walked here without your trust.

In the end, I want to thank my wife, Yang Liu. You are my best.

List of Publications

[1] Deng W, Sudheendra L, **Zhao J**, Fu J, Jin D, Kennedy I M, Goldys E M, "Upconversion in NaYF4:Yb,Er nanoparticles amplified by metal nanostructures". *Nanotechnology*, 2011, **22**: 325604.

[2] Jin D, Lu Y, **Zhao J**, Deng W, Lu J, Piper J A, "Advances in lanthanide bioprobes and high-throughput background-free biophotonics sensing". *Quantum Electronics Conference & Lasers and Electro-Optics* (CLEO/IQEC/PACIFIC RIM 2011), pp. 80-82, 2011.

[3] **Zhao J**, Piper J A, Dawes J M, Jin D, Goldys E M, "Mechanisms of Size-Dependent Lifetime Quenching in Luminescent Upconverting Colloidal NaYF4:Yb,Er Nanocrystals". *Quantum Electronics Conference & Lasers and Electro-Optics* (CLEO/IQEC/PACIFIC RIM 2011), pp. 384-386, 2011.

[4] **Zhao J**, Lu Z, Yin Y, McRae C, Piper J A, Dawes J M, Jin D, Goldys E M, "Upconversion Luminescence with Tunable Lifetime in NaYF4:Yb,Er Nanocrystals: Role of Nanocrystal Size". *NanoScale*, 2013, **5**, 944-952.

[5] **Zhao J**, Jin D, Schartner E P, Lu Y, Liu Y, Zvyagin A V, Zhang L, Dawes J M, Xi P, Piper J A, Goldys E M, Monro T M, "Single-nanocrystal sensitivity achieved by enhanced upconversion luminescence". *Nature Nanotechnology* **8**, 729–734, 2013.

[6] Schartner E P, Jin D, **Zhao J**, Monro T M, "Sensitive detection of NaYF4:Yb/Tm nanoparticles using suspended core microstructured optical fibers". *The International Society for Optical Engineering-SPIE proceeding* (2013), Volume 8595, *Colloidal Nanocrystals for Biomedical Applications VIII*.

[7] Lu Y, **Zhao J**, Zhang R, Liu Y, Liu D, Goldys E M, Yang X, Xi P, Sunna A, Lu J, Shi Y, Leif R C, Huo Y, Shen J, Piper J A, Robinson J P, Jin D, "Tunable lifetime multiplexing using luminescent nanocrystals". *Nature Photonics* **8**, 32–36, 2014.

[8] Lu Y, Lu J, **Zhao J**, Cusido J, Raymo F, Yuan J, Yang S, Leif R, Huo Y, Piper J, Robinson J, Goldys E, Jin D, "On-the-fly decoding luminescence lifetimes in the microsecond region for lanthanide-encoded suspension arrays", *Nature Communications*, **5**, 3741–4741, 2014.

([1]-[8] are closely related to my PhD program)

[9] Lu J, Martin J, Lu Y, **Zhao J**, Yuan J, Ostrowski M, Paulsen I, Piper J A, Jin D, "Resolving low-expression cell surface antigens by time-gated orthogonal scanning automated microscopy". *Analytical Chemistry* **84** (22), 9674-9678, 2012.

[10] Song Z, Anissimov Y, **Zhao J**, Nechaev A V, Nadort A, Jin D, Prow T W, Roberts M S, Zvyagin A V, "Background-free imaging of upconversion nanoparticle distribution in human skin". *J. Biomed. Opt.*, 2013, 18 (6): 061215.

([9]-[10] are from other projects during my PhD program)

[11] Jin D, **Zhao J**, "Enhancing upconversion luminescence in rare earth doped particles". PCT/AU2013/001055, previously known as Australian provisional patent application No. 2012904043.

[12] Jin D, Lu Y, **Zhao J**, "Multiplex suspension assay/array using lifetime coding". PCT/AU2013/000672, previously known as Australian provisional patent application No. 2012902652.

([11]-[12] are patent applications directly coming from my PhD program)

Abstract

This thesis explores the next-generation inorganic luminescent nanomaterial — upconversion nanocrystals, for the advanced cell imaging and molecular sensing. Unlike traditional fluorochromes, e.g. fluorescent proteins and organic dyes, lanthanide-doped upconversion nanocrystals are able to efficiently convert the near-infrared excitation light to shorter wavelength emissions, e.g., the visible light. Upconversion nanocrystals are non-blinking, non-bleaching and immune to the autofluorescence interference, ideal for long-term background-free detecting trace amounts of target biomolecules or rare-event cells.

The investigation of this thesis falls into two categories to advance upconversion nanocrystals to address needs of frontiers of bioimaging, biosensing, and biomedical diagnostics. The first part presents the exploration towards lifetime-encoded multiplexed upconversion nanocrystals. We studied the impact of different nanocrystal sizes on optical properties of $NaYF_4$:Er/Yb nanocrystals in both the spectral and temporal domains. We discovered the upconversion lifetime can be precisely tuned by controlling sizes of nanocrystals since the effect of surface quenching becomes increasingly dominating as the nanocrystals size shrinks. Combining with the fact that the lifetime can be engineered through varying dopants concentrations and tuning the fluorescence resonance energy transfer efficiency, respectively, we have established three independent mechanisms to produce non-crosstalking lifetimes and succeeded in demonstrating the lifetime multiplexing concept in the upconversion luminescence.

In the second part, by first time we discovered that the brightness of highly doped upconversion nanocrystals can be leveraged by a large dynamic range of excitation irradiance. We found that under the intense irradiance (unexplored regime previously), the concentration of Tm^{3+} emitters could be significantly increased from 0.5 mol% to 8 mol% in $NaYF_4$ nanocrystals without quenching the upconversion luminescence. This finding realized the remote tracking a single nanocrystal within the microstructured fibre dip sensor, which represents three orders of magnitude improvement than that of quantum dots. We also described that a combination of low-/high-Tm^{3+} doped

upconversion nanocrystals holds the promise of being desirable luminescent nanomaterials for sensing, imaging, and security printing applications.

Key words: lanthanide; upconversion luminescence; lifetime; optical multiplexing; luminescence enhancement; bio-/nano-interface; ultrasensitive detection

Contents

Glossary of Acronyms (in Alphabetic Order)

ABP	antibody binding protein
BSA	bovine serum albumin
CCD	charge-coupled device
CD	cyclodextrin
ConA	concanavalin A
COOH	carboxyl groups
CS	chitosan
CT	computerized tomography
CV	coefficient of variation
Cy5	cyanin 5
DAPI	4',6-diamidino-2-phenylindole
DCM	dichloromethane
DNA	deoxyribonucleic acid
DOX	doxorubicin
DSPE	1,2-distearoyl-*sn*-glycero-3-phosphoethanolamine
FACS	fluorescence-activated cell sorting
FISH	fluorescence *in situ* hybridization
FITC	fluorescein isothiocyanate
FRET	fluorescence resonance energy transfer
FWHM	full width at half maximum
G203	anti-*Giardia* monoclonal antibody
GFP	green fluorescent protein
GO	graphene oxide
IgG	immunoglobulin
Ln	lanthanide
MRI	magnetic resonance imaging
NA	numerical aperture
NH_2	amino groups

NIR	near infrared
OA	oleic acid
PAA	polyacrylic acid
PBS	phosphate buffered saline
PDT	photodynamic therapy
PEG	poly(ethyleneglycol)
PET	positron emission tomography
PMT	photomultiplier tube
PVA	polyvinyl alcohol
QDs	quantum dots
RNA	ribonucleic acid
ROS	reactive oxygen species
SA	streptavidin
SDS-PAGE	sodium dodecyl sulphate polyacrylamide gel electrophoresis
SEM	scanning electron microscope
SHG	second-harmonic generation
siRNA	small interfering ribonucleic acid
SPR	surface plasmon resonance
STED	stimulated emission depletion
TEM	transmission electron microscope
TEOS	tetraethyl orthosilicate
TPA	two-photon absorption
TR-OSAM	time-resolved orthogonal scanning automated microscope
UCNPs	upconversion nanocrystals
UV	ultraviolet

Chapter 1: Introduction

This chapter identifies key motivations of improving optical properties of upconversion nanocrystals (UCNPs) for advanced biosensing and bioimaging applications. It first reviews availabilities of a broad spectrum of fluorescent bioprobes, such as molecular bioprobe — organic dyes and fluorescent proteins, and fluorescent nanomaterials — quantum dots (QDs), followed by discussions of their properties aligned to applications in modern biological sciences. The conventional fluorescent bioprobes are based on the single-photon excitation requiring higher energy photons, typically in the violet or even ultraviolet (UV) wavelength range, and therefore have intrinsic limitations, such as the photobleaching problem and autofluorescence background noise. To overcome the photobleaching issue, inorganic nanocrystals, such as QDs, have been developed. To avoid the autofluorescence background, multiphoton excitation approaches, such as two-photon absorption (TPA) and second-harmonic generation (SHG), have been developed to work as bioprobes that can be excited by near infrared (NIR) pulsed illumination (femtosecond laser) and convert into visible emissions, at which wavelength biological samples are typically dark. The focus of this thesis is the emerging UCNPs and their optical properties, such as being photostable and capable of converting NIR photons into visible emissions with the long lifetime, to address challenges in biosensing and bioimaging areas. Towards an ideal bioprobe, opportunities of the rational design to manipulate their optical properties of UCNPs are discussed by the end of this introduction chapter, so that priorities have been given to the new scope in expanding their optical multiplexing capabilities and enhancing their emission brightness.

1.1 Down-conversion Fluorescence Bioprobes

1.1.1 Fluorescence Techniques

Fluorescent bioprobes are at the core of bioimaging and biosensing applications in modern biomedical research. Since biological samples themselves are insufficient in

providing distinguishable features from one to another, it has necessitated the application of contrast agents for detecting, imaging, monitoring, and tracking targets of interest in biological systems. Of a variety of techniques available, the fluorescence approach offers rapid, sensitive, specific, and non-invasive measurements since the specific fluorescent bioprobe can be engineered to encompass many unique optical parameters, such as emission color, spectral intensity, polarization, and lifetime. The fluorescence microscopy techniques are able to provide high resolution images of yeast, bacterial, cells, tissues, and organisms, as well as to monitor spatio-temporal cellular processes (dynamic behaviour) at the molecular level in complex biological environments.

In the cell biology, fluorescent bioprobes can be functionalized to recognize and stain intra- and inter-cellular structures and to identify a particular cell type or to visualize cellular organelles, through high affinity biomolecular interactions, such as the antibody-antigen binding. Currently, several well-established fluorescence techniques have been routinely utilized in research and analytical labs. For example, the organic dye Hoechst 33342 efflux is often used to label hematopoietic and embryonic stem cells, then Hoechst-negative cells (immature stem cells) can be sorted out by the method of fluorescence-activated cell sorting (FACS) using flow cytometry (Scharenberg, Harkey et al. 2002). The green fluorescent protein (GFP) can be applied to visualize and trace the local synthesis and breakdown of actin cytoskeleton in cells, since the actin cytoskeleton could be transfected by GFP-tagged actin-binding proteins (Fig. 1.1a) (Weijer 2003). In pathogenic bacteria study, fluorescent bioprobes are broadly used for many interesting applications, including the observation of living pathogens within host cells that causes illnesses and infections (Fig. 1.1b) (Grant, Morgan et al. 2012). Waterborne pathogens — *Cryptosporidium* and *Giardia* from industrial wastewater streams can be detected by the specific fluorescence labelling (Ferrari, Stoner et al. 2006). In the biomedical research, fluorescent bioprobes are meant to investigate the presence and progression of a specific antibody correlating with a virus, thereby evaluating the risk of a disease or pharmacological responses to a given therapeutic intervention. The significance of fluorescent bioprobes is further emphasized by the grand challenge of imaging sensitivity down to the single-molecule level with nanoscale resolution, when combined with state-of-art techniques, e.g. stimulated emission

depletion (STED) microscopy (Donnert, Keller et al. 2006). It becomes possible to predominantly explore single molecules and their reactions in living cells, such as reaction rate constants and diffusion coefficients (Sako 2006).

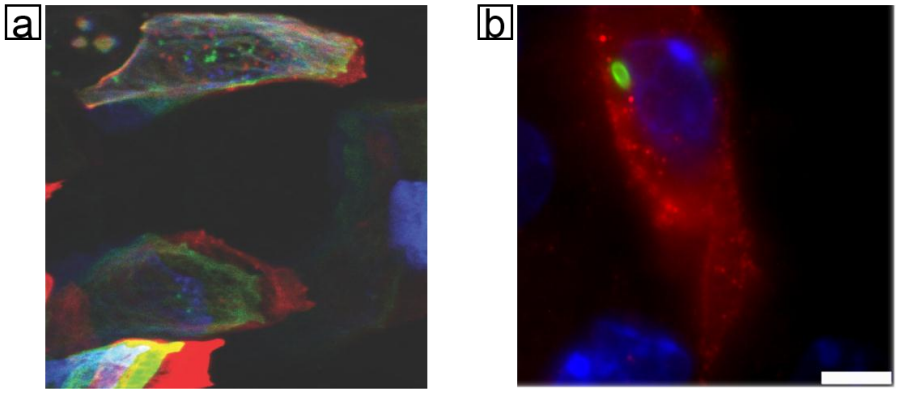

Figure 1.1. (a) Visualization of actin dynamics in cells moving in a *Dictyostelium* slug. *Dictyostelium* cells were transfected with the GFP-tagged actin-binding protein of ABP120. Cells moved from left to right of composite image. Three successive images taken 10 s interval are overlaid in different colours: first image, red; second, green; third, blue. Actin filaments are white, indicating that they do not move with respect to the substrate. (Reprinted with permission from Ref. (Weijer 2003), copyright 2003) (b) Representative fluorescence micrographs of *Salmonella* within phagocytes in infected livers of C57BL/6 mice. $CD18^{+}$ cells (red), *Salmonella* (green), nucleic acid is stained with 4',6-diamidino-2-phenylindole (DAPI) (blue). Scale bar, 5 μm. (Reprinted with permission from Ref. (Grant, Morgan et al. 2012), copyright 2012)

1.1.2 Molecular Fluorescence Bioprobes

Molecular fluorescent bioprobes, including synthetic organic dyes, fluorescent proteins, and metal-ligand complexes such as lanthanide (Ln^{3+}) chelates, are most widely used in bioimaging and biosensing applications. With key features summarized in Table 1.1, they are small (<5 nm), bright and specific for labelling by well-established staining protocols. However, traditional molecular bioprobes have four major inherent limitations for many critical applications.

Table 1.1: Comparison of optical properties of typical down-conversion fluorescent bioprobes.

Property	Organic dyes; Fluorescent proteins	Lanthanide chelates	Quantum Dots
Size	< 5 nm, molecule	~ 5 nm, molecule	4-60 nm (hydrodynamic diameter), nanocrystals colloidal
Excitation spectra (λ_{ex})	UV/Visible (lamp or laser)	UV/ Visible (lamp or laser)	UV/ Visible (lamp or laser)
Absorption cross-section	Good, having optimal excitation	Moderate, having optimal excitation	Excellent, increasing towards UV or shorter wavelength from absorption onset
Emission spectra (λ_{em})	Single band with asymmetric shape; FWHM 50-100 nm;	Multiple bands with symmetric shape; FWHM 10-20 nm;	Single band with symmetric shape; FWHM 30-50 nm;
Quantum yield (η)	0.5-1.0	0.1-0.8 (not absolute quantum yield)	0.1-0.8
Fluorescence lifetime (τ)	1-10 ns	> 10 μs	Typically 10-100 ns
Photostability	Poor; limited by photobleaching and photo saturation	Moderate; limited by photobleaching	Moderate; limited by photo blinking and bluring
Photo-toxicity to living cells	problematic	problematic	problematic
Background Autofluorescence	problematic	avoidable through time-gated detections	moderate
Tissue penetration for deep tissue imaging	poor	poor	poor

- Photobleaching

Photobleaching is a photo-induced chemical process to destruct emissions of a fluorochrome exposed to the accumulated illumination of the incident light (Widengren and Rigler 1996, Lippincott-Schwartz, Altan-Bonnet et al. 2003). It takes place that, when fluorochromes are excited onto a triplet state, one of relaxations is to couple with the surrounding oxygen as an irreversible quenching way. Given a constant illumination on fluorochromes, the cycle of such irreversible absorption-quenching stacks up, which

eventually renders fluorochromes unable to fluorescence. For common molecular bioprobes, fluoresceins, rhodamines, cyanines, and fluorescent proteins, and so on, are all prone to a high photobleaching rate, preventing long-term *in vitro* and *in vivo* observations of fluorescent molecules labelled targets, as shown in Fig. 1.2. The photobleaching particularly causes difficulties for the single molecular imaging as it requires the high excitation intensity but the photobleaching rate usually scales up nonlinearly under the elevated excitation intensity.

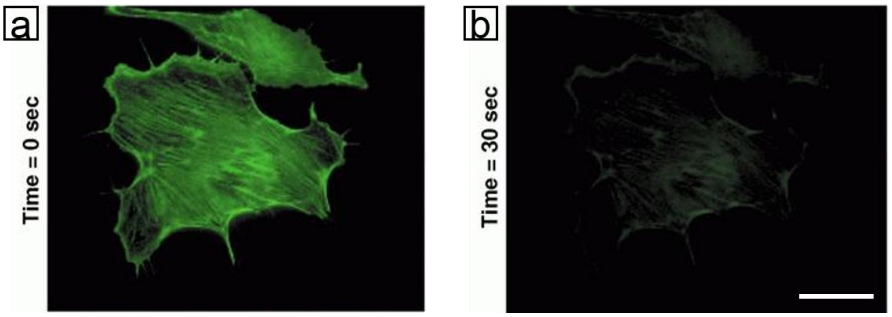

Figure 1.2. (a, b) Bovine pulmonary artery endothelial cells labelled with fluorescein were photobleached to about 12% of the initial intensity in 30 s in phosphate buffered saline (PBS) buffer under continuous illumination on the microscope with a fluorescein isothiocyanate (FITC) filter set using a 60× objective. Images were acquired at one-second intervals for 30 s. Scale bar: 20 μm. (Reprinted with permission from Life Technologies website)

- Fluorescence saturation

Fluorescence saturation is limiting the maximum brightness of a molecular bioprobe. It is the deviation of the linear relationship between the fluorescence intensity and excitation intensity. As shown in Fig. 1.3, the maximum photons output in a given time will reach the plateau at the relatively high irradiance (Deschenes and Vanden Bout 2002). Under the saturated excitation light intensity, a molecular bioprobe cannot absorb more than one photon before returning to its ground state. The rate of absorption is determined by the decay rate of the excited state, and the longer the fluorescence lifetime is the easier for a bioprobe reaches its saturation plateau.

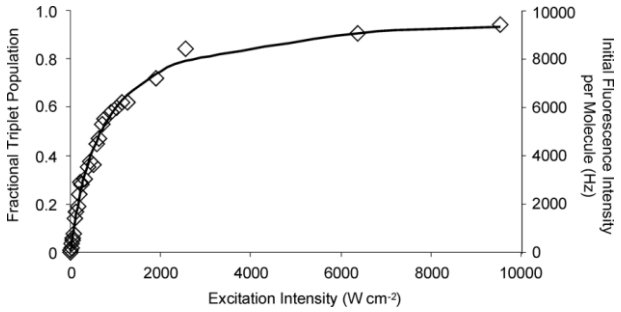

Figure 1.3. Fluorescence intensity (open diamonds) of rhodamine 6G as a function of the excitation intensity, showing that the saturation causes the limited intensity value. (Reprinted with permission from Ref. (Deschenes and Vanden Bout 2002), copyright 2002). For the laser confocal scanning microscope with the strong excitation intensity, the saturation is often yielded (Visscher, Brakenhoff et al. 1994).

- Excitation complexity and emission overlapping

Excitation complexity results in complexities and cost of an analytical instrument. A bioprobe has its best excitation peak, and therefore when multiple bioprobes employed in an experiment, multiple lasers and separation filters become necessary to optimize their performances as well as avoiding the mutual interference. The emission of each bioprobe will typically overlap each other in the crowded visible spectrum, therefore spectral compensation and de-convolution are frequently used with aids of sophisticated filters and optical configurations.

- UV or short wavelength excitation

UV or short wavelength excitation can generate a series of drawbacks for molecular bioprobes, such as photo-toxicity to living cells, autofluorescence background issues and poor penetration property to deep tissues, as indicated in Table 1.1. As many fluorescent inorganic nanoparticles still share this problem, we discuss this in details in the following section.

1.1.3 Fluorescent Inorganic Nanoparticles

Currently, primary fluorescent inorganic nanoparticles include dyes encapsulated nanoparticles, defect-induced nanodiamonds, and semiconductor QDs. They are

attracting many new developments in the last decade because of their unique properties which can potentially resolve limitations associated with traditional molecular bioprobes for bioimaging and biosensing applications. One of overwhelming benefits of fluorescent inorganic nanoparticles resides in their excellent resistance to photobleaching and chemical-degradation. A typical experiment result is shown in Fig. 1.4 that QDs are good at long-term tracking targets at high temporal and spatial resolutions (Wu, Liu et al. 2002). The improved photostability of fluorescent inorganic nanoparticles is particularly useful for three-dimensional optical sectioning with successive *z*-scanning.

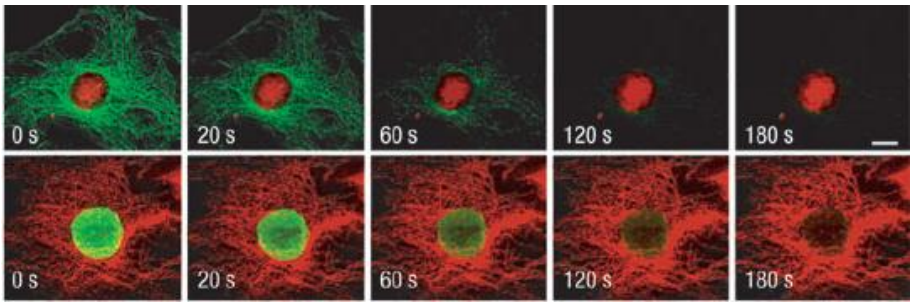

Figure 1.4. Cell labelling with QDs and illustration of QDs photostability, compared with the dye Alexa 488. In the upper panel, the nucleus is stained red with QDs and actin fibres are stained green with the dye. In the lower panel, the labelling is reversed. (Reprinted with permission from Ref. (Wu, Liu et al. 2002), copyright 2002)

QDs have become one of prevailing bioprobes over the past decade. Thanks to their larger extinction coefficients, QDs generally yield stronger emissions in contrast to molecular bioprobes. The shape of emission band of QDs is symmetric, and spectral peaks of QDs emissions are highly dependent on the size of dots. The larger dots tend to emit longer wavelength emission. QDs have a broadband absorption spectrum, and the corresponding absorption probability increases towards UV range. Different from organic dyes, a single laser at UV or violet can excite all QDs (Fig. 1.5) (Resch-Genger, Grabolle et al. 2008). Up to date, QDs have achieved successes in a range of applications, including but not limiting to the immunolabeling of nuclear antigens, membrane proteins, fixed cells and tissues (Bruchez, Moronne et al. 1998, Wu, Liu et al. 2002, Lidke, Nagy et al. 2004, Sukhanova, Devy et al. 2004); fluorescence *in situ*

hybridization (FISH) on chromosomes (Pathak, Choi et al. 2001, Xiao and Barker 2004) or combed deoxyribonucleic acid (DNA) (Michalet, Pinaud et al. 2001); organisms visualization (Gao, Cui et al. 2004) and living animal imaging (Ballou, Lagerholm et al. 2004). However, on the other side of a coin, fluorescent inorganic nanoparticles (e.g. QDs) have not yet solve other standing problems which organic dyes have encountered:

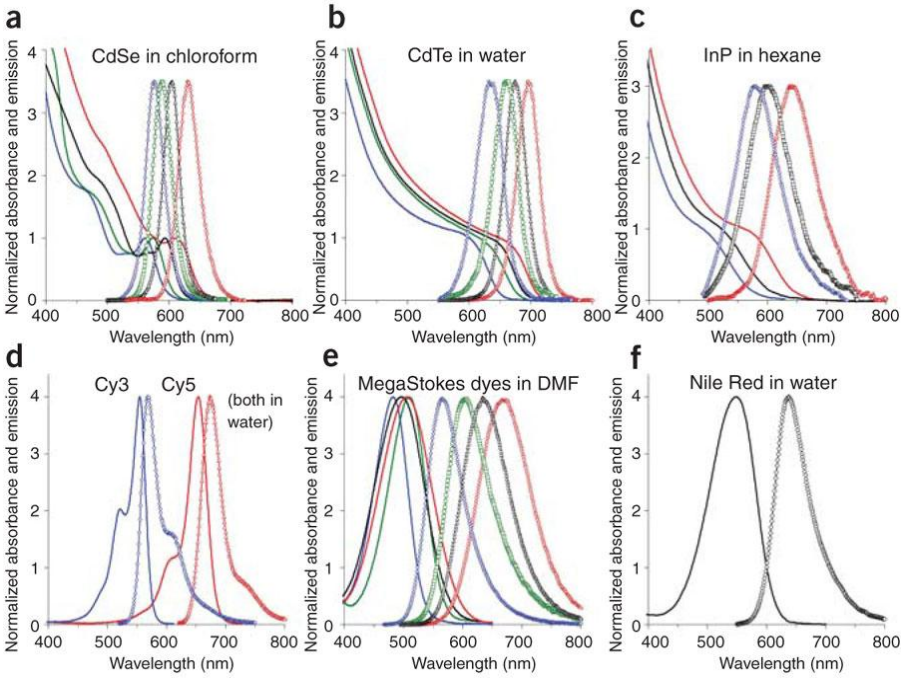

Figure 1.5. Absorption (solid lines) and emission (lines with symbols) spectra of representative QDs (a–c) and organic dyes (d–f). The colour of QDs is coded by size (blue < green < black < red). (Reprinted with permission from Ref. (Resch-Genger, Grabolle et al. 2008), copyright 2008)

- UV or short wavelength excitation

The short-wavelength excitation can unavoidably illuminate many intrinsic components in biological samples such as proteins, collagen, elastin, mitochondria, and lysosomes, and create the noisy background autofluorescence across nearly the whole visible spectrum. The background autofluorescence can blur the delicate bioimaging, and particularly pose difficulties for ultrasensitive detection and quantification of trace amount of target analytes of interest. The UV or short wavelength light can cause serious photo-toxicity, by directly or indirectly damaging biomolecules, i.e. cells death

by long-term illumination. The photo-toxicity becomes more serious under a fluorescence microscope with high density excitation, such as laser scanning confocal microscope. Furthermore, the UV or short wavelength light can be strongly absorbed or scattered by various biomolecules, limiting its penetration depth into the deep tissue.

- Spectral overlapping

Though QDs have improved their emission sharpness than organic dyes with full width at half maximum (FWHM) emission band typically at 50 nm, it remains challenging due to the high-degree spectral overlapping when multiple QDs have to be used, as shown in Fig. 1.5. Thus, when different QDs are designed for spectral multiplexing or multicolour imaging experiment, it curbs the number of distinguishable emissions in a single test and still requires the colour compensation with sophisticated deconvolution algorithms.

- Photoblinking

Photoblinking is the intermittence in emissions of QDs, which is universally observable from QDs during time scales longer than ~200 μs (Nirmal, Dabbousi et al. 1996, Brokmann, Hermier et al. 2003, Won, Kim et al. 2010). This limitation can interrupt the temporal resolution in imaging or tracking of individual labeled biomolecules with difficulties for quantitative data analysis. Photoblinking of QDs becomes more prominent at the elevated excitation intensity. In Fig. 1.6, it has revealed that QDs are seriously blinking within 0.55 s.

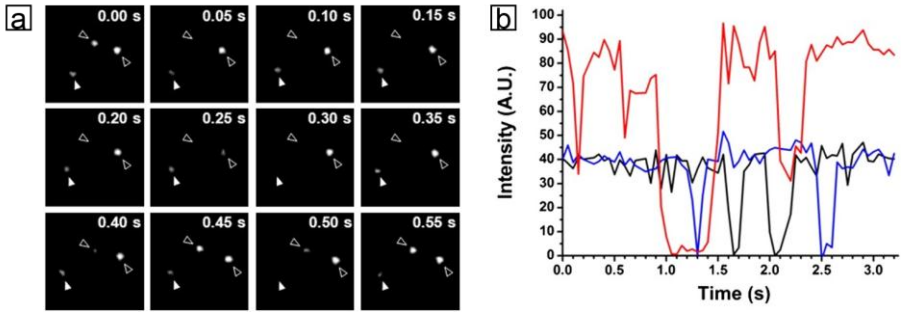

Figure 1.6. (a) Photoblinking of QDs in cells was revealed by time-lapse images of three different fluorescence spots (over 0.05 s intervals). Each symbol indicates identical spots blinking intermittently in all frames. (b) Representative traces for the fluorescence intensity of

QDs as studied in (a). (Reprinted with permission from Ref. (Won, Kim et al. 2010), copyright 2010)

In addition, QDs are composed of the toxic II and VI group elements, like Cd, Se, *et al*., and have intrinsic toxicity concerns.

Alternatively, other fluorescent inorganic nanoparticles have been explored in the last decade. In the case of dyes encapsulated nanoparticles, the leakage of organic dyes or metal-ligand chelates is a concern. For defect-vacancy nanodiamonds, though biologically inert, defect-emission centres have low absorption efficiency, and the preparation of nanodiamonds with a narrow size distribution has been another challenge.

1.2 Multiphoton Fluorescence Bioprobes

Multiphoton fluorescence bioprobes are designed to circumvent persistent problems of down-conversion bioprobes. Since most problems of conventional bioprobes literately can be attributed to the UV or violet excitation, a simple solution is to develop a bioprobe capable of efficiently converting two or more low-energy NIR excitation photons to one visible emission high-energy photon. This optical process is called anti-Stokes emission, and bioprobes undertaking anti-Stokes responsibilities are named as multiphoton fluorescence bioprobes (Fig. 1.7).

The NIR illumination can only excite purpose-engineered multiphoton fluorescence bioprobes with large multiphoton absorption cross-section, at which the excitation is negligible for intrinsic background biological species. For this reason, both signal contrast and biomolecules viability can be significantly improved in multiphoton fluorescence approaches. The NIR excitation light also lies in the biological optical window (typically from 664 nm to 934 nm) in which range biological tissues are transparent, preferable for in-depth bioimaging and/or multilayer monitoring.

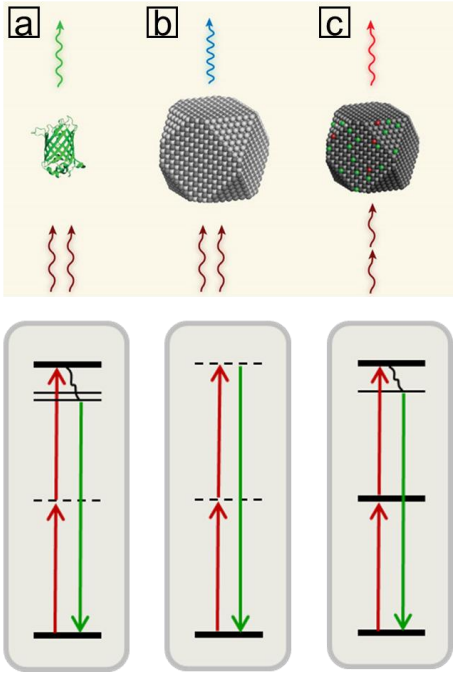

Figure 1.7. Multiphoton fluorescence bioprobes (examples in top panel) can be illuminated using three different mechanisms (lower panel). (a) In TPA, two low-energy photons are absorbed by a probe almost simultaneously. The excited probe then emits the higher-energy fluorescence. As an example, GFP can be excited by two NIR photons from the femtosecond laser pulse, and emits green light. (b) In SHG, when the intense coherent light is shone on materials that do not possess inversion symmetry, the vibrating electric field of the incident beam results in the polarization of the medium, therefore the re-emitting light at the original wavelength but also half of the original one. Exactly twice the incident excitation energies. As an example the barium titanate nanoparticles scatter NIR photons to produce the higher-energy blue light, through a SHG mechanism. (c) In upconversion luminescence, two NIR photons are sequentially absorbed, accompanied with higher-energy emissions. As an example, Ln^{3+}-doped UCNPs absorb two NIR photons in sequence then produce the visible light. Ln^{3+} ions in nanocrystals are symbolized in red and green dots. (top panel reprinted with permission from Ref. (Cohen 2010), copyright 2010))

1.2.1 Two-photon Absorption Fluorescence

TPA fluorescence is produced by simultaneously absorbing two identical photons with the probe being pumped onto its excited state. The mechanism is illustrated in Fig. 1.7a.

The first demonstration of TPA fluorescence was presented by Denk and his colleagues at the beginning of the 1990s (Denk, Strickler et al. 1990). Over the last few years, the advancement of femtosecond mode-locked lasers has triggered a fast development of TPA bioimaging techniques (Curley, Ferguson et al. 1992, Fisher, Partridge et al. 1997, Smolorz, Wise et al. 1999, Larson, Zipfel et al. 2003). TPA has offered a set of advantages in their applications, such as the minimum photodamage to biological species for long-term tracking or observation, the effective removal of autofluorescence with enhanced detection sensitivity and the deep light penetration into tissues. Besides, the three-dimensional optical sectioning without a confocal aperture can be easily achieved by TPA, since TPA only occurs at the focus of a microscope objective where the sufficient excitation intensity is confined within a microscale volume.

But, TPA fluorescence has a low quantum yield ~10^{-13}, combined from the low absorption cross-section (virtual intermediate state) and the essential requirement of the simultaneous absorption of two coherent photons (Table 1.2). The generation of detectable TPA fluorescence needs the extremely high density excitation, but in the same time it often saturates and bleaches TPA bioprobes on the focal plane with toxicity concerns. TPA was found less practical for spectral multiplexing detection, where different TPA bioprobes have to be used with overlapped spectra.

Table 1.2: Comparison of optical properties of multiphoton fluorescence bioprobes.

Property	Two-photon absorption	Second-harmonic generation	Upconversion nanocrystals
Material requirement	excited states in visible emission range	Asymmetric media (nonlinear optical materials)	Lanthanide doped nanocrystals
Excitation spectra (λ_{ex})	Femtoseconds pulsed NIR laser; $>10^9$ W cm^{-2}	Femtoseconds pulsed NIR laser; $>10^9$ W cm^{-2}	NIR laser; > 10 W cm^{-2}
Absorption cross-section	Poor	Poor	Moderate
Emission spectra (e.g., by two photon) (λ_{em})	Single band with asymmetric shape; FWHM 50-100 nm; $\lambda_{em} > \lambda_{ex}/2$	Single band with symmetric shape; FWHM ~ 5 nm; $\lambda_{em} = \lambda_{ex}/2$	Multiple bands with symmetric shape; FWHM 10-20 nm; $\lambda_{em} > \lambda_{ex}/2$
Quantum efficiency (η)	~ 10^{-13}	~ 10^{-11}	~ 10^{-3}
Fluorescence lifetime (τ)	1-10 ns	< 200 fs	10-1000 μs
Spectral Multiplexing	4 colours, limited by spectral multiplexing due to wide FWHM	5 colours, good for multiplexing	4-5 colours,
Photostability	Moderate; limited by photobleaching and fluorescence saturation	Good	Excellent
Photo-toxicity to living cells	Minimum	Minimum	Minimum
Background Autofluorescence	Low	Low	Low
Deeper tissue imaging	Good	Good	Good

1.2.2 Second-harmonic Generation

SHG is a nonabsorptive optical process (Fig. 1.7b), in which two identical photons delivered by a powerful NIR laser interact with asymmetric media to emit a scattered single photon with twice the energy of the incident photon (exactly half the excitation wavelength). In this way, SHG is in fact based on scattering rather than fluorescence process, only involving the virtual excited state.

SHG has now been widely applied in imaging cellular structures as well as other biological species *in vivo*/ *in vitro* by SHG-active bioprobes, such as asymmetric cytoskeletal proteins (Nuriya, Jiang et al. 2006, Salafsky and Cohen 2008). The excitation density for SHG signal is comparable to TPA fluorescence, at ~10^9 W cm^{-2} excitation level; at least 100 times lower than the biological tissue damage threshold (Pantazis, Maloney et al. 2010). While SHG retains as many as benefits of TPA, it also alleviates certain limitations in TPA, without the observable photobleaching, photoblinking or fluorescence saturation. It suggests that SHG-tagged biomolecules can survive from continuous excitation for several hours. The light scattering based SHG signal has a very narrow emission, $1/\sqrt{2}$ bandwidth of the excitation light, and can be highly tuned for spectrally distinct emission output *via* the different given excitation. SHG involves only virtual energy transition, while TPA involves real energy transition at the excited state. As a result, the response time of SHG is at the femtosecond level, about several orders of magnitude faster than the nanosecond lifetime of TPA fluorescence, allowing very fast and sensitive detection.

Unfortunately, the quantum yield of SHG is only slightly higher than TPA, around 10^{-11}, since it has small absorption cross-section and requires simultaneous combination of two coherent photons.

1.2.3 Upconversion Nanocrystals

Unlike TPA and SHG which lack of physically real intermediate energy levels, Ln elements have rich long-lifetime intermediate energy levels, which can be used to overcome the low efficiency issue of multi-photon process. As depicted in Fig. 1.7c, a real intermediate energy level in Ln^{3+} ions can facilitate the sequential absorption of at least two NIR excitation photons to emit one visible photon. The intermediate energy levels in Ln^{3+} have exceptionally long lifetime in the range of 10-1000 μs, which can accumulate photons as a reservoir and increase the chance of upconverting sequential coming photons. The existence of physical energy levels (i.e. intermediate and long-lifetime excited states) in Ln^{3+} ions breaks down the requirement of the simultaneous conversion of coherent photons, so that two sequentially arriving photons can be absorbed in a cascade way towards higher excited states before emitting the high-energy upconversion photon, and therefore it becomes profitable to achieve a high efficiency of

multiphoton fluorescence under moderate excitation (Table 1.2). As a result, the efficiency of UCNPs reaches seven orders of magnitude higher than that of CdSe-ZnS QDs used in TPA (Larson, Zipfel et al. 2003, Heer, Kömpe et al. 2004).

More than the efficient upconversion optical properties in UCNPs, recent advances made in material science have realized in precisely controlled growth of highly monodisperse UCNPs with different size spanning 5-100 nm aligned to varieties of applications. Furthermore, using the knowledge and experiences developed for QDs and QDs surface, many bio-/nano-interface protocols (i.e. surface functionalization and bioconjugation) have been adopted and transferred to produce bio-conjugated UCNPs. As a consequence, UCNPs have been proven as a viable and versatile bioprobe in many fields of biological and biomedical applications, as classified in Fig. 1.8.

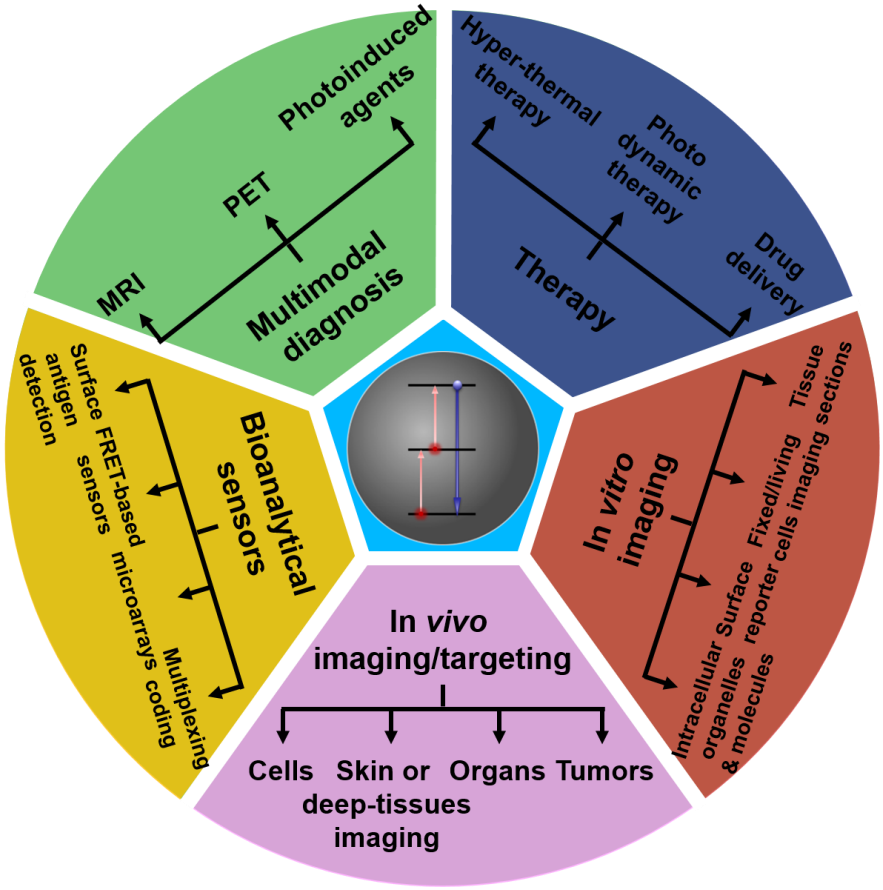

Figure 1.8. Biological applications of UCNPs as a fluorescent bioprobe for a range of biological and biomedical applications.

***In vitro* imaging**:

The *in vitro* imaging using UCNPs has made most progresses. As the fast moving field, numerous reports appeared to describe advantages of UCNPs *in vitro* labeling of tissue sections, fixed/living cells, and intracellular organelles and molecules. For example, Cohen *et al*. (Wu, Han et al. 2009) showed UCNPs endocytosed by living NIH 3T3 murine fibroblasts persevered in strong upconversion luminescence with no measurable background autofluorescence. The prolonged observation (~6 h) was taken to track UCNPs in living HeLa, allowing to visualize the active transport by motor proteins in real time. Lu *et al*. (Li, Wu et al. 2013) demonstrated the uniform DNA-modified UCNPs as a versatile bioprobe can cross cell membranes without the need of transfection agents and target breast cancer cells for imaging. DNA molecules on the DNA-modified UCNPs retain their biorecognition ability, allowing programmable assembly of hybrid nanostructures. Lu's group also explored coating phospholipids to mimic cells' external membrane and they found this simple strategy can facilitate the binding and internalization of UCNPs into cancer cells, evidenced by the upconverting signal spots in the cytoplasm (Li, Zhang et al. 2012).

***In vivo* imaging/targeting:**

Thanks to the NIR excitation, the widespread use of UCNPs *in vivo* imaging or targeting to cells, skin, organs and tumors has been promoted from advantages of the removal of biological background autofluorescence and deep light penetration into biological specimens. By intracutaneous injection of UCNPs into paws and the chin of mouse, Liu *et al*. (Cheng, Yang et al. 2010) demonstrated the *in vivo* multicolour upconversion luminescence imaging capable of mapping lymph node. They also applied multicolour *in vivo* upconversion luminescence to visualize and track the development of tumors that labelled with UCNPs. Zhang *et al*. (Idris, Li et al. 2009) directly observed UCNPs flowing from a mouse tail vein to ear blood vessels under *in vivo* confocal imaging system, showing the unobtrusive visualization of cell dynamics in the native tissue over a 4 hrs time course. In all *in vivo* upconversion studies, Li *et al*. (Liu, Sun et al. 2011) achieved the detection limit of cells labeled by <50 UCNPs when imaging the

whole body of a small animal (mouse) through the use of sub-10 nm β-$NaLuF_4$:Gd/Yb/Tm UCNPs as a bioprobe. For the high-contrast upconversion tissue imaging, Chen *et al*. (Chen, Shen et al. 2012) recorded the luminescent signal from 3.2 cm-depth animal tissue (pork) with core/shell α-$NaYbF_4$:Tm/CaF_2 UCNPs under low intensity 980 nm illumination.

Bioanalytical sensors:

In vitro bioanalytical sensors, including immunofluorescent surface antigen reporter, FRET-based sensor, microarrays, and multiplexing coding, are emerging as new promising applications for UCNPs. For surface antigen reporter, the pioneer work has been reported by Tanke *et al* (Zijlmans, Bonnet et al. 1999) towards the sensitive detection and quantification test, who conjugated upconversion Y_2O_2S:Yb,Er particles to NeutrAvidin with the subsequent use of this functionalized UCNPs specifically binding to CD4 membrane antigen on intact human lymphocytes or prostate-specific antigen in tissue sections. In a parallel development, Tanke's group (van de Rijke, Zijlmans et al. 2001) exploited upconversion Y_2O_2S:Yb,Er particles (~400 nm) as luminescent reporters for robotically spotted DNA microarrays. The unique upconversion property allowed them to detect 1 ng μl^{-1} DNA probe, which is a four-fold increase in the detection limit compared to that carried out by cyanin 5 (Cy5). Liu *et al* (Zhang, Yuan et al. 2011) presented a glucose sensor based on FRET between concanavalin A (ConA)-labeled UCNPs and chitosan (CS)-labeled graphene oxide (GO). Although the binding of ConA to CS quenches the luminescence intensity of UCNPs, the presence of glucose can restore the upconversion luminescence owing to the competition between glucose and CS for ConA. To simultaneous detection of biological species in clinical, food, and environment, Stucky *et al* (Zhang, Shi et al. 2011) have successfully developed UCNPs-encoded microbarcodes for multiplexed signaling and nucleic-acid encoding. They generated the different colour coding by combining different UCNPs into microbeads and used this novel barcode for the rapid and sensitive analysis of nucleic acids and antigens.

Multimodal diagnosis:

The multimodal diagnosis, including magnetic resonance imaging (MRI), positron emission tomography (PET), computerized tomography (CT), and photoinduced imaging, has been developed as the state-of-the-art tool in biomedical research, clinical diagnostics and therapeutics. Its importance becomes more remarkable in the context of that a single technique can not possess all the required capabilities for the comprehensive imaging. Due to the seven unpaired 4f electrons of Gd^{3+}, the incorporation of Gd^{3+} into hosts or onto the surface layer of UCNPs is one of most useful strategies for positive-T_1 weighted MRI imaging. The representative example is that Gao and co-workers (Liu, Gao et al. 2013) have covalently bound antitumor antibody with PEGylated $NaGdF_4$:Yb,Er UCNPs to image intraperitoneal tumors and subcutaneous tumors *in vivo*. Their systematic investigations suggest tumors smaller than 2 mm can be successfully detected and imaged, critical for early diagnosis. As a result of the superparamagnetic properties of Fe_3O_4 nanoparticles, the synthesis of Fe_3O_4/UCNPs hetero-nanocomposities has been stated as another important approach for negative-T2 weighted MRI. By using this method, Li *et al*. (Zhu, Zhou et al. 2012) proved as-prepared Fe_3O_4 cores enable the $NaLuF_4$:Yb,Er shell exhibit superparamagnetic property and serve as magnetic contrast to image the tumor-bearing mice. In terms of PET imaging, as one whole-body imaging technique featured in picomolar detection sensitivity and millimeter spatial resolution, ^{18}F is the most widespread radionuclide. Thus, producing ^{18}F-labelled UCNPs has attracted many attentions. For example, Li *et al*. (Sun, Yu et al. 2011) developed a simple, efficient and general synthesis strategy to generate ^{18}F-modified UCNPs (>90% yielding) within 5 mins at room temperature, followed by PET imaging of their *in vivo* distribution and application in the lymph monitoring.

Therapy and drug delivery:

The proper nanostructure design has made UCNPs apply as therapeutic agent in photodynamic therapy (PDT) and hyper-thermal therapy and drug carriers in the drug delivery system. The PDT has great potentials in killing of diseased cells, e.g., deep-tissue cancer, by excitation of a photosensitizer to produce cytotoxic reactive oxygen species (ROS), providing the localized and specific treatment to large and deep-seated tumors. Scholfield *et al*. (Zhang, Steelant et al. 2007) firstly manifested that mesoporous

silica coated $NaYF_4$:Yb/Er UCNPs with the encapsulation of photosensitizer merocyanine 540 in the silica layer can trigger to the release of ROS in the deep tissue, where the penetration depth was increased for several times. To improve the efficiency of PDT, other photosensitizers releasing high amount of ROS upon NIR excitation, such as *meso*-tetraphenyl porphine (Shan, Budijono et al. 2011), zinc phthalocyanine (Wang, Shrestha et al. 2013), $Ru(bpy)_3^{2+}$ (Guo, Kumar et al. 2007), and Chlorin e6 (Wang, Cheng et al. 2013), have been investigated. The recent breakthrough has been reported by Zhang *et al*. (Idris, Gnanasammandhan et al. 2012), who utilized multicolour emissions of UCNPs at a single excitation wavelength to simultaneously activate two photosensitizers, and achieved a satisfied PDT efficiency as required in therapy.

The photo-induced hyper-thermal therapy is another noninvasive, nontoxic, and inexpensive method to prevent the development of diseased cells and even cause their death. Chow *et al*. (Qian, Zhou et al. 2011) observed hybrid nanoparticles, $NaYF_4$:Yb,Er/$NaYF_4$/silica (core/shell/shell) UCNPs deposited by Au nanoparticles, are efficient to destroy BE(2)-C cancer cells, as the rapid heat conversion can be induced by the coupling of upconverting visible light with the surface plasmon resonance (SPR) of Au. Song *et al*. (Dong, Xu et al. 2011) presented the core-shell structured $NaYF_4$:Yb,Er/Ag UCNPs can photothermally induce the death of HepG2 cells from human hepatic cancer and BCap-37 cells from human breast cancer under the 980 nm excitation. They found the optimum mortality approaches 95% with a power density of 1.5 W cm^{-2} much lower than that of Au nanoshells-decorated UCNPs. Hilderbrand *et al*. (Shan, Weissleder et al. 2013) designed $NaYF_4$:Yb,Er/silica (core-shell) nanocomposites incorporating the NIR highly-absorbed carbocyanine dyes in the outer silica shell. Due to the effectively improved absorption of NIR light by dyes, they enable to use this new functional nanocomposities for both optical imaging and photo-thermal treatment *in vitro* experiments.

For cancer diagnosis and treatment, directly ferrying the drug to diseased cells *via* smart-functional UCNPs is an alternative way. This UCNPs-based drug delivery system can be employed for tracking and reading the efficiency of the drug release and delivery mechanism. Lin *et al*. (Gai, Yang et al. 2010) prepared Fe_3O_4/nSiO_2/mSiO_2/$NaYF_4$:Yb,Er core-shell-structured nanomaterials loaded with drug

molecules. They demonstrated this drug carrier system have a controlled drug release property and multifunctions, which can realize the targeted ferrying and monitoring of drugs simultaneously. Shi *et al*. (Liu, Bu et al. 2013) illustrated that the release of anticancer drug doxorubicin (DOX) molecules from the pore network of mesoporous silica-coated UCNPs can be triggered by NIR light. They also regulated the DOX release by the *trans-cis* photoisomerization of azobenzene molecules that are encapsulated in the silica outer layer. Zhang *et al*. (Jiang, Zhang et al. 2009) conjugated the small interfering ribonucleic acid (siRNA) with anti-Her2 antibody functionalized UCNPs and used them to control the tumor in the context of the gene silencing effect of siRNA to cancer cells.

1.3 Fundamentals for Upconversion Nanocrystals

Though a broad range of applications using UCNPs become feasible and promising, there are remaining several scopes for further improving UCNPs towards an ideal bioprobe. In order to make new advances, at fundamental level, the principal knowledge of upconversion luminescence should be better explored so that new solutions can be tailored for the rational design and synthesis for the next generation UCNPs.

1.3.1 Upconversion Luminescence

Upconversion luminescence occurs with the aid of long-lifetime intermediate energy levels. Its excitation and emission process can be schematically depicted by a simple three-energy-level system (Fig. 1.9). The excitation photon “1” can first populate the ion to the intermediate level E_1, and stay for long enough (long lifetime) to wait for the following photon “2”, while the ion would be pumped to the higher excited level E_2, where two low-energy photons being upconverted into one photon and emitted. The illustrated upconversion process also indicates that the efficient upconversion luminescence only happens to the physical system with a long-lived metastable state between a ground level and an emitting level. The metastable state with relative long lifetime helps to accumulate sufficient transient population on E_1 and increases the conversion probability from E_1 to E_2.

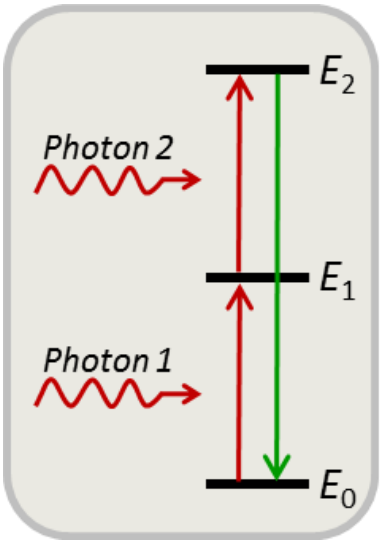

Figure 1.9. The simplified scheme shows the upconversion luminescence is emitted by the sequential absorption of two NIR photons *via* the intermediate energy level.

1.3.2 Upconversion Nanocrystals

To generate efficient upconversion luminescence, a type of luminescent centres with matching energy levels is essential. Thanks to various Ln^{3+} ions with ladder-like energy levels, they are regularly selected as the upconversion luminescence centres to be embedded within nanocrystal hosts.

Lanthanide doping

Trivalent Ln^{3+} ions, luminescent centers, are the stable oxidation state for Ln metals (the group of elements from lanthanum to lutetium together with scandium and yttrium). They belong to large atomic number group. The electronic configuration of Ln^{3+} ions is arranged as below:

$$1s^2 2s^2 2p^6 3s^2 3p^6 3d^{10} 4s^2 4p^6 4d^{10} 4f^n 5s^2 5p^6,$$

or

$[Xe]4f^n$, where n=0~14.

Energies of $5s^2$ and $5p^6$ electrons on shells are lower than that of 4*f* orbitals, so that Ln^{3+} ions are characterized by a gradual fill on 4*f* orbitals after $5s^2$ and $5p^6$ outer shells have been fully occupied. In other words, 4*f* orbital electrons of Ln^{3+} ions are completely shielded by $5s^2$ and $5p^6$ outer orbitals. By virtue of the shielding effect, there is weak electron-phonon coupling for 4*f* electrons by chemical bonding or surroundings field. Accordingly, energy levels for Ln^{3+} ions vary by a small amount in different host lattices, strongly resembling the free Ln^{3+} ions. This makes possible to rationally assign energy levels in a new host lattice by referring to the well-known "Dieke diagram" (Fig. 1.10). The energy level ($^{2S+1}L_J$), denoted by the horizontal bar in the diagram, is actually split into several Stark states by the crystal field influence. The width of the various horizontal bars represents the order of magnitude of the crystal field splitting. By the same token, the shielding effect yields sharp and narrow Ln^{3+} emissions (10~20 nm FWHM) originating from 4*f*-4*f* transitions. As 4*f*-4*f* transitions are governed by *Laporte* forbidden rule, energy levels of Ln^{3+} ions are relatively long-lived; their lifetime is typically in the range of 10-1000 μs.

According to roles of Ln^{3+} ions in producing the upconversion luminescence, there are essentially requiring an activator (emitter) and a sensitizer (donor). The activator is populated to the excited state to emit upconversion luminescence *via* successively absorbing sensitized excitation photons. To date, most of activators are homogeneously distributed, but restricted at a low concentration level, typically less than 2 mol %, in the host lattice. This is because that, when the doped activator amount is higher than the optimal concentration threshold, activators tend to quench each other, resulting in dimmer upconversion luminescence, called "concentration quenching".

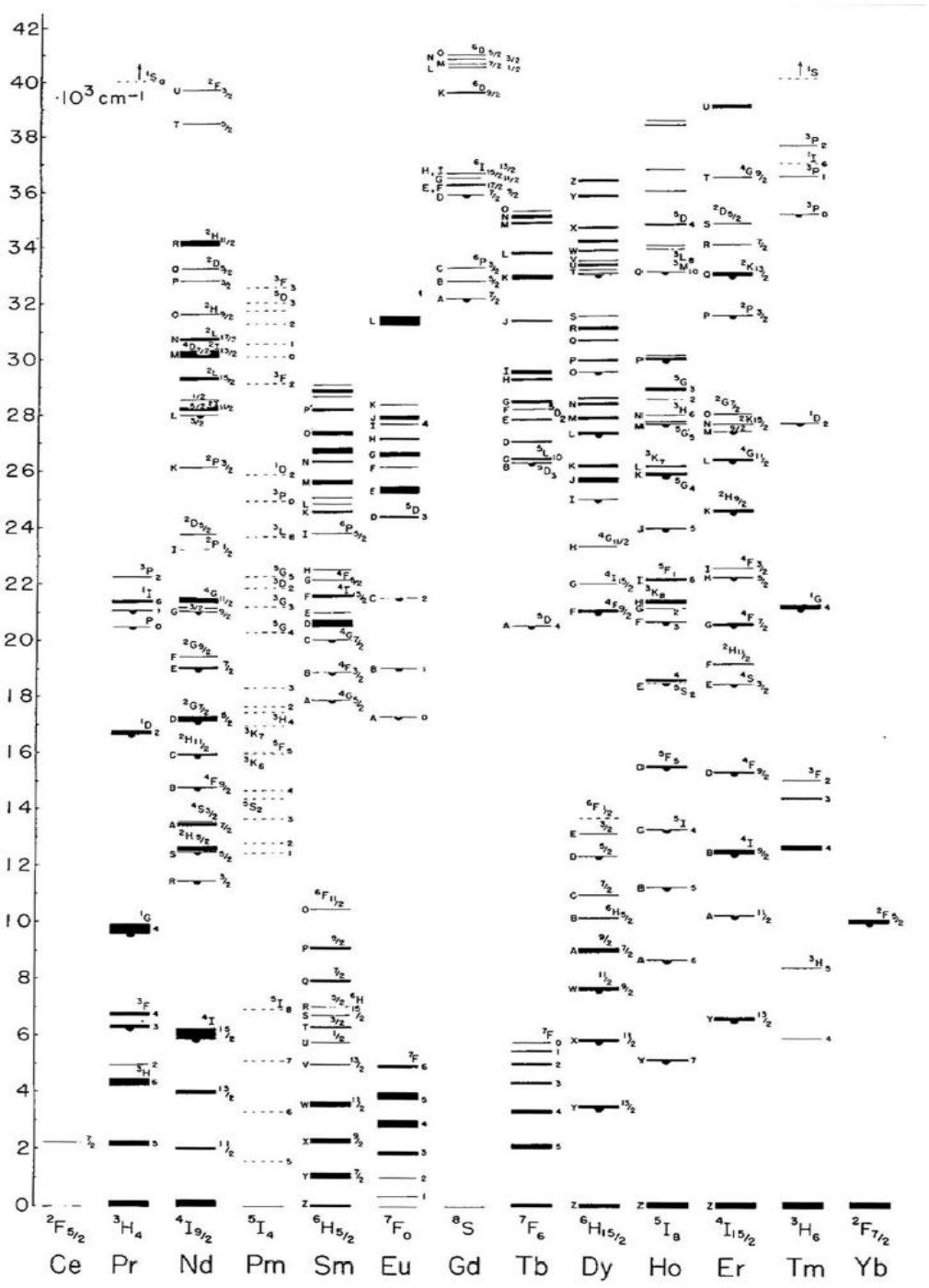

Figure 1.10. The Dieke diagram depicts energy levels of Ln^{3+} in $LaCl_3$ (Dieke and Crosswhite 1963).

The sensitizer is also essential since it can enhance the upconversion efficiency through its larger absorption cross sections. The concentration of sensitizer ions is typically

much higher than activators, so that sensitizers will form a network of photo-antennas for enlarged harvesting of incident excitation photons. To achieve the high efficiency of resonance energy transfer, the sensitizer should have matching energy level to the intermediate state of the activator, with spectral overlapping. For instance, Yb^{3+} is the most used sensitizer in combination with common activators, Er^{3+}, or Tm^{3+}, to produce the bright visible upconversion emissions (Fig. 1.11) (Song, Anissimov et al. 2013).

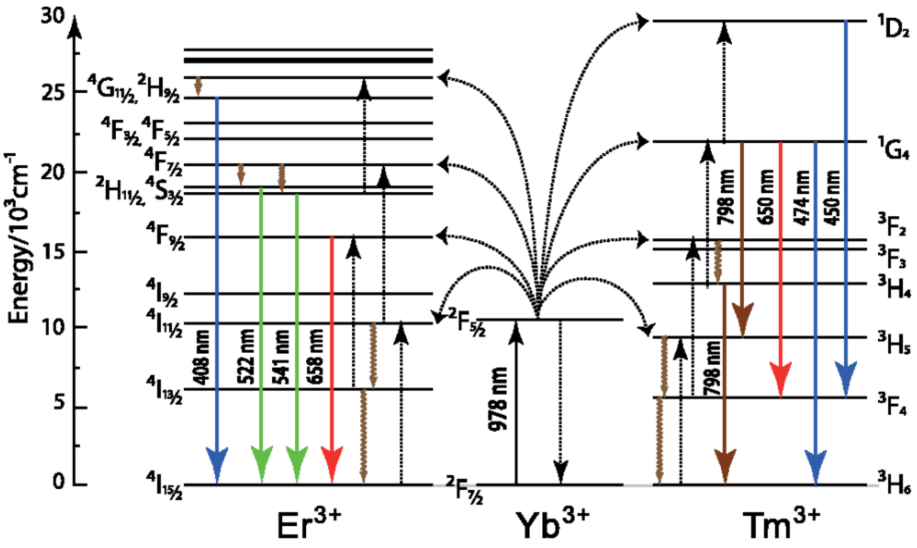

Figure 1.11. Upconversion luminescence sensitized by energy transfer between Yb^{3+} and Er^{3+} (left) and Yb^{3+} and Tm^{3+} (right). Solid, dotted, and curly arrows indicate radiative, nonradiative energy transfer, and multiphonon relaxation processes, respectively. (Reprinted with permission from Ref. (Song, Anissimov et al. 2013), copyright 2013)

Host lattice

The host lattice has a profound impact on the upconversion efficiency of Ln^{3+} ions, although it does not affect a lot on the position of emissions (wavelength). The favorable host lattice should fulfill following criteria: (1) the host lattice should be transparent to upconversion emissions; (2) the constituent node of host lattice that is supposed to accommodate Ln^{3+} ions or other metal elements should have very close ionic radius to doped Ln^{3+} ions or other metal elements, which can be replaced by any dosage of the sensitizer and activator and minimize defects due to the lattice mismatch; (3) the host lattice should have the strong crystal field to break down the *Laporte*

forbidden effect, and facilitate 4*f*-4*f* transitions; (4) the host lattice should have low intrinsic energy phonons, curbing the nonradiative multiphonon relaxation (Table 1.3).

Therefore, the most suitable host lattice for the upconversion luminescence is the compromise of these four conditions. To our best knowledge, β-$NaYF_4$ (hexagonal phase) crystal has been reported as the most efficient lattice for the upconversion luminescence. The identification was completed by pioneer Sommerdijk *et al*.,(Sommerdijk and Bril 1974) who investigated upconversion efficiencies of the Yb^{3+}-Er^{3+} pair in various host lattices under NIR excitation. The low phonon energy (Table 1.3), strong crystal field (as in Fig. 1.12b), and high transparence to the NIR excitation and visible light together contribute to β-$NaYF_4$ as the champion of host lattices for the upconversion luminescence now.

Table 1.3: Phonon energies of various host lattices for Ln^{3+} ions (Diamente, Raudsepp et al. 2007).

Host Lattice	Phonon Energy/cm^{-1}	Host Lattice	Phonon Energy/cm^{-1}
phosphate glass	1200	CaF_2	466
silica glass	1100	SrF_2	366
fluoride glass	5500	BaF_2	319
chalcogenide glass	400	LaF_3	350
$LaPO_4$	1050	YF_3	450
YAG	860	$NaYF_4$	370
YVO_4	600	$LaCl_3$	240

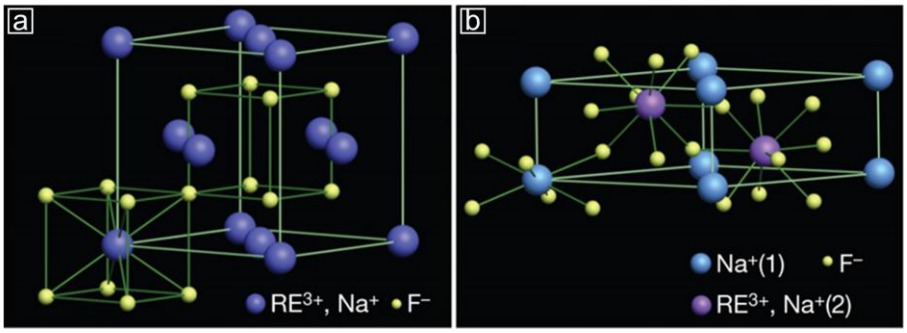

Figure 1.12. (a, b) Schematic presentation of cubic (α)- and hexagonal (β)-phase $NaReF_4$ structures, respectively. In α phase, equal numbers of F^- cubes contain cations and vacancies. In β phase, an ordered array of F^- ions offers two types of cation sites: one occupied by Na^+ and the other occupied randomly by Re^{3+} and Na^+. (Reprinted with permission from Ref. (Wang, Han et al. 2010), copyright 2010)

1.4 Frontiers in Upconversion Nanocrystals

In spite of outstanding strengths of UCNPs towards new-level biomedical applications, but evidently, they have been hampered by two optical limitations being the ideal fluorescence bioprobes: the unsatisfied spectral multiplexing and the low upconversion efficiency accompanied with the relatively weak brightness. These two challenging issues naturally become frontiers in the investigation of the upconversion luminescence. In this section, an overview of the current multiplexing techniques and amplifying signal strategies is presented.

1.4.1 Unsatisfied Spectral Multiplexing

For the high-throughput analysis of different analytes or the simultaneous study of complex cellular behaviours in a single test, the multiplexing detection is required. By realizing that two or more spectrally distinguishable bioprobes work in parallel to screen multiple targets, spectral multiplexing or multicolour detection is typically performed.

Regarding to the spectral multiplexing scheme in UCNPs, narrow emissions of Ln^{3+} ions could be assembled to output different visible upconversion colours. For instance, Wang *et al*. manipulated the color display of a single $NaYF_4$ upconversion system by varying Yb^{3+}, Er^{3+}, and Tm^{3+} dopants (Wang and Liu 2008). This method accesses to a

wide range of upconversion colours by a single wavelength 980 nm excitation, as shown in Fig. 1.13. Recently, the rational design of a core-shell structure that facilitates the sub-lattice mediated energy migration was described to extend traditional Er^{3+}, Tm^{3+}, and Ho^{3+} activators to other Ln^{3+} ions, such as Tb^{3+}, Eu^{3+}, Dy^{3+}, and Sm^{3+}, for efficient and multiplexed upconversion emissions (Wang, Deng et al. 2011).

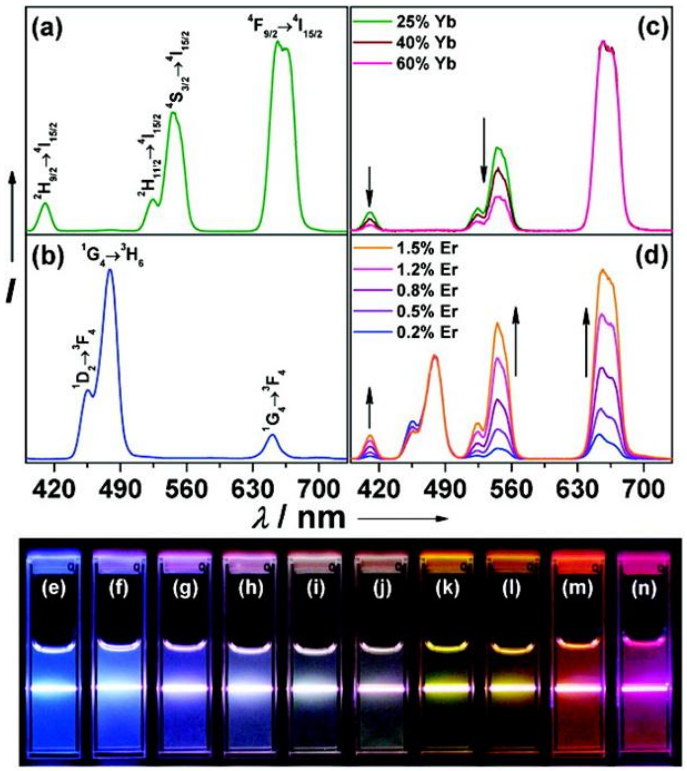

Figure 1.13. Upconversion emission spectra of (a) NaYF4:Yb/Er (18/2 mol%), (b) NaYF4:Yb/Tm (20/0.2 mol%), (c) NaYF4:Yb/Er (25–60/2 mol%), and (d) NaYF4:Yb/Tm/Er (20/0.2/0.2–1.5 mol%) particles in ethanol solutions. The spectra in (c) and (d) were normalized to Er^{3+} 650 nm and Tm^{3+} 480 emissions, respectively. Compiled luminescent photos showing corresponding colloidal solutions of (e) NaYF4:Yb/Tm (20/0.2 mol%), (f–j) NaYF4:Yb/Tm/Er (20/0.2/0.2–1.5 mol%), and (k–n) NaYF4:Yb/Er (18–60/2 mol%). Samples were excited at 980 nm NIR diode laser with 600 mW. (Reprinted with permission from Ref. (Wang and Liu 2008), copyright 2008)

Despite these progresses, the suitability of UCNPs for multicolour detection at a single wavelength excitation is limited. The first drawback is related to the way of reaching

upconversion colours. Currently, upconversion colours are produced by integrating a set of narrow emission bands originating from transitions between discrete Ln^{3+} energy levels, rather the respective single Gaussian emission band as simple as in organic dyes and QDs. It implies that any upconversion colour does have a complete or partial overlapping of emissions. Such crosstalking problem, therefore, can create challenges for spectral deconvolution of measured signals and make fluctuations for quantifying different analytes in the spectral multiplexing. Besides, as one type of nonlinear optics, relative upconversion intensities are highly influenced by excitation conditions, so that the upconversion colour can be partially or completely changed by controlling the excitation light, leading to ratiometric emissions. This feature emphasizes the excitation beam has to be controlled very carefully to gain the consistence.

1.4.2 Limited Signal Amplification

The quantum efficiency or brightness level is self-evident as one determinant factor in evaluating how good a fluorescence bioprobe is. The brightness is of importance for every fluorescence imaging or sensing techniques. The detection limit of low-abundance biomolecules and the quantification accuracy of multiple targets are influenced by the luminescent brightness as well as the spectroscopic stability of bioprobes. Poor brightness reduces the threshold of rare-events detection or deviate the reliability of quantification test; although some labelled biomolecules exist, beyond the detection limit make them in non-detectable states.

In this context, finding out an approach to enhance the brightness of UCNPs (signal amplification) has been one of research focuses for ages. Up to now, there are three approaches majorly applicable through different physical designs, with amplification factors of ~10 up to a few hundred. The most versatile method is the growth of an additional passivation or active shell architecture to supress the nonradiative loss of the excited energy to surface quenchers. The separation of doped UCNPs with surface quenchers and solvents or biological media is advantageous to overall enhancement of upconversion emissions. An impressive illustration was provided by Boyer and Veggel (Boyer and van Veggel 2010), who have demonstrated that the absolute quantum yield of core-shell β-$NaYF_4$:20%Yb,2%Er@$NaYF_4$ UCNPs has a 300% increase after growing an undoped $NaYF_4$ shell. The Schuck *et al*. (Ostrowski, Chan et al. 2012)

recently observed the signal of core-shell β-$NaYF_4$:20%Yb,2%Er@$NaYF_4$ UCNPs (<10 nm) can be higher than only core β-$NaYF_4$:20%Yb,2%Er UCNPs (>25nm). And yet, nanoscale shells increase the diameter of UCNPs, larger than original cores. Over-sized UCNPs can disturb bioconjugation reactions and affect biolabelling efficiency. In addition, the bioimaging quality can be distorted or some bioimaging truth will be hidden, owing to the additional shell spacer between UCNPs and biomolecules.

The second increasingly used method is *via* SPR occurring at the interface of excited activators and metals (gold or silver), which can strengthen the localized electric field (concentrating excitation light) and accelerate the radiative rate. One fresh plasmonic interaction example reported by Duan *et al*. (Zhang, Li et al. 2010) is that the upconversion signal amplification in visible range can be achieved by attaching Au nanoparticles onto individual β-$NaYF_4$:Yb,Tm UCNPs. However, complexities in preparing the metal-UCNPs hybrid nanostructure have raised several concerns, including difficulties of the following surface modification and bioconjugation. Furthermore, since the metal-UCNPs system has a sophisticated relationship with the shape and size of the metal, and the distance between the metal and UCNPs, the extremely delicate control on all geometrical parameters are needed. Sometimes, the metal (e.g. gold) shell around the surface of UCNPs can considerably scatter the excitation light and prevent SPR in effect.

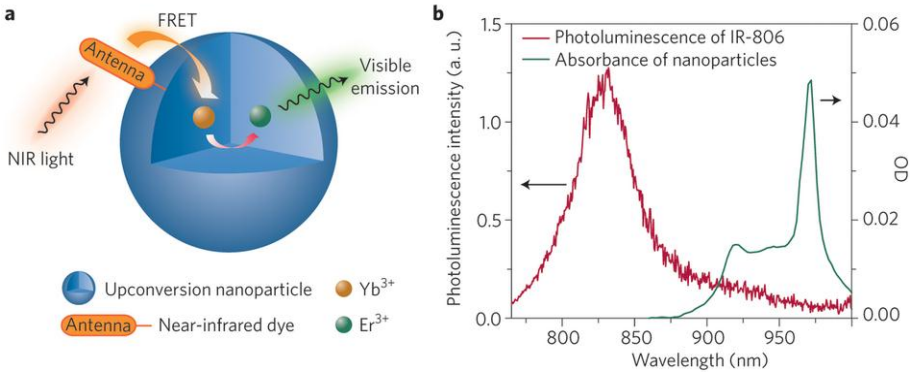

Figure 1.14. (a) Schematic of dye-sensitized UCNPs. NIR light is absorbed and the energy transmitted to the Yb^{3+} ion through a so-called FRET. The Er^{3+} ion then accepts the energy from the excited Yb^{3+} ion, giving rise to upconverted Er^{3+} emission. (b) Emission (red) and absorption (green) spectra of the cyanine dye (IR-806) and $NaYF_4$:Yb,Er UCNPs. (Reprinted with permission from Ref. (Xie and Liu 2012), copyright 2012)

Very recently, using the third-party NIR absorber as an antenna has been demonstrated to dramatically enhance the upconversion luminescence of UCNPs (Fig. 1.14) (Xie and Liu 2012, Zou, Visser et al. 2012). It is well known that Yb^{3+} ions as a sensitizer are co-doped with the common activator (Er, Ho, Tm) to increase the upconversion emission, because Yb^{3+} ions have a larger absorption cross section to NIR light and are able to resonantly transfer the accumulated excitation energy to nearby activators. However, as a type of Ln^{3+} element, the Yb^{3+} ion is constrained by the narrowband NIR absorption, only at wavelengths around 980 nm, which highly requires that the excitation light must be perfectly matched with the absorption band of Yb^{3+} ions for the efficient upconversion luminescence. Zou and colleagues (Zou, Visser et al. 2012) now show that the introduction of an organic NIR dye (closely bound to the surface of UCNPs) with a much broader absorption spectrum (740-850 nm) can strikingly enhance the upconversion brightness, where dyes act as an antenna to trap broadband excitation photons, followed by the energy transfer to Yb^{3+} ions and then activators, such as Er^{3+} in Fig. 1.14. Eventually, the activator accepting more excitation energy can give the much efficient upconversion luminescence as a return.

1.5 Rational Design of Upconversion Nanocrystals

In order to enhance the multiplexing capability of UCNPs and their brightness, it is critical and urgent to explore the novel but facile methodology to head for better-performing UCNPs. Firstly, we are over the commonly used spectral multiplexing but going to investigate the lifetime multiplexing. With in-depth understanding of basics in the upconversion luminescence, we propose three mechanisms to finely tune temporal decay behaviors of the upconversion luminescence, in hope of eventually accomplishing various lifetimes. Secondly, we conceive a direct upconversion amplification route by enriching activators in individual UCNPs. By introducing the previously untapped high density excitation, we predict that the threshold of concentration quenching may be shifted upper, allowing a larger ensemble of effective activators in UCNPs to emit the brighter luminescence.

1.5.1 Lifetime Multiplexing (temporal)

For the replacement of the spectral multiplexing, the refreshing multiplexed scheme is required. Lifetime multiplexing, the temporal discrimination, is considered as an alternative exploitable methodology. The rationale behind the lifetime multiplexing is mainly reinforced by following reasons: (1) The upconversion lifetime can be engineered to produce multiplexed non-crosstalking lifetime bands (Fig. 1.15a). For Ln^{3+} ions, parity-forbidden electronic transitions permit the excited state to commonly persist hundreds of μs (Fig. 1.15b). Fine-tuning upconversion lifetime is accessible for several well-established routes, which provide the high flexibility in pursuit of sufficiently distinguishable multiplexed lifetimes. (2) The upconversion lifetime is a stable temporal decay constant measured at a single excitation wavelength, relatively insensitive to measurement conditions. Since the excited state lifetime of interest is determined by the inverse of total decay rates through a number of different (radiative and/or nonradiative) decay pathways, UCNPs prepared in identical conditions exhibit a consistent lifetime value with minor fluctuations. In the end, the statistic lifetime acquisition of abundant UCNPs would lead to a narrow lifetime distribution histogram with symmetric shape (Fig. 1.15a).

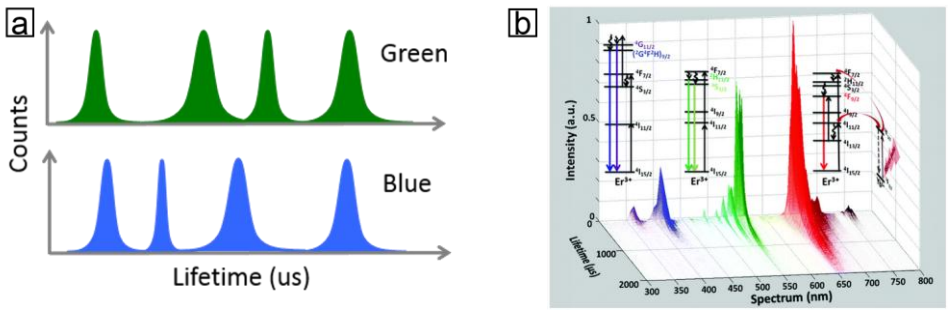

Figure 1.15. (a) Scheme of lifetime histograms on top of upconversion colours (e.g., green and blue). Each lifetime channel has different CVs, but they are narrow and avoid the overlapping problem. This is designed for the lifetime multiplexing. (b) The 3-dimensional time-resolved luminescence spectra from $NaYF_4$:Yb/Er UCNPs showing the long lifetime of upconversion emissions when wavelengths spaning from blue to red. The transparency factor was adjusted according to intensity values on each colour channels for the improved visibility on lifetime decays. (Reprinted with permission from Ref. (Zhang, McKay et al. 2013), copyright 2013)

Underpinned by above positives, we predict that the multiplexing imaging or sensing can be steadily performed by making use of distinct lifetimes to discriminate targets. The lifetime multiplexing has great potentials as an applicable and adorable approach to expand optical multiplexed channels. The lifetime multiplexing is fully compatible with the spectral discrimination. This offers the multiplexing capability can be enlarged by the multiplication instead of sum when combining lifetime and spectral multiplexing channels. For example, on top of current upconversion colours (blue, green and red), 10 distinguishable lifetimes for each colour and three independent colours principally result in a coding capacity of 999 (=10^3-1).

To separate upconversion lifetimes, two established mechanisms are available to influence the nonradiative energy transfer efficiency: varying the average distance between sensitizers and activators through doping different level of Ln^{3+} ions and controlling the FRET *via* managing ratios of the donor and the acceptor. Furthermore, the fact that the upconversion lifetime decreases with the reduction of particle size is developed to attain the lifetime multiplexing. Different from microscale or bulk luminescent materials, the size of UCNPs has a profound impact on their own optical properties, partially attributed to that the higher surface-to-volume ratio in nanoscale can accelerate the nonradiative decay to surface quenchers. Although the primary principle of the size-tunable upconversion lifetime has been discovered, the comprehensive understanding on the role of particle size in the upconversion luminescence is still not on the ground, in particular from the temporal decay perspective. Hence, our first result chapter (Chapter 3) is aimed to strengthen the knowledge on the size-dependent upconversion luminescence and lay the foundation for the size-controllable lifetime multiplexing.

1.5.2 Enriching Activators to Enhance Brightness

At present, the brightness of UCNPs is not at satisfying level. In the pool of various amplifying methods, the simplest way is to directly increase activators in individual UCNPs (Fig. 1.16). In theory, the larger ensemble of activators could emit the stronger upconversion signal. Nevertheless, to our knowledge, no attempt has been successful to

enhance the upconversion brightness by continuous doping activators in UCNPs, because it is strictly restricted by concentration quenching effect. The concentration quenching causes the diminished brightness when the doping level of activators is higher than the optimal concentration threshold. This concentration threshold confines a very small number of effective activators in individual UCNPs. For example, 2 mol% Er^{3+} doped in ~25 nm UCNPs only corresponds to approximately 700 Er^{3+} ions (Wu, Han et al. 2009).

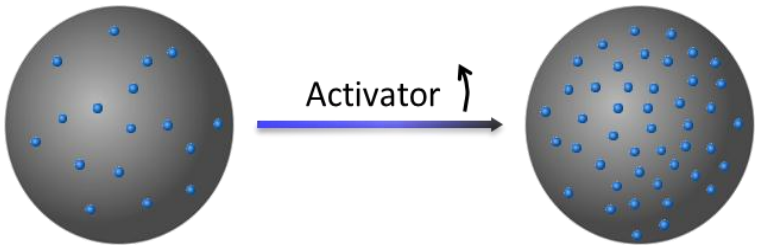

Figure 1.16. An ideal and direct way to amplify the upconversion signal *via* enriching activators. The larger amount of ensemble of activators should emit the stronger light than before without concentration quenching.

Therefore, the core issue that remain to be addressed is to find out a solution to elevate the concentration quenching threshold. If successful, more effective activators will be allowed to incorporated into UCNPs for the essentially enhancement of the upconversion emission. In combination with other established amplification methods, the conversion efficiency and optical brightness of UCNPs are anticipated to be notably leveraged.

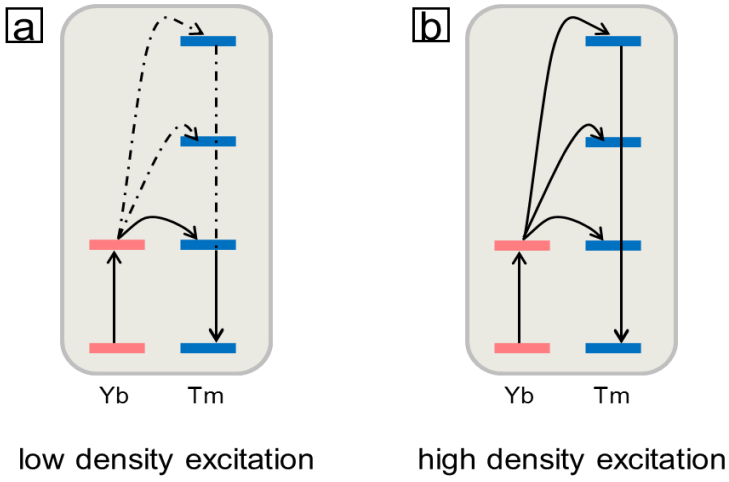

Figure 1.17. The hypothesized upconversion process of heavy-doping Tm^{3+} in UCNPs under the low density excitation (a) and the high density excitation (b). The low power excitation is hard to populate all Tm^{3+} at excited states (only to the metastable state), but the high power excitation recover the upconversion process. For simplification, the existed concentration quenching due to the deleterious cross relaxation is not illustrated in this scheme.

The upconversion concentration quenching has been ascribed to the deleterious cross relaxation in heavily doped UCNPs, but it appears that all results were given under the low excitation irradiance (<100 W cm^{-2}) (Zhang, Li et al. 2011). Enormously different from this excitation, much denser excitation is illuminated on UCNPs when they are used as fluorescence bioprobes for observation under fluorescence microscopy or confocal microscopy. Considering the experimental difference in the excitation irradiance, we are encouraged to hypothesize that the cross relaxation may not be the only reason resulting in concentration quenching, and the low excitation irradiance can fairly account for the low concentration quenching threshold as well. This is because that, for heavily doped UCNPs, the excitation irradiance is shared by more activators. In contrast to low excitation irradiance and low activator concentrations, the low excitation irradiance but high activator concentrations have to leave the majority of input photons staying in the lowest excited state instead of higher emitting excited states (Fig. 1.17a). If such analysis is real now but hidden before, we deduce that the sufficient excitation irradiance on heavily doped UCNPs can populate previously inactive higher excited states again (Fig. 1.17b). To this end, the upconversion brightness is enhanced due to

the enrichment of activators in combination with the strong excitation irradiance (>10^4 W cm^{-2}). To shed light on this hypothesis, the Chapter 5 is designed to investigate the unexplored excitation range for a series of UCNPs with different doping levels of activators; a novel way towards the upconversion emission enhancement.

Chapter 2: Methodology

In Chapter 2, we describe key features of two advanced instruments which have been used to characterize optical properties of our purpose-designed UCNPs. To demonstrate the lifetime multiplexing strategy, I worked closely with Dr. Yiqing Lu, who built a time-resolved orthogonal scanning automated microscope (TR-OSAM) implanting with the time-gated detection and lifetime analysing algorithms. To convince the hypothesis that the enhanced upconversion luminescence can be conferred by enriching active emitters through increasing the excitation irradiance, we collaborated with Prof. Tanya Monro's group (University of Adelaide), who has developed the microstructured fibre dip sensor, to ideally achieve the intense excitation irradiance along the fibre and quantify luminescent intensities.

2.1 Time-Resolved Orthogonal Scanning Automated Microscope

2.1.1 Optical configurations

The TR-OSAM was modified from an epi-fluorescence inverted microscope (Olympus IX71) (Fig. 1.1a). The TR-OSAM is equipped with a motorised stage (H117, Prior Scientific) and coupled with a single-mode NIR diode laser 980 nm as the excitation source (LE-LS-980-300-FCS, LEO Photonics, Shenzhen, China). The excitation light reflected by a dichroic filter (FF750-SDi02, Semrock) is focused onto the sample slide through a 60× objective lens (NT38-340, NA = 0.75, Edmund Optics). The luminescence signal is collected by the same objective, split from the excitation optical path by the dichroic mirror. It is then transmitted through a band-pass emission filter (e.g., FF02-475/50, Semrock, for blue emission) before being coupled into a multi-mode fibre (M24L01, Thorlabs). The luminescence signal is eventually delivered to a time-gated photomultiplier tube (PMT, H10304-20, Hamamatsu, electron amplification gain

10^6). The output current signal is converted into the voltage signal *via* a low-noise preamplifier (transimpedance gain 10^5 μV/μA, DLPCA-200, FEMTO, Germany).

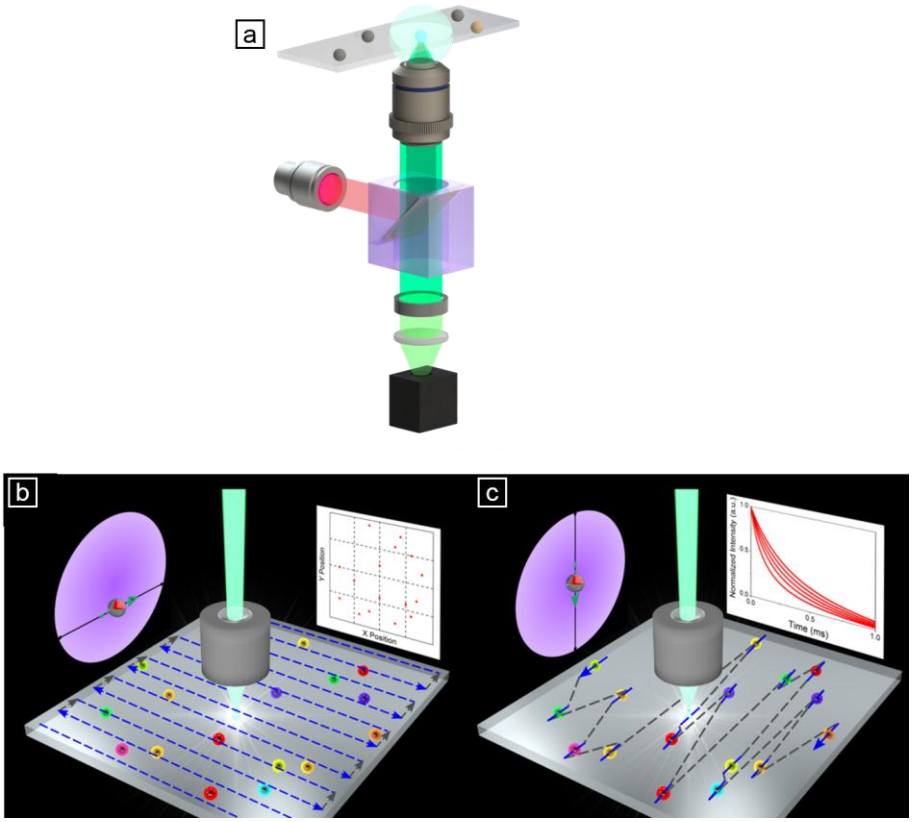

Figure 1.1. (a) Schematic of the optical layout of the TR-OSAM. (b) Cartoon showing the TR-OSAM maps targets by recording signal trains of luminescent intensities in the background-free condition. (c) The TR-OSAM decoding the luminescence lifetime of each detected target in real time. Positional coordinates of targets identified in (b) can guide sequential orthogonal scans for the spot-by-spot inspection at the centre of the field of view.

2.1.2 Orthogonal scanning strategy

One major advance in the TR-OSAM is that signal trains acquired from the field-of-view detection can be used to locate precise coordinates of targets (luminescent particles or labelled microorganisms) across the sample slide under the free-background condition. Fig. 1.1b illustrates the novel two-step on-the-fly orthogonal scanning strategy that we have implemented in the microscope for the rapid detection and precise

location of targets. Firstly, the sample slide is fully scanned following the serpentine pattern, with the continuous motion along the X-axis and the stepwise translation along the Y-axis. The interval of Y-axis translation lines can be adjusted by the field-of-view size. By doing this continuous X-axis scan, X-coordinate values of luminescent targets are essentially identified by recording signal trains. Then, the second orthogonal continuous scan along Y-axis is carried, but where the corresponding X- coordinate have been memorized in the system owing to the initial X-axis scanning to guide the Y-axis scan. In this way, each Y-axis scan line only transits targets confirmed in X-axis scanning, so that the total inspection time is substantially decreased, typically around 3.3 minutes for a slide area of 15 × 15 mm^2. Such two-step orthogonal scanning is capable of localizing the precise X- and Y-coordinates of any randomly-distributed target.

2.1.3 Lifetime decoding

In addition to the orthogonal scanning technique, the capability of decoding luminescence decay profiles of the TR-OSAM allows to read and distinguish lifetimes of the different UCNPs-stained individual target at the high speed (Fig. 1.1c). This real-time computation for lifetimes and lifetime populations is based on the Method of Successive Integration, a high-throughput analytical technique with the algorithm for the fast fitting and data binning. The process is related to respective waveforms of lifetimes, consisting of counts of photons individually collected at *M* temporal intervals (channels) of the same length *T*. The detail of optimizing configurations of *M* and *T*, and the lifetime fitting algorithm can be found in our publications (Lu, Jin et al. 2011, Lu, Xi et al. 2012).

In the measurement, the period of the time-gating cycle is set to 4 ms. The NIR laser is modulated to produce the 190 μs excitation pulse. With the 10 μs delay after the laser pulse, the time-gated PMT is switched on to capture the long-lifetime signal for 3.8 ms (detection window). Here, emission photons are counted and registered into 190 time intervals (channels, with the equal width of 20 μs). The pulse excitation, time-gated data collection and exponential decay profiles fitting (in real-time to calculate lifetimes of individual targets) are synchronised, followed by processing by a multifunction data acquisition device (USB-6353, National Instruments) and a purposely-built Labview

program. This instrument can be used to identify and on-the-fly analyse lifetimes of multiple targets, capable of producing statistical datasets to distinguish their lifetime-coded populations.

2.2 The Fibre Sensing System

2.2.1 Experimental configuration

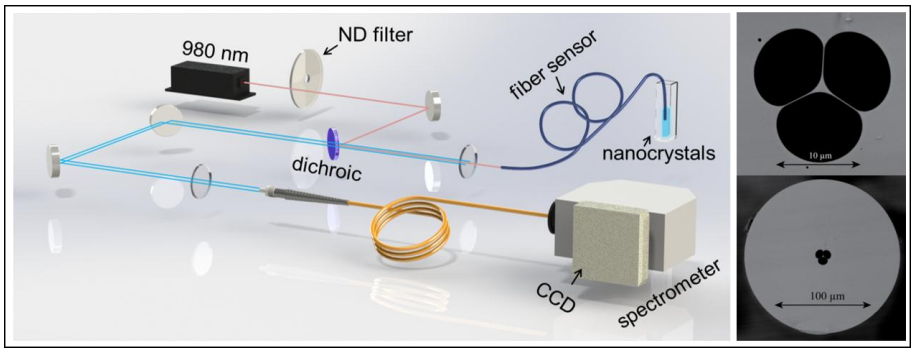

Figure 1.2. Schematic of the set up for capturing the upconversion luminescence of UCNPs using a suspended-core microstructured optical fibre (insert panel: SEM image the cross section of the microstructured optical fibre at different magnifications. The diameter of the fibre core is ~1.43 μm with three ~160 μm air holes.).

The suspended-core microstructured optical fibre is used in this study to capture the luminescent signal of UCNPs (Fig. 1.2). The microstructured optical fibre contains a solid glass core surrounded by three holes that run the length of the fibre (Ebendorff-Heidepriem and Monro 2007, Ebendorff-Heidepriem, Warren-Smith et al. 2009). The homogenized 980 nm CW diode laser in a single mode optical fibre can be coupled into the fibre through a dichroic mirror and guided to converge into the suspended glass core *via* a 60× microscope objective. Uniform UCNPs dispersed in cyclohexane are drawn into holes of the fibre by capillary motion, which brings UCNPs into the vicinity of the guided excitation light. While the incident NIR light propagates along the fibre towards exit, UCNPs filled in holes can be efficiently excited to emit light. Their emissions are collected by the same fibre core and captured by detector for the light propagating in the

backward direction (i.e. light travelling towards the launch/input end of the fibre), with the dichroic mirror passing the visible-NIR emission. A broad band-pass filter (405 nm to 842 nm; Semrock FF01-842) before the detector is used to further suppress the scattered NIR light. A Horiba iHR320 monochromator with the charged-coupled device (CCD) is installed with the fibre-coupled configuration for the signal collection.

2.2.2 Microstructured optical fibre

The microstructured optical fibre used in these experiments was fabricated in-house at the University of Adelaide. It was made from F2 glass, a commercially available lead-silicate glass from Schott Glass Co. and tailored to supress the background luminescence of the glass itself. The microstructured optical fibre was produced *via* preform extrusion and subsequently drawn into fibre using a cane-in-tube technique (Ebendorff-Heidepriem and Monro 2007). The extrusion process involves heating up the glass to its softening point, and then applying a force to the top of the billet so that the softened glass is pushed through the extrusion die. The fibre core diameter defined as the diameter of a circle with the equivalent area as that of the largest triangle which can be wholly contained within the core structure (Ebendorff-Heidepriem, Warren-Smith et al. 2009), was 1.43 μm and the outer diameter was 160 μm, as determined by SEM images (Fig. 1.2). The suspended glass core design is used to provide the large light-matter interaction between the excited light and analytes (UCNPs in our case) along the fibre. The fabricated fibre had a loss of 0.7 ± 0.2 dB/m at 980 nm, 0.8 ± 0.2 dB/m at 802 nm, 0.9 ± 0.2 dB/m at 744 nm, 1.1 ± 0.2 dB/m at 660 nm, 1.4 ± 0.2 dB/m at 514 nm, 1.7 ± 0.3 dB/m at 480 nm, 1.9 ± 0.3 dB/m at 455 nm.

2.2.3 Features of Fibre-Sensing System

The microstructured optical fibre provides a powerful platform to probe and quantify the upconversion luminescence, and main features for such applications are outlined below:

- High density laser excitation along the fibre

  A single-mode 980 nm CW diode laser beam (100 mW) launched into a suspended-core microstructured optical fibre can produce the excitation

irradiance up to 2.5×10^6 W cm^{-2}. To generate the high density excitation irradiance, the suspended core in the optical fibre is devised to concentrate the incident NIR laser into a submicro spot. Consequently, the input of 1 mW laser power undergoes a substantial boost to a power density of ~10^4 W cm^{-2}. The unique fibre design with sub-wavelength feature and high-index glass encourages the high-intensity excitation light to be confined at the glass-hole interface and to propagate along the fibre in a long distance, e.g., ~10 cm (Afshar V, Warren-Smith et al. 2007). The choice of the microstructured optical fibre is thus superior to the conventional fluorescence microscope and confocal microscope that only localize the high-density laser excitation at the focal plane within the laser spot size and depth in micrometre scale.

- Ultrasensitive-detection capability

  The microstructured optical fibre has been proven as an ultrasensitive sensing system. Neither the glass fibre (fabricated by lead-silicate glass) nor the analyte (e.g., biological molecules) responds to NIR 980 nm excitation light, so that the background autofluorescence can be supressed or removed. As the intensity I of an upconversion luminescence *via* the sequential absorption of n photons has a dependence on the pumping light irradiance P

$$I \propto P^n.$$

  Thus, the strong (high laser irradiance) and long (along the fibre length) light-matter interaction in the microstructured optical fibre enables to maximize the upconversion signal. In terms of the signal collection, the backward luminescence signal is captured as the higher efficiency of luminescence collection occurring in backward modes in comparison with that of forward modes (Afshar V, Ruan et al. 2008), which has been demonstrated by numerically simulating with experimentally confirming ratios of the forward luminescence capture fraction (Φ_F) and the backward luminescence capture fraction(Φ_B). The Φ_F and Φ_B can be expressed as

$$\Phi_F = 2\mathrm{A}\frac{\exp(-\gamma_i^F L)}{\gamma_j^E - \gamma_i^F}\{1 - \exp[(\gamma_i^F - \gamma_j^E)L]\},$$

$$\Phi_B = 2\mathrm{A}\frac{1}{\gamma_j^E + \gamma_i^F}\{1 - \exp[-(\gamma_i^F + \gamma_j^E)L]\},$$

where A is the effective area of the fundamental mode for the specific geometry of the microstructured fibre; γ_j represents all absorption mechanisms to the *j*th mode light in the fibre, including absorption due to the Beer-Lambert law; *L* refers to the length of the filled-hole region.

- Nanolitre-scale sensor

  Owing to the design of microscale hollow holes of the fibre, volumes of analytes in nanolitre scale will be loaded in the optical fibre dip sensor. It offers the fibre as a dip sensor applicable to detect the trace amount of analytes labelled by UCNPs.

2.3 Conclusion

In summary, we have developed the advanced TR-OSAM system from an epi-fluorescence inverted microscope. With the novel on-the-fly orthogonal scanning strategy and high-throughput analytical algorithm and technique, the TR-OSAM is powerful to read and distinguish populations of lifetime-encoded targets in real time. This paves the way to assess for the lifetime multiplexing in hardware part. The remaining very important step is to design and explore different methods of tuning lifetimes of UCNPs as well as to examine lifetime multiplexing applications (Chapter 3 and 4).

Moreover, we have adopted the microstructured optical fibre as the platform to enhance the upconversion brightness. As the delivered excitation light can be converged in the core of the optical fibre and well transmit along the solid glass core with few loss in a certain distance, the microstructured optical fibre ideally ensure all absorbed UCNPs available to the exposure to high excitation irradiance. This advantage remarkably increases the number of individual UCNPs exposed to the focused light compared to that of with the microscope, e.g., laser confocal microscope. Thus, the microstructured fibre is promising to amplify the signal and disclose the hidden phenomena in an easier way. The unique merit of the microstructured fibre is audited in Chapter 5, where the varying activator concentrations doped UCNPs are synthesized, and the Tm^{3+}-Yb^{3+} binary dopants system is selected to minimize unrelated factors (such as energy back

transfer) to focus on the relationship between the excitation irradiance and activator concentrations.

Chapter 3: Size-dependent Upconversion

This chapter establishes the route to synthesize $NaYF_4$:Er,Yb UCNPs in different sizes and crystal phases. Characterizing luminescent properties of as-prepared UCNPs, we observed that the spectra and lifetime of upconversion luminescence are size-dependent. To comprehensively understand the role of the nanocrystal size, rate equations were developed for the quantitative analysis of upconversion luminescence dynamics and a core-shell physical model was employed to further explain the relation between the upconversion luminescence and the UCNPs size. Applying the core-shell model and fitting the experimental data in our and others' reports, we clarified the influence of four non-radiative recombination mechanisms in UCNPs, and concluded that the surface defect density becomes dominant in nonradiative decays when the nanocrystal size is smaller than 15 nm. This work is presented in the form of a journal publication from *Nanoscale*.

3.1 Contributions to Paper 1

TABLE 3-1 Author contributions.

	J.Z.	Z.L.	Y.Y.	C.M.	J.A.P.	J.M.D.	D.J.	E.M.G.
Project Design	●				●		●	●
Materials	●	●	●				●	
System Setup	●			●				
Data Collection	●						●	
Analysis	●				●	●	●	●
Manuscript & Figures	●	●	●		●	●	●	●
Modelling	●					●	●	●
Supplementary Information	●						●	●

The research project in Chapter 3 was mainly conceived by myself, Ewa Goldys, and Dayong Jin. I carried out the experimental section, including setting up the UCNPs fabrication system, samples preparation, building the upconversion microscope (with Dayong Jin), and characterizations, and analysed the acquired data. Under the supervision of Ewa Goldys, Dayong Jin, and Judith Dawes, I am responsible for drafting the manuscript, preparing figures and the supplementary information. Ewa Goldys and I led the theoretical modelling with active discussions with Judith Dawes and Dayong Jin to account for the size-dependent upconversion luminescence.

3.2 Paper 1

Zhao J, Lu Z, Yin Y, McRae C, Piper J A, Dawes J M, Jin D, Goldys E G, "Upconversion luminescence with tunable lifetime in NaYF4:Yb,Er nanocrystals: role of nanocrystal size". ***Nanoscale***, 2013, **5**, 944-952.

(First published online: 12 Nov 2012)

Nanoscale

www.rsc.org/nanoscale Volume 5 | Number 3 | 7 February 2013 | Pages 825–1236

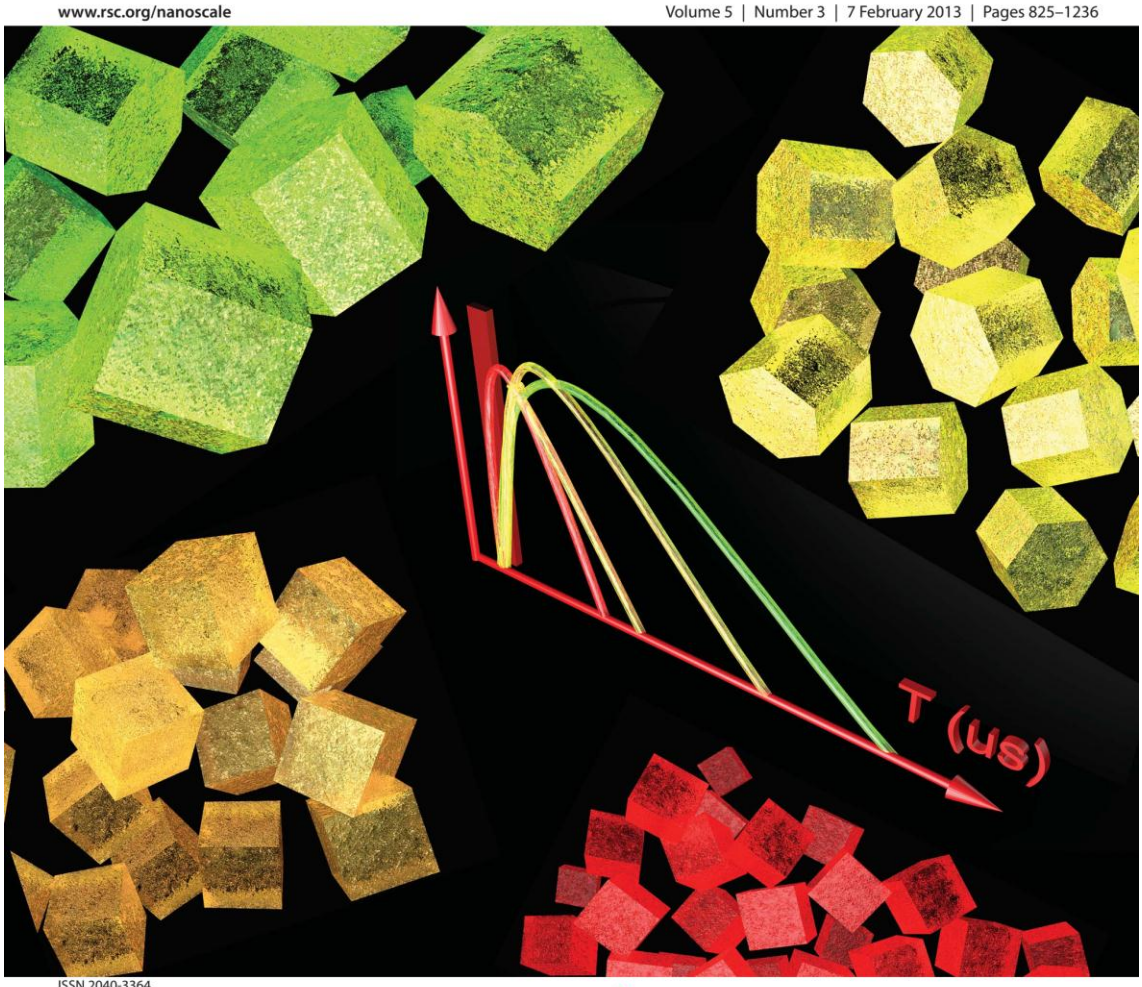

ISSN 2040-3364

RSC Publishing

PAPER
Jin *et al.*
Upconversion luminescence with tunable lifetime in $NaYF_4$:Yb,Er nanocrystals: role of nanocrystal size

NCNST

2040-3364(2013)5:3;1-L

Nanoscale

RSC Publishing

PAPER

View Article Online
View Journal | View Issue

Upconversion luminescence with tunable lifetime in $NaYF_4$:Yb,Er nanocrystals: role of nanocrystal size†

Cite this: *Nanoscale*, 2013, **5**, 944

Jiangbo Zhao,[a] Zhenda Lu,[b] Yadong Yin,[b] Christopher McRae,[c] James A. Piper,[a] Judith M. Dawes,[a] Dayong Jin*[a] and Ewa M. Goldys*[a]

Despite recent achievements to reduce surface quenching in $NaYF_4$:Yb,Er nanocrystals, a complete understanding of how the nanocrystal size affects the brightness of upconversion luminescence is still incomplete. Here we investigated upconversion luminescence of Yb,Er-doped nanocrystals in a broad range of sizes from 6 nm to 45 nm (cubic or hexagonal phases), displaying an increasing red-to-green luminescence intensity ratio and reduced luminescence lifetimes with decreasing size. By analyzing the upconversion process with a set of rate equations, we found that their asymptotic analytic solutions explain lower decay rates of red compared to green upconversion luminescence. Furthermore, we quantified the effect of the surface on luminescence lifetime in a model where nanocrystal emitters are divided between the near-surface and inside regions of each nanocrystal. We clarify the influence of the four nonradiative recombination mechanisms (intrinsic phonon modes, vibration energy of surface ligands, solvent-mediated quenching, and surface defects) on the decay rates for different-size nanocrystals, and find that the defect density dominates decay rates for small (below 15 nm) nanocrystals. Our results indicate that a defect-reduction strategy is a key step in producing small upconversion nanocrystals with increased brightness for a variety of bioimaging and biosensing applications.

Received 28th August 2012
Accepted 6th November 2012

DOI: 10.1039/c2nr32482b

www.rsc.org/nanoscale

Introduction

Lanthanide-doped upconversion nanocrystals are uniquely suited to a range of applications including displays,[1–3] solar cells,[4–8] nano-thermometry in cells,[9] photodynamic therapy,[10] labelling for *in vitro* and *in vivo* photoluminescence bioimaging,[11–14] bioassays,[15] and others.[16–19] These nanocrystals can be excited by near-infrared (NIR) radiation in the optimum transparency window of biological tissue, and they produce comparatively bright, visible multi-colour emissions. This NIR excitation makes it possible to avoid the autofluorescence background which otherwise is a major challenge in conventional fluorescent labelling under UV or visible excitation.[20,21] Furthermore, upconversion nanocrystals exhibit low toxicity and are photostable, non-blinking, and applicable as dual labels.[22] Among upconversion nanomaterials, $NaYF_4$ nanocrystals have been intensely investigated as the most efficient upconversion host materials available to date.[23] They are bright enough so that single upconversion nanocrystals as small as 27 nm can be observed in confocal microscopy.[11]

Currently, well-developed synthesis methods allow good control over the nanocrystal phase,[1,24] doping concentration, and particle size within a broad range.[25–28] Such fine control is needed to ensure an efficient luminescence yield due to a complicated energy transfer between the lanthanide elements in the upconversion process.[29] Small nanocrystals are preferred for biological applications but it has been difficult to synthesize upconversion nanocrystals smaller than 30 nm with high quantum yield since a small size is accompanied by a decrease in the total number of emitters and proportionally increased surface quenching. Although empirical strategies such as deposition of an undoped $NaYF_4$ shell over the lanthanide-doped nanocrystal core have been used to address the loss in brightness[30–32] and mitigate the surface quenching effect responsible for the size-dependent upconversion luminescence,[33] the understanding of fundamental aspects of upconversion emission, particularly the upconversion kinetics and the details of the quenching mechanisms in different-size nanocrystals, is still incomplete.

Here we show that the optical properties such as the intensity ratio and decay lifetimes of upconversion red and green emission of $NaYF_4$:Yb,Er nanocrystals can be tailored by tuning

[a]*MQ BioFocus Research Centre, Faculty of Science, Macquarie University, NSW 2109, Sydney, Australia. E-mail: dayong.jin@mq.edu.au; ewa.goldys@mq.edu.au*
[b]*Department of Chemistry, University of California, Riverside, CA 92521, USA*
[c]*Department of Chemistry and Biomolecular Sciences, Faculty of Science, Macquarie University, NSW 2109, Sydney, Australia*

† Electronic supplementary information (ESI) available: Additional information for size distribution histograms (Fig. S1), upconversion power-dependence gradients (Fig. S2), upconversion luminescence decay in different surroundings (Fig. S3), and rate equations for Yb,Er-doped nanocrystals and the asymptotic solutions are available. See DOI: 10.1039/c2nr32482b

the size of the nanocrystals. We also quantitatively analyse the upconversion processes, based on rate equations for the populations of the relevant 4f lanthanide electron states. We derive analytical asymptotic solutions of these rate equations, thereby interpreting the observed luminescence decay lifetimes which can be regarded as the fingerprints of the multiple radiative, nonradiative and energy transfer processes in these nanocrystals. Furthermore, we quantify the proposed "surface effects" to clarify the underpinning mechanisms with their varying contributions to the upconversion lifetimes. By investigating their dependence on the particle size and surface conditions in both cubic and hexagonal nanocrystals, we confirm that increasing crystalline defect density is the major reason for the observed lifetime decrease in very small nanocrystals.

It is widely known that the crystalline phase has a significant effect on the upconversion luminescence. In bulk materials and large-size nanocrystals the upconversion efficiency in hexagonal phase of $NaYF_4$ (β-$NaYF_4$) is at least an order of magnitude higher than the cubic phase (α-$NaYF_4$).[1,34,35] However, as the size of the nanocrystals is reduced below 40 nm, the effect of the size tends to become more pronounced. For example, Wang *et al.* observed that 10–25 nm α-$NaYF_4$ nanocrystals produce a stronger emission than similar sized β-$NaYF_4$.[1] Other authors reported that sub-10 nm β-$NaYF_4$ shows a higher red to green ratio compared to the 37 nm β-$NaYF_4$.[36] The influence of the size on fluorescence decay has also been established,[36,37] and small sub-10 nm α- and β-$NaYF_4$ have been found to have similar decay times but 20 nm α-phase nanocrystals have longer decays than a similar size β-phase.

Results and discussion

Morphology and crystalline structure of different-size $NaYF_4$ nanocrystals

In this study, monodisperse nanocrystals with controllable size and phase were synthesized *via* thermal decomposition of metal oleate precursors by modifying the reported procedure[1,38] (See Methods for more details). The resulting nanocrystals form single crystallites which are uniform in size, as shown in transmission electron microscopy (TEM) images (Fig. 1a–f). The size of the upconversion nanocrystals was varied from 6 nm to 45 nm by tuning the experimental variables, specifically reaction time and temperature.[1,27] For example, uniform $NaYF_4$ average nanoplates with a top/bottom surface area ~45 nm × 45 nm and length (~48 nm) were obtained at long reaction times at elevated temperatures (Fig. 1f). More information on the size distribution can be found in the ESI, Fig. S1.† Good crystallinity of the as-synthesized nanocrystals was confirmed by X-ray diffraction (XRD) patterns (Fig. 2a), which are characterised by well-defined peaks. XRD indicates that smaller nanocrystals (6–14 nm) are cubic (α-phase, Fig. 1a–c) and larger ones (20–45 nm) are hexagonal (β-phase, Fig. 1d–f). This is consistent with the findings in ref. 1 and 27, where harsher reaction conditions (longer time and/or higher temperature) facilitate growth and transformation of $NaYF_4$ nanocrystals from α- to β-phase. All diffraction peaks have been fully identified in accordance with the Joint Committee on Powder Diffraction Standards (JCPDS) (file numbers #77-2042 for cubic $NaYF_4$ and #16-0334 for hexagonal $NaYF_4$ crystals). No trace of diffraction peaks corresponding to other phases or impurities was observed. The full width at half maximum (FWHM) of these peaks *versus* the X-ray reflection angle plotted in Fig. 2b and c shows that decreasing nanocrystal size leads to peak broadening.

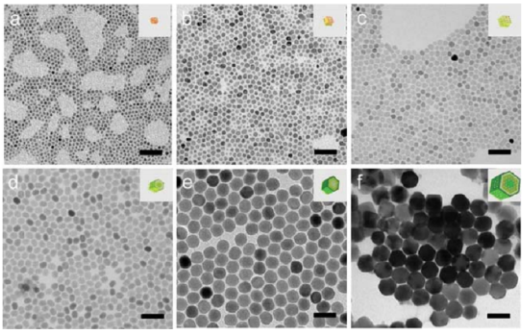

Fig. 1 Transmission electron microscopy characterization of $NaYF_4$:Yb,Er nanocrystals indicating morphology. (a–f) TEM images show nanocrystals with average diameters of 6 nm (a), 9 nm (b), 14 nm (c), 20 nm (d), 31 nm (e) and 45 nm (W) × 48 (L) nm (f), respectively. Scale bars are 50 nm (insets are the corresponding shapes of the nanocrystals in the TEM image).

Upconversion fluorescence and upconversion decay times, dependence on $NaYF_4$ nanocrystals size

Under NIR 980 nm laser excitation, Er^{3+} ions in $NaYF_4$ nanocrystals exhibit dual emission bands (green and red) associated with upconversion processes.[39,40] The simplified scheme in Fig. 3a illustrates the upconversion, nonradiative, radiative processes in the Yb^{3+}/Er^{3+} system. It shows that following absorption of pumping light by the Yb^{3+} sensitizers *via* the $^2F_{7/2} \rightarrow {}^2F_{5/2}$ transition, the nearby Er^{3+} ions are excited to the $^4F_{7/2}$ state by a two-step energy transfer from the excited Yb^{3+} ions. Subsequent nonradiative processes within the Er^{3+} ions populate their radiating states. The characteristic emission peaks are attributed to the $^2H_{11/2}$, $^4S_{3/2} \rightarrow {}^4I_{15/2}$ transitions in the green spectral region with the red emission arising from $^4F_{9/2} \rightarrow {}^4I_{15/2}$. It is well established that the green and red emission channels compete for transferred energy due to the nonradiative decays of $^4I_{11/2} \rightarrow {}^4I_{13/2}$ (~3598 cm^{-1}) and $^4S_{3/2} \rightarrow {}^4F_{9/2}$ (~3142 cm^{-1}).[41] Therefore, although the luminescence intensities in both emission bands increase for larger nanocrystals, smaller nanocrystals display a relatively higher red-to-green ratio of upconversion emission (Fig. 3b). As reported in ref. 42 and 43, this is because nonradiative decays across the relevant energy gaps ($^4I_{11/2} \rightarrow {}^4I_{13/2}$ and $^4S_{3/2} \rightarrow {}^4F_{9/2}$) are more efficient for such smaller particles. Fig. 3c and d show that smaller size nanocrystals exhibit shorter decay times than the larger ones, and in each case the decay time of the red emission is longer than the green emission, as observed in previous reports.[44,45] The red and green lifetimes have been reported to be practically unchanged with varying excitation power density up

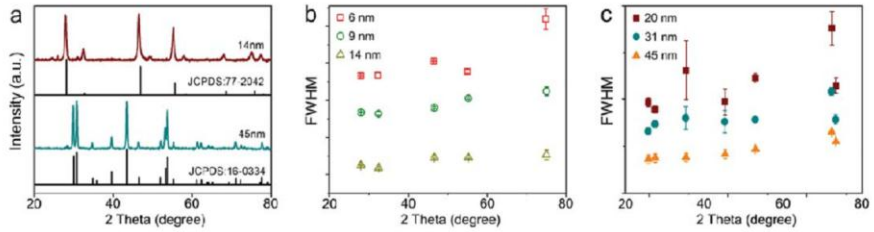

Fig. 2 (a) The X-ray powder diffraction patterns for α-/β-NaYF4:Yb,Er nanocrystals. The figure shows the representative data for 14 nm and 45 nm nanocrystals, identified as cubic and hexagonal phase, respectively (in comparison with JCPDS:77-204 and JCPDS:16-0334 file shown). (b and c) X-ray powder peak full width at half maximum (FWHM) as a function of diffraction angle for various nanocrystal sizes as labeled.

to 500 W cm^{-2}.[41] The measured power-dependence of luminescence for all size nanocrystals shows that the upconversion intensity is proportional to the n-th power of excitation with n between 1 and 2 for both red and green emission (see the ESI, Fig. S2†). This suggests that the cooperative upconversion is significant, while emission from other intermediate states to the ground state can be neglected.[46] These assumptions inform our rate equation analysis below. We also note that the size-dependence of the green to red ratio at constant incident power observed in this work has also been reported by other authors; for example, Schietinger *et al.*[47] and Niu *et al.*[48] The green-to-red ratio also depends on the excitation power.[11].

Quantitative analysis using rate equations

To shed more light on the size-dependent upconversion luminescent properties in the investigated nanocrystals and enable quantitative analysis, a set of rate equations was established. They were based on the key upconversion processes in this Yb^{3+}/Er^{3+} doped material, as qualitatively discussed in ref. 49 and 50. The relevant Yb^{3+} and Er^{3+}states are indexed as in Fig. 3a. These simplified rate equations describe the evolution of occupied state populations in the Yb^{3+} excited state (Yb,2) and four Er^{3+} states (Er,2), (Er,3), (Er,5), and (Er,6). We denote $N_{Er(Yb),i}$ as the population density of the occupied level i of Er(Yb), and N_{Er} is the total density of Er^{3+} ions. We assume that the Er^{3+} states

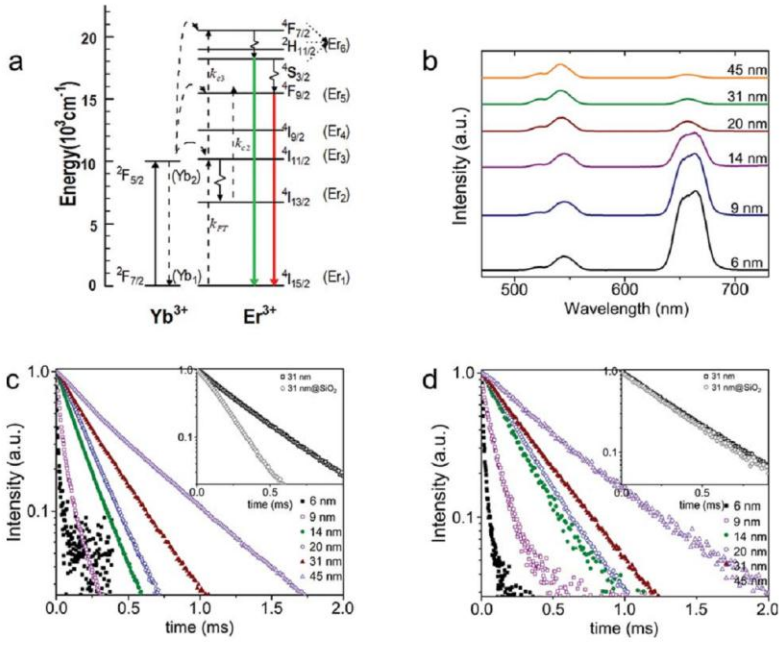

Fig. 3 (a) Main radiative/nonradiative transitions and energy transfer processes relevant for the upconversion luminescence in $NaYF_4$:Yb,Er nanocrystals. Arrows indicate: ⟶ NIR excitation, ⇢ energy transfers, ⇝ multiphonon nonradiative relaxation, and → → upconversion emission. (b) Room-temperature upconversion emission spectra of $NaYF_4$:Yb,Er nanocrystals with varying size from 6 nm to 45 nm (IR excitation intensity ~ 5 W cm^{-2}). The spectrum was normalized to Er^{3+} emission at ~540 nm. (c and d) Evolution of lifetime decays for a series of $NaYF_4$:Yb,Er nanocrystals at the green (c) and red (d) upconversion emission bands, respectively. Insets indicate the lifetime variation of green (c) and red (d) upconversion luminescence for 31 nm nanocrystals after coating with a ~10 nm-thick silica layer.

above (Er,6) relax very rapidly to the state (Er,6) by multiphonon relaxation due to the small energy gaps, and the same argument applies to the state (Er,4), thus these are ignored in the rate equations. In our analysis, the rate equations involve single-ion and two-ion processes only. The first single ion mechanism accounts for decay processes occurring within Er^{3+} starting from level i ($i = 2, 3, 5, 6$). Their corresponding population decays are described by the total radiative and nonradiative rates.

$$W_i = W_{i(\mathrm{R})} + W_{i(\mathrm{NR})} \tag{1}$$

which is equal to the reciprocal of the measured lifetime τ_i. W_{ij} refers to the rate of transfer of population from the i-th level to the j-th level ($i > j$). We also include single-ion processes of Yb^{3+} absorption and excited state absorption in Er^{3+}, described by the absorption cross sections σ_{Yb} for ground state Yb^{3+} and $\sigma_{\mathrm{ESA2(3)}}$ for levels 2 and 3 in Er^{3+}. The latter process produces upconversion *via* excited state absorption. Among the two-ion process, we only consider those that involve pairs of Yb^{3+}–Er^{3+} (cooperative upconversion *via* energy transfer), and neglect the pairwise Er–Er energy transfer (cumulative upconversion). This is because Yb^{3+} sensitisation is well-known to be critical for strong upconversion emission in Er^{3+} doped nanocrystals.[39] We define $k_{\mathrm{c2(3)}}$ as the cooperative upconversion coefficient for the $2 \rightarrow 5$ and $3 \rightarrow 6$ upconversion processes, respectively. k_{FT} is the coefficient of forward energy transfer $Yb^{3+} \rightarrow Er^{3+}$, the main pathway for pumping Er^{3+}. However, we neglect the decay of Yb^{3+} by other channels than forward energy transfer to Er^{3+} because it is comparatively weak[51] and can be neglected at high pumping levels. Back energy transfer from Er^{3+} to Yb^{3+} is neglected as well.[51,52] Radiative and non-radiative decay from Er^{3+} level 2 is considered to be negligible.[53,54]

With these conditions, the rate equations are formulated as follows:

$$\frac{\mathrm{d}N_{\mathrm{Yb,2}}}{\mathrm{d}t} = \rho_{\mathrm{p}}\,\sigma_{\mathrm{Yb}}N_{\mathrm{Yb}} - k_{\mathrm{FT}}N_{\mathrm{Er,1}}N_{\mathrm{Yb,2}} - k_{\mathrm{c2}}N_{\mathrm{Er,2}}N_{\mathrm{Yb,2}} - k_{\mathrm{c3}}N_{\mathrm{Er,3}}N_{\mathrm{Yb,2}} \tag{2}$$

$$\frac{\mathrm{d}N_{\mathrm{Er,2}}}{\mathrm{d}t} = -k_{\mathrm{c2}}N_{\mathrm{Er,2}}N_{\mathrm{Yb,2}} - \rho_{\mathrm{p}}\,\sigma_{\mathrm{ESA2}}N_{\mathrm{Er,2}} - W_2N_{\mathrm{Er,2}} + W_{32}N_{\mathrm{Er,3}} + W_{52}N_{\mathrm{Er,5}} + W_{62}N_{\mathrm{Er,6}} \tag{3}$$

$$\frac{\mathrm{d}N_{\mathrm{Er,3}}}{\mathrm{d}t} = k_{\mathrm{FT}}N_{\mathrm{Er,1}}N_{\mathrm{Yb,2}} - \rho_{\mathrm{p}}\,\sigma_{\mathrm{ESA3}}N_{\mathrm{Er3}} - k_{\mathrm{c3}}N_{\mathrm{Er,3}}N_{\mathrm{Yb,2}} - W_3N_{\mathrm{Er,3}} + W_{53}N_{\mathrm{Er,5}} + W_{63}N_{\mathrm{Er,6}} \tag{4}$$

$$\frac{\mathrm{d}N_{\mathrm{Er,5}}}{\mathrm{d}t} = k_{\mathrm{c2}}N_{\mathrm{Er,2}}N_{\mathrm{Yb,2}} + \rho_{\mathrm{p}}\,\sigma_{\mathrm{ESA2}}N_{\mathrm{Er,2}} - W_5N_{\mathrm{Er,5}} + W_{65}N_{\mathrm{Er,6}} \tag{5}$$

$$\frac{\mathrm{d}N_{\mathrm{Er,6}}}{\mathrm{d}t} = k_{\mathrm{c3}}N_{\mathrm{Er,3}}N_{\mathrm{Yb,2}} + \rho_{\mathrm{p}}\,\sigma_{\mathrm{ESA3}}N_{\mathrm{Er,3}} - W_6N_{\mathrm{Er,6}} \tag{6}$$

The symbol ρ_{p} denotes the excitation power variable, given by

$$\rho_{\mathrm{p}} = \frac{\lambda_{\mathrm{p}}}{hc\pi {w_{\mathrm{p}}}^2}P \tag{7}$$

Here, P is the incident pump power, λ_{p} and w_{p} are the pump wavelength and beam radius, respectively, h is Planck's constant and c is the speed of light.

The observed fluorescence decay times can be interpreted by a simpler set of equations as below, which reflect that the excitation light is pulsed and decay times are measured after the pulse has ceased:

$$\frac{\mathrm{d}N_{\mathrm{Yb,2}}}{\mathrm{d}t} = -k_{\mathrm{FT}}N_{\mathrm{Er}}N_{\mathrm{Yb,2}} - k_{\mathrm{c2}}N_{\mathrm{Er,2}}N_{\mathrm{Yb,2}} - k_{\mathrm{c3}}N_{\mathrm{Er,3}}N_{\mathrm{Yb,2}} \tag{8}$$

$$\frac{\mathrm{d}N_{\mathrm{Er,2}}}{\mathrm{d}t} = -k_{\mathrm{c2}}N_{\mathrm{Er,2}}N_{\mathrm{Yb,2}} - W_2N_{\mathrm{Er,2}} + W_{32}N_{\mathrm{Er,3}} + W_{52}N_{\mathrm{Er,5}} + W_{62}N_{\mathrm{Er,6}} \tag{9}$$

$$\frac{\mathrm{d}N_{\mathrm{Er,3}}}{\mathrm{d}t} = k_{\mathrm{FT}}N_{\mathrm{Er}}N_{\mathrm{Yb,2}} - k_{\mathrm{c3}}N_{\mathrm{Er,3}}N_{\mathrm{Yb,2}} - W_3N_{\mathrm{Er,3}} + W_{53}N_{\mathrm{Er,5}} + W_{63}N_{\mathrm{Er,6}} \tag{10}$$

$$\frac{\mathrm{d}N_{Er,5}}{\mathrm{d}t} = k_{\mathrm{c2}}N_{\mathrm{Er,2}}N_{\mathrm{Yb,2}} - W_5N_{\mathrm{Er,5}} + W_{65}N_{\mathrm{Er,6}} \tag{11}$$

$$\frac{\mathrm{d}N_{\mathrm{Er,6}}}{\mathrm{d}t} = k_{\mathrm{c3}}N_{\mathrm{Er,3}}N_{\mathrm{Yb,2}} - W_6N_{\mathrm{Er,6}} \tag{12}$$

Here, we take advantage of the fact that long after the pulse has ceased, the density of Er^{3+} on level 1 can be approximated by the total density of Er^{3+} ions.[55]

The usual approach is to numerically solve such system or rate equations; however, this requires numerical values of all rate coefficients which are difficult or sometimes impossible to measure accurately. However it is possible to obtain some properties of the solutions in an alternative, analytical approach. Although this system of differential equations is nonlinear and it cannot be solved analytically, one can analytically establish the asymptotic behaviour of the solutions (see the ESI† for more details). The underlying idea is that, at times long after excitation has ceased, all excited state populations become small and the nonlinear terms in the rate equations become dominated by the exponential decay. The equations have asymptotic exponential solutions, provided in the ESI†. We have mathematically shown (see the ESI†) that, asymptotically, $N_{\mathrm{Er,6}}$ and $N_{\mathrm{Er,5}}$ decay exponentially with rates γ_6 and γ_5, which are given by $\gamma_6 = \min(W_6, k_{\mathrm{FT}}N_{\mathrm{Er}})$ and $\gamma_5 = \min(W_6, W_5, k_{\mathrm{FT}}N_{\mathrm{Er}})$. Consequently, for 2% Er^{3+} concentration used in this work and k_{FT} measured to be larger than 1.0×10^{-17} $\mathrm{cm^3\ s^{-1}}$ in earlier studies,[51,56,57] we obtain that the term $k_{\mathrm{FT}}N_{\mathrm{Er}}$ is larger than the observed red and green rates (hence non-limiting), and thus $\gamma_6 = W_6$ and $\gamma_5 = \min(W_6, W_5)$. Because in the experiment the two rates are unequal, this means that $N_{\mathrm{Er,6}}$ decays with the rate W_6, and $N_{\mathrm{Er,5}}$ with a rate W_5, where $W_6 > W_5$ (see the ESI†). Thus our rate equations predict that the red decay rate (W_5) is always lower than the green decay rate (W_6), which is fully consistent with our experimental data (Fig. 4a) and those published by other authors.[44,45,58]

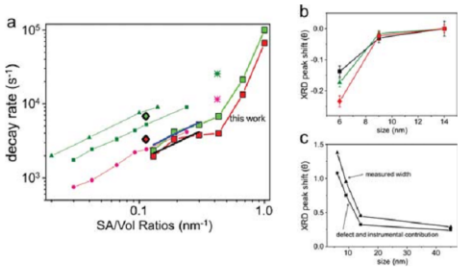

Fig. 4 (a) Luminescence decay times as a function of surface-to-volume ratio. Filled green and red symbols denote green and red luminescence, respectively. Framed symbols: this work (black-frame squares – $NaYF_4$ nanocrystals in a range of sizes, black-frame diamonds – $NaYF_4$ nanocrystals with 10 nm silica shell). Triangles – ref. 44, squares and circles – ref. 58, and stars – ref. 45. (b) X-ray diffraction peak position shift for various alpha phase nanocrystals, with respect to 14 nm diameter nanocrystals. Diffraction peaks corresponding to ~28.0, ~46.5, and ~55.2 degrees are marked by the black, green and red colour, respectively. (c) The evolution of X-ray diffraction peak width at ~46.5°. Triangles – measured peak width, squares – difference between measured width and fitted predictions of Scherrer's formula.[70]

Different models explaining the relation between decay times and nanocrystal size

Our rate equation analysis links the observed decay rates to microscopic, molecular level parameters in the rate equations. This makes it possible to theoretically analyse the relationship between the observed decay rates and nanocrystal size. As discussed above the asymptotic decay rates of populations on levels 5 (red) and 6 (green) are determined by the decay rate constants W_5 and W_6 which, in turn, depend on the respective nonradiative rates shown in eqn (1). The nonradiative rate $W_{i(\mathrm{NR})}$, in a homogeneous crystalline material with small defect density, obeys the "gap" rule,[59,60]

$$W_{i(\mathrm{NR})} \propto \mathrm{e}^{-\alpha p} \tag{13}$$

Here α is a parameter associated with the host material characteristics, and $p = \Delta E/\hbar\omega$ is the number of phonons required to bridge ΔE. ΔE is the energy gap between the initial and final states, and $\hbar\omega$ is the maximum vibrational energy. The "gap" rule indicates that the key factor determining both W_5 and W_6 rates is the energy of the highest vibrational mode, either in the nanocrystal interior (mechanism A-intrinsic phonon modes[30–33,45,61–63]), or associated with surface ligands at the nanocrystal surface (mechanism B-vibrational energy of surface ligands[64–66]), or in the surrounding solvent (mechanism C-solvent mediated quenching[22,62]). Moreover, an independent defect-related mechanism (D) attributes variations of decay rates (W_5 and W_6) to defect density, as crystalline defects provide the channels for nonradiative recombination. Thus a higher defect density leads to a reduced lifetime, as described by the Stern–Volmer equation[67]

$$W_{i(\mathrm{NR})} = k_{\mathrm{Q}}[Q] \tag{14}$$

where k_{Q} is the quenching rate constant and $[Q]$ is the density of quenching defects. The density of quenching defects that can be extracted from the X-ray diffraction peak width profile is demonstrated to be related to the nanocrystal size.[68] Such defect-related mechanism (D) often becomes apparent when comparing lifetimes for nanocrystals of the same material grown by different synthesis methods. The identification of the leading mechanism in a given type of nanocrystal is frequently not straightforward and it will not be attempted here. The contributions of the nonradiative recombination mechanisms (A–D) in the centre and near surface of nanocrystals are, generally, different. This makes it possible to propose a quantitative model of the observed upconversion decay times which takes into account different material properties near the nanocrystal surface and within its volume.

Our model is as follows. The nanocrystal is separated into the near-surface region of a fixed thickness of d and a spherical internal core.[33,69] The corresponding luminescence decay rates are $W_{5,\mathrm{ns}}$ and $W_{6,\mathrm{ns}}$ in the near-surface region and $W_{5,\mathrm{c}}$ and $W_{6,\mathrm{c}}$ in the internal core, for red and green luminescence, respectively. In the first instance, we assume that these rates are no longer size-dependent. The observed population decay for green luminescence from Er^{3+} level 6 for nanocrystals with radius $R > d$ is now given by a weighted average of the rates $W_{6,\mathrm{ns}}$ and $W_{6,\mathrm{c}}$ with weights determined by the respective fractions of the near surface/core volume. Hence the observed rate becomes a function of the nanocrystal's radius R and shell size d, as follows:

$$W_6(R,d) = W_{6,\mathrm{ns}}\frac{\frac{4}{3}\pi R^3 - \frac{4}{3}\pi(R-d)^3}{\frac{4}{3}\pi R^3} + W_{6,\mathrm{c}}\frac{\frac{4}{3}\pi(R-d)^3}{\frac{4}{3}\pi R^3} \tag{15}$$

This equation applies to green luminescence. Red luminescence, whose decay rate is described by $W_5(R,d)$, satisfies a similar relationship. The actual value of d for red and green luminescence is not known and it may be different for red and green luminescence. This model quantifies the idea already mentioned by other authors[69] that nanocrystal properties such as decay time depends on the surface-to-volume ratio, for a certain shell thickness d. Since the behaviour of the observed decay rates in smaller nanocrystals is increasingly dominated by the contribution from the near-surface decay rate, our model is able to describe a reduction of the decay time with decreasing size.

Application of our model to experimental data

To understand and clarify the origin of lifetime variations, our data were plotted together with those published by other authors as a function of surface-to-volume ratio (Fig. 4a). We see that the data from ref. 44 and 58 follow an approximately linear relationship. Our values for β-phase nanocrystals (data points with black frames and SA/Vol ratios less than 0.3 nm^{-1}), follow linear relationships for red and green luminescence, while the remaining three pairs of points for the α-phase nanocrystals show a different trend. The data points corresponding to β-phase nanocrystals can be fitted by the relationship (15), but a similar fit is not possible for the three smaller (α-phase) nanocrystals assuming constant rates. The parameters of our fitting

shown in Fig. 4a are $d = 1.5$ nm, and constant rates of $W_{6,ns} = 13\,040\ s^{-1}$, $W_{6,c} = 340\ s^{-1}$, $W_{5,ns} = 9800 s^{-1}$, and $W_{5,c} = 230 s^{-1}$.

We now discuss how the decay time observations in Fig. 4a relate to mechanisms A–D. With regard to quenching mechanism A, the nonradiative decay rate is given by eqn (13), and the difference of radiative decay constants between the near-surface and core are ignored. The different decay rates may be due to the fact that the maximum frequency of phonons arising from "surface relaxation" varies with nanoparticle size. However, it is well established that the phonon frequencies decrease only very slightly, or not at all, for the size range of particles under investigation (see, for example, solid squares and circles in Fig. 4a). Because of such a limited variation, mechanism A is unable to effectively explain major shifts of the nanocrystals' decay times, a conclusion also recently drawn by Shan *et al.*[58] and Wang *et al.*[33] Mechanism B, discussed in ref. 58, assumes that the decay rate in the particle core is constant and size-independent, while the rate at the surface is different and related to the type and density of the surface ligands. In the case of a particular fixed nanocrystal chemistry, the surface ligand density should remain constant for different sizes. However, our data for very small α-phase nanocrystals cannot be fitted with such constant rates, which rules out mechanism B. Similarly, mechanism C, which uses the same idea in eqn (15) except that the surface rate is now due to the proximity of the liquid, is in contradiction with our results for small α-phase nanocrystals, as already discussed, in relation to mechanism B. This leaves the defect-related decay (mechanism D) as dominant in the very small, α-phase nanocrystals. We hypothesize that the α-phase nanocrystals have different defect densities for each different size; hence they cannot be fitted by eqn (15) with constant decay rates in the core and the near-surface region. This postulate is tested and independently confirmed by the analysis of the X-ray data which shows the variation of peak position (Fig. 4b) and increasing XRD peak width with decreasing size (Fig. 4c). The former is a reflection of varying lattice constants due to defect-induced strain. The experimental peak width is comprised of three major contributions, that is, crystallite size, instrumental broadening, and defect density. Generally, the contribution due to crystallite size, W_{Sch}, satisfies the Scherrer equation:[70]

$$W_{Sch}(2\theta) = \frac{K\lambda}{L\cos\theta} \quad (16)$$

Here L is the crystallite size, 2θ is the position of the XRD peak, λ is the X-ray wavelength, and K is the proportionality constant. In Fig. 4c, we show the residual peak width after subtracting the crystallite size broadening obtained by Scherrer's relationship, from the measured experimental width, resulting in a peak width attributed to instrument resolution and defects. As the instrumental contribution is sample-independent, Fig. 4c clearly shows that the defect density increases as the nanocrystal size decreases. Thus the observed lifetime results (Fig. 4a) and the XRD analysis (Fig. 4b and c) are generally consistent as long as the density of quenching defects is proportional to the total defect density in nanocrystals.

Mechanism D is also consistent with our observations for the β-phase nanocrystals. In particular, the decay rates of the three β-phase nanocrystals that follow eqn (15) as well as the data from ref. 44 and 58 can be interpreted as having different decay rates on the surface and in the core due to different defect densities in the near-surface region and inside. We also note that all β-phase nanocrystals are brighter than the α-phase, which is an indication of higher quality crystals and lower defect density. Additional support for the significance of the defect-mediated mechanism is provided by the decay time of nanocrystals which have been coated with a ~10 nm silica shell (Fig. 4a). They show increased decay rates compared to uncoated nanocrystals, which contradicts mechanisms A and C but is consistent with mechanism D because the shell may generate extra surface defects through interface strain. It is also consistent with Mechanism B where increased decay rates may be attributed to high ($\sim 1100\ cm^{-1}$) phonon energy in silica. Mechanisms B and C cannot be ruled out in the case of β-phase nanocrystals; however, different decay times reported by various authors are most simply attributed to different defect densities retained on the surface. The significance of liquid quenching (mechanism C) is shown in the ESI, Fig. S3,† which illustrates the effects of measuring β-phase nanocrystal samples in dry conditions.

Conclusions

In summary, we present a comprehensive analysis of the upconversion luminescence decay rates in colloidal $NaYF_4$:Yb,Er nanocrystals. We propose a system of rate equations to describe the evolution of upconversion green and red luminescence, which is solved in the limit of a long time after an exciting light pulse. Our rate equations predict that the red decay rate is always lower than the green decay rate, in full agreement with our data and those of other authors. We then formulate a simple mathematical model of the decay times which takes into account that the nanocrystal properties are different between the near-surface and inside regions. This formalism explains why emission lifetimes vary with the surface area to volume ratio. It also makes it possible to quantitatively interpret the nanocrystal properties, which are dependent on the surface-to-volume ratio, and link them with atomic-scale mechanisms such as nonradiative recombination mediated by nanocrystal phonons, vibrations of surface ligands, solvent mediated quenching, and surface defects. We have been able to demonstrate that higher quality β-phase particles exhibit the behaviour consistent with three different models based on the vibration energy of surface ligands, solvent quenching and surface defects; all three influence the emission lifetimes to a significant degree. For smaller α-phase nanocrystals, the defect density dominates the decay times. By removing the connection between nanocrystal geometry, their size-to-volume ratio, and the upconversion decay times, our work paves the way towards synthesis of very small and very bright upconversion nanocrystals for biological applications by using defect reduction strategies.

Methods

Reagents and materials

Yttrium chloride hexahydrate ($YCl_3 \cdot 6H_2O$, 99.99%), ytterbium chloride hexahydrate ($YbCl_3 \cdot 6H_2O$, 99.998%), erbium chloride hexahydrate ($ErCl_3 \cdot 6H_2O$, 99.9%), sodium hydroxide (NaOH, 98+%), ammonium fluoride (NH_4F, 99.99+%), oleic acid (OA, 90%), 1-octadecene (ODE, 90%), tetraethyl orthosilicate (TEOS), Igepal CO-520, and ammonium hydroxide solution (NH_4OH, 30%) were all purchased from Sigma–Aldrich and used as received without further purification.

Synthesis

We used a modified user-friendly synthesis method[38] following a nominally oxygen-free protocol except where noted. In a typical procedure for the synthesis of ~31 nm $NaYF_4$:Yb (18%), Er (2%) nanocrystals, 200 μL of aqueous solution of $LnCl_3$ (1.0 mmol, Ln = Y, Yb, Er) was magnetically mixed with OA (6 mL) and ODE (15 mL) in a 100 mL three-neck round-bottom flask. The mixture was degassed under Ar flow and heated to 150 °C for 30 min to form a clear light yellow solution, and then cooled to room temperature. 10 mL of methanol solution containing NH_4F (0.1481 g) and NaOH (0.1 g) was added and stirred for 30 min. Then, the solution was slowly heated to 110 °C and kept at 110 °C for 30 min to completely remove methanol and some water. During this period, one neck of the flask was left open under the flow of Ar gas. After that, the reaction mixture was sealed again and protected with Ar flow and quickly heated to 320 °C and aged for 1 h. After the solution cooled, acetone was added to precipitate the nanocrystals. The final $NaYF_4$:Yb,Er nanocrystals were redispersed in 5 mL of cyclohexane after washing with cyclohexane/acetone two times. Other nanocrystals with different sizes were synthesized using an identical procedure, except for the reaction temperature and time (6 nm – 260 °C, 30 min; 9 nm – 280 °C, 30 min; 14 nm – 280 °C, 45 min; 20 nm – 300 °C, 60 min; 45 nm – 310 °C, 90 min) respectively.

To produce silica-coated nanocrystals, a modified water-in-oil (W/O) microemulsion method was used.[71,72] Briefly, a cyclohexane dispersion of $NaYF_4$:Yb,Er nanocrystals (5 mg mL^{-1}, 300 μL), Igepal CO-520 (0.25 g) and cyclohexane (4.2 mL) were mixed in a glass vial by ultrasonication for 10 min. Then, 35 μL of ammonia (wt 28%) was injected into the solution and a transparent emulsion formed after vigorous stirring for several minutes. Thereafter, 20 μL of TEOS was added as the silica shell precursor and the system was kept at room temperature for 36 h with moderate stirring. After that, acetone (~10 mL) was added to isolate the silica-coated nanocrystals from the microemulsion. The precipitates were centrifugally washed with ethanol at least three times to remove excess surfactant, and finally re-dispersed in ethanol.

Characterization

Powder X-ray diffraction (XRD) patterns were obtained on a PANalytical X'Pert Pro MPD X-ray diffractometer using Cu Kα1 radiation (40 kV, 40 mA, $\lambda = 0.15418$ nm). The XRD samples were prepared by repeatedly drying drops of nanocrystal dispersions in cyclohexane cast on a zero-background silicon wafer. The transmission electron microscope (TEM) measurements were performed using a Philips CM10 TEM with Olympus Sis Megaview G2 Digital Camera. The samples for TEM analysis were prepared by placing a drop of a dilute suspension of nanocrystals onto formvar-coated copper grids (300 meshes) and allowing it to dry in a desiccator at room temperature. The upconversion luminescence spectra of colloidal solutions in quartz cuvettes with 10 mm path length were acquired with a Fluorolog-Tau3 spectrofluorometer (JobinYvon-Horiba) equipped with an external 980 nm CW diode laser with a pump power of ~1.2 W. Upconversion decay properties were measured by placing the samples into a modified fluorescence microscope, using a 980 nm CW diode-pumped solid state laser with maximum power output of ~1.2 W as the excitation source, coupled to a fibre with a 200 μm core. The excitation beam was focused by a 10× microscope objective, and the luminescence was collected by a condenser lens with numerical aperture of ~0.8. The NIR excitation light was blocked by a short wavelength-pass filter (Semrock, FF01-842/SP-25) and additional filters were used to separate green (Semrock, FF01-540/50-25 bandpass filter) and red (Semrock, FF01-655/40-25 bandpass filter) upconversion emissions before detection. The signal was collected with a solid-state photomultiplier tube (SPMT) (SPMMini3035 × 08A1 at photon amplification gain of 10^6; the preamplifier was configured with a 10 kΩ resistor to deliver a current-to-voltage gain of 10^4 V/A at bandwidth of 2 MHz, SensL) with 100 cycles of averaging. In order to characterise the decay profile, 500 μs rectangular excitation pulses were generated by a pulse generator with a repetition rate of 50 Hz (DG 535 Digital Delay/Pulse Generator, Stanford Research). The power-dependence of upconversion emissions for various size nanocrystals was investigated by varying laser excitation power. All luminescence properties of upconversion nanocrystals were studied at room temperature and recorded from samples in the colloidal state.

Acknowledgements

We thank D. Birch, N. Vella, and R. Field for their help in sample characterization. D. Jin acknowledges financial support from the Australian Research Council (DP1095465). J. Zhao acknowledges a Macquarie University Research Excellence Scholarship.

Notes and references

1 F. Wang, Y. Han, C. S. Lim, Y. H. Lu, J. Wang, J. Xu, H. Y. Chen, C. Zhang, M. H. Hong and X. G. Liu, *Nature*, 2010, **463**, 1061–1065.
2 E. Downing, L. Hesselink, J. Ralston and R. Macfarlane, *Science*, 1996, **273**, 1185–1189.
3 X. F. Liu, G. P. Dong, Y. B. Qiao and J. R. Qiu, *Appl. Opt.*, 2008, **47**, 6416–6421.
4 M. Liu, Y. Lu, Z. B. Xie and G. M. Chow, *Sol. Energy Mater. Sol. Cells*, 2011, **95**, 800–803.

5 J. de Wild, J. K. Rath, A. Meijerink, W. G. J. H. M. van Sark and R. E. I. Schropp, *Sol. Energy Mater. Sol. Cells*, 2010, **94**, 2395–2398.
6 J. de Wild, A. Meijerink, J. K. Rath, W. G. J. H. M. van Sark and R. E. I. Schropp, *Sol. Energy Mater. Sol. Cells*, 2010, **94**, 1919–1922.
7 D. Chen, Y. Wang and M. Hong, *Nano Energy*, 2012, **1**, 73–90.
8 D. Chen, L. Lei, A. Yang, Z. Wang and Y. Wang, *Chem. Commun.*, 2012, **48**, 5898–5900.
9 F. Vetrone, R. Naccache, A. Zamarron, A. J. de la Fuente, F. Sanz-Rodriguez, L. M. Maestro, E. M. Rodriguez, D. Jaque, J. G. Sole and J. A. Capobianco, *ACS Nano*, 2010, **4**, 3254–3258.
10 H. S. Qian, H. C. Guo, P. C. L. Ho, R. Mahendran and Y. Zhang, *Small*, 2009, **5**, 2285–2290.
11 S. W. Wu, G. Han, D. J. Milliron, S. Aloni, V. Altoe, D. V. Talapin, B. E. Cohen and P. J. Schuck, *Proc. Natl. Acad. Sci. U. S. A.*, 2009, **106**, 10917–10921.
12 R. A. Jalil and Y. Zhang, *Biomaterials*, 2008, **29**, 4122–4128.
13 M. Nyk, R. Kumar, T. Y. Ohulchanskyy, E. J. Bergey and P. N. Prasad, *Nano Lett.*, 2008, **8**, 3834–3838.
14 Y. Yang, Q. Shao, R. Deng, C. Wang, X. Teng, K. Cheng, Z. Cheng, L. Huang, Z. Liu, X. Liu and B. Xing, *Angew. Chem.*, 2012, **51**, 3125–3129.
15 F. van de Rijke, H. Zijlmans, S. Li, T. Vail, A. K. Raap, R. S. Niedbala and H. J. Tanke, *Nat. Biotechnol.*, 2001, **19**, 273–276.
16 F. Wang and X. G. Liu, *Chem. Soc. Rev.*, 2009, **38**, 976–989.
17 J. C. Boyer, C. J. Carling, B. D. Gates and N. R. Branda, *J. Am. Chem. Soc.*, 2010, **132**, 15766–15772.
18 S. Schietinger, T. Aichele, H. Q. Wang, T. Nann and O. Benson, *Nano Lett.*, 2010, **10**, 134–138.
19 Z. Q. Li, L. M. Wang, Z. Y. Wang, X. H. Liu and Y. J. Xiong, *J. Phys. Chem. C*, 2011, **115**, 3291–3296.
20 D. Jin and J. A. Piper, *Anal. Chem.*, 2011, **83**, 2294–2300.
21 D. Jin, J. A. Piper, R. C. Leif, S. Yang, B. C. Ferrari, J. Yuan, G. Wang, L. M. Vallarino and J. W. Williams, *J. Biomed. Opt.*, 2009, **14**, 024023.
22 R. Kumar, M. Nyk, T. Y. Ohulchanskyy, C. A. Flask and P. N. Prasad, *Adv. Funct. Mater.*, 2009, **19**, 853–859.
23 J. F. Suyver, J. Grimm, M. K. van Veen, D. Biner, K. W. Kramer and H. U. Gudel, *J. Lumin.*, 2006, **117**, 1–12.
24 J. H. Zeng, J. Su, Z. H. Li, R. X. Yan and Y. D. Li, *Adv. Mater.*, 2005, **17**, 2119–2123.
25 J. N. Shan and Y. G. Ju, *Nanotechnology*, 2009, **20**, 275603–275615.
26 X. C. Ye, J. E. Collins, Y. J. Kang, J. Chen, D. T. N. Chen, A. G. Yodh and C. B. Murray, *Proc. Natl. Acad. Sci. U. S. A.*, 2010, **107**, 22430–22435.
27 H. X. Mai, Y. W. Zhang, R. Si, Z. G. Yan, L. D. Sun, L. P. You and C. H. Yan, *J. Am. Chem. Soc.*, 2006, **128**, 6426–6436.
28 S. Lechevallier, P. Hammer, J. M. A. Caiut, S. Mazeres, R. Mauricot, M. Verelst, H. Dexpert, S. J. L. Ribeiro and J. Dexpert-Ghys, *Langmuir*, 2012, **28**, 3962–3971.
29 F. Wang, R. Deng, J. Wang, Q. Wang, Y. Han, H. Zhu, X. Chen and X. Liu, *Nat. Mater.*, 2011, **10**, 968–973.
30 G. S. Yi and G. M. Chow, *Chem. Mater.*, 2007, **19**, 341–343.
31 J. C. Boyer and F. C. J. M. van Veggel, *Nanoscale*, 2010, **2**, 1417–1419.
32 F. Vetrone, R. Naccache, V. Mahalingam, C. G. Morgan and J. A. Capobianco, *Adv. Funct. Mater.*, 2009, **19**, 2924–2929.
33 F. Wang, J. A. Wang and X. G. Liu, *Angew. Chem., Int. Ed.*, 2010, **49**, 7456–7460.
34 G. S. Yi and G. M. Chow, *Adv. Funct. Mater.*, 2006, **16**, 2324–2329.
35 K. W. Kramer, D. Biner, G. Frei, H. U. Gudel, M. P. Hehlen and S. R. Luthi, *Chem. Mater.*, 2004, **16**, 1244–1251.
36 A. D. Ostrowski, E. M. Chan, D. J. Gargas, E. M. Katz, G. Han, P. J. Schuck, D. J. Milliron and B. E. Cohen, *ACS Nano*, 2012, **6**, 2686–2692.
37 T. Yang, Y. Sun, Q. Liu, W. Feng, P. Yang and F. Li, *Biomaterials*, 2012, **33**, 3733–3742.
38 Z. Q. Li, Y. Zhang and S. Jiang, *Adv. Mater.*, 2008, **20**, 4765–4769.
39 F. Auzel, *Chem. Rev.*, 2004, **104**, 139–173.
40 S. Heer, K. Kompe, H. U. Gudel and M. Haase, *Adv. Mater.*, 2004, **16**, 2102–2105.
41 E. M. Chan, D. J. Gargas, P. J. Schuck and D. J. Milliron, *J. Phys. Chem. B*, 2012, **116**, 10561–10570.
42 A. Aebischer, S. Heer, D. Biner, K. Kramer, M. Haase and H. U. Gudel, *Chem. Phys. Lett.*, 2005, **407**, 124–128.
43 Y. Li, J. Zhang, X. Zhang, Y. Luo, X. Ren, H. Zhao, X. Wang, L. Sun and C. Yan, *J. Phys. Chem. C*, 2009, **113**, 4413–4418.
44 S. F. Lim, W. S. Ryu and R. H. Austin, *Opt. Express*, 2010, **18**, 2309–2316.
45 Y. Wang, L. P. Tu, J. W. Zhao, Y. J. Sun, X. G. Kong and H. Zhang, *J. Phys. Chem. C*, 2009, **113**, 7164–7169.
46 J. F. Suyver, A. Aebischer, S. Garcia-Revilla, P. Gerner and H. U. Gudel, *Phys. Rev. B: Condens. Matter Mater. Phys.*, 2005, **71**, 125123–125131.
47 S. Schietinger, L. D. Menezes, B. Lauritzen and O. Benson, *Nano Lett.*, 2009, **9**, 2477–2481.
48 W. B. Niu, S. L. Wu, S. F. Zhang and L. Li, *Chem. Commun.*, 2010, **46**, 3908–3910.
49 S. Bjurshagen, J. E. Hellstrom, V. Pasiskevicius, M. C. Pujol, M. Aguilo and F. Diaz, *Appl. Opt.*, 2006, **45**, 4715–4725.
50 E. Cantelar and F. Cusso, *Appl. Phys. B: Lasers Opt.*, 1999, **69**, 29–33.
51 P. A. Burns, J. M. Dawes, P. Dekker, J. A. Piper, H. D. Jiang and J. Y. Wang, *IEEE J. Quantum Electron.*, 2004, **40**, 1575–1582.
52 C. Li, C. Wyon and R. Moncorge, *IEEE J. Quantum Electron.*, 1992, **28**, 1209–1221.
53 W. Wang, M. M. Wu and G. K. Liu, *Spectrosc. Lett.*, 2007, **40**, 259–269.
54 N. Bogdan, F. Vetrone, G. A. Ozin and J. A. Capobianco, *Nano Lett.*, 2011, **11**, 835–840.
55 D. A. Simpson, W. E. K. Gibbs, S. F. Collins, W. Blanc, B. Dussardier, G. Monnom, P. Peterka and G. W. Baxter, *Opt. Express*, 2008, **16**, 13781–13799.
56 R. H. Page, K. I. Schaffers, P. A. Waide, J. B. Tassano, S. A. Payne, W. F. Krupke and W. K. Bischel, *J. Opt. Soc. Am. B*, 1998, **15**, 996–1008.

57 X. Jiang, Z. Yang, T. Liu and S. Xu, *J. Appl. Phys.*, 2009, **105**, 103113–103116.
58 J. N. Shan, M. Uddi, N. Yao and Y. G. Ju, *Adv. Funct. Mater.*, 2010, **20**, 3530–3537.
59 M. Wermuth, T. Riedener and H. U. Gudel, *Phys. Rev. B: Condens. Matter Mater. Phys.*, 1998, **57**, 4369–4376.
60 B. Camille and A. P. Stephen, *Picosecond Nonradiative Processes in Neodymium-doped Crystals and Glasses: Mechanism for the Energy Gap Law**, 1998.
61 H. X. Mai, Y. W. Zhang, L. D. Sun and C. H. Yan, *J. Phys. Chem. C*, 2007, **111**, 13721–13729.
62 J. C. Boyer, M. P. Manseau, J. I. Murray and F. van Veggel, *Langmuir*, 2010, **26**, 1157–1164.
63 M. Wang, C. C. Mi, Y. X. Zhang, J. L. Liu, F. Li, C. B. Mao and S. K. Xu, *J. Phys. Chem. C*, 2009, **113**, 19021–19027.
64 P. Ghosh, J. Oliva, E. De la Rosa, K. K. Haldar, D. Solis and A. Patra, *J. Phys. Chem. C*, 2008, **112**, 9650–9658.
65 R. Naccache, F. Vetrone, V. Mahalingam, L. A. Cuccia and J. A. Capobianco, *Chem. Mater.*, 2009, **21**, 717–723.
66 Y. F. Wang, L. D. Sun, J. W. Xiao, W. Feng, J. C. Zhou, J. Shen and C. H. Yan, *Chem.–Eur. J.*, 2012, **18**, 5558–5564.
67 J. R. Lakowicz, *Principles of Fluorescence Spectroscopy*, Springer, 2006.
68 T. Ungar, J. Gubicza, G. Ribarik and A. Borbely, *J. Appl. Crystallogr.*, 2001, **34**, 298–310.
69 Q. Lü, F. Guo, L. Sun, A. Li and L. Zhao, *J. Phys. Chem. C*, 2008, **112**, 2836–2844.
70 J. I. Langford and A. J. C. Wilson, *J. Appl. Crystallogr.*, 1978, **11**, 102–113.
71 D. K. Yi, S. S. Lee, G. C. Papaefthymiou and J. Y. Ying, *Chem. Mater.*, 2006, **18**, 614–619.
72 D. K. Yi, S. S. Lee and J. Y. Ying, *Chem. Mater.*, 2006, **18**, 2459–2461.

Supporting Information

Upconversion Luminescence with Tunable Lifetime in $NaYF_4$:Yb,Er Nanocrystals: Role of Nanocrystal Size

Jiangbo Zhao[a], Zhenda Lu[b], Yadong Yin[b], Christopher McRae[c], James A. Piper[a], Judith M. Dawes[a], Dayong Jin[a], and Ewa M. Goldys[a*]*

[*] To whom correspondence should be addressed. E-mail: dayong.jin@mq.edu.au, ewa.goldys@mq.edu.au.

[a] MQ BioFocus Centre, Faculty of Science, Macquarie University, NSW 2109, Sydney, Australia

[b] Department of Chemistry, University of California, Riverside, CA 92521, USA

[c] Department of Chemistry and Biomolecular Sciences, Faculty of Science, Macquarie University, NSW 2109, Sydney, Australia

Contents:

-S2-

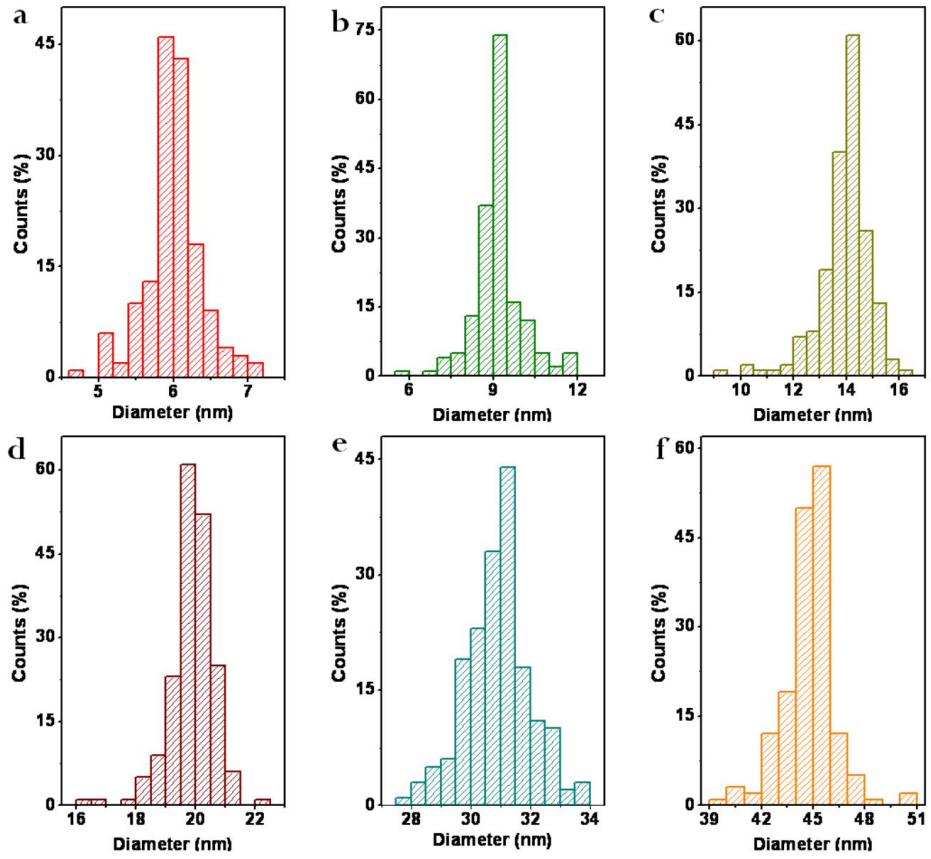

Fig. S1. (a-f) The particle size distribution histograms corresponding to TEM images in Figure 1. Histograms of the particle sizes are drawn from analysis of > 150 particles for each sample. The mean and standard deviation for each nanocrystalline size are, respectively, 5.99±0.38 nm in **a**; 9.20±0.85 nm in **b**; 13.94±0.97 nm in **c**; 19.89± 0.76nm in **d**; 30.90±1.11 nm in **e**; 44.81±1.54 nm in **f** only measuring top/bottom surface area.

-S3-

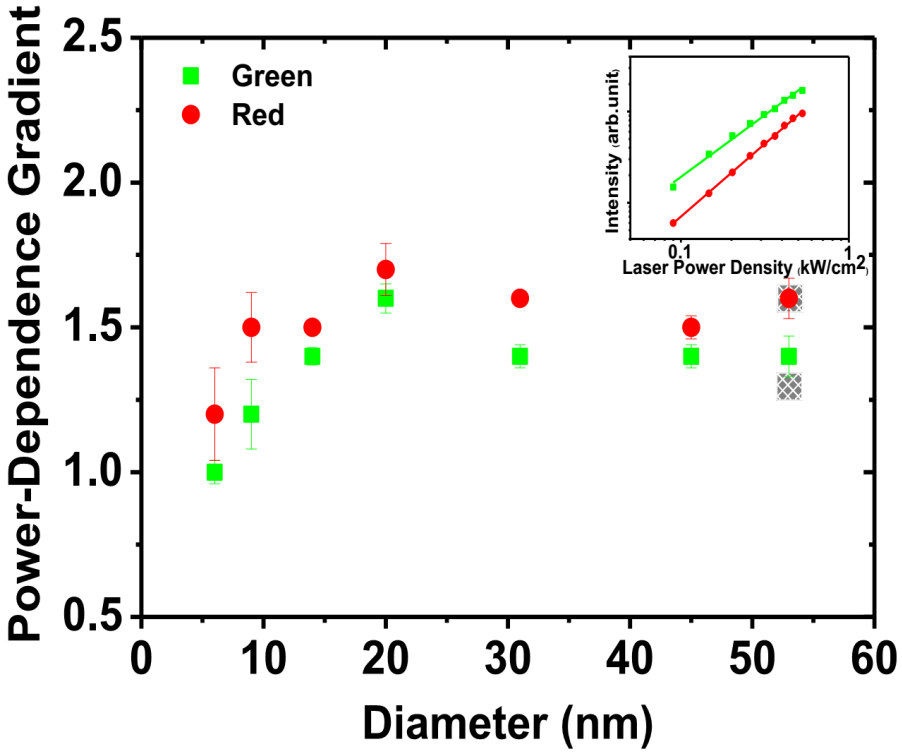

Fig. S2. Gradients for power dependence of the green and red upconverted luminescence of $NaYF_4$ nanocrystals with various sizes from 6 nm to 45 nm. The log-log plots of upconversion intensities versus NIR excitation power were fitted to straight lines, and the gradients of these lines have been plotted for green and red luminescence. One selected example plot is shown in the corresponding inset, indicating the upconversion emission intensities of the green and red emission versus NIR excitation laser power density. ▩ symbols represent silica-coated nanoparticles.

-S4-

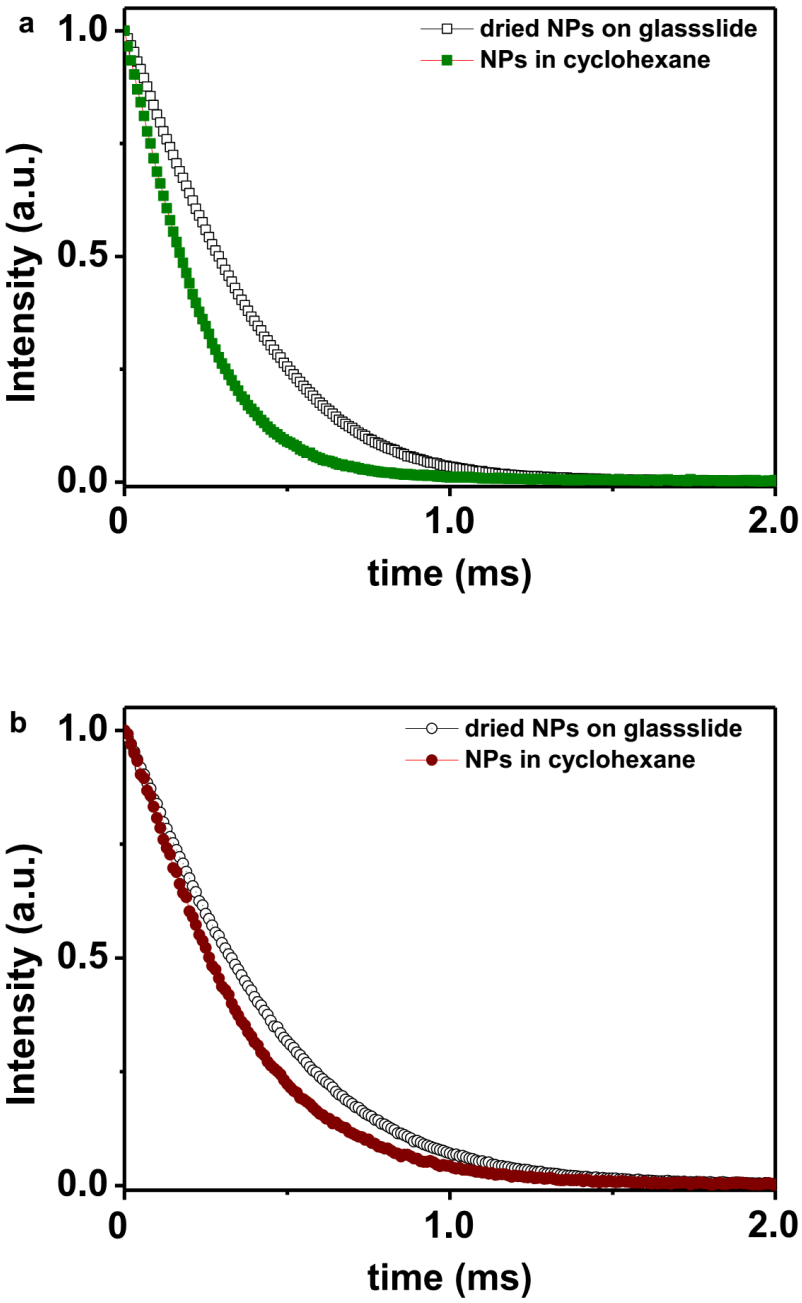

Fig. S3. Normalized upconversion fluorescence decays for ~31 nm nanocrystals in dried state and organic solvent cyclohexane: green emission (a) and red emission (b), respectively. All the measurements were obtained at an excitation wavelength of 980 nm.

-S5-

RATE EQUATIONS FOR ER:YB UNPCONVERTING NANOPARTICLES AND ASYMPTOTIC BEHAVIOUR OF THE SOLUTIONS

1. Rate equations for an arbitrary excitation

$$\frac{dN_{Yb,2}}{dt} = -k_{FT}N_{Er}N_{Yb,2} - k_{c2}N_{Er,2}N_{Yb,2} - k_{c3}N_{Er,3}N_{Yb,2}$$
$$\frac{dN_{Er,2}}{dt} = -k_{c2}N_{Er,2}N_{Yb,2} - W_2N_{Er,2} + W_{32}N_{Er,3} + W_{52}N_{Er,5} + W_{62}N_{Er,6}$$
$$\frac{dN_{Er,3}}{dt} = k_{FT}N_{Er}N_{Yb,2} - k_{c3}N_{Er,3}N_{Yb,2} - W_3N_{Er,3} + W_{53}N_{Er,5} + W_{63}N_{Er,6}$$
$$\frac{dN_{Er,5}}{dt} = k_{c2}N_{Er,2}N_{Yb,2} - W_5N_{Er,5} + W_{65}N_{Er,6}$$
$$\frac{dN_{Er,6}}{dt} = k_{c3}N_{Er,3}N_{Yb,2} - W_6N_{Er,6}$$

The rate equations for the upconverting $NaYF_4$ doped with Er and Yb are:

(1.1) $$\frac{dN_{Yb,2}}{dt} = \rho_p\sigma_{Yb}N_{Yb} - k_{FT}N_{Er,1}N_{Yb,2} - k_{c2}N_{Er,2}N_{Yb,2} - k_{c3}N_{Er,3}N_{Yb,2}$$

(1.2)
$$\frac{dN_{Er,2}}{dt} = -k_{c2}N_{Er,2}N_{Yb,2} - \rho_p\sigma_{ESA2}N_{Er,2} - W_2N_{Er,2} + W_{32}N_{Er,3} + W_{52}N_{Er,5} + W_{62}N_{Er,6}$$

(1.3)
$$\frac{dN_{Er,3}}{dt} = k_{FT}N_{Er,1}N_{Yb,2} - \rho_p\sigma_{ESA3}N_{Er,3} - k_{c3}N_{Er,3}N_{Yb,2} - W_3N_{Er,3} + W_{53}N_{Er,5} + W_{63}N_{Er,6}$$

(1.4) $$\frac{dN_{Er,5}}{dt} = k_{c2}N_{Er,2}N_{Yb,2} + \rho_p\sigma_{ESA2}N_{Er,2} - W_5N_{Er,5} + W_{65}N_{Er,6}$$

(1.5) $$\frac{dN_{Er,6}}{dt} = k_{c3}N_{Er,3}N_{Yb,2} + \rho_p\sigma_{ESA3}N_{Er,3} - W_6N_{Er,6}$$

Here, $N_{Er(Yb),i}$ denotes the population of level i of Er(Yb). W_i denotes total radiative and nonradiative decay rate of the relevant population, while W_{ij} is the decay rate of population of level i decaying into j. σ_{Yb} is the absorption cross section of ground state Yb, while $\sigma_{ESA2(3)}$ refers to absorption cross section of Er in level 2(3) at 980 nm. K_{FT} is the coefficient of forward energy transfer, while $k_{c2(3)}$ is the cooperative upconversion coefficient for the 2→5 and 3→6 upconversion. ρ_p is the power constant defined as excitation power variable. See main body of the paper for justification of these equations and underlying assumptions.

-S6-

2. Rate equations for pulsed excitation, between the pulses

In the case of pulsed excitation, after the excitation has ceased (at $t = 0$), these equations assume a simpler form:

$$\frac{dN_{Yb,2}}{dt} = -k_{FT}N_{Er}N_{Yb,2} - k_{c2}N_{Er,2}N_{Yb,2} - k_{c3}N_{Er,3}N_{Yb,2} \tag{2.1}$$

$$\frac{dN_{Er,2}}{dt} = -k_{c2}N_{Er,2}N_{Yb,2} - W_2N_{Er,2} + W_{32}N_{Er,3} + W_{52}N_{Er,5} + W_{62}N_{Er,6} \tag{2.2}$$

$$\frac{dN_{Er,3}}{dt} = k_{FT}N_{Er}N_{Yb,2} - k_{c3}N_{Er,3}N_{Yb,2} - W_3N_{Er,3} + W_{53}N_{Er,5} + W_{63}N_{Er,6} \tag{2.3}$$

$$\frac{dN_{Er,5}}{dt} = k_{c2}N_{Er,2}N_{Yb,2} - W_5N_{Er,5} + W_{65}N_{Er,6} \tag{2.4}$$

$$\frac{dN_{Er,6}}{dt} = k_{c3}N_{Er,3}N_{Yb,2} - W_6N_{Er,6} \tag{2.5}$$

Here, $N_{Er,1}$ is approximated by N_{Er}=const, the density of Er ions.

3. Asymptotic behaviour of the solutions

We now establish the asymptotic behaviour of the solutions.This is done in several steps.

1. Positivity of the solutions
It is easy to show that if the initial conditions are all positive then solutions stay positive for all times.

2. Upper bound of the solution for $N_{Yb,2}$
First we find the upper bound for $N_{Yb,2}$. It satisfies the equation:

$$\frac{dN_{Yb,2}}{dt} = -k_{FT}N_{Er}N_{Yb,2} - k_{c2}N_{Er,2}N_{Yb,2} - k_{c3}N_{Er,3}N_{Yb,2} \tag{3.1}$$

Clearly, by 1. we have

$$\frac{dN_{Yb,2}}{dt} \leq -k_{FT}N_{Er}N_{Yb,2} \tag{3.2}$$

Solving this inequality we obtain

$$N_{Yb,2}(t) \leq e^{-k_{FT}N_{Er}t}N_{Yb,2}(0) \tag{3.3}$$

3. Upper bounds of the solution for $N_{Er,2} - N_{Er,6}$

-S7-
We now consider equations for $N_{Er,2}, N_{Er,3}, N_{Er,5}$ and $N_{Er,6}$

$$\frac{dN_{Er,2}}{dt} = -\left(k_{c2}N_{Yb,2} + W_2\right)N_{Er,2} + W_{32}N_{Er,3} + W_{52}N_{Er,5} + W_{62}N_{Er,6}, \tag{3.4}$$

$$\frac{dN_{Er,3}}{dt} = -\left(k_{c3}N_{Yb,2} + W_3\right)N_{Er,3} + W_{53}N_{Er,5} + W_{63}N_{Er,6} + k_{FT}N_{Er}N_{Yb,2}, \tag{3.5}$$

$$\frac{dN_{Er,5}}{dt} = -W_5N_{Er,5} + W_{65}N_{Er,6} + k_{c2}N_{Er,2}N_{Yb,2}, \tag{3.6}$$

$$\frac{dN_{Er,6}}{dt} = -W_6N_{Er,6} + k_{c3}N_{Er,3}N_{Yb,2}. \tag{3.7}$$

Clearly

$$\frac{dN_{Er,2}}{dt} < -W_2N_{Er,2} + W_{32}N_{Er,3} + W_{52}N_{Er,5} + W_{62}N_{Er,6} \tag{3.8}$$

AND

$$\frac{dN_{Er,3}}{dt} < -W_3N_{Er,3} + W_{53}N_{Er,5} + W_{63}N_{Er,6} + k_{FT}N_{Er}N_{Yb,2} \tag{3.9}$$

By point 2. for every $\epsilon > 0$ we can choose $t_0 = t_0(\epsilon, N_{Yb,2}(0), k_{FT}N_{Er})$, such that for all $t \geq t_0$ we have $N_{Yb,2}(t) < \frac{\epsilon}{k_{c2}}$ AND $N_{Yb,2}(t) < \frac{\epsilon}{k_{c3}}$.
Then, for $t \geq t_0$ we have

$$\frac{dN_{Er,2}}{dt} < -W_2N_{Er,2} + W_{32}N_{Er,3} + W_{52}N_{Er,5} + W_{62}N_{Er,6} \tag{3.10}$$

$$\frac{dN_{Er,3}}{dt} < -W_3N_{Er,3} + W_{53}N_{Er,5} + W_{63}N_{Er,6} + k_{FT}N_{Er}N_{Yb,2} \tag{3.11}$$

$$\frac{dN_{Er,5}}{dt} < -W_5N_{Er,5} + W_{65}N_{Er,6} + \epsilon N_{Er,2} \tag{3.12}$$

$$\frac{dN_{Er,6}}{dt} < -W_6N_{Er,6} + \epsilon N_{Er,3} \tag{3.13}$$

Now, for a given $A, B, C > 0$ let

$$V_t = N_{Er,2} + AN_{Er,3} + BN_{Er,5} + CN_{Er,6}.$$

-S8-

For simplicity we denote $f(t) = k_{FT} N_{Er} N_{Yb,2}$. By taking the first derivative of V_t and using the equations for $N_{Er,2}, \ldots, N_{Er,6}$ we obtain:

(3.14)

$$\begin{aligned}
\frac{dV}{dt} &= \frac{dN_{Er,2}}{dt} + A\frac{dN_{Er,3}}{dt} + B\frac{dN_{Er,5}}{dt} + C\frac{dN_{Er,6}}{dt} \\
&< -W_2 N_{Er,2} + W_{32} N_{Er,3} + W_{52} N_{Er,5} + W_{62} N_{Er,6} \\
&- AW_3 N_{Er,3} + AW_{53} N_{Er,5} + AW_{63} N_{Er,6} + Af(t) \\
&- BW_5 N_{Er,5} + BW_{65} N_{Er,6} + B\epsilon N_{Er,2} \\
&- CW_6 N_{Er,6} + C\epsilon N_{Er,3} \\
&= -\left(W_2 - B\epsilon\right) N_{Er,2} - \left(AW_3 - W_{32} - C\epsilon\right) N_{Er,3} \\
&- \left(BW_5 - W_{52} - AW_{53}\right) N_{Er,5} - \left(CW_6 - W_{62} - AW_{63} - BW_{65}\right) N_{Er,6} + Af(t)
\end{aligned}$$

Now we need to choose A, B, C and ϵ in such a way that all the prefactors in brackets in front of $N_{Er,2,3,5,6}$ are positive. So we need to ensure that, simultaneously

$$W_2 - B\epsilon > 0 \tag{3.15}$$

$$AW_3 - W_{32} - C\epsilon > 0 \tag{3.16}$$

$$BW_5 - W_{52} - AW_{53} > 0 \tag{3.17}$$

$$CW_6 - W_{62} - AW_{63} - BW_{65} > 0 \tag{3.18}$$

This is easily achievable. We choose $A = 1$. Then we take Equation 3.17 and choose a sufficiently large B, so that the left hand side becomes positive, this is always possible. With this choice of B and the previously chosen $A = 1$ we take Equation 3.18 and choose C that is large enough to make the left hand side positive. Now we return to Equation 3.16. We note that for our choice of $A = 1$ the value of $AW_3 - W_{32} = W_3 - W_{32}$ is always positive, on the basis of physical argument that $W_3 = W_{31} + W_{32}$. In order to satisfy the inequality 3.16 it is enough to choose a sufficiently small ϵ so that, for our previously chosen C the term $C\epsilon$ is still smaller than $W_3 - W_{32}$. Finally we check whether the ϵ found in this way will satisfy Equation 3.15; if it does not we choose an even smaller ϵ that would satisfy 3.15, for example less than W_2/B, and it would obviously also satisfy Equation 3.16. Similar arguments are used to satisfy 3.17 and 3.18.

Now we reformulate Equation 3.14 so that we can see the form of V_t on the right hand side.

(3.19)

$$\begin{aligned}
\frac{dV}{dt} &< -\left(W_2 - B\epsilon\right) N_{Er,2} - \left(AW_3 - W_{32} - C\epsilon\right) N_{Er,3} \\
&- \left(BW_5 - W_{52} - AW_{53}\right) N_{Er,5} - \left(CW_6 - W_{62} - AW_{63} - BW_{65}\right) N_{Er,6} + Af(t) \\
&= -\left(W_2 - B\epsilon\right) N_{Er,2} - \left(W_3 - W_{32}/A - C\epsilon/A\right) AN_{Er,3} + Af(t) \\
&- \left(W_5 - W_{52}/B - AW_{53}/B\right) BN_{Er,5} - \left(W_6 - W_{62}/C - AW_{63}/C - BW_{65}/C\right) CN_{Er,6}
\end{aligned}$$

-S9-
Now we choose α to be the smallest of these prefactors in brackets, so
$\alpha = \min(W_2 - B\epsilon, W_3 - W_{32}/A - C\epsilon/A, W_5 - W_{52}/B - AW_{53}/B, W_6 - W_{62}/C - AW_{63}/C - BW_{65}/C)$.
We recall that $A = 1$, then, for $t > t_0$ we have

$$\frac{dV}{dt} \leq -\alpha V_t + f(t) \tag{3.20}$$

Now we use the Gronwall Lemma which gives

$$V_t \leq e^{-\alpha(t-t_0)} V_{t_0} + \int_{t_0}^{t} e^{-\alpha(t-s)} f(s) ds \tag{3.21}$$

By point 2 above we have $f(t) \leq De^{-k_{FT}N_{Er}t}$, therefore

$$\begin{aligned} V_t &\leq e^{-\alpha(t-t_0)} V_{t_0} + De^{-\alpha t} \int_{t_0}^{t} e^{\alpha s - k_{FT}N_{Er}s} ds \\ &\leq e^{-\alpha(t-t_0)} V_{t_0} + \frac{D}{\alpha - k_{FT}N_{Er}} \left(e^{-k_{FT}N_{Er}t} - e^{-\alpha(t-t_0) - k_{FT}N_{Er}t_0} \right) \end{aligned} \tag{3.22}$$

We assumed here that the denominator $\alpha - k_{FT}N_{Er}$ is nonzero, if it is then we should change α slightly.
It follows that there exist positive constants $M, \gamma > 0, \gamma = \min(\alpha, k_{FT}N_{Er})$ such that $V_t \leq Me^{-\gamma t}$. We immediately get that $N_{Er,2}(t) \leq Me^{-\gamma t}$ and $N_{Er,3}(t) \leq Me^{-\gamma t}$. Also $N_{Er,5} \leq M/Be^{-\gamma t}$ and $N_{Er,6} \leq M/Ce^{-\gamma t}$.

4. Optimal decay rates for $N_{Yb,2}$ and $N_{Er,2} - N_{Er,6}$

Now we need to find optimal rates of decay for all functions $N_{Er,2,3,5,6}$. We start with $N_{Yb,2}$. From Equation 3.1 we get

$$N_{Yb,2}(t) = N_{Yb,2}(0)e^{-(k_{FT}N_{Er}t)} \times \exp\left[-\int_0^t k_{c2}N_{Er,2}(s)ds - \int_0^t k_{c3}N_{Er,3}(s)ds \right] \tag{3.23}$$

However we have just proved that $\int_0^\infty k_{c2}N_{Er,2}(s)ds < \infty$ and $\int_0^\infty k_{c3}N_{Er,3}(s)ds < \infty$. Therefore again

$$0 < \lim_{t\to\infty} \left[e^{k_{FT}N_{Er}t} N_{Yb,2}(t) \right] < \infty \tag{3.24}$$

that is $\gamma_0 = k_{FT}N_{Er}$ is the optimal rate of decay for $N_{Yb,2}$

For Er we use the following expression for the solution of the first order differential equation

$$\frac{dy}{dt} = \alpha(t)y(t) + f(t) \tag{3.25}$$

It can be expressed using the function $G(t, s)$ given by

$$G(t, s) = \exp\left(\int_s^t \alpha(u)du \right) \tag{3.26}$$

-S10-
The solution can be expressed as

$$y(t) = G(t,0)y(0) + \int_0^t G(t,s)f(s)ds \tag{3.27}$$

For $N_{Er,3}$ we obtain

$$\begin{aligned} N_{Er,3}(t) = G(t,0)N_{Er,3}(0) + \int_0^t G(t,s)\left(W_{53}N_{Er,5}(s) + W_{63}N_{Er,6}(s)\right)ds \\ + \int_0^t G(t,s)k_{FT}N_{Er}N_{Yb,2}(s)ds \end{aligned} \tag{3.28}$$

where

$$G(t,s) = \exp\left[-W_3(t-s) - k_{c3}\int_s^t N_{Yb,2}(u)du\right] \tag{3.29}$$

Since $0 < \int_0^\infty N_{Yb,2}(u)du < \infty$ we have

$$C_1 e^{-W_3(t-s)} \leq G(t,s) \leq C_2 e^{-W_3(t-s)} \tag{3.30}$$

These considerations indicate that $N_{Er,3}$ decays exponentially. This is because $G(t,0)N_{Er,3}(0)$ decays exponentially and there are two other terms that can, potentially make convergence worse. But we have already shown in point 3 that $N_{Er,3}$ has an exponential upper bound. Hence these two terms can not destroy the exponential decay rate, we will see this in more detail in a moment.

We denote γ_0 to be the decay rate for $N_{Yb,2}$,γ_i the decay rate for $N_{Er,i}, i = 2,3,5,6$. Now we calculate γ_3 the exact decay rate for $N_{Er,3}$. By using 3.28 we obtain
(3.31)

$$\begin{aligned} e^{\gamma_3 t}N_{Er,3}(t) \sim e^{(\gamma_3 - W_3)t}N_{Er,3}(0) + e^{\gamma_3 t}\int_0^t W_{53}e^{-W_3(t-s)}N_{Er,5}(s)ds \\ + e^{\gamma_3 t}\int_0^t W_{63}e^{-W_3(t-s)}N_{Er,6}(s)ds + e^{\gamma_3 t}\int_0^t k_{FT}N_{Er}e^{-W_3(t-s)}N_{Yb,2}(s)ds \end{aligned}$$

-S11-

Now we substitute the relevant exponential functions for $N_{Yb,2}, N_{Er,5}$ and $N_{Er,6}$. We carry out the integrations to obtain

$$\begin{aligned} e^{\gamma_3 t} N_{Er,3}(t) &\sim e^{(\gamma_3 - W_3)t} N_{Er,3}(0) + e^{(\gamma_3 - W_3)t} \int_0^t W_{53} e^{(W_3 - \gamma_5)s} ds \\ &+ e^{(\gamma_3 - W_3)t} \int_0^t W_{63} e^{(W_3 - \gamma_6)s} ds + e^{(\gamma_3 - W_3)t} \int_0^t k_{FT} N_{Er} e^{(W_3 - \gamma_0)s} ds \\ &= e^{(\gamma_3 - W_3)t} N_{Er,3}(0) \\ &+ e^{(\gamma_3 - W_3)t} W_{53} \frac{1}{(W_3 - \gamma_5)} \left[e^{(W_3 - \gamma_5)t} - 1 \right] \\ &+ e^{(\gamma_3 - W_3)t} W_{63} \frac{1}{(W_3 - \gamma_6)} \left[e^{(W_3 - \gamma_6)t} - 1 \right] \\ &+ e^{(\gamma_3 - W_3)t} k_{FT} N_{Er} \frac{1}{(W_3 - \gamma_0)} \left[e^{(W_3 - \gamma_0)t} - 1 \right] \end{aligned} \tag{3.32}$$

Now the terms on the right must not tend to infinity because γ_3 is optimal; this gives the conditions that

$$\begin{aligned} \gamma_3 &\leq W_3 \\ \gamma_3 &\leq \gamma_5 \\ \gamma_3 &\leq \gamma_6 \\ \gamma_3 &\leq \gamma_0 \end{aligned} \tag{3.33}$$

Here, γ_3 is, by definition, the largest number that satisfies this condition. In addition, because γ_3 is optimal, at least one of the terms on the right must not tend to zero. Hence at least one of the above inequalities is, in fact, an equality.
By the same argument but using the rate equations for the $N_{Er,2}, N_{Er,5}, N_{Er,6}$ we get:

$$\begin{aligned} \gamma_2 &\leq W_2 \\ \gamma_2 &\leq \gamma_3 \\ \gamma_2 &\leq \gamma_5 \\ \gamma_2 &\leq \gamma_6 \end{aligned} \tag{3.34}$$

and at least one of the above inequalities is an equality. We also obtain that

$$\begin{aligned} \gamma_5 &\leq W_5 \\ \gamma_5 &\leq W_6 \\ \gamma_5 &\leq \gamma_0 + \gamma_2 \end{aligned} \tag{3.35}$$

where at least one of the above inequalities is an equality, and

$$\begin{aligned} \gamma_6 &\leq W_6 \\ \gamma_6 &\leq \gamma_0 + \gamma_3 \end{aligned} \tag{3.36}$$

where at least one of the above inequalities is an equality.

-S12-

From the equations 3.33,..., 3.36 and noting that in each case above we have at least one equality we obtain that

$$\begin{aligned}\gamma_3 &= \min(W_3, \gamma_0, \gamma_5, \gamma_6)\\ \gamma_2 &= \min(W_2, \gamma_3, \gamma_5, \gamma_6)\\ \gamma_5 &= \min(W_5, W_6, \gamma_0 + \gamma_2)\\ \gamma_6 &= \min(W_6, \gamma_0 + \gamma_3)\end{aligned} \tag{3.37}$$

For $W_6 > W_5$ we obtain:

$$\gamma_5 = \min(W_5, \gamma_0 + \gamma_2) \tag{3.38}$$

Therefore, taking into account 3.33 we find that

$$\begin{aligned}\gamma_3 &= \min(W_3, \gamma_0, W_5, \gamma_0 + \gamma_2, W_6, \gamma_0 + \gamma_3)\\ &= \min(W_3, \gamma_0)\end{aligned} \tag{3.39}$$

Similarly, taking into account 3.34 we obtain

$$\begin{aligned}\gamma_2 &= \min(W_2, W_3, \gamma_0, W_5, \gamma_0 + \gamma_2, W_6, \gamma_0 + \gamma_3)\\ &= \min(W_2, \gamma_0)\end{aligned} \tag{3.40}$$

After one more substitution we get

$$\gamma_5 = \min(W_5, W_2 + \gamma_0, 2\gamma_0) \tag{3.41}$$

$$\gamma_6 = \min(W_6, W_3 + \gamma_0, 2\gamma_0) \tag{3.42}$$

We recall that in γ_0 is the decay rate for Yb ions which can be higher than each of the rates within Er, because it is controlled by (arbitrarily high) Er concentration and the forward energy transfer coefficient. In this case we get that $\gamma_6 = W_6$ and $\gamma_5 = W_5$. For low enough γ_0, the terms $W_2 + \gamma_0$, $W_3 + \gamma_0$ and $2\gamma_0$ may become rate-limiting. In the case of $W_6 < W_5$ we get

$$\gamma_5 = \min(W_6, W_2 + \gamma_0, 2\gamma_0) \tag{3.43}$$

$$\gamma_6 = \min(W_6, W_3 + \gamma_0, 2\gamma_0) \tag{3.44}$$

For high enough values of $\gamma_0 = k_{FT} N_{Er}$ we obtain that $\gamma_6 = \gamma_5$, contrary to the experimental observations. This indicates that $W_6 > W_5$.

3.3 Remarks

Different-sized UCNPs were synthesized in a controllable way. The success of precise tuning nanocrystal size is of significance to investigate the size-dependent upconversion luminescence. On the basis of a comprehensive study of upconversion luminescence in both spectral and temporal domains, we found that the smaller $NaYF_4$:Yb,Er UCNPs, the higher ratio of red to green emissions and the shorter lifetime for each emission band. On top of experimental work, the role of the UCNPs size in upconversion luminescence was analytically interpreted by disclosing luminescence dynamics according to rate equations and quantitatively clarified by establishing the core-shell model. Weighting quenching mechanisms in upconversion luminescence and digging out observed decay profiles, we have determined the leading contribution of quenching mechanisms to upconversion luminescence of different-sized UCNPs, revealing that the reduction of the surface defect density is particularly fundamental to enhance the brightness of small UCNPs, i.e., <10 nm.

Distinguished lifetimes associated with different-sized UCNPs provide a new route to realize the lifetime multiplexing of the upconversion luminescence, even in the same spectral characteristic. It thereby formulates one of sections of the Chapter 4 that addresses the creation of a library of multiplexing identities in temporal domain for bioimaging and biosensing applications.

It is beyond the capability of current synthetic techniques of considerably suppressing the surface defect density of very small UCNPs to increase the upconversion brightness. Alternatively, to advance highly bright UCNPs towards an ideal bioprobe, it is urged to increase the effective doping level of an activator in individual UCNPs, which has been suffering from a proportional drop when the UCNPs size shrinks. The Chapter 5 will investigate the method of enriching the amount of an effective activator in UCNPs for the enhanced upconversion luminescence.

Chapter 4: Lifetime Multiplexing

Multiplexing technique, capable of simultaneous identification and quantification of thousands of biomolecular species, plays a critical role in high-throughput biotechnology. However, the capacity of currently most applied spectra-based multiplexing strategy has been limited due to the spectra overlapping of fluorescent materials thus posing the grand challenge to insert or extend new colour codes into current spectral library. In this chapter, we introduced the temporal domain on top of colours to release the constraint in the spectral domain and achieved the lifetime multiplexing by creating multiple non-crosstalking lifetime codes in the temporal domain. We succeeded in using three different optical dynamic mechanisms to engineer decay rates for discrete lifetime codes. We emphasized lifetime-encoded suspension arrays as a proof-of-concept model to display the technological development and applications of the lifetime multiplexing method.

In Chapter 4, I presented results by a traditional way as I extracted my core contributions to data and figures of two journal papers, one published on *Nature Photonics* as the second author and the other published on *Nature Communications* as the third author. For the project, Dayong Jin majorly conceived the lifetime multiplexing concept, and Yiqing Lu and I produced the proof-of-principle demonstration, where I am totally in charge of the material synthesis, lifetime tuning design, sample preparation, immunofluorescence staining test, and security printing.

4.1 Introduction

To meet the increasing demand of multiplexing assays, planar arrays also known as "biochips", were developed in 1990s (Fig. 4.1a) (Fodor, Read et al. 1991, Schena, Shalon et al. 1995, Southern 1996, Wang, Liu et al. 2002, Balboni, Chan et al. 2006). The technique utilizes the microlithography and robotic micro-printing to fix capture molecules onto a Cartesian grid on a substrate, which provides numerous reaction wells (~μL) to screen multiple analytes simultaneously. Virtually, planar arrays are supposed to hold the unlimited multiplexing capacity as micron-sized spots can be predetermined and printed on the planar substrate. However, positional encoded planar arrays lack the reproducibility to yield the quantitative precision (the variation in number of capture molecules on each spot), and in most cases only confer Boolean values of positive or negative for an assay test. An additional concern arises from the fact that molecules on the planar substrate could behave differently from real biological environments, leading to the need of supporting analysis. From a kinetic interaction perspective, the diffusion mechanism between capture molecules and analytes may limit the binding rate and efficiency, especially when the entire volume of sample is small. Planar arrays are also costly to manufacture and customize, as well as require the complicated experimental setup and data acquisition system.

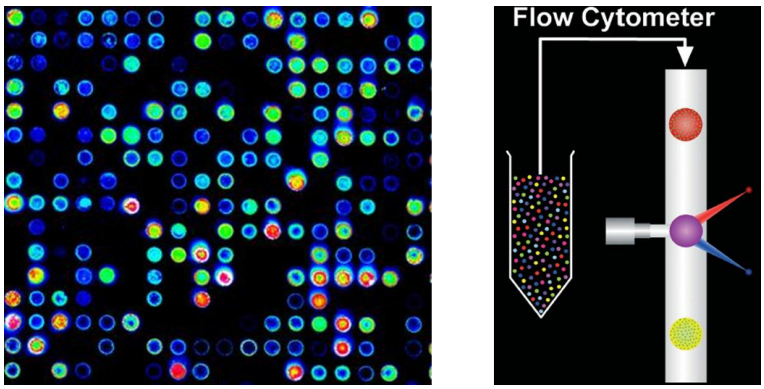

Figure 4.1. (a) The typical scheme of a planar array consists of a two-dimensional grid of recognition molecules (antibodies, peptides, oligonucleotides, etc.). The identity of recognition molecules at each spot in the array is known from its location in the grid. (b) A suspension array is composed of recognition molecules attached to encoded beads (in this image beads are encoded with different colours). The identity of recognition molecules attached to each bead is

revealed by reading the code. (Reprinted with permission from Ref. (Wilson, Cossins et al. 2006), copyright 2006.)

Suspension arrays are emerging as a promising solution for a feasible multiplexed molecular detection (Fig. 4.1b), based on ensembles of microspheres that have been specifically coded with chemical, physical, spectrometric (Cao, Jin et al. 2002, Cunin, Schmedake et al. 2002), colloidal (Trau and Battersby 2001), graphical (Nicewarner-Pena, Freeman et al. 2001, Braeckmans, De Smedt et al. 2003, Pregibon, Toner et al. 2007, Lee, Kim et al. 2010), electronic (Mandecki, Ardelt et al. 2006) and optical encoding (Fulton, McDade et al. 1997, Han, Gao et al. 2001, Li, Cu et al. 2005, Wang, Deng et al. 2011). Major advantages of suspension arrays include rapid reaction kinetics, the absence of tedious washing steps, the improved sample throughput, as well as the reproducible manufacture of microsphere families. Moreover, suspension arrays have potentials as quantitative assays owing to the uniform surface of microspheres, the simplicity of use, and their reduced expense compared to alternatives. The test panel is flexible to design by simply selecting a different combination of microspheres.

Over the past two decades significant efforts have been devoted to expand multiplexing capacities towards the desired advance of suspension arrays over planar array biochips. Through endowing microspheres with varying combinations of fluorescent dyes, suspension arrays are most frequently distinguished by a range of identifiable colour codes that are individually assigned to a specific analyte. Although the fluorescence encoding and decoding strategy appears to be more practical than non-fluorescence schemes in terms of Assay design, Cost per test, Binding kinetics, Instrumental simplicity, and Throughput, producing a very large number of independent fluorescence codes by engineering the intensity ratio of different colours has been restrained in the crowded spectral domain (Han, Gao et al. 2001). Moreover, this colour-code competition may generate unavoidable interfering background for a quantitative surface bioassay. Thus the highlighted challenge is to find a way of expanding coding dimensions (domains) to significantly increasing the number of optical codes or multiplexing levels in which the surface quantitative binding assays would be optically immune to these added codes and the upgraded suspension arrays should not trade off the simplicity, assay speed, and low cost.

4.2 Concept underpinning this chapter

Fig. 4.2 illustrates the core idea of significantly increasing the multiplexing capability in suspension arrays by exploring the untapped luminescent property in temporal domain to achieve the lifetime multiplexing as an additional coding dimension. Firstly, to create multiple lifetime identities, Ln^{3+}-doped materials emitting the exceptionally long-lifetime luminescence has been utilized, which is however inaccessible to QDs, fluorescent molecules and colour centres of nanodiamonds (Table 1.1). Secondly, Ln^{3+}-doped materials can access for three practical mechanisms to precisely tune luminescent decays in the microsecond range and produce individual populations of microspheres with distinct lifetimes (Selvin 2002, Bunzli 2010). Thirdly, using our purpose-built TR-OSAM, lifetime decays and luminescent spectra of individual microspheres can be simultaneously, rapidly and precisely resolved. The real-time lifetime fitting algorithm of the decoding system allows to process maximum 0.58 million microspheres per hour at a high recovery rate of more than 99%.

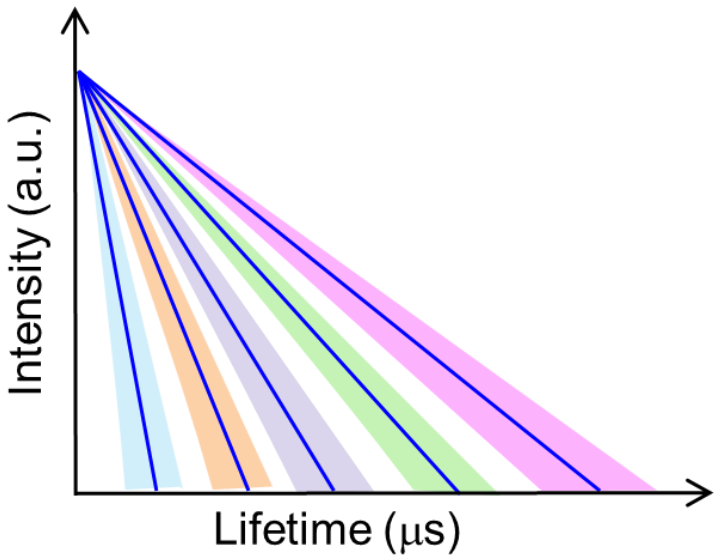

Figure 4.2. The concept of tuning lifetimes of Ln^{3+} luminescence to achieve optical multiplexing in the temporal domain.

4.3 Experimental section

Synthesis of $NaYF_4$:Yb, Tm/Er UCNPs

Chapter 3 provided detailed procedures to prepare monodisperse UCNPs with varying particle sizes, crystal phases and dopant concentrations. All as-prepared $NaYF_4$:Yb,Tm/Er UCNPs were dispersed in cyclohexane with 10 mg/mL concentration.

Preparation of microspheres encoded by UCNPs

Encoding microspheres by incorporating UCNPs can be achieved by any of following method: (i) UCNPs are captured or affinity-partitioned on the surface or subsurface of microspheres (Han, Gao et al. 2001); (ii) UCNPs are bound onto oppositely charged microspheres *via* a layer-by-layer strategy (Wang, Rogach et al. 2002); (iii) UCNPs are loaded when synthesizing polystyrene microspheres, either by the emulsion (Yang and Zhang 2004) or suspension polymerization technique (Li, Liu et al. 2005).

In this proof-of-concept experiment, UCNPs encoded microspheres were prepared through method (i) for simplicity. Briefly, swelling beads (~2.6×10^5 beads, ~15.14 μm) were obtained in a 200 μL solvent mixture with 5 % chloroform and 95 % butanol (vol/vol) with mild stirring for 1 hr. The UCNP solution (50 μL, 10mg/mL) was added and incubated with polystyrene beads. The incorporation process lasted for 12 h at room temperature. Finally, encoded beads were collected by centrifugation, washed three times with ethanol, and re-dispersed in deionized water.

Preparation of microspheres encapsulated by $Eu(TTFA)_3$

Solutions of fluorescent dyes were prepared by dissolving the fixed $Eu(TTFA)_3$ complex (2.5 μmol) with varied molar quantities of hexafluorophosphate salt ranging from 0.1~1.2 μmol in 200 μL dichloromethane (DCM). Then, 900 μL of polystyrene microspheres suspension in ethanol (~15.14 μm, 2.6×10^5 beads) was mixed with 200 μL of the respective fluorescent dye in DCM for encapsulation. The mixture was stirred for 48 hrs to ensure the impregnation, before these impregnated microspheres were shrunk in absolute ethanol. Encoded microspheres were then quickly isolated by centrifugation and washed in ethanol:water (vol/vol 1:1) by three times. Finally, encoded microspheres were stored in 500 μL water.

Preparation of microspheres encoded by UCNPs and $Eu(TTFA)_3$

Microspheres (~2.6×10^5) were first swelled in a 200 μL solvent of 5 % chloroform and 95 % butanol (vol/vol) as above. Then, UCNPs (25 uL, 20mg/mL) and $Eu(TTFA)_3$ (25 uL, 2.5 μmol) were thoroughly mixed, followed by the incubation with as-prepared swollen microspheres for 24 hrs. Such incubation can encapsulate UCNPs and fluorescent dyes into polystyrene microspheres by a single step. These encoded beads were isolated by centrifugation, washed by ethanol: water (vol/vol 1/1) and absolute ethanol for several times, and re-dispersed in deionized water.

Preparation of individual microspheres on glass slides

An amount of polystyrene microspheres was drop-cast onto a glass slide. To prevent microspheres aggregating, the slide was covered by a 1 cm × 2 cm coverslip and dried at 40 ^oC for 4 hrs. After the solvent evaporation, encoded microspheres were individually distributed on the slide for the microscope characterization under a 100× objective with a working distance of 0.3 mm.

4.4 Results and discussion

Green-channel lifetimes *via* Er^{3+}-doped UCNPs

The first lifetime-tuned scheme is based on varying the size of UCNPs. As demonstrated in Chapter 3, for Yb^{3+} and Er^{3+} concentrations fixed at 20 mol% and 2 mol%, respectively, smaller-sized UCNPs typically yield shorter lifetimes because of the increased level of surface quenching effects accompanying with their larger surface-to-volume ratios. With this principle, 6 nm (cubic phase), 15 nm (cubic phase), 30 nm (hexagonal phase) and 40 nm (hexagonal phase) UCNPs were selected to encode microspheres by the single-step encapsulation method. As SEM image shown in Fig. 4.3a, UCNPs were uniformly deposited on microspheres. These encoded microspheres measured by TR-OSAM, can generate four clearly separated green-channel lifetime histograms with mean values at 33 μs, 63 μs, 101 μs, and 137 μs, respectively (Fig. 4.3b). Additionally, the CV obtained by plotting statistical lifetime histograms was quite narrow, ranging from 1.8% to 8.4%.

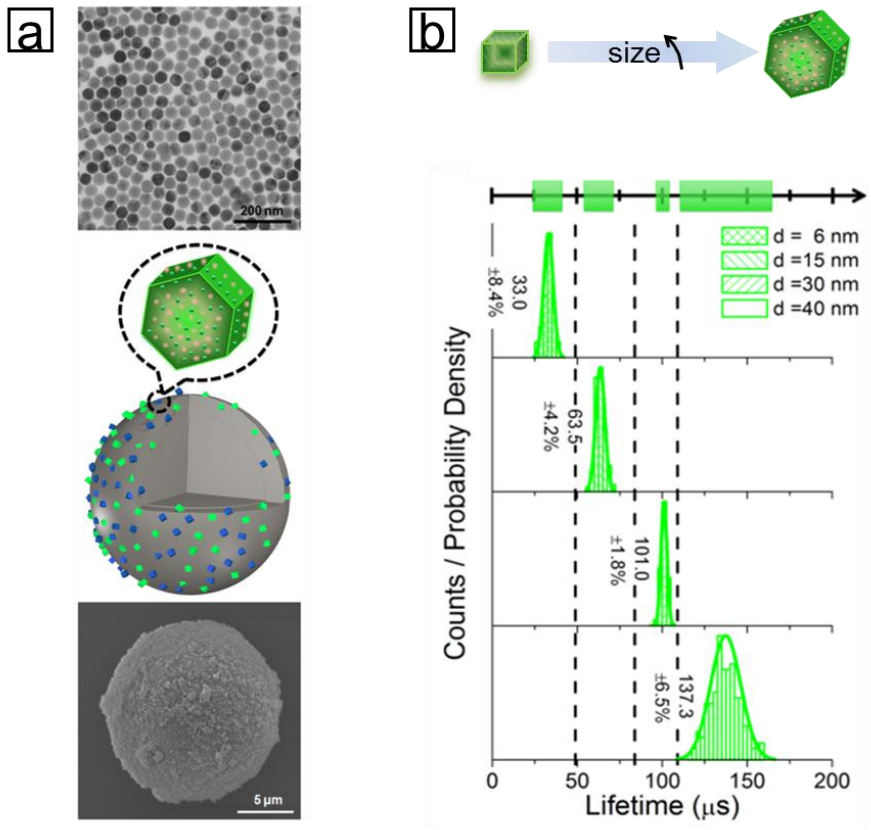

Fig 3. (a) The scheme of suspension arrays by assembling UCNPs as building blocks on microspheres. Top panel: TEM of ~30 nm UCNPs; bottom panel: SEM of UCNPs-encoded microspheres. (b) Size-dependent lifetimes of UCNPs have produced 4 populations of Er^{3+} encoded microspheres at green band. Numerals at the left of each histogram population are the mean lifetime ± CV from Gaussian statistics fitting.

Blue-channel lifetimes *via* Tm^{3+}-doped UCNPs

The second scheme is based on stepwise varying co-dopant concentrations of sensitizer Yb^{3+} ions and activator Tm^{3+} ions (blue emission) in $NaYF_4$ nanocrystals. In this case, the lifetime tunability is provided by tuning the energy transfer rate from Yb^{3+} to Tm^{3+}, which is dependent on the sensitizer-activator distance. In Fig. 4.4, the Tm^{3+} variation from 0.2 mol% to 8 mol% (Yb^{3+} fixed at 20 mol%) resulted in a remarkably large range of blue-channel lifetimes from 25.6 μs to 662.4 μs. Increasing the Yb^{3+} concentration from 10 mol% to 30 mol% (Tm^{3+} fixed at 1 mol%) also significantly accelerated blue emission decays, inducing the decrease of lifetime from 206.7 μs to 120.2 μs. This

reflects the fact that higher concentrations of activator and/or sensitizer shorten the average sensitizer-activator distance, and enhance the energy transfer rate. Furthermore, the size-dependent lifetime mechanism has also been verified in Tm^{3+} emission. Owing to the smaller size of $NaYF_4$:20%Yb,1%Tm UCNPs in cubic phase than that in hexagonal phase, we tuned their lifetime from 155.1 μs to 104.1 μs. More importantly, for each of these population groups, the lifetime CV can be as low as 1.5% (the first two shortest lifetimes have slightly larger CV due to small average lifetime values). The narrow CV facilitated the realization of at least eight completely separated lifetime channels in blue, and there are sufficient potential for ten channels or more in total (note large gaps among the last three populations).

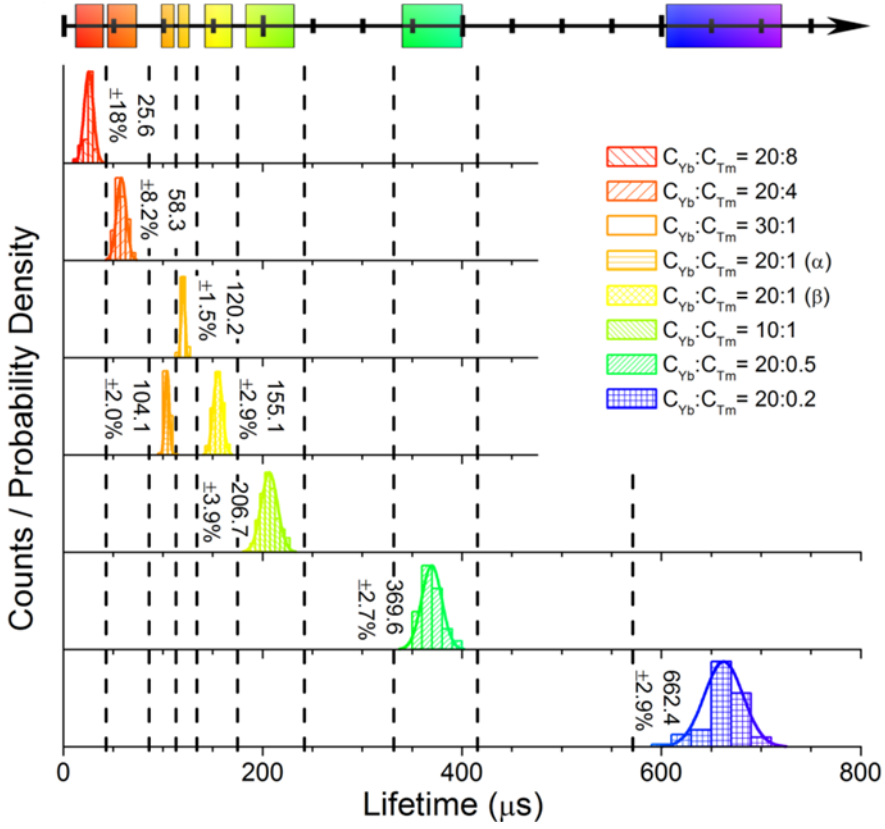

Figure 4.4. The unique lifetime-encoded populations of microspheres as multiplexing suspension arrays. Eight lifetime populations of microspheres at Tm^{3+} blue emission band can be generated *via* adjusting co-dopant concentrations of sensitizer-activator, referred to the mechanism of upconversion energy transfer. Numerals beside each histogram is the mean lifetime ± CV from Gaussian distribution fitting.

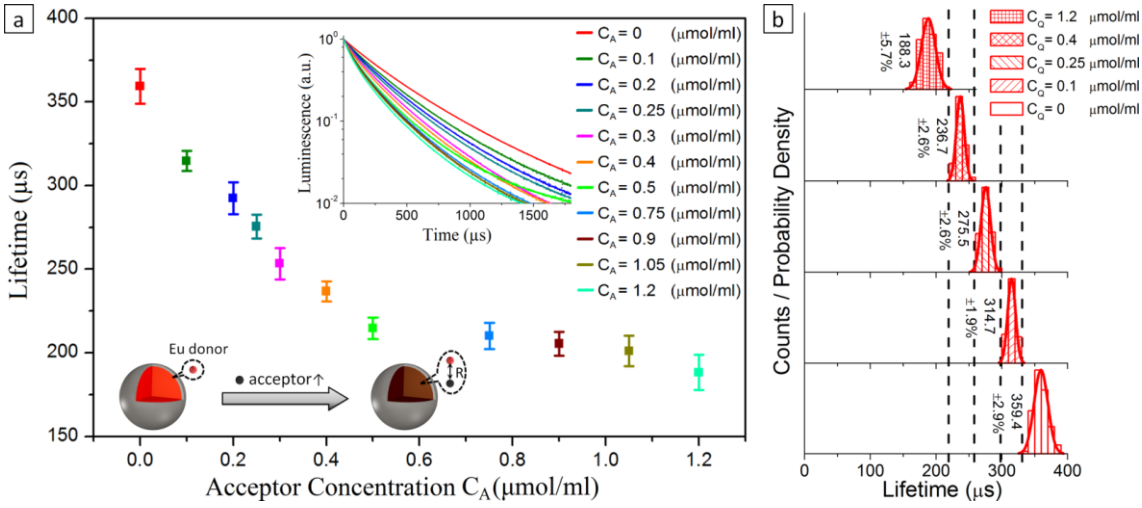

Figure 4.5. Different lifetimes of individual Eu^{3+}-containing microspheres are engineered by FRET. Solutions containing identical amount of Eu^{3+} complexes as donor but incremental amounts of acceptor dyes were encapsulated into individual groups of polymer microspheres, followed by TR-OSAM analysis. (a) The luminescence lifetime measured at Eu^{3+} red emission band shortens since the acceptor concentration increases as a result of FRET effect. Inset curves are luminescence decay signals measured from many individual Eu^{3+}-FRET microspheres. (b) Five completely separate lifetime histograms are generated from impregnated microspheres. Numerals at the left of each histogram are the mean lifetime ± CV for the Gaussian fitting.

Red lifetime *via* FRET

The third lifetime-tunable suspension arrays are produced through FRET mechanism (Selvin, Rana et al. 1994, Kurner, Klimant et al. 2001, Xiao and Selvin 2001). The rate of FRET from a donor and an acceptor $k_T(r)$ is given by

$$k_T(r) = \frac{1}{\tau_D}\left(\frac{R_0}{r}\right)^6$$

where τ_D is the lifetime of the donor in the absence of acceptor, R_0 is the Föster distance, and r is the donor-to-acceptor distance. Hence, the rate of energy transfer depends strongly on the distance, and is proportional to r^{-6}. The condition that affects the distance of donor and acceptor will affect $k_T(r)$, resulting in the change of lifetime of the donor.

For the red channel lifetime, the $Eu(TTFA)_3$ complex as the donor is encapsulated into porous polystyrene beads that can have dipole-dipole interactions with the coumarin acceptor in beads, allowing energy transfer to occur (Deniz, Sortino et al. 2010). In this type

of application, the efficiency of energy transfer for a fixed concentration $Eu(TTFA)_3$ donor can be tuned by the donor-to-acceptor distance by stepwise varying the respective concentrations of the acceptor dye (Heyduk and Heyduk 2001, Selvin 2002). It allows to refine the luminescence lifetime of the Eu^{3+} complex at the red emission band around 612 nm. Fig. 4.5a illustrates that as the acceptor concentration increases (at the identical donor concentration), the mean value of the donor lifetime is effectively shorten down from 359 µs to 188 µs. The lifetime histogram of different combinations of the donor and acceptor encoded beads shows five distinguishable populations (at 183 µs, 236 µs, 275 µs, 314 µs, and 359 µs) with the CV from 1.9% to 5.7%, as shown in Fig. 4.5b.

Lifetimes at the respective green, blue, and red emission are spectrally well separated, thanks to narrow Ln^{3+} luminescence (Fig. 4.6). To demonstrate the absence of crosstalk between three lifetime channels, we synthesized a population of microspheres coded by a unique combination of lifetime codes “3” in red (representing the third lifetime population of Eu^{3+} emission at 275 µs), “5” in blue (the fifth lifetime population of Tm^{3+} emission at 369.6 µs) and “3” in green (the third lifetime emission of Er^{3+} at 101 µs). These beads have been successfully decoded and their three-dimensional lifetime scatter plot forms a very tight cluster, as shown in Fig. 4.6a and 4.6c. The extracted values for mean lifetime and CV are consistent with populations identified in above three individual lifetime-coded suspension arrays.

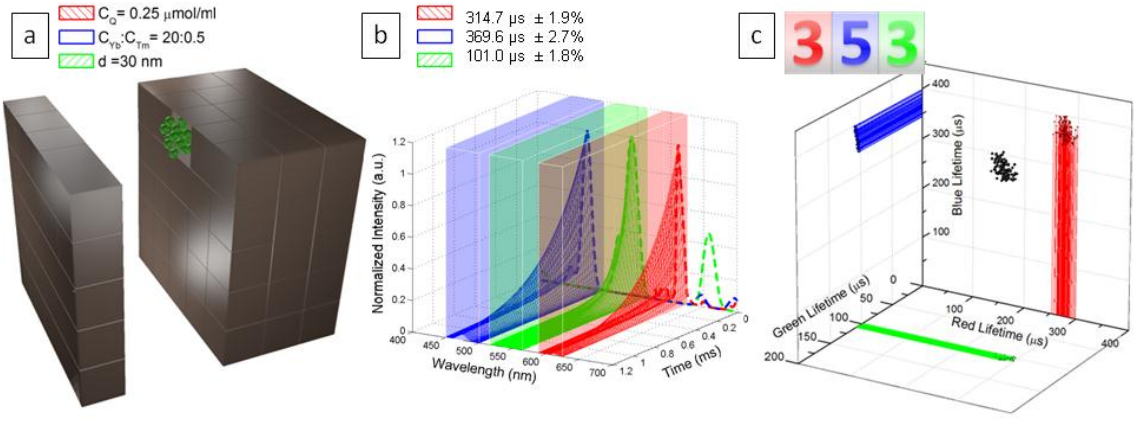

Figure 4.6. An optical library of 100 time-resolved suspension arrays, carrying combinational lifetime codes at three non-crosstalk spectral region: (a) one particular population was synthesized according to recipes of three lifetime tuning schemes; (b) the time-resolved spectral

scanned to recover the 314.7 µs Red, 369.6 µs Blue and 101.0 µs Green codes; (c) The cluster of dots in the 3D plot of lifetime space shows the discriminative population of "353" microspheres.

Lifetime-based multiplexing channels based on Ln^{3+} luminescence bring following advantages: (1) The lifetime is less prone to decoding errors induced by optical defocusing, ambient background, and electronic noise, since it is based on the decay profile rather than on absolute intensity measurements. (2) The time-resolved detection of exceptionally long luminescence in the microsecond domain can completely suppress all autofluorescence background from usually complex biological samples as well as any surface-bound assay reporter dye on microspheres (Rajapakse, Gahlaut et al. 2010). (3) Ln^{3+}-doped materials employed here emit luminescence only under UV (300 nm to 370 nm) and NIR (~980 nm) irradiation; thus luminescence signals carrying lifetime codes are not observed when microspheres are excited by visible light to read the surface bioassay signal. (4) The decoding instrument is simple, consisting of two diode sources (365 nm LED and ~980 nm NIR laser diode) and a single detector design. With this combination of attractive features, we provide an optical library of analytical channels; each specifically assigned to probe one of not tens, but thousands of distinctive molecular targets at high throughput.

4.5 Conclusions

Grand challenges of life sciences underpinned by biological complexity require high-throughput analytical technologies (Schena, Shalon et al. 1995, Han, Gao et al. 2001, Nicewarner-Pena, Freeman et al. 2001, Cao, Jin et al. 2002, Cunin, Schmedake et al. 2002, Braeckmans, De Smedt et al. 2003, Thomson, Parker et al. 2004, Li, Cu et al. 2005, Pregibon, Toner et al. 2007, Bendall, Simonds et al. 2011, Wang, Deng et al. 2011), capable of simultaneous identification and quantification of thousands of biomolecular species, known as multiplexing. Multiplexing diagnostics is important in areas of genomics (Lander, Linton et al. 2001, Bartel 2004), proteomics (Pawson and Nash 2003), metabolomics (Nicholson and Lindon 2008), cytomics (Bendall, Simonds

et al. 2011), and across medicine (van 't Veer and Bernards 2008). In this work, we radically extended the multiplexing capability of spectrally-coded suspension arrays by adding the yet untapped temporal domain. We experimentally demonstrated time-resolved suspension arrays comprising lifetime-encoded microspheres, independent from those used in spectral multiplexing. When used concurrently, they may bring the total available multiplexing level to 10,000 or more. To produce lifetime codes, we designed three spectrally different Ln^{3+} materials with distinguishable emissions: 610-625 nm of Eu^{3+} emission excited by pulsed UV light, and 525-545 nm of Er^{3+} and 450-490 nm of Tm^{3+} emission, both excited by pulsed NIR light. The emission lifetime of each Ln^{3+} can be tuned over a large dynamic range. By combining three materials, one from each family, we produced populations of microspheres characterized by three independent values of lifetime that can be read separately in red, green, or blue. The multiplexing level in the entire microsphere set is 160 and equals to combinations of available lifetime in each Ln^{3+} families (e.g. 4 for green, 8 for blue, and 5 for green). The large dynamic range and narrow CV of each microsphere population indicates that additional lifetime channels can be obtained, and up to 10 lifetime codes for each spectral band should be realistically achievable. Furthermore, at least two more spectral bands are available under UV excitation (e.g. ~545 nm of Tb^{3+} emission and ~700 nm of Pt^{3+} emission) (Hennink, deHaas et al. 1996, Ye, Tan et al. 2004), which can create the number of lifetime coding bands up to $\sim 10^5$ independent spectrum-lifetime codes. Here, we have laid the foundation for future libraries of microspheres carrying more than 10,000 codes, offering far greater scope and more flexibility with assay design. Therefore, this work unlocks the hidden potential of suspension arrays as the outstanding analytical technique to cope with complexities in life sciences and medicine.

Chapter 5: Enhanced Upconversion

This chapter describes the methodology of enhancing the upconversion luminescence by enriching effective activators in individual UCNPs levered by the sufficient excitation irradiance. For the consistent comparison, different activator concentrations (Tm^{3+}) doped $NaYF_4$ UCNPs were synthesized with the uniform size ~40 nm in the hexagonal phase. To produce the high excitation irradiance, a single-mode NIR 980 nm laser beam was guided into the suspended-core microstructured optical fibre. A series of diluted UCNPs suspensions were drawn into the fibre *via* the capillary action, followed by the quantitative characterization of their upconversion intensities. The continuous increase of the upconversion luminescence was observed when increasing Tm^{3+} concentration doped in $NaYF_4$ UCNPs from 0.2 mol% to 8 mol% under the high excitation irradiance, without any quenching occurring. This result indicates that the high irradiance is able to pump the larger amount of Yb^{3+} ions to the excited state which then sensitize more Tm^{3+} ions from the intermediate level to higher energy states, thereby significantly boosting the upconversion signal even for heavily doped UCNPs. It eventually leads to the remote track of a single nanocrystal in the fibre dip sensor, representing the ultimate nanocrystal sensitivity in the fibre dip sensor. The novel discovery of the enhanced upconversion brightness and the improved detection sensitivity was extended to a range of different applications, such as immunofluorescence imaging, rare-event cells detection and quantification, and security ink for printing. This work is presented in the form of a journal publication from *Nature Nanotechnology*.

5.1 Contributions to Paper 2

TABLE 5-1 Author contributions.

	J.Z.	D.J.	E.P.S.	Y.Lu.	Y.Liu.	A.V.Z.	L.Z.	J.M.D.	P.X.	J.A.P.	E.M.G.	T.M.M.
Project Design	●	●										●
Materials	●					●						
System Setup	●	●	●	●								●
Data Collection	●	●	●		●		●					
Analysis	●	●	●		●	●	●	●	●	●	●	●
Manuscript & Figures	●	●	●	●	●			●		●	●	●
Modelling	●										●	
Supplementary Information	●	●				●	●				●	

The research in Chapter 5 was mainly conceived and supervised by Dayong Jin and Tanya Monro. The data acquisition and results analysis were primarily undertaken by myself, Erik Schartner, and Dayong Jin. The manuscript and main figures were completed by myself, Dayong Jin, Ewa Goldys, and Tanya Monro. Major supplementary materials were prepared by myself, Andrei Zvyagin, and Dayong Jin. The theoretical modelling and numerical simulations were conducted by myself, Ewa Goldys and Dayong Jin. All coauthors involved in the data analysis, results discussion and manuscript preparation.

5.2 Paper 2

Zhao J, Jin D, Schartner E P, Lu Y, Liu Y, Zvyagin A V, Zhang L, Dawes J M, Xi P, Piper J A, Goldys E G, Monro T M, "Single-nanocrystal sensitivity achieved by enhanced upconversion luminescence". ***Nature Nanotechnology***, 2013, **8**, 794-796.

(First published online: 01 Sep 2013)

nature nanotechnology

LETTERS

PUBLISHED ONLINE: 1 SEPTEMBER 2013 | DOI: 10.1038/NNANO.2013.171

Single-nanocrystal sensitivity achieved by enhanced upconversion luminescence

Jiangbo Zhao[1], Dayong Jin[1]*, Erik P. Schartner[2], Yiqing Lu[1], Yujia Liu[1,3], Andrei V. Zvyagin[1], Lixin Zhang[1], Judith M. Dawes[1], Peng Xi[3,4], James A. Piper[1], Ewa M. Goldys[1] and Tanya M. Monro[2]

Upconversion nanocrystals convert infrared radiation to visible luminescence, and are promising for applications in biodetection[1–3], bioimaging[4–7], solar cells[8–10] and three-dimensional display technologies[8,9,11]. Although the design of suitable nanocrystals has improved the performance of upconversion nanocrystals[10,12–14], their emission brightness is limited by the low doping concentration of activator ions needed to avoid the luminescence quenching that occurs at high concentrations[15,16]. Here, we demonstrate that high excitation irradiance can alleviate concentration quenching in upconversion luminescence when combined with higher activator concentration, which can be increased from 0.5 mol% to 8 mol% Tm^{3+} in $NaYF_4$. This leads to significantly enhanced luminescence signals, by up to a factor of 70. By using such bright nanocrystals, we demonstrate remote tracking of a single nanocrystal with a microstructured optical-fibre dip sensor. This represents a sensitivity improvement of three orders of magnitude over benchmark nanocrystals such as quantum dots[17].

Lanthanide-doped upconversion nanocrystals[8,9] are typically doped with ytterbium (Yb^{3+}) sensitizer ions, which absorb infrared radiation and non-radiatively transfer their excitation to activator ions such as erbium (Er^{3+}), thulium (Tm^{3+}) or holmium (Ho^{3+}). Although recent advances in synthesis have led to accurate control of upconversion nanocrystal morphology, crystal phase and emission colours[7,11,15,16,18–21], it has been difficult to achieve strong upconversion luminescence. Attempts to overcome this problem include coating nanocrystals with an inert/active shell to minimize surface quenching[12,14,22,23], or using noble metal nanostructures to enhance the energy transfer rate by surface plasmons[24,25]. However, these approaches do not address the intrinsic limitation of concentration quenching[15,16,18], where brightness decreases with increasing dopant density beyond the optimal concentration threshold. The optimal Tm^{3+} concentration in $NaYF_4$ host lattices is low, in the range of ~0.2–0.5 mol% at excitation irradiance below 100 W cm^{-2} (with ~20–40 mol% Yb^{3+})[16,26–29]. Such nanocrystals have small numbers of activators and therefore produce weak upconversion emission.

Here we present evidence that upconversion luminescence can be significantly enhanced by using much higher activator concentrations under relatively high-irradiance excitation. We have found that this previously unexplored regime achieves a new balance between the sensitizers, activators and excitation irradiance, and can overcome the widely reported concentration quenching in upconversion[15,16,18,26–29]. As a result, it has been possible to realize high bright upconversion luminescence in 8 mol% Tm^{3+}-doped $NaYF_4$ nanocrystals co-doped with 20 mol% Yb^{3+}. Their high brightness originates from a combination of high excitation intensity, increased activator concentration, and accelerated sensitizer–activator energy transfer rate arising from the decreased average minimum distance between adjacent Ln^{3+} ions. This significantly enhanced upconversion has enabled the remote detection of a single nanocrystal using a fibre dip sensor.

Hexagonal-phase $NaYF_4$ nanocrystals were synthesized with Tm^{3+} concentrations in the range ~0.2–8 mol% co-doped with 20 mol% Yb^{3+} (Supplementary Section S1 and Fig. S1). A single-mode continuous-wave 980 nm diode laser beam launched into a suspended-core microstructured optical fibre (Fig. 1) produced excitation irradiance values of up to 2.5×10^6 W cm^{-2}. The uniform ~40 nm nanocrystals dispersed in cyclohexane (39 pM) were drawn into the holes in the fibre for upconversion luminescence measurements (Supplementary Section S2). This brings the nanocrystals into the vicinity of sufficiently high intensity guided light, and also provides a platform suitable for efficiently collecting their emission. At 2.5×10^6 W cm^{-2} irradiance, we observed that the 8 mol% Tm^{3+} nanocrystals generate a previously unreported bright upconversion emission that is much stronger than in 0.5 mol% Tm^{3+} nanocrystals (the 802 nm emission is increased by a factor of 70, Fig. 1c). In contrast, at a low excitation of 10 W cm^{-2}, our results (Supplementary Fig. S2) show that the upconversion intensity as a function of Tm^{3+} concentration first increases and then decreases above 0.5 mol% Tm^{3+}, consistent with previous reports[16,26–29]. This observation indicates that efficient upconversion emission can be realized at a high activator doping, but only when sufficient irradiance is provided (~1×10^6 W cm^{-2}, achieved in laser scanning microscopy). Sufficient excitation irradiance can unlock otherwise dark activators, thereby enhancing the upconversion brightness (Supplementary Fig S3). This effect is independent of nanocrystal size (from tens to several hundreds of nanometres), surface conditions and synthesis conditions (Supplementary Sections S3, S4, Figs S3–S7).

To understand the relationship between the upconversion signal, activator concentration and excitation irradiance, we collected a matrix of power-dependent (1.6×10^4 W cm^{-2} to 2.5×10^6 W cm^{-2}) luminescence spectra for same sized ~40 nm upconversion nanocrystals at varying Tm^{3+} concentrations. The spectra, which are similar to those in Fig. 2b were decomposed into individual Gaussian peaks (Fig. 2c). These were divided into three groups according to the initial Tm^{3+} levels: the $^3H_4$ group, comprising a single peak at 802 nm, the $^1G_4$ group, with 650 nm and 480 nm peaks, and the $^1D_2$ group, with peaks at 455 nm, 514 nm, 744 nm and 782 nm (see Fig. 2a for a simplified diagram of transitions in the Yb^{3+}–Tm^{3+} system). The integrated intensity ratios of the $^1D_2$

[1]Advanced Cytometry Laboratories, MQ Photonics Research Centre and MQ BioFocus Research Centre, Macquarie University, Sydney, New South Wales 2109, Australia, [2]Institute of Photonics and Advanced Sensing and School of Chemistry and Physics, University of Adelaide, Adelaide, South Australia 5005, Australia, [3]School of Biomedical Engineering, Shanghai Jiao Tong University, Shanghai, China, [4]Department of Biomedical Engineering, College of Engineering, Peking University, Beijing 100871, China. *e-mail: dayong.jin@mq.edu.au

LETTERS NATURE NANOTECHNOLOGY DOI: 10.1038/NNANO.2013.171

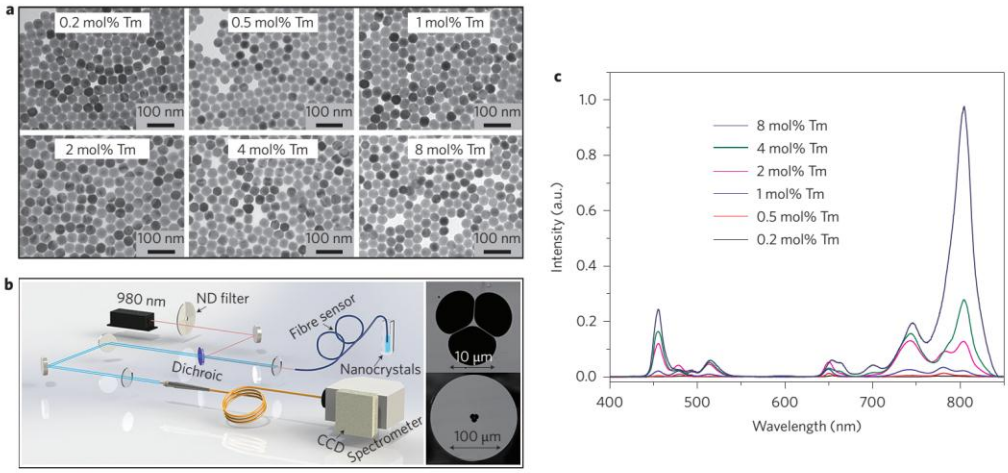

Figure 1 | Highly Tm^{3+}-doped $NaYF_4$ nanocrystals exhibit enhanced upconversion in a suspended-core fibre. a, Transmission electron microscopy images of monodispersed $NaYF_4$:Yb/Tm nanocrystals at different doping levels. All nanoparticles have a similar average size with a narrow size distribution. **b**, Schematic of the experimental configuration for capturing upconversion luminescence of $NaYF_4$:Yb/Tm nanocrystals using a suspended-core microstructured optical-fibre dip sensor. The continuous-wave 980-nm diode laser is targeted at the suspended core. Light propagates along the length of the fibre and interacts with the upconversion nanocrystals located within the surrounding holes. The excited upconversion luminescence is coupled into the fibre core and the backward-propagating light is captured by a spectrometer. Inset: scanning electron microscope images showing a cross-section of the F2 suspended-core microstructured optical fibre at different magnifications. The fibre outer diameter is 160 μm with a 17 μm hole and 1.43 μm core. **c**, Upconversion spectra of a series of $NaYF_4$:Yb/Tm nanocrystals with varied Tm^{3+} concentrations under an excitation irradiance of 2.5×10^6 W cm^{-2}, showing a steady increase in upconversion luminescence with increasing Tm^{3+} content from 0.2 mol% to 8 mol%.

to $^3H_4$ and $^1G_4$ to $^3H_4$ groups (Fig. 2d) show a decreasing contribution of emissions from the $^1G_4$ and $^1D_2$ groups with increasing Tm^{3+} content compared to $^3H_4$ emission. This suggests that the respective population ratios of $^1D_2$ and $^1G_4$ levels to $^3H_4$ decrease in these conditions, to a point where the 8 mol% Tm^{3+} nanocrystals mainly produce the $^3H_4$ (802 nm) emission within our excitation range. We also note that the emission ratios of $^1G_4$:$^3H_4$ and $^1D_2$:$^3H_4$ increase with excitation irradiance in all samples. This suggests that, with increasing excitation irradiance, the population of $^1D_2$ and $^1G_4$ levels increases faster than the population of $^3H_4$. These trends also suggest that a low activator concentration causes an energy transfer bottleneck: at increasing excitation powers the $^3H_4$ level eventually reaches its full capacity to release the 802 nm emission energy (Fig. 2e), and, in order to release any additional energy transferred from Yb^{3+}, the higher energy level emissions in Tm^{3+} ($^1G_4$ and $^1D_2$) become progressively activated. At higher Tm^{3+} concentrations the decay rate of the $^3H_4$ population increases, and this shifts the bottleneck to proportionately higher excitation energies.

Moreover, we have confirmed that the absolute conversion efficiency strongly increases with increasing irradiance, which is attributed to increased excited-state populations of sensitizer and activator ions. The absolute conversion efficiency is defined as the ratio of the emitted to absorbed power (Supplementary Section S5 and Fig. S8)[14]. The absolute conversion efficiency in the low concentration (0.5 mol%) sample reaches a plateau at 3×10^2 W cm^{-2}, whereas in the high concentration (4 mol%) sample it continues to increase within this range. We also measured the power-dependent relative upconversion efficiency for the different nanocrystal samples (Fig. 3a). Increasing the excitation irradiance from 1.6×10^4 W cm^{-2} to 2.5×10^6 W cm^{-2} enhances the overall upconversion luminescence intensity by factors of 5.6, 71 and 1,105 for 0.5 mol%, 4 mol% and 8 mol% Tm^{3+}, respectively. Additionally, this figure indicates that the partitioning of excitation energy flux between the 'effective' 980 nm quanta actually producing upconversion and those 980 nm quanta that are lost on other processes (such as various non-radiative recombination and unobserved emissions) changes dramatically with excitation irradiance and concentration of Tm^{3+} ions. Importantly, at high excitation and high Tm^{3+} doping level, the fraction of excitation energy producing upconversion emission is increased. This shows that upconversion is more efficient at high excitation and for high Tm^{3+} doping. The effect is observed to be especially strong for the 8 mol% Tm^{3+} samples, as is evident from the extremely steep slope above 2×10^6 W cm^{-2} excitation irradiance. Figure 3b shows the same integrated upconversion intensity per Tm^{3+} ion for different Tm^{3+} doping levels. Although the observation of significant enhancement in upconversion intensity from 0.2 mol% to 1 mol% may be due to the fact that upconversion from five photon excitations, previously reported in 0.2 mol% Tm^{3+} (refs 30–32), was not collected in this work, the increase from 1 mol% to 2 mol% clearly shows that the energy transfer efficiency from Yb^{3+} sensitizers to Tm^{3+} activators has been significantly enhanced. This work has therefore shown that the decreased excited sensitizer-to-excited activator distance has indeed increased the energy transfer efficiency, which makes a significant contribution to enhancing the overall conversion efficiency.

To verify that increasing the excitation irradiance enhances the upconversion luminescence and changes the optimal activator/sensitizer concentration ratio, we formulated the rate equations in a generalized upconverting Yb^{3+}–Ln^{3+} system (Supplementary Section S6 and Fig. S9a). In our model the lanthanide ion (activator) is represented by three states—Ln_0, Ln_1 and Ln_2—with equal energy spacing $E_2-E_1 = E_1-E_0$, and the upconversion emission takes place from the excited Ln_2 state to the ground Ln_0 state. The lanthanide ions are excited by energy transfer from the excited states of Yb^{3+} (Yb_1) populated by transitions from the ground-state Yb_0, which have the same energy spacing of E_1-E_0. Using our rate equations,

NATURE NANOTECHNOLOGY DOI: 10.1038/NNANO.2013.171 LETTERS

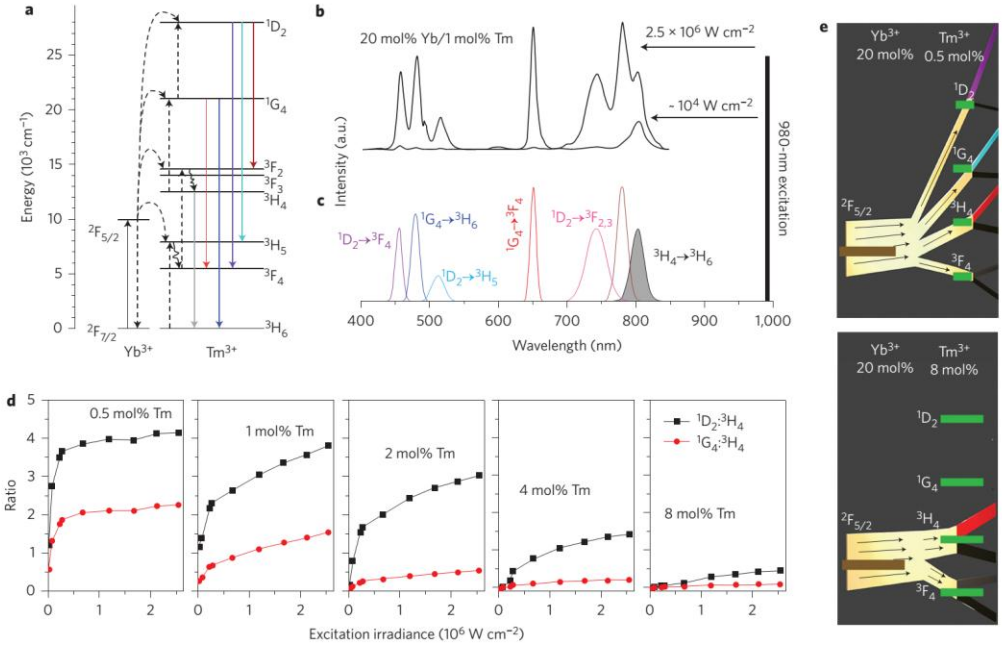

Figure 2 | Analysis of power-dependent multiphoton upconversion. a, Simplified energy-level scheme of $NaYF_4$:Yb/Tm nanocrystals indicating major upconversion processes. Dashed lines indicate non-radiative energy transfer, and curved arrows indicate multiphonon relaxation. **b**, Typical evolution of spectra for 1 mol% Tm^{3+} as a function of excitation, showing substantial growth of emissions from the $^1G_4$ and $^1D_2$ levels with increasing excitation from 1×10^4 W cm^{-2} to 2.5×10^6 W cm^{-2}. **c**, Decomposition of the spectra into individual Gaussian peaks. Integrated intensities are given by I_λ where λ is the peak wavelength. Different transitions are indicated by the colours shown in the energy-level scheme in **a**. For example, the shaded area represents the $^3H_4 \rightarrow {}^3H_6$ transitions. **d**, Intensity ratios of the $^1D_2$ to $^3H_4$ classes $(I_{455} + I_{514} + I_{744} + I_{782})/I_{802}$ and $^1G_4$ to $^3H_4$ classes $(I_{480} + I_{660})/I_{802}$ as a function of excitation irradiance. **e**, Diagram illustrating energy transfer between the ensemble of Yb^{3+} and Tm^{3+} ions and subsequent radiative and non-radiative pathways. Top (bottom) panels: low (high) Tm^{3+}/Yb^{3+} ratio. In the case of a low Tm^{3+}/Yb^{3+} ratio, the limited number of Tm^{3+} ions creates an energy transfer bottleneck, due to the limited capacity of Tm^{3+} to release energy from the $^3F_4$ and $^3H_4$ states. Thus, at increasing excitation, alternative energy loss channels (radiative and non-radiative) involving higher states $^1G_4$ and $^1D_2$ progressively switch on. Brown, excitation light; green, simplified energy levels; red, blue and purple, radiative energy flux; grey, radiative flux not observed in this work; black, non-radiative energy loss.

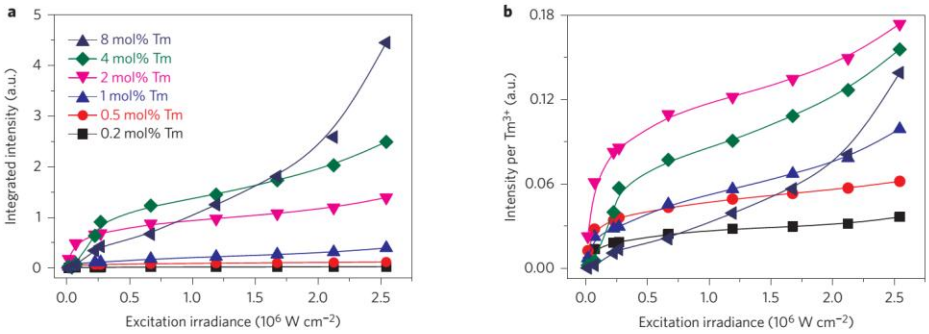

Figure 3 | Analysis of power-dependent upconversion efficiency. a, Integrated upconversion luminescence intensity (~400–850 nm) as a function of excitation irradiance for a series of Tm^{3+}-doped nanocrystals. All samples have the same volume and number of nanocrystals. **b**, As in **a**, but divided by the concentration of Tm^{3+} ions. Under an excitation irradiance of 2.5×10^6 W cm^{-2}, 2 mol% Tm^{3+} has the highest relative upconversion efficiency, whereas the strongest upconversion signal is observed in 8 mol% Tm^{3+} due to the larger number of activators available with sufficient excitation.

the population in the Ln_2 state is expressed in terms of the density of lanthanide ions in the ground state, the excited Yb^{3+} population, excitation irradiance and various intrinsic macroscopic rate constants, such as the energy transfer and upconversion rates. The experimental and simulated upconversion luminescence intensities show concentration quenching at low irradiance, but increase at

LETTERS NATURE NANOTECHNOLOGY DOI: 10.1038/NNANO.2013.171

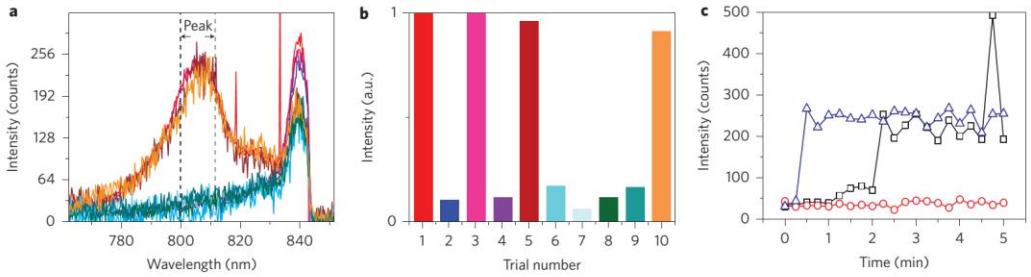

Figure 4 | Detecting a single nanocrystal in a suspended-core microstructured fibre dip sensor. a, Results of 10 trials of loading 3.9 fM nanocrystal solution into the fibre dip sensor. Four positive trials, shown in red, magenta, dark red and orange, show comparable ~800–810 nm emission peaks, and six trials result in consistent background noise baselines (presented in the remaining colours). The baseline level is due to scattering of 980-nm excitation. **b**, Normalized nanocrystal emission integrated from ~800 to 810 nm. The four positive trials shown in red, magenta, dark red and orange produce intensities of ~250 with a low coefficient of variation (CV) of 4.7%, and high signal-to-noise ratio of >8. **c**, Time-dependent dynamics of three independent trials. Red: trial with no nanocrystals observed (only background is observed). Blue: one nanocrystal appears shortly after the start of the trial. Black: single nanocrystal appears in the fibre after 2 min, followed by a second at ~5 min; one of the nanocrystals then exits the observation volume.

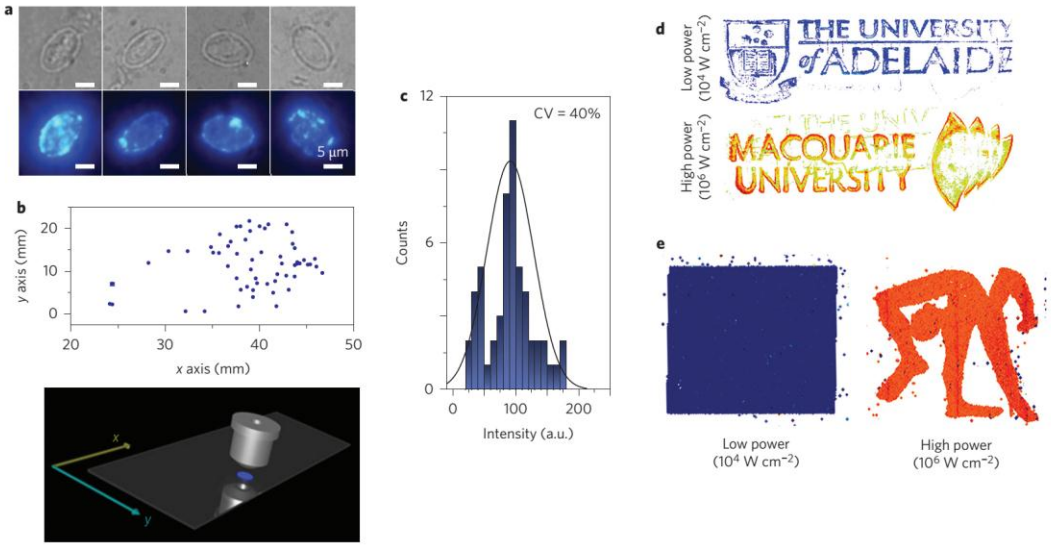

Figure 5 | Proof-of-principle experiments demonstrating a broad spectrum of applications. a, Images of *Giardia lamblia* cells labelled with antibody-conjugated 4 mol% Tm^{3+} upconversion nanocrystals under transmission (top) and luminescence (bottom) modes. The 980-nm wide-field excitation and upconversion detection yield negligible autofluorescence background, so absolute signal intensities of each single microorganism (see histogram in **c**) provide quantification of the level of surface antigens. **b**, Individual cells localized on a glass slide by a scanning cytometry system (top), and its schematic (bottom). Targeted cells are symbolized by blue dots. **c**, Histogram showing the quantification results of the population of nanocrystal-labelled *Giarida lamblia* (CV, coefficient of variation). **d**, Demonstrations of security inks using the power-dependent optimal Tm^{3+} concentration. Low-concentration (0.2 mol% Tm^{3+}) nanocrystals were used to stain the masking pattern (University of Adelaide logo), which is visible under both low-power illumination (top) and high-power illumination (bottom). High-concentration (4 mol% Tm^{3+}) nanocrystals were used to stain the hidden pattern (Macquarie University logo), which is over 10 times brighter than the masking pattern. At this dynamic range the masking pattern is almost unnoticeable. **e**, Nanocrystal solution 'security inks' were used in an inkjet printer with 0.5 mol% Tm^{3+} nanocrystals as a rectangular mask to confound the signal image from 8 mol% Tm^{3+} nanocrystals. At laser scanning confocal setting ($>1 \times 10^6$ W cm^{-2}), the hidden trademark image of the 8 mol% Tm^{3+} nanocrystals becomes visible and dominant.

high irradiance, in agreement with our observations (Supplementary Fig. S9b–f). Moreover, the simulations show increasing relative upconversion efficiency with increasing excitation irradiance (Supplementary Fig. S9g), which is in agreement with Fig. 3a. To the best of our knowledge, this is the first analytical approach to describe the upconversion quenching process at increasing activator concentrations and excitation powers.

We have demonstrated that these bright nanocrystals can significantly extend the detection limit in a fibre-based dip sensor, a novel nanoscale sensing platform for clinical point-of-care, chemical and

biological applications[17]. The detection limit for fluorescent quantum dots in such sensors was earlier reported to be ~10 pM due to competing autofluorescence background from the fibre itself. In this work the fibre autofluorescence problem is avoided by using 980 nm excitation and 802 nm emission of Tm^{3+}, wavelengths that are well separated from the glass background fluorescence (Supplementary Fig. S11). To investigate the achievable detection limit, we measured our brightest 8 mol% Tm^{3+} nanocrystals at 3.9 fM dilution in ten identical fibre dip sensors (Supplementary Section S8). The respective 802 nm peaks (Fig. 4a) show a consistent intensity of 250 ± 30 counts in four experiments, whereas six other experiments show a consistent background level of ~30 counts (Fig. 4b). We attribute these strongly quantized values of the peak intensity (~220 net counts) to the observation of single nanocrystals in these four trials. To confirm this hypothesis we calculated the average number of particles expected to be located within the detection volume in a microstructured fibre, and found this to be 0.55, consistent with our observations of a single nanocrystal in 40% of trials. The Poissonian probability of observing two or more nanocrystals in a single trial for our average of 0.55 particles is 11%. To validate our assignment further, we set up an experiment to continuously monitor the 802 nm upconversion intensity during sample intake as the holes of the fibre fill with the nanocrystal suspension by capillary action (Fig. 4c). One of these trials (red) showed the background signal only, indicating that in this trial no nanocrystals entered the detection volume. The second (blue) showed a single nanocrystal appearing in the detection volume halfway through the experiment. The third (black) showed one nanocrystal entering the detection region, followed by a second one after 6 min; one nanocrystal is then observed to exit while the other continues to be observed. The signal of both combined nanocrystals is 470 ± 30 (440 net counts), twice the single nanocrystal net count of 220. These experiments show that high brightness of upconversion emission achieved at sufficient irradiance excitation enables, for the first time, the detection of a single high Tm^{3+}-doped nanocrystal within the fibre platform. Furthermore, these single nanocrystals are bright enough to be visible to the naked eye and could be recorded by a low-cost digital camera in a wide-field microscopy system (Fig. S10 in Supplementary Section S7).

This exceptional nanocrystal brightness provides compelling advantages to a wide range of fields including immunofluorescence imaging (Fig. 5a), rare event cell detection and quantification (Fig. 5b,c), document security (Fig. 5d) and security printing (Fig. 5e). We demonstrated that the new ultrabright upconversion nanocrystals provide high-contrast biolabels. To this end, *Giardia lamblia* cells were labelled by nanocrystals conjugated to suitable monoclonal antibodies (G203). Figure 5a shows the labelled Giardia cells imaged by a scanning system at only 0.1 s exposure time by a standard charge-coupled device (CCD) camera. The absence of autofluorescence background at 980 nm excitation enabled the quantification of the absolute signal intensities of each single microorganism, as well as quantification of the level of surface antigens (Fig. 5c)[33]. Single labelled cells on a glass slide have been detected within 3 min without background interference (Fig. 5b). This shows that these bioprobes are capable of rare event detection. Moreover, excitation-dependent upconversion has also enabled a new approach to 'security inks' (Fig. 5d,e), because the highly doped (>4 mol%) Tm^{3+} nanocrystals remain dark unless high infrared excitation irradiance is used, in contrast to low doped nanocrystals (Fig. 5d). Additionally, the nanocrystal suspensions can be dispersed in traditional inkjet printer inks to print highly secure trademarks/images on papers/plastics (Fig. 5e).

In conclusion, we have demonstrated a novel approach to significantly enhance the upconversion luminescence of nanocrystals, by increasing the activator concentration in combination with elevated irradiance excitation ($\sim 1 \times 10^6$ W cm^{-2}). The microstructured fibre dip sensor used here easily achieves such excitation intensities, making it possible to detect single nanocrystals while probing subcellular fluid volumes. These results show that the nanocrystals can be detected at one end of the fibre as they enter the fibre from the other end, enabling measurements to be made from a significant distance, and leading the way to *in vivo* measurements. Highly Ln^{3+}-doped nanocrystals at sufficient irradiance excitation have strong potential for use as photostable, background-free and extremely bright labelling probes for bioimaging. Furthermore, this work presents a new approach for understanding and predicting the behaviour of lanthanide-based upconversion systems, and provides new directions both for nanoscale sensing and the materials science of Ln^{3+}-doped nanomaterials.

Received 13 May 2013; accepted 26 July 2013;
published online 1 September 2013

References

1. Zhang, C., Yuan, Y., Zhang, S., Wang, Y. & Liu, Z. Biosensing platform based on fluorescence resonance energy transfer from upconverting nanocrystals to graphene oxide. *Angew. Chem. Int. Ed.* **50,** 6851–6854 (2011).
2. Wu, S. W. *et al.* Non-blinking and photostable upconverted luminescence from single lanthanide-doped nanocrystals. *Proc. Natl Acad. Sci. USA* **106,** 10917–10921 (2009).
3. Stepuk, A. *et al.* Use of NIR light and upconversion phosphors in light-curable polymers. *Dental Mater.* **28,** 304–311 (2012).
4. Nyk, M., Kumar, R., Ohulchanskyy, T. Y., Bergey, E. J. & Prasad, P. N. High contrast *in vitro* and *in vivo* photoluminescence bioimaging using near infrared to near infrared up-conversion in Tm^{3+} and Yb^{3+} doped fluoride nanophosphors. *Nano Lett.* **8,** 3834–3838 (2008).
5. Wang, M. *et al.* Immunolabeling and NIR-excited fluorescent imaging of HeLa cells by using $NaYF_4$:Yb,Er upconversion nanoparticles. *ACS Nano* **3,** 1580–1586 (2009).
6. Yang, Y. M. *et al. In vitro* and *in vivo* uncaging and bioluminescence imaging by using photocaged upconversion nanoparticles. *Angew. Chem. Int. Ed.* **51,** 3125–3129 (2012).
7. Tian, G. *et al.* Mn^{2+} dopant-controlled synthesis of $NaYF_4$:Yb/Er upconversion nanoparticles for *in vivo* imaging and drug delivery. *Adv. Mater.* **24,** 1226–1231 (2012).
8. Haase, M. & Schäfer, H. Upconverting nanoparticles. *Angew. Chem. Int. Ed.* **50,** 5808–5829 (2011).
9. Auzel, F. Upconversion and anti-Stokes processes with *f* and *d* ions in solids. *Chem. Rev.* **104,** 139–173 (2004).
10. Zou, W. Q., Visser, C., Maduro, J. A., Pshenichnikov, M. S. & Hummelen, J. C. Broadband dye-sensitized upconversion of near-infrared light. *Nature Photon.* **6,** 560–564 (2012).
11. Wang, F. *et al.* Simultaneous phase and size control of upconversion nanocrystals through lanthanide doping. *Nature* **463,** 1061–1065 (2010).
12. Vetrone, F., Naccache, R., Mahalingam, V., Morgan, C. G. & Capobianco, J. A. The active-core/active-shell approach: a strategy to enhance the upconversion luminescence in lanthanide-doped nanoparticles. *Adv. Funct. Mater.* **19,** 2924–2929 (2009).
13. Liu, X. *et al.* Breakthrough in concentration quenching threshold of upconversion luminescence via spatial separation of the emitter doping area for bio-applications. *Chem. Commun.* **47,** 11957–11959 (2011).
14. Boyer, J. C. & van Veggel, F. C. Absolute quantum yield measurements of colloidal $NaYF_4$: Er^{3+}, Yb^{3+} upconverting nanoparticles. *Nanoscale* **2,** 1417–1419 (2010).
15. Wang, F. & Liu, X. Upconversion multicolor fine-tuning: visible to near-infrared emission from lanthanide-doped $NaYF_4$ nanoparticles. *J. Am. Chem. Soc.* **130,** 5642–5643 (2008).
16. Zhang, H., Li, Y., Lin, Y., Huang, Y. & Duan, X. Composition tuning the upconversion emission in $NaYF_4$:Yb/Tm hexaplate nanocrystals. *Nanoscale* **3,** 963–966 (2011).
17. Schartner, E. P., Ebendorff-Heidepriem, H., Warren-Smith, S. C., White, R. T. & Monro, T. M. Driving down the detection limit in microstructured fiber-based chemical dip sensors. *Sensors* **11,** 2961–2971 (2011).
18. Wang, F. *et al.* Tuning upconversion through energy migration in core–shell nanoparticles. *Nature Mater.* **10,** 968–973 (2011).
19. Ye, X. C. *et al.* Morphologically controlled synthesis of colloidal upconversion nanophosphors and their shape-directed self-assembly. *Proc. Natl Acad. Sci. USA* **107,** 22430–22435 (2010).
20. Yan, C., Dadvand, A., Rosei, F. & Perepichka, D. F. Near-IR photoresponse in new up-converting CdSe/$NaYF_4$:Yb,Er nanoheterostructures. *J. Am. Chem. Soc.* **132,** 8868–8869 (2010).

21. Gorris, H. H., Ali, R., Saleh, S. M. & Wolfbeis, O. S. Tuning the dual emission of photon-upconverting nanoparticles for ratiometric multiplexed encoding. *Adv. Mater.* **23,** 1652–1655 (2011).
22. Wang, F., Wang, J. A. & Liu, X. G. Direct evidence of a surface quenching effect on size-dependent luminescence of upconversion nanoparticles. *Angew. Chem. Int. Ed.* **49,** 7456–7460 (2010).
23. Mai, H. X., Zhang, Y. W., Sun, L. D. & Yan, C. H. Highly efficient multicolor up-conversion emissions and their mechanisms of monodisperse $NaYF_4$:Yb,Er core and core/shell-structured nanocrystals. *J. Phys. Chem. C* **111,** 13721–13729 (2007).
24. Priyam, A., Idris, N. M. & Zhang, Y. Gold nanoshell coated $NaYF_4$ nanoparticles for simultaneously enhanced upconversion fluorescence and darkfield imaging. *J. Mater. Chem.* **22,** 960–965 (2012).
25. Zhang, F. *et al.* Fabrication of $Ag@SiO_2@Y_2O_3$:Er nanostructures for bioimaging: tuning of the upconversion fluorescence with silver nanoparticles. *J. Am. Chem. Soc.* **132,** 2850–2851 (2010).
26. Yin, A., Zhang, Y., Sun, L. & Yan, C. Colloidal synthesis and blue based multicolor upconversion emissions of size and composition controlled monodisperse hexagonal $NaYF_4$:Yb,Tm nanocrystals. *Nanoscale* **2,** 953–959 (2010).
27. Mahalingam, V., Vetrone, F., Naccache, R., Speghini, A. & Capobianco, J. A. Colloidal Tm^{3+}/Yb^{3+}-doped $LiYF_4$ nanocrystals: multiple luminescence spanning the UV to NIR regions via low-energy excitation. *Adv. Mater.* **21,** 4025–4028 (2009).
28. Kramer, K. W. *et al.* Hexagonal sodium yttrium fluoride based green and blue emitting upconversion phosphors. *Chem. Mater.* **16,** 1244–1251 (2004).
29. Liang, L. F., Wu, H., Hu, H. L., Wu, M. M. & Su, Q. Enhanced blue and green upconversion in hydrothermally synthesized hexagonal $NaY_{1-x}Yb_xF_4:Ln^{3+}$. *J. Alloys Comp.* **368,** 94–100 (2004).
30. Chen, X. & Song, Z. Study on six-photon and five-photon ultraviolet upconversion luminescence. *J. Opt. Soc. Am. B* **24,** 965–971 (2007).
31. Chen, G. Y., Somesfalean, G., Zhang, Z. G., Sun, Q. & Wang, E. P. Ultraviolet upconversion fluorescence in rare-earth-ion-doped Y_2O_3 induced by infrared diode laser excitation. *Opt. Lett.* **32,** 87–89 (2007).
32. Qin, G. S. *et al.* Intense ultraviolet upconversion luminescence from Yb^{3+} and Tm^{3+} codoped amorphous fluoride particles synthesized by pulsed laser ablation. *Opt. Commun.* **242,** 215–219 (2004).
33. Lu, Y., Xi, P., Piper, J. A., Huo, Y. & Jin, D. Time-gated orthogonal scanning automated microscopy (OSAM) for high-speed cell detection and analysis. *Sci. Rep.* **2,** 837 (2012).

Acknowledgements

The authors thank D. Birch, D. Inglis, N. Vella, A. Nadort, R. Field, M. Nguyen, D. Liu, C. Yan and J. Shen (Olympus Australia) for sample characterization, H. Ebendorff-Heidepriem for providing the suspended-core fibres, which were fabricated at the OptoFab node of the Australian National Fabrication Facility (ANFF), and A. Nechaev (Lomonosov Moscow State University of Fine Chemical Technologies, Russia) for bulk crystal preparation. J.Z. acknowledges a Macquarie University Research Excellence Scholarship, and D.J. and J.P. acknowledge support from the Australian Research Council (DP1095465, LP130100517). P.X. acknowledges support from the '973 program' of China (2011CB707502, 2011CB809101) and T.M. acknowledges the support of an ARC Federation Fellowship.

Author contributions

D.J. and T.M. conceived the project, designed the experiments and supervised the research. J.Z., E.S., Y.Lu and D.J. were primarily responsible for data collection and analysis. D.J., E.G., J.Z. and T.M. prepared figures and wrote the main manuscript text. J.Z., E.G., A.Z. and D.J. were primarily responsible for supporting information and numerical simulations. All authors contributed to data analysis, discussions and manuscript preparation.

Additional information

Supplementary information is available in the online version of the paper. Reprints and permissions information is available online at www.nature.com/reprints. Correspondence and requests for materials should be addressed to D.J.

Competing financial interests

The authors declare no competing financial interests.

nature nanotechnology

SUPPLEMENTARY INFORMATION

DOI: 10.1038/NNANO.2013.171

Single nanocrystal sensitivity achieved by enhanced upconversion

Jiangbo Zhao[1], Dayong Jin[1*], Erik P. Schartner[2], Yiqing Lu[1], Yujia Liu[1,4], Andrei V. Zvyagin[1], Lixin Zhang[1], Judith M. Dawes[1], Peng Xi[3,4], James A. Piper[1], Ewa M. Goldys[1], Tanya M. Monro[2]

1. Synthesis of the Yb/Tm-doped $NaYF_4$ nanocrystals:

1.1. Reagents:

$YCl_3 \cdot 6H_2O$ (99.99%), Y_2O_3 (99.99%), $YbCl_3 \cdot 6H_2O$ (99.998%), Yb_2O_3 (99.99%), $TmCl_3 \cdot 6H_2O$ (99.99%), Tm_2O_3 (99.99%), NaOH (98%), CF_3COONa (98%), NH_4F (99.99%), CF_3COOH (99%), oleic acid (OA, 90%), 1-octadecene (ODE, 90%) were purchased from Sigma-Aldrich. Unless otherwise noted, all chemicals were used as received without further purification.

1.2. Method

Upconverting $NaYF_4$:Yb/Tm nanocrystals were synthesised using an organometallic method described previously[1,2]. Briefly, 5 mL of methanol solution of $LnCl_3$ (1.0 mmol, Ln = Y, Yb, Tm/Er) was magnetically mixed with 6 mL OA and 15 mL ODE in a three-neck round-bottom flask. The resulting mixture was heated at 150 °C under argon flow for 30 min to form a clear light yellow solution. After cooling down to 50 °C, 10 mL of methanol solution containing 0.16 g NH_4F and 0.10 g NaOH was added with vigorous stirring for 30 min. Then, the slurry was slowly heated and kept at 110 °C for 30 min to remove methanol and residual water. Next, the reaction mixture was protected with an argon atmosphere, quickly heated to 305 °C and maintained for 1.5 h. The products were isolated by adding ethanol, and centrifuged without size-selective fractionation. The final $NaYF_4$:Yb/Tm nanocrystals were redispersed in cyclohexane with 5 mg/mL concentration after washing with cyclohexane/ethanol several times.

1.3. XRD Characterization:

Powder X-ray diffraction (XRD) patterns were obtained on a PANalyticalX'Pert Pro MPD X-ray diffractometer using Cu Kα1 radiation (40 kV, 40 mA, λ=0.15418 nm). Transmission electron microscope (TEM) measurements were performed using a Philips CM10 TEM with Olympus Sis Megaview G2 Digital Camera. The samples for TEM analysis were prepared by placing a drop of a dilute suspension of nanocrystals onto formvar-coated copper grids (300 mesh).

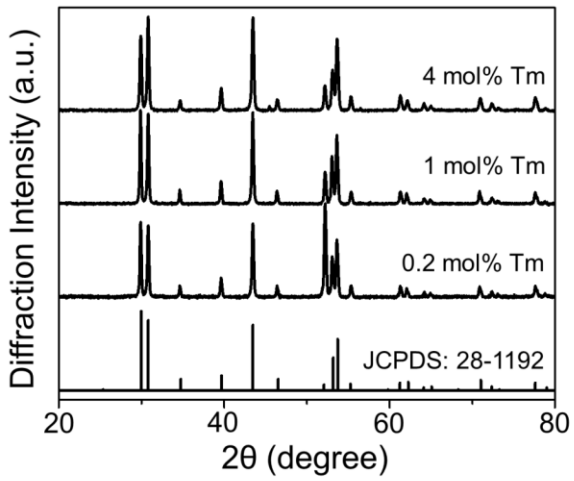

Fig S1. Selected powder XRD patterns of the as-synthesized $NaYF_4$:Yb/Tm nanocrystals doped with various concentrations of Tm^{3+}ions. *The diffraction peaks are indexed according to the standard XRD pattern of hexagonal-phase $NaYF_4$ (Joint Committee on Powder Diffraction Standards file number 28-1192), confirming that all the samples have hexagonal phase.*

2. Optical fibre dip sensor:

2.1. Fabrication of soft glass microstructured optical fibre:

The fibre used in these experiments was a suspended core microstructured optical fibre (MOF) fabricated in-house at the University of Adelaide. This fibre was fabricated from F2 glass, a commercially available lead-silicate glass from Schott Glass Co. The fibre was fabricated via preform extrusion and subsequently drawn into fibre using a cane-in-tube technique[3]. The extrusion process involves heating up the glass to its softening point, and then applying a force to the top of the billet such that the softened glass is pushed through the extrusion die. The fibre core diameter defined as the diameter of a circle with the equivalent area as that of the largest triangle which can be wholly contained within the core structure[4], was 1.43 μm and the outer diameter was 160 μm. The fabricated fibre had a loss of 0.7 ± 0.2 dB/m at 980 nm, 0.8 ± 0.2 dB/m at 802 nm, 0.9 ± 0.2 dB/m at 744 nm, 1.1 ± 0.2 dB/m at 660 nm, 1.4 ± 0.2 dB/m at 514 nm, 1.7 ± 0.3 dB/m at 480 nm, 1.9 ± 0.3 dB/m at 455 nm.

2.2. Operation of fibre dip sensor

A 300 mW 980 nm single-mode fibre-coupled diode laser source was used for excitation. It was coupled into the MOF using a dichroic mirror (HT @ 980 nm, HR @ 544 nm) and a 60 × microscope objective. The coupling efficiency into the MOF was measured as 30%, giving a total coupled power in the fibre of 100 mW. The upconversion emission was collected by the fibre core and measured for light propagating in the backwards direction (i.e. light travelling towards the launch/input end of the fibre), with the dichroic filter passing visible-near IR emission. A broad band-pass filter (405 nm to 842 nm; Semrock FF01-842) was used to further suppress residual pump light. For detection a Horiba iHR320 monochromator with CCD detector was used with a fibre-coupled configuration. The experimental procedure involved first optimising and recording the amount of power coupled into the suspended core of the fibre by varying the fibre position using XYZ stages. The lens was then removed from the output coupling stage, and the tip of the fibre immersed in the nanoparticle solution and allowed to fill using capillary forces for 5 minutes. The fibre was then removed from the solution and the measurement was performed, altering the input power using a variable attenuator. To calculate the intensity of the excitation light inside the fibre a commercial finite element modelling programme (COMSOL Multiphysics) was used to simulate the fundamental guided mode within the fibre. The intensity quoted in the main text is the peak intensity of the fundamental guided mode at the glass:liquid interface within the fibre. Since this varies slightly between the three holes due to the subtle asymmetries in the fabricated fibre the average of these values was used.

3. Material characterisation of nanocrystals used in this work and other similar crystals

The main body of the paper describes results for a single Yb^{3+} concentration of 20 mol% and a range of Tm^{3+} concentrations from 0.2 mol% to 8 mol%, a uniform size of 40 nm and suspended in cyclohexane. Here, we present additional results of fluorescence characterisation for these and other $NaYF_4$:Yb/Tm nanocrystals grown by the same synthesis technique, spanning a range of experimental variables such as Yb^{3+} concentration, particle size, and surface conditions (modified with water-soluble ligands: Polyethylene Glycol). The bulk $NaYF_4$ crystals (up to 600 nm in diameter) were prepared by Dr. A. V. Nechaev (Lomonosov Moscow State University of Fine Chemical Technologies, Russia) following the synthetic procedure in the literature, using the corresponding lanthanide oxides and trifluoroacetic acid to grow micron-size samples [5].

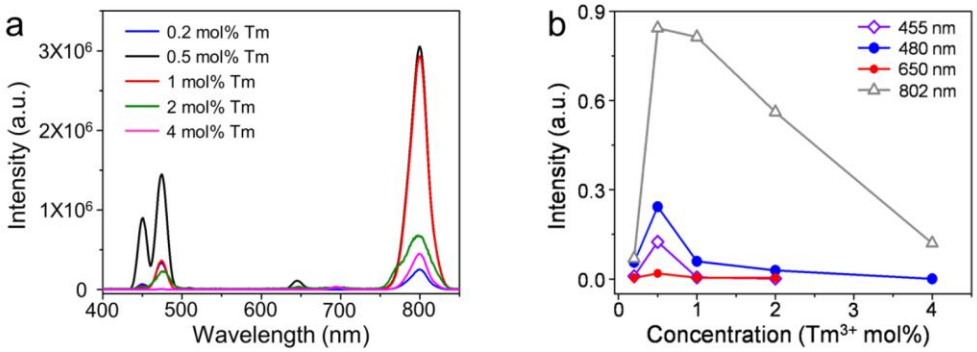

Fig S2. Comparison of upconversion spectra of the as-synthesised $NaYF_4$:Yb/Tm nanocrystals with different Tm^{3+} concentrations excited at 10 W/cm^2. a) *The spectra at various Tm^{3+} concentrations indicated in the figure. At 10 W/cm^2 irradiance, the 0.5 mol% Tm^{3+} doped nanocrystals emit the brightest upconversion luminescence. This is in good agreement with earlier reports of upconversion concentration quenching in Tm^{3+} doped $NaYF_4$.* ***b)*** *The evolution of emission intensity of various upconversion peaks as a function of Tm^{3+} concentration.*

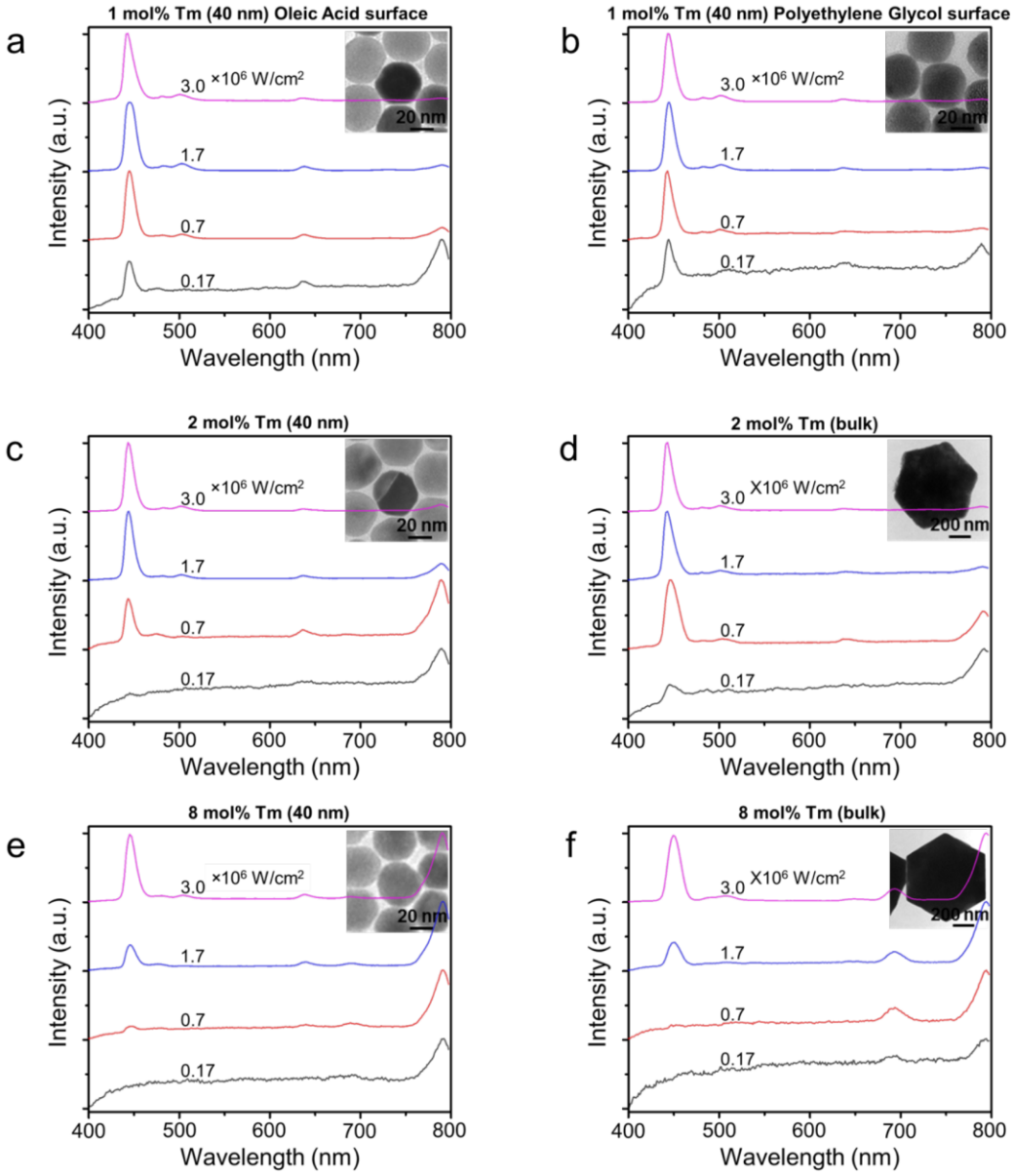

Fig S3. Power dependent spectra (400 nm~800 nm) of different Tm^{3+} upconversion crystals characterized by laser scanning confocal microscopy. a) *and* ***b)*** *indicate that the normalized power-dependent spectra do not depend on different surface conditions of the same nanocrystals;* ***a)****,* ***c)*** *and* ***e)*** *show that the spectra measured in laser scanning microscopy are consistent with the spectra taken in suspended-core optical fibre dip sensors as shown in Fig 2 in the main text;* ***d)*** *and* ***f)*** *the spectra of microscale crystals;* ***c) vs. d)*** *and* ***e) vs. f)*** *indicate that the upconversion luminescence spectra at varying excitation power for different activator concentrations are broadly independent on particle size and they are similar in nanocrystals and in bulk materials.*

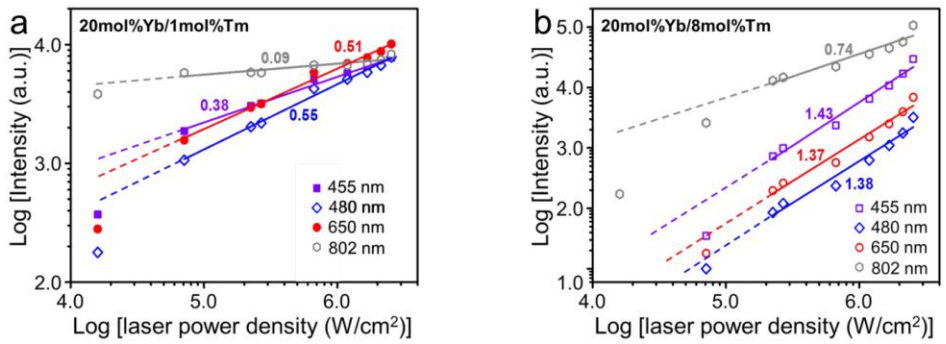

Fig S4. Power dependence of the upconversion luminescence at varying wavelength of 455, 480, 650 and 802 nm *in 1 mol % Tm^{3+} (a) and 8 mol% Tm^{3+} (b) doped nanocrystals as a function of excitation power density (980 nm excitation). Purple: 455 nm, blue: 480 nm, red: 650 nm, grey: 802 nm. Symbols- measured values, straight intervals have been fitted to determine the gradients whose colour-coded values for each interval are indicated in the figure.*

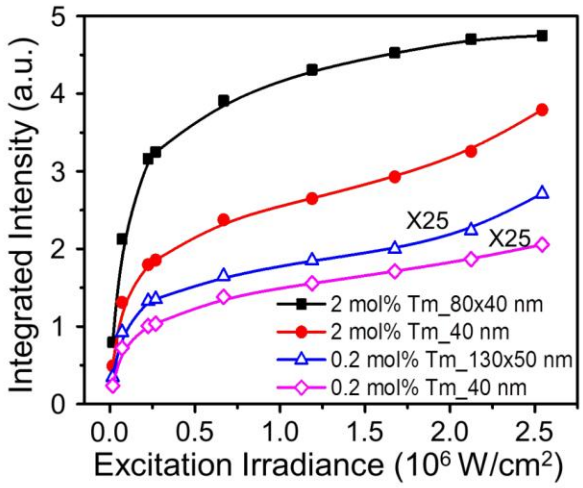

Fig S5. Integrated upconversion luminescence intensity (400~850 nm) as a function of excitation irradiance for varying size nanocrystals. *Full symbols: 2 mol % Tm^{3+}, hollow symbols: 0.2 mol % Tm^{3+}. Nanocrystal sizes are indicated in the figure. The results for 0.2 % Tm^{3+} have been scaled by a factor of 25 for clarity.*

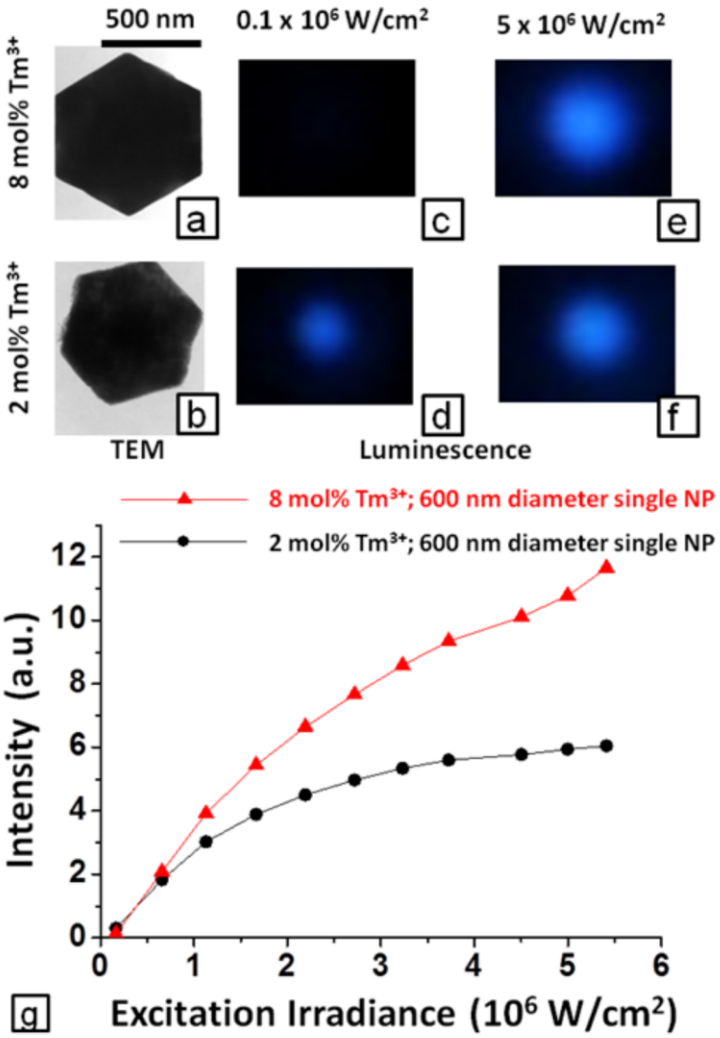

Fig S6. Power dependent single bulk crystal measurement under wide-field upconversion luminescence microscope. *Figures a) and b) are the TEM images of as-prepared bulk crystals at Tm^{3+} doping concentration of 8 mol% and 2 mol% respectively (same samples as Fig S3 d and f); c) and d) are the luminescence images in the visible range (400 ~700nm) at excitation power density of 0.1 × 10^6 W/cm^2 and e) and f) are taken at higher excitation of 5 × 10^6 W/cm^2 for 8 mol% Tm^{3+} and 2 mol% Tm^{3+} single bulk crystals, respectively. All the luminescence images are produced at the same CCD exposure time of 60 milliseconds. g) power-dependent intensities (integrated over 400~850 nm range) of the same single bulk crystals measured by a single-photon counting avalanche diode.*

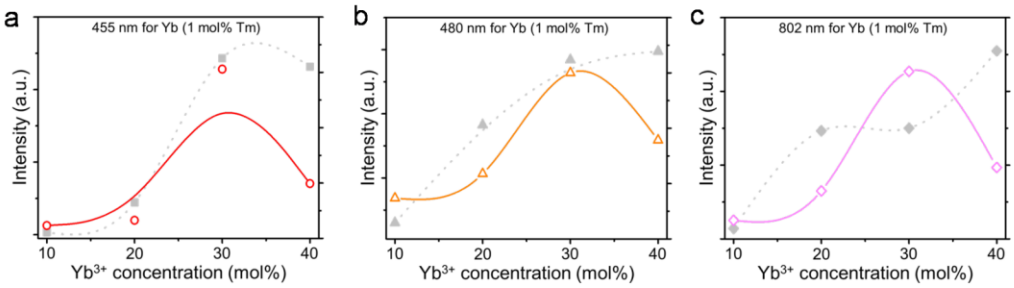

Fig S7. *Evolution of the integrated upconversion intensity of the respective 455 nm (a), 480 nm (b), and 802 nm (c) peak for a series of $NaYF_4$:Yb/Tm nanocrystals with varying Yb^{3+} concentration. Data taken at 980 nm excitation irradiance at 10 W/cm^2 (grey colour), and 2.5×10^6 W/cm^2 (red, orange, and magenta).*

4. Discussion of the effect of size and other conditions on nanocrystal brightness.

The new physical effect reported in the main body of the paper - the increase of the concentration quenching threshold at high excitation irradiance, producing superbright nanocrystals, has been demonstrated in nanocrystals of similar size ~40 nm, in the same solvent and synthesised under the same conditions. This has been done as to demonstrate this reduction in concentration quenching one must control for the other factors affecting brightness. These factors are well established in the literature and they include nanoparticle phase, the presence or absence as well as the type of solvent, and any near-surface recombination centres such as crystalline defects, or surface adsorbates [6,7]. All of these factors (except for crystalline phase) make a contribution to surface quenching which is increased in smaller nanocrystals [6,7], thus effectively producing size-dependent emission characteristics. We developed a quantitative model of this size dependence where the nanoparticle is separated into the inner and near-surface region with varying luminescence decay rates, which is in excellent agreement with the observations [7].This size-dependent surface quenching affects upconversion lifetimes in the first instance, but, as the luminescence intensity is inversely dependent on its lifetime at the same excitation conditions, it manifests itself as the dependence of brightness on size. This is, for example, apparent in our Figure S5 which shows that at the same excitation conditions and Tm^{3+} concentration, larger crystals are always brighter (have higher integrated luminescence intensity) than the smaller ones.

5. Measurement of the absolute conversion efficiency of the upconversion nanoparticle samples

The absolute conversion efficiency, η_{uc} is defined as a ratio of the total emitted power, P_{em} to the absorbed power, P_{abs}. In order to evaluate η_{uc} of the upconversion crystals, an integrating sphere measurement system was set up and calibrated, as shown in Figure S8a. The upconversion nanocrystal powder to be measured was pressed into a 1-mm circular well and sandwiched between two glass coverslips mounted in a sample holder at the exit port of a 4-inch integrating sphere (Labsphere). A laser excitation at wavelength of 980 nm was delivered to the sample *via* a multimode optical fibre (core diameter, 400 μm, N.A. 0.22) that was butted against the sample holder and aligned to the well axis to ensure homogeneous excitation of the sample. The excitation irradiance, I_{ex}, was varied by two orders of magnitude (3-300 W/cm^2). The emission (luminescence) from the excited upconversion sample, P_{em}, emitted in all directions was spatially homogenised by multiple reflections from the highly scattering integrating sphere walls, and eventually detected by a photoreceiver (PDA-55, Thorlabs). The emissions were passed through a collection lens and a short-pass filter (cut-off wavelength, 842 nm, Semrock), all mounted in the exit port positioned perpendicularly to the illumination path. The unabsorbed excitation power, P_{upcon} was measured by replacing the short-pass filter with a band-pass filter (980±10 nm, Thorlabs). An additional measurement of the unabsorbed excitation power by replacing the upconversion sample with a transparent TiO_2 powder, P_{ref} allowed the accurate evaluation of the power absorbed by the upconversion sample: $P_{abs} = P_{ref} - P_{upcon}$. The spectral response of the integrating sphere and photoreceiver was calibrated over a spectral range of 470~1050 nm. The measurements were repeated for several values of I_{ex} and linearly fitted to calculate the absorbed fraction of the excitation light ($r^2 > 0.99$).

The above measurement technique allows the absolute conversion efficiency for the upconversion nanocrystals to be measured for irradiances up to 3×10^2 W/cm^2. The results in 0.5 mol% Tm^{3+} nanocrystals are power-dependent reaching a plateau of ~ 4.7% at 3×10^2 W/cm^2, which is consistent with literature reports [8-10].

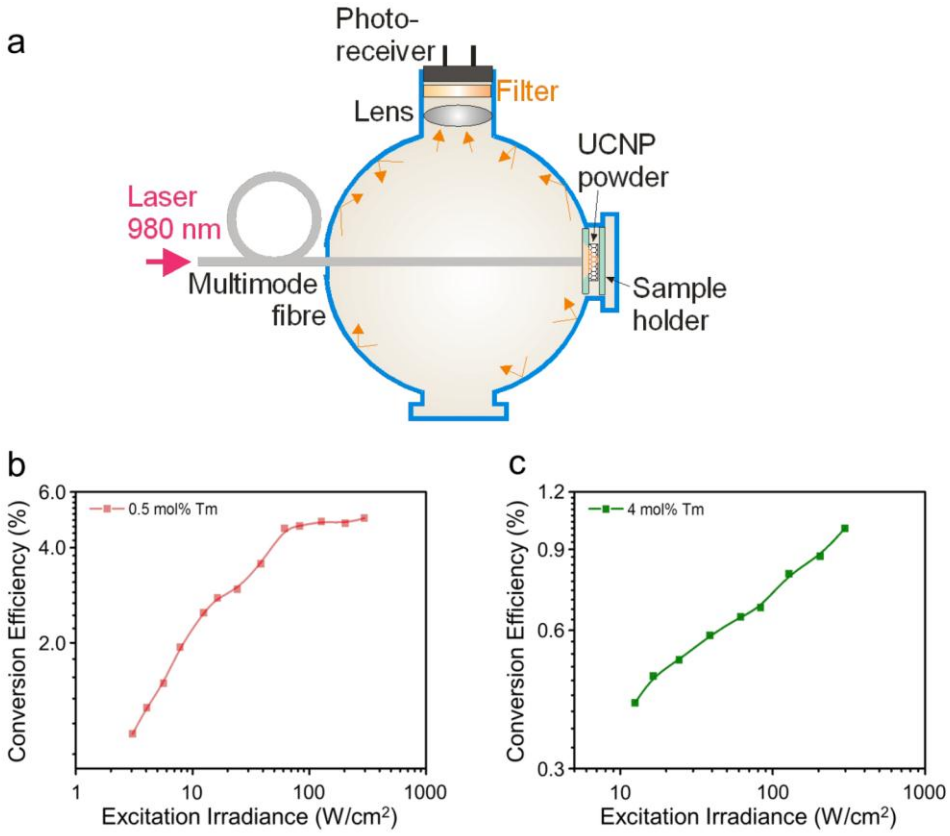

Fig S8. Integrating sphere set up for measurement of the absolute conversion efficiency. ***a)*** *schematic layout of integrating sphere;* ***b***, ***c)*** *calibrated power- dependent conversion efficiencies of 0.5 mol% Tm^{3+} and 4 mol% Tm^{3+} nanocrystals, respectively.*

6. Theoretical analysis of upconversion luminescence at high excitation conditions

We formulate the rate equations for the coupled Yb^{3+}-Ln^{3+} system in the limit of high irradiance excitation. Such conditions ensure that the excited ion distribution is spatially homogeneous. In this case, by suitable statistical averaging over the distribution of Ln^{3+} ions, the excitation probabilities can be related to a set of differential equations with macroscopic rate constants for the populations on various excited states. Our system of coupled Yb^{3+}-Ln^{3+} ions is described in a simplified model, following the approach developed in Ref [11]. The lanthanide ion (activator) is represented by three states, Ln_0, Ln_1, and Ln_2, with the same energy spacing$E_2 - E_1 = E_1 - E_0$. The lanthanide ions are excited through Yb^{3+} transitions between two energy states Yb_0 and Yb_1. We also assume that various energy transfer processes occur only between nearest neighbours, as the population-based rate equations do not naturally describe the spatial relationships that are represented by appropriate leading terms. As established in Refs [11,12], the density of occupied second lanthanide states $N_{Ln,2}$ is small compared with $N_{Ln,0}$ and $N_{Ln,1}$. Due to the short range of the energy transfer in the Foerster formalism, each specific energy transfer rate is characterised by a different constant dependent on the density of the relevant states. The reverse energy transfer back to Yb^{3+} is ignored, consistent with the situation in the Yb^{3+}-Tm^{3+} system, and the Ln^{3+}-Ln^{3+} cross-relaxation is taken into account. We also ignore radiative and nonradiative recombination within Yb. The key energy transfer processes are illustrated in Fig S9.

The rate equations for the excited state population of the Yb^{3+} and Ln^{3+} ions are as follows:

$$dN_{Yb1}/_{dt} = AI_0 N_{Yb,0} - FN_{Ln,0} - C_{up}N_{Ln,1} \quad /1/$$

$$dN_{Ln2}/_{dt} = -k_1 cN_{Ln,2} - \frac{N_{Ln,2}}{\tau} + C_{up}N_{Ln,1} \quad /2/$$

$$dN_{Ln1}/_{dt} = k_1 cN_{Ln2} - WN_{Ln,1} - C_{up}N_{Ln,1} + FN_{Ln,0} \quad /3/$$

$$dN_{Ln0}/_{dt} = \frac{N_{Ln,2}}{\tau} + WN_{Ln,1} - FN_{Ln,0} \quad /4/$$

Here $F = N_{Yb1}r_{FET}$ where r_{FET} is the forward energy transfer rate from Yb^{3+} to Ln^{3+}, and $C_{up} = k_{C,up}N_{Yb,1}$ is related to the upconversion process, involving excited Yb^{3+} and Ln^{3+} in its first excited state. AI_0 is a product of the power constant and absorption cross section, $AI_0 = \rho_p\sigma_0$. The parameter $k_{c,up} = \alpha\left(\frac{R_{UC}}{R_0}\right)^6$ where R_0 is the nearest neighbour distance between Yb ions and Ln ions who both have the first state occupied, thus ${R_0}^{-6} = \delta N_{Yb,1}N_{Ln,1}$. At a constant irradiance level, the nearest neighbour distance between these types of ions is proportional to the nearest neighbour distance between Yb^{3+} ions with the first state occupied and Ln^{3+} ions in the ground state, thus ${R_0}^{-6} = \delta' N_{Yb,1}N_{Ln,0}$, and we will assume that δ' depends only weakly on excitation irradiance in the high excitation regime where our model is applicable. The R_{UC} represents the upconversion radius - the parameter that reflects the likelihood of upconversion. $k_1 = \beta\left(\frac{R_{ET1}}{R_1}\right)^6$ where R_{ET1} is the energy transfer radius - the parameter that reflects the likelihood of energy transfer between the second and first state

of two nearest neighbour Ln^{3+} ions. R_1 is proportional to the nearest neighbour distance between adjacent lanthanides, ${R_1}^{-6} = \gamma {N_{Ln,0}}^2$.

In steady state conditions we can use Equations /1/-/4/ to express the population of the second lanthanide state (upconversion intensity) in terms of lanthanide doping and excited Yb^{3+} population, as follows.

$$N_{Ln,2} = N_{Ln,0} N_{Yb,1} \boldsymbol{r_{ETF}} \tau \Big/ \left[1 + \frac{W\left(1 + \beta\left(\frac{R_{ET1}}{R_1}\right)^6 N_{Ln,0}\tau\right)}{\alpha\left(\frac{R_{UC}}{R_0}\right)^6 N_{Yb,1}}\right] \qquad /5/$$

The observed upconversion fluorescence intensity is a function of $N_{Ln,0}$, the density of lanthanides with empty first state and also a function of the light intensity through the dependence of F. F is an increasing function of light irradiance. After substituting the expressions for R_0 and R_1Equation /5/ takes the following functional form:

$$N_{Ln2} \propto N_{Ln,0} N_{Yb,1} \Big/ \left[1 + \frac{W\left(1 + aN_{Ln,0}^3\right)}{bN_{Yb1}^2 N_{Ln,0}}\right] \qquad /6/$$

where $a = \beta\gamma\tau R_{ET1}^6$and $b = \alpha\delta' R_{UC}^6$.

The above equation has been plotted as a function of $N_{Ln,0}$ for various values of excited Yb^{3+} population as shown in Fig S9 d- f. It shows the effect of concentration quenching at low irradiance and increasing upconversion signal with increasing concentrations observed at high irradiance conditions (Fig S 9b, c). It also shows that the upconversion signal increases as a function of the energy transfer rate F from Yb^{3+} to Tm (remembering that $F = N_{Yb1}{r_{FET}}^3$). As illustrated in Figure S 9a (top), the net energy flux absorbed by Yb^{3+} (yellow arrow) is almost equal to the energy transfer rate F.as the upconversion energy flux (pink arrow) makes only a small contribution. In the case of large density of Yb^{3+} the net flux absorbed by Yb^{3+} is proportional to incident irradiance until the Yb^{3+} population starts to approach saturation. In these conditions Fig S 9g represents the dependence of upconversion intensity on the incident irradiance. This Figure shows that the upconversion signal increases in a nonlinear fashion as a function of irradiance for fixed concentration of Ln^{3+}, in agreement with observations. It also shows that increasing the Ln^{3+} concentration increases the upconversion signal, as presented in Figure 3.

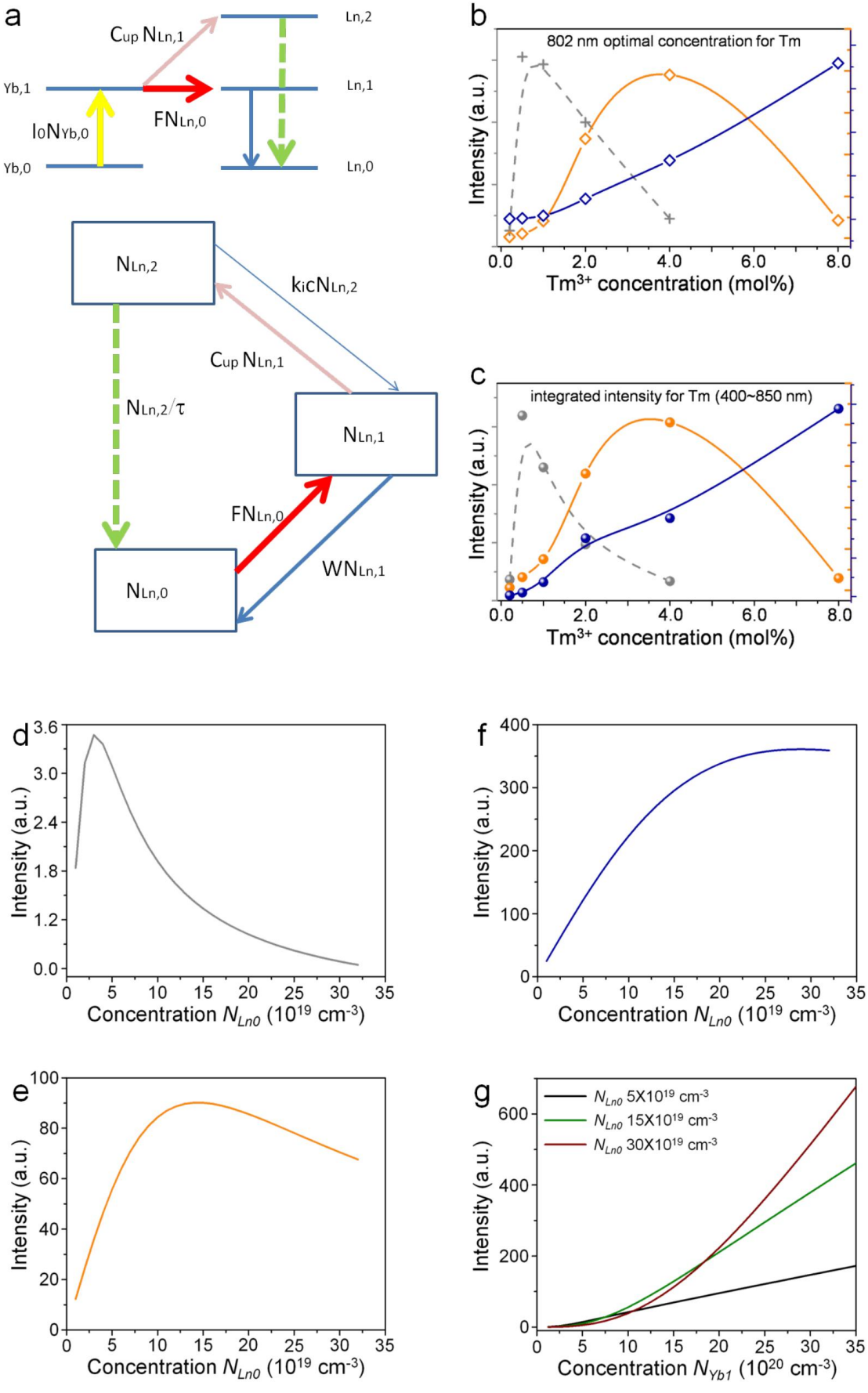

Fig S9. The experimental observations and theoretical predictions of upconversion luminescence under low and high irradiance conditions. a) *Schematic diagram of energy transfer processes in the upconversion model used in this paper.* ***b, c)*** *Evolution of the upconversion emission intensity (integrated intensity of the 802 nm peak and the overall intensity integrated from 400 nm to 850 nm) of a series of $NaYF_4$:Yb/Tm nanocrystals with 980 nm excitation irradiance at 10 W/cm^2(grey colour), 1.5×10^5 W/cm^2(orange) and 2.5×10^6 W/cm^2(blue), respectively. All emission spectra were recorded under identical conditions.* ***d-f)*** *Simulations of the population on the Ln_2 level as a function of N_{Ln0} (Equation /6/) at varying excitation irradiance: 10 W/cm^2(d), 1.5×10^5 W/cm^2(e) and 2.5×10^6 W/cm^2(f), respectively, showing that the high excitation irradiance increases the upconversion intensity and concentration quenching threshold.* ***g)*** *Simulations of population on the Ln_2 level as a function of N_{Yb1} (proportional to F which is approximately equal to irradiance) at different Tm^{3+} doping concentration, showing that dark activators can be unlocked under high excitation irradiance, as experimentally observed in Fig 3a. The parameters in Equation /6/ used in d-g are: a=0.5, b=0.4, and W=0.6.*

7. Single nanoparticle imaging results

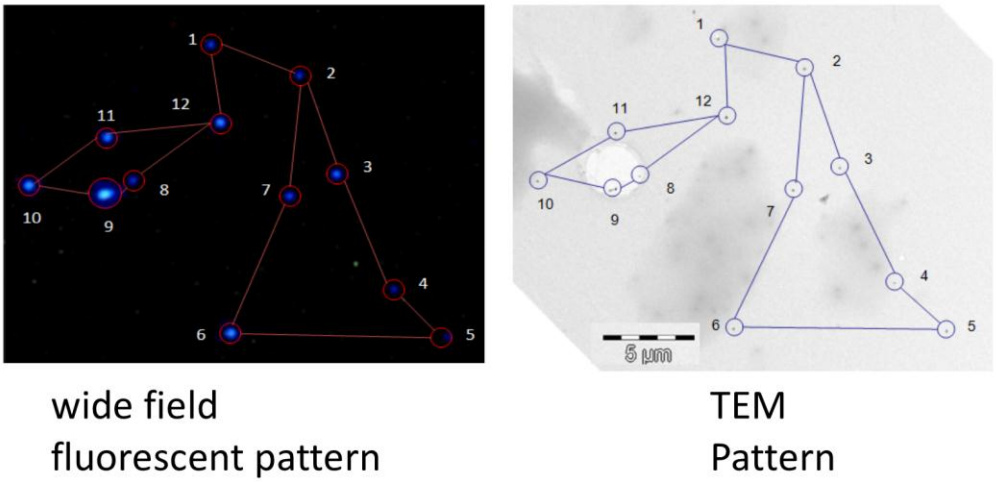

Fig S10. Single nanoparticle detection in wide-field microscopy. a) *Laser scanning microscopy image (excitation at 980 nm) of a 4 mol% Tm^{3+} doped nanocrystals on a glass slide.* ***b)*** *A corresponding TEM image of the same area.*

8. Nanocrystal detection in fibre dip sensors

To establish the potential of Tm^{3+} upconversion nanocrystals as fluorescent probes for trace-molecular detection, $NaYF_4$:Yb/Tm (20/4 mol%) nanocrystals in cyclohexane at various dilutions were introduced into the voids within suspended core optical fibres (total length was 19cm, with a filled length of 12cm). Fig S11 shows that the Tm^{3+} emission was clearly detectable at the level of 5 ng/mL, corresponding to 39 fM nanocrystals in 20 nL suspension (equivalent to approximately 469 nanocrystals in the fibre sensor). This enabled us to use higher dilution of 3.9 fM, as discussed in the main text of this paper. Modelling shows that for this fibre structure the intensity of the guided light at the glass:air interface drops off to 1/e at a distance of 0.125 µm from this interface, so that the area within the hole in which the light is sufficiently intense to excite the nanocrystals (from the glass core surface till the 1/e point in the evanescent field, within one hole) is approximately 0.61 µm². The ratio of this area to the total hole (one hole: 51.9µm²) is thus ~0.0118. For a nanocrystal concentration of 3.9 fM, the filled fibre contains only ~47 nanocrystals, with an average of 0.55 nanocrystals within the detection region.

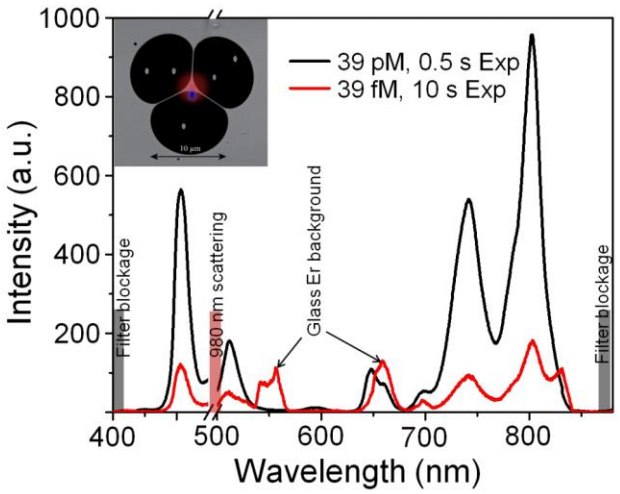

Fig S11. Demonstration of the ability of microstructured optical fibre to sense trace amounts of upconversion nanocrystal with 4 mol% Tm^{3+}. *Both the 39 pM (0.5 second exposure time for spectrometer CCD) and the 39 fM (10 second exposure time) samples show clearly distinguishable emission peaks at 455 nm, 514 nm, 744 nm and 802 nm at excitation irradiance of 2.5×10^6 W/cm^2. These peaks are spectrally separated from both 980 nm scattering and autofluorescence from the trace-level impurities found within the glass from which the fibre is made. These impurities include erbium as seen from the emission lines at 550 nm and 660 nm.*

9. Bio-conjugation and immuno-labelling

9.1 Preparation of phospholipids upconversion nanocrystals [13-16]**.** The oleic acid-capped $NaYF_4$:Yb/Tm nanocrystals were dispersed in a chloroform solution (10 mg/mL). The suspension was mixed with 1, 2-distearoyl-sn-glycero-3- phosphoethanolamine-N-[carboxy(polyethylene glycol)-2000] (DSPE-mPEG-COOH, Avanti Polar Lipids, Inc.) in chloroform with gentle stirring for 1 hour, and the solvent was evaporated. The dry nanocrystals were re-dispersed in water under ultrasonication and purified from excess DSPE-mPEG-COOH *via* centrifugation. After filtration using a 0.22 μm cellulose acetate syringe filter, the phospholipids coated nanocrystals were kept at 4 ˚C.

9.2 Preparation of upconversion nanocrystals bio-conjugates. The upconversion nanocrystals containing carboxylate groups were activated and coupled to streptavidin by an EDC/sulfo-NHS-mediated coupling reaction. Briefly, 1 mg DSPE-PEG-COOH functionalized upconversion nanocrystals were dispersed into activation buffer (50 mM MES buffer, pH 6.0), and then added with 1 mg EDC and 4 mg Sulfo-NHS in 50 mM MES buffer. The mixture was well stirred for 4 hours at room temperature, washed by centrifugation, and re-suspended into 1 mL coupling buffer (100 mM PB buffer, pH 7.2). Subsequently, the suspension was then added into 1 mL PBS buffer solution containing 6.0 mg streptavidin, and incubated for 48 hours at 4 ˚C. Then, 4 mg of L-lysine was used to neutralize any unreacted Sulfo-NHS. The resulting streptavidin-nanocrystals conjugates were pelleted by centrifuging for 10 mins, and supernatant was discarded. Finally, streptavidin-nanocrystal conjugates were stored at 4 ˚C in 100 μl coupling buffer, 10 mg/mL.

9.3 Immuno-labelling of cells. 5 μl of *Giardia Lamblia* preparation (10^5 cells in 1.8 mL, 6-9 μm in diameter, BTF Pty Ltd., Sydeny, Australia) was placed on a poly-L-lysine-coated glass slide in humidified chamber and was allowed to settle down and spread on the piece of glass for 90 min. The fixed cells were then washed with 100 μL phosphate buffered saline (PBS) (pH 7.4) for 5 min ×2 and 0.05% Tween 20 in PBS (v/v) for 5 min, followed by blocking for 30 min with 5% BSA in PBS (w/v). The BSA-blocked cells were incubated with 30 μL anti-*Giardia* antibodies (G203, 0.44 mg/mL, cyst-wall specific, BTF Pty Ltd.) for 60 min at room temperature, and then washed to remove unbound antibodies. 30 μL biotinylated secondary antibodies in 5% BSA in PBS were added (a 1:10 dilution of goat anti-mouse biotin-conjugated IgG antibody, Millipore Australia Pty Ltd.), and washed and blocked as above. Finally, apply 50 μL of 10 mg/mL streptavidin-conjugated upconversion nanocrystals to stain the cells for 2 hours. After several washing with PBS, the slide was mounted in 20% glycerol, 10% Mowiol 4-88, and 70% Tris-HCl buffer with coverslips.

10. Upconversion time-gated Orthogonal Scanning Automated Microscopy (OSAM)/Scanning Cytometry

The operational principle of our time-gated OSAM used with down-conversion luminescence probes has been recently reported by us [17]. Here we modified our OSAM scanning cytometer by a 980 nm single mode diode laser (maximum power of 350 mW in continuous mode, maximum irradiance of ~10^6 W/cm^2). Briefly, it operates in a CW mode as well as in a time-gated mode. In the time-gated mode, it synchronizes the pulsed IR laser with a time-gated photomultiplier tube (PMT) to remove both autofluorescence background and laser scattering from the nearby optics. An X-axis raster scan (maximum speed 24 mm/sec) reads the total number of cells, and calculates their accurate positions according to the signal intensity profile; the following Y-axis scans only access the previously registered cells and read their absolute intensity. In order to eliminate the possibility to confuse doublet (two cells in close proximity) or triplet (three cells in close proximity) events the system ensures visual inspection of points of interest after rapid scanning. A single slide with ~50 cells takes 3 minutes to scan.

11. Upconversion inks for security printing and stamping pads. The upconversion nanocrystals at low (0.2 mol% and 0.5 mol%) and high (4 mol% and 8 mol%) Tm^{3+} doping level in THF (1 mg/mL) were injected to the yellow and cyan based commercial ink cartridge, respectively, and mixed thoroughly with the cartridge pigment. The modified Acrobat (masterpiece by Pablo Picasso, 1930) was directly printed onto a piece of normal A4-size paper by a commercial inkjet printer (pattern dimensions: 15 mm × 18 mm). The pigment containing Tm^{3+}-doped upconversion nanocrystals has been precisely printed on the paper in accordance with the pre-defined pattern. After printing, the pattern was laminated and mounted on glass slide for image scanning by the OSAM scanning cytometer. The rubber stamps (dimensions: 20 mm × 40 mm) mounted on an acrylic block were laser engraved to form separate logos of Macquarie University and Adelaide University. The low and high doping upconversion nanocrystals in cyclohexane with the same concentration (0.1 mg/mL) and volume (100 µl) were prepared in flat glass chambers. The upconversion nanocrystals coated rubber stamps were firmly and accurately pressed onto paper to create overlapping logos. Finally, the stamped patterns were fixed on the glass slide and protected by a coverslip.

References

1 Liu, Y. *et al.* A strategy to achieve efficient dual-mode luminescence of Eu(3+) in lanthanides doped multifunctional NaGdF(4) nanocrystals. *Adv Mater* **22**, 3266-3271 (2010).

2 Wang, F. *et al.* Simultaneous phase and size control of upconversion nanocrystals through lanthanide doping. *Nature* **463**, 1061-1065 (2010).

3 Ebendorff-Heidepriem, H. & Monro, T. M. Extrusion of complex preforms for microstructured optical fibers. *Opt Express* **15**, 15086-15092 (2007).

4 Ebendorff-Heidepriem, H., Warren-Smith, S. C. & Monro, T. M. Suspended nanowires: fabrication, design and characterization of fibers with nanoscale cores. *Opt Express* **17**, 2646-2657 (2009).

5 Boyer, J. C. & van Veggel, F. C. Absolute quantum yield measurements of colloidal NaYF4: Er3+, Yb3+ upconverting nanoparticles. *Nanoscale* **2**, 1417-1419 (2010).

6 Wang, F., Wang, J. A. & Liu, X. G. Direct Evidence of a Surface Quenching Effect on Size-Dependent Luminescence of Upconversion Nanoparticles. *Angew Chem Int Edit* **49**, 7456-7460 (2010).

7 Zhao, J. B. *et al.* Upconversion luminescence with tunable lifetime in NaYF4:Yb,Er nanocrystals: role of nanocrystal size. *Nanoscale* **5**, 944-952 (2013).

8 Page, R. H. *et al.* Upconversion-pumped luminescence efficiency of rare-earth-doped hosts sensitized with trivalent ytterbium. *J Opt Soc Am B* **15**, 996-1008 (1998).

9 Liu, Q. *et al.* Sub-10 nm Hexagonal Lanthanide-Doped NaLuF4 Upconversion Nanocrystals for Sensitive Bioimaging in Vivo. *J Am Chem Soc* **133**, 17122-17125 (2011).

10 Nadort, A. *et al.* Quantitative Imaging of Single Upconversion Nanoparticles in Biological Tissue. *Plos One* **8** (2013).

11 Burshtein, A. & Ivanov, K. Reversible Photoionisation in Liquid Solution. *J. Phys. Chem A*, 3158 -3166 (2001).

12 Auzel, F. Upconversion and anti-Stokes processes with f and d ions in solids. *Chemical reviews* **104**, 139-173 (2004).

13 Li, L. L. *et al.* Biomimetic surface engineering of lanthanide-doped upconversion nanoparticles as versatile bioprobes. *Angew Chem Int Ed Engl* **51**, 6121-6125 (2012).

14 Dubertret, B. *et al.* In vivo imaging of quantum dots encapsulated in phospholipid micelles. *Science* **298**, 1759-1762 (2002).

15 Chen, Z. G. *et al.* Versatile synthesis strategy for carboxylic acid-functionalized upconverting nanophosphors as biological labels. *J Am Chem Soc* **130**, 3023-3029 (2008).

16 Wang, Z., Liu, C. H., Chang, L. J. & Li, Z. P. One-pot synthesis of water-soluble and carboxyl-functionalized beta-NaYF4:Yb,Er(Tm) upconversion nanocrystals and their application for bioimaging. *J Mater Chem* **22**, 12186-12192 (2012).

17 Lu, Y., Xi, P., Piper, J. A., Huo, Y. & Jin, D. Time-gated orthogonal scanning automated microscopy (OSAM) for high-speed cell detection and analysis. *Sci Rep* **2**, 837 (2012).

5.3 Remarks

By screening various Tm^{3+} concentrations in $NaYF_4$ UCNPs, we have demonstrated the upconversion luminescence can be remarkably amplified by a new strategy: using the elevated irradiance to excite highly doped individual UCNPs. The finding has allowed to increase the effective amount of activators in individual UCNPs through raising the stubborn concentration quenching threshold. As a result, it becomes realistic to capture the upconversion signal in the fibre dip sensor for a trace amount of UCNPs due to the enhanced upconversion brightness and the suppressed fibre autofluorescence by the 980 nm excitation. With the true observation of UCNPs at even 3.9 fM dilution (corresponding to a single nanocrystal in the fixed length of the fibre), three orders of magnitude better than the detection limit of QDs in the same fibre, we confirmed the powerfulness of the microstructured fibre dip sensor as a nanoscale sensing platform when UCNPs act as a probe or reporter in the fibre. Moreover, our report contributes to the new understanding of the Ln^{3+}-doped upconversion luminescence, lays foundations to explore upconversion nanomaterials, and opens up new horizons for applications of UCNPs.

Chapter 6: Nano-/Bio-Interface Chemistry

Optical properties of UCNPs have been studied and designed with new features across chapters 3-5. The tunable lifetime decay (Chapter 3) at single UCNPs level has evolved into the lifetime multiplexing technique (Chapter 4); and the new balance between sensitizers, activators and excitation irradiance in the upconversion luminescence has been utilized to efficiently increase the upconversion brightness to achieve the single nanocrystal detection sensitivity (Chapter 5). Although, all discovered properties of UCNPs are promising for the analytical imaging and sensing in cellular and molecular biology, it is needed to resolve the pending subject of functionalizing UCNPs with the suitable surface for the specific protein conjugation. In this chapter, we focused on developing the feasible functionalization and conjugation chemistry at the nano-/bio-interface to make UCNPs proper to stain, detect, image, and quantify labelled cells through the high speed scanning microscope.

6.1 Introduction

UCNPs have been broadly investigated as fluorescent bioprobes for bioimaging and biosensing as well as the tracer of the targeted drug delivery to guide biomedical research and clinical decisions (Nyk, Kumar et al. 2008, Liu, Sun et al. 2011, Wang, Cheng et al. 2011, Wang, Liu et al. 2012, Dong, An et al. 2013, Liu, Bu et al. 2013). The momentum of applying UCNPs was majorly forced by stunning upconversion properties, the step-wise absorption of two or more NIR photons to convert into higher energy emissions, e.g., the visible light, that enables the non-invasive visualization of molecules, single cells and organisms within the deeper tissue (up to 10 mm) (Wang, Wang et al. 2011, Cui, Yin et al. 2013, Nadort, Sreenivasan et al. 2013). Moreover, the NIR excitation capable of eliminating the background autofluorescence can greatly improve the detection sensitivity associated with the higher signal to noise ratio. In comparison to conventional TPA and SHG bioprobes requiring the simultaneous involvement of two photons from the incident femtosecond laser, UCNPs that sequentially absorb and accumulate multiple photons to radiate the upconversion signal could be switched on under relatively low power excitations to constrain the photodamage on biological samples (Chatteriee, Rufalhah et al. 2008, Wang, Wang et al. 2011, Dong, An et al. 2013).

In spite of favorable characters and promising prospects of UCNPs as a bioprobe, their broad use has been limited by the lack of robust surface functionalization and bioconjugation protocols that are committed to make UCNPs satisfy the criteria of biocompatibility, stability, specific binding ability, and high binding efficiency in biological systems. On the one hand, as-prepared UCNPs are hydrophobic, since the typical nanocrystal synthesis occurs in the presence of organic solvents that eventually act as capping ligands to control nanocrystals growth and stabilize nanocrystals against aggregation. Hence, the additional functionalization of UCNPs is required to render a hydrophilic and biocompatible functional surface on UCNPs. To endow the effective and specific binding of functionalized UCNPs with proteins and biomolecules, functionalized UCNPs must be stable in biomimetic or real biological surroundings where the pH ranges from about 5 to 9, at salt concentrations up to a few hundred mM, and remain active for the targeted recognition.

To explore a prototypical protocol, we evaluated two widely employed surface functionalization strategies in this chapter, as illustrated in the schematic Fig. 6.1, based on the silanization and hydrophobic-hydrophobic interaction, respectively. We proposed to stain and detect rare-event environmental pathogen microorganisms, such as *Giardia lamblia*, to examine the conjugation chemistry of functionalized UCNPs with biological targets at the nano-/bio-interface.

In terms of the silanization route, the biocompatible silica layer can deposit as a shell around UCNPs by the hydrolysis of tetraethyl orthosilicate (TEOS). Currently, existing conjugation protocols between silica and biomolecules of interest are advantageous to adapt for silica-coated UCNPs. The well-developed silica coating chemistry has allowed the precise control of the silica shell thickness around UCNPs. The porosity of a silica shell is controllable, endowing the flexibility to devise multifunctional UCNPs with encapsulated dyes, magnetic agents, or molecule drugs (Liong, Lu et al. 2008, Tsai, Hung et al. 2008, Lee, Lee et al. 2010, Kim, Momin et al. 2011). To functionalize oleic acid (OA)-capped hydrophobic UCNPs, the reverse microemulsion method is used to generate a silica coating layer.

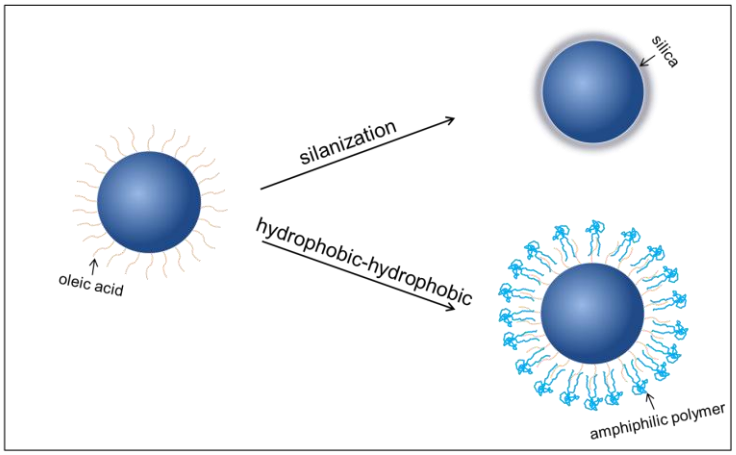

Fig 6.1. Schematic illustration of two general surface functionalization strategies for OA-capped UCNPs: the silica shell formed by silanization; the amphiphilic polymer embedded into UCNPs *via* the hydrophobic-hydrophobic interaction.

Regarding to the hydrophobic-hydrophobic interaction, the conversion from the hydrophobic to hydrophilic surface relies on the adsorption of an amphiphilic polymer onto the hydrophobic surface of UCNPs to form a double layer of ligands (Fig. 6.1). In this approach, the hydrophobic segment of the amphiphilic polymer rapidly interacts with the hydrocarbon chain of the original surface ligands (e.g. OA) with the short-term stirring, so that the hydrophilic end points outwards the aqueous phase without laborious post-treatment procedures. Amphiphilic polymers, such as poly(ethyleneglycol) (PEG)-phospholipids (Li, Zhang et al. 2012), OA-polyacrylic acid (PAA)-PEG (Cheng, Yang et al. 2010), and poly(maleic anhydride-alt-1-octadecene) (PMAO) (Jiang, Pichaandi et al. 2012) are frequently used. Following the same principle, cyclodextrin (e.g. α-CD or β-CD) has been reported to self-assemble on OA-capped UCNPs through the hydrophobic-hydrophobic interaction (Liu, Li et al. 2010, Liu, Chen et al. 2011).

6.2 Conjugation Experiment I: silica-coated UCNPs + antibody binding protein linker + primary antibody

Experimental Design:

To conjugate silica-coated UCNPs, we introduced a novel peptide-based antibody binding protein (ABP) linker (developed by Dr. Anwar Sunna at Macquarie University) (Sunna, Chi et al. 2013). The linker composes of the peptide and Protein G, in which a peptide sequence displaying the high affinity to silica materials is fused to a truncated form of *Streptococcus* strain G148 antibody binding protein, Protein G. Hence, the recombinant ABP linker retains the respective high binding affinity of the peptide to silica materials and Protein G to immunoglobulin (IgG), such as the cyst-wall specific anti-*Giardia* monoclonal antibody (G203) used in this work. In this way, the ABP linker is tested to conjugate silica-coated UCNPs with the primary antibody G203, with the aim to develop an easy but universal conjugation protocol between the nanoscale silica shell and the specific antibody.

Experimental Procedure:

1. Preparation of UCNPs with a silica shell

Monodisperse UCNPs synthesized by the organometallic approach were encapsulated within a thin silica layer *via* a facile water-in-oil microemulsion technique (Fig. 6.2a). The formation of a silica coating layer on UCNPs is confirmed by TEM images (Fig. 6.2b and Fig. 6.2c). Sequential TEM images (Fig. 6.2d) verified the nanoscale silica layer growth as the hydrolysis of TEOS progressed for 36 h, implying that the longer reaction time allows to form the thicker and uniform silica shell.

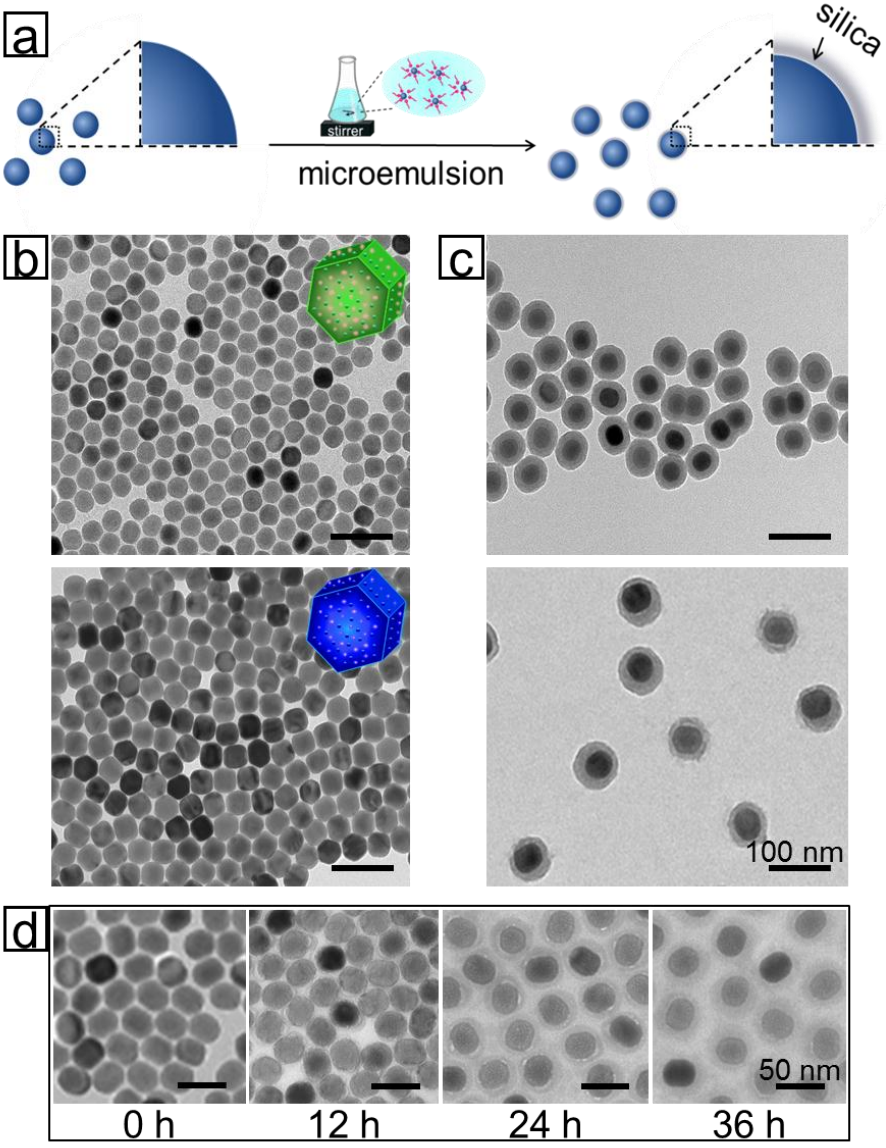

Figure 6.2. (a) Schematic illustration of the general protocol to coat UCNPs with a thin layer of silica shell. TEM images of (b) monodisperse $NaYF_4$:Yb,Er/Tm UCNPs and (c) silica-coated UCNPs. (d) The growth of the silica layer *via* the microemulsion method was monitored by taking batches of samples at different times for TEM.

The silica coating protocol is described as follows:

(1) Igepal CO-520 (0.25 mL) was dissolved in cyclohexane (4 mL) under the ultrasonication and stirring for 10 mins to form the equilibrium of Igepal micelles (Fig. 6.3a).

In this step, cyclohexane provides the oil phase environment, and CO-520 is used as the non-ionic surfactant to encapsulate hydrophobic UCNPs within aqueous nanoscale droplets when the reverse microemulsion is formed later.

(2) 0.5 mL of $NaYF_4$ UCNPs (10 mg/mL) in cyclohexane was added into the mixture in the glass vial. Moderately stirring for 30 mins facilitates the diffusion of UCNPs to Igepal CO-520 micelles (Fig. 6.3b).

This step allows hydrophobic UCNPs to become monodisperse in the oil phase.

(3) 35 μL ammonia hydroxide (wt 28~30%) was then dropwise added to obtain a transparent reverse microemulsion for 30 mins stirring.

Here, ammonia hydroxide forms nanoscale aqueous phase droplets in Igepal CO-520 micelles. This can disperse hydrophobic UCNPs into the reverse microemulsion (Fig. 6.3c).

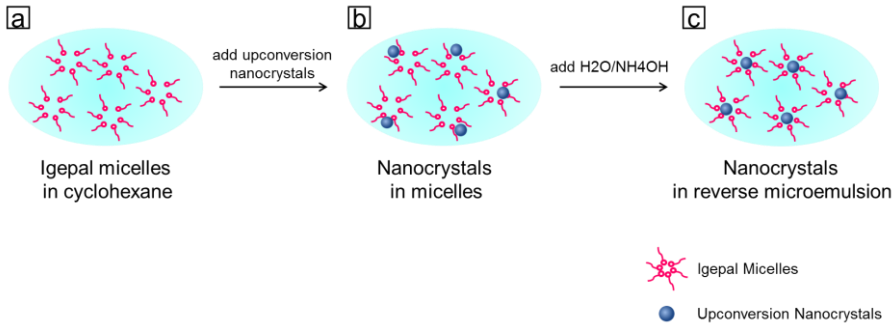

Figure 6.3. Scheme of (a) the formation of Igepal CO-520 micelles in cyclohexane and (b) the encapsulation of hydrophobic UCNPs within Igepal CO-520 micelles and (c) within a reverse microemulsion.

(4) 10 μL TEOS was slowly injected into the system by needle and this reaction lasted for 24 hrs at room temperature.

The silica growth was initiated by hydrolysing TEOS at the oil/water interface, where the reaction is catalysed by ammonia hydroxide. It therefore encapsulates

hydrophobic UCNPs within a silica shell. The thickness of the silica layer can be controlled by adding different volumes of TEOS (e.g. from 2 μL to 150 μL). The silica coating layer enables UCNPs to be charged by the negative potential owing to –OH bonds on the silica surface, resulting in a relatively stable silica-coated UCNPs suspension in buffers with pH>7.

(5) 10 mL acetone was added to precipitate silica-coated UCNPs.

(6) After centrifugal washing for couple of times, silica-coated UCNPs were stored for use at 4 ^{o}C.

Silica is chemically inert and optically transparent, with the established coupling route with a variety of functional molecules. Fig. 6.4a and 6.4b show silica-coated UCNPs are stable as long as a week in the appropriate buffer, without observing degradation and aggregation of silica-coated UCNPs.

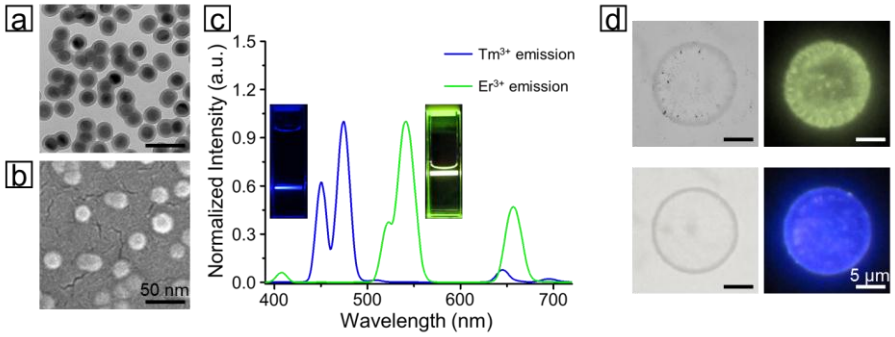

Figure 6.4. (a) TEM and (b) SEM images show silica-coated UCNPs remain stable in the buffer for a week. (c) Upconversion spectra of silica-coated $NaYF_4$:Yb,Er/Tm UCNPs dispersed in water under a 980 nm laser excitation (inset: luminescence photograph of silica-coated UCNPs). (d) Transmission and luminescence microscopy images of polystyrene microspheres stained with silica-coated UCNPs ($NaYF_4$:Yb,Er@silica and $NaYF_4$:Yb,Tm@silica). Silica-coated UCNPs were deposited onto polystyrene microspheres by the affinity adsorption to gain the uniform layer of silica-coated UCNPs.

2. ABP linker mediated conjugation of antibody to silica shell

The Fig. 6.5 illustrates the schematic of the high affinity conjugation between silica-coated UCNPs and the ABP linker. In the experiment, a silica-binding peptide of the

ABP linker mediates the affinity attachment of the ABP linker to UCNPs coated with a silica shell. On the other end of the ABP linker, the fusion protein, Protein G, mediates the binding to the specific antibody. This technique provides a prompt, direct and universal platform for the conjugation of specific antibodies, such as G203, to silica-coated UCNPs at room temperature.

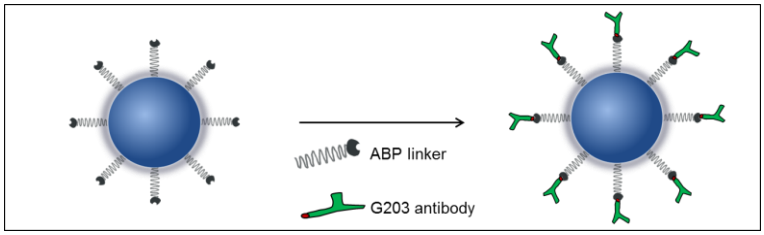

Figure 6.5. The diagram of the conjugation of G203 antibody to silica-functionalized UCNPs *via* the ABP linker.

Firstly, to evaluate the binding efficiency (affinity) of the ABP linker with silica-coated UCNPs, we employed the sodium dodecyl sulphate polyacrylamide gel electrophoresis (SDS-PAGE) method. Procedures of the SDS-PAGE experiment are described as follows:

(1) 100 μL of the ABP linker (~1 μg/μL) was mixed with silica-coated UCNPs by vortex. In less than 30 mins, the conjugation reaction was completed.

(2) ABP linker modified silica-coated UCNPs (ABP-UCNPs) were then collected by centrifugation. The supernatant was checked by SDS-PAGE to determine the unbound ABP linker (Fig. 6.6a).

(3) ABP-UCNPs were subsequently resuspended in Tris-HCl buffer and the residual and/or unstable ABP linker attaching on silica-coated UCNPs can be extracted in in buffer through the centrifugal washing. The cycle of suspending and centrifugal washing was repeated for 3 times within the same Tris-HCl buffer. Supernatants obtained from the 1st, 2nd, and 3rd washing step were analysed by SDS-PAGE (Fig. 6.6a).

(4) To confirm the successful conjugation of the ABP linker to silica-coated UCNPs, the ABP linker was eluted from ABP-UCNPs by the incubation at 99 ^{o}C for 10 mins in 100 μL of SDS-PAGE loading buffer (with short shaking every 2 mins interval). This process released the bound ABP linker from ABP-UCNPs into the supernatant. The resulting supernatant was analyzed by SDS-PAGE (Fig. 6.6a).

Secondly, to evaluate the binding affinity of G203 antibody with ABP-UCNPs, we conducted the following experiment with SDS-PAGE methods:

(1) ABP-UCNPs were mixed with 100 μL of G203 antibody and the mixture was incubated by vortex at room temperature for 1 hr.

(2) G203 conjugated ABP-UCNPs (G203-ABP-UCNPs) were centrifuged for the collection. The supernatant with unbound G203 antibody was kept for SDS-PAGE (Fig. 6.6b).

(3) The pellet of G203-ABP-UCNPs was suspended and washed three times with Tris-HCl buffer. Supernatant fractions from the 1st, 2nd, and 3rd washing step were analysed by SDS-PAGE (Fig. 6.6b).

(4) To confirm the successful conjugation of G203 antibody with ABP-UCNPs, G203 antibody was eluted from G203-ABP-UCNPs by incubation at 99 ^{o}C for 10 mins in 100 μL of SDS-PAGE loading buffer (with short shaking every 2 mins interval). This treatment released both conjugated G203 antibody and the bound ABP linker from G203-ABP-UCNPs into the supernatant. The supernatant was further analysed by SDS-PAGE (Fig. 6.6b).

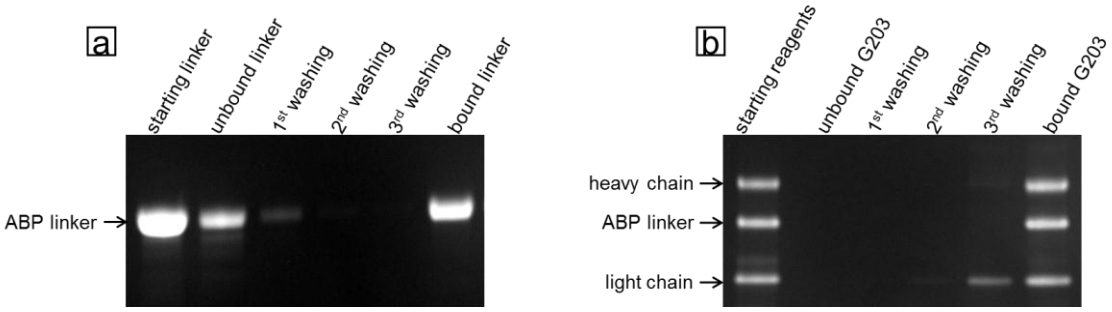

Figure 6.6. (a) SDS-PAGE results confirm the binding affinity of the ABP linker to the silica shell of UNCPs. The gel segment of the ABP linker represents G148 Protein G on one end of the ABP linker. "starting linker" represents the initial ABP linker before incubation with UNCPs as the experimental reference; "unbound linker" is the unbound fraction of the ABP linker in the supernatant after the conjugation with silica-coated UCNPs; "1st, 2nd and 3rd washing" represent the respective supernatant after the sequential washing of ABP-UCNPs; "bound linker" is the eluted ABP linker from ABP-UCNPs in the supernatant after the heat treatment. (b) The SDS-PAGE method was used to confirm the successful conjugation of G203 antibody to ABP-UCNPs *via* the ABP linker. Gel segments of the heavy chain and the light

chain represent components of G203 antibody. “starting reagents” contain the initial ABP linker and G203 antibody before incubation with UNCPs as a reference; “unbound G203” is the unbound fraction of G203 antibody after the conjugation to ABP-UCNPs; “1st, 2nd and 3rd washing” are the respective supernatant after the sequential washing of G203-ABP-UCNPs; “bound G203” is the supernatant containing eluted G203 antibody and the ABP linker that were conjugated on silica-coated UCNPs after the heat treatment.

Fig. 6.6a demonstrated the affinity of the ABP linker to the silica shell of UCNPs. The ABP linker that was fused on silica-coated UCNPs can be eluted off by heating and then pipetted into the gel well, which was marked as “bound linker”. In contrast to the original ABP linker that was symbolized as starting linker, the visualization of exactly the same protein fragments on gel has verified the presence of the ABP linker on the silica-coated UCNPs. In Fig. 6.6b, it provided the evidence of the steady conjugation of G203 antibody to ABP-UCNPs. The same protein fragments for identical bands of “starting reagents” and “bound G203” unambiguously showed the specific binding of G203 antibody to silica-coated UCNPs *via* the ABP linker. Heavy and light chains are typical components of G203 antibody. The presence of a light chain fragment in the 3rd washing fraction in Fig. 6.6b indicates the relative instability of this chain in G203 antibody, which might shed off for the prolonged storage or under vigorous conditions. Therefore, harsh process should be avoided when handling G203-ABP-UCNPs.

3. Immunofluorescence labeling of *Giardia lamblia* cysts

As shown above, the ABP linker can be used to mediate the direct functionalization of silica-coated UCNPs with the specific antibody. In this section, antigen specific G203-ABP-UCNPs were used for immunofluorescence labeling of *Giardia lamblia* cysts in the suspension according to following procedures:

(1) Silica-coated UCNPs (4 mg/mL) were washed once with Tris-HCl buffer (10 mM, pH 7.5, 100 mM NaCl and 0.02% Tween-20).
(2) 25 μL silica-coated UCNPs were mixed with 30 μg the ABP linker in Tris-HCl buffer. The functionalization reaction lasted for 15 mins under gentle mixing. The final volume of 100 μL was kept for following steps.

(3) ABP-UCNPs were purified by centrifugation (9000 rpm, 3 mins) and washed three times. Large aggregates were removed by low speed centrifugation at 1500 rpm for 5 s. Short ultrasonication for 5 s was necessary to re-suspend ABP-UCNPs after centrifugation to reduce aggregates. ABP-UCNPs were stable enough to withstand the gentle ultrasonication procedure.

(4) G203 antibody was purified by centrifugation at 3000 rpm for 20 s to discard the degenerated or aggregated antibody. 75 μL ABP-UCNPs were mixed with 15 μL purified G203 antibody (1.323 mg/mL) in Tris-HCl buffer for 30 mins. Excessive G203 antibody were removed by centrifugal washing, and aggregates were discarded by low speed centrifugation or ultrafiltration through centrifugal filter units (Ultrafree-MC DV centrifugal filter 0.65 μm from Millipore).

(5) Resulting G203-ABP-UCNPs were used to label 1.5 μL of *Giardia lamblia* (7.5×10^3 cysts, 6~9 μm in diameter) through the antibody-antigen interaction as shown in Fig. 6.7a.

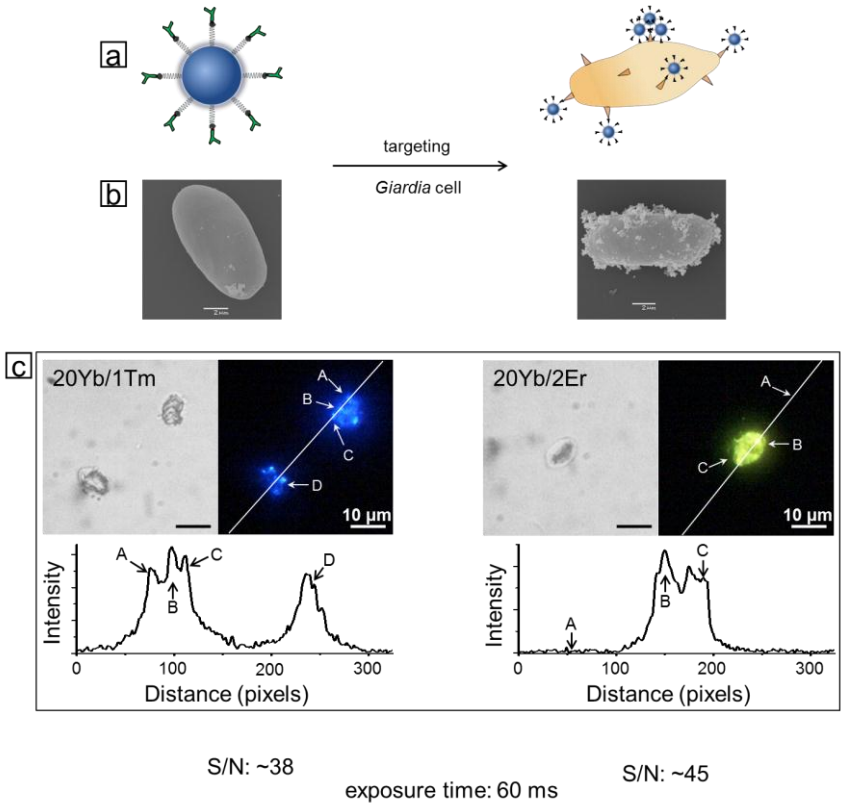

Figure 6.7. (a) The schematic of labeling *Giardia* cysts with G203-ABP-UCNPs. (b) SEM images of unlabeled *Giardia* cysts (left) and G203-ABP-UCNPs labeled cysts (right). (c)

Microscopy images of labeled *Giardia* cysts by modified $NaYF_4$:Yb,Tm and $NaYF_4$:Yb,Er UCNPs under the bright field and luminescence mode with the corresponding intensity profile (bottom) analysis. Image exposure time: 60 ms.

G203-ABP-UCNPs labeled *Giardia* cysts were imaged by SEM (JEOL JSM-6480), shown in Fig. 6.7b to confirm the distribution of UCNPs on the *Giardia* cysts wall. Labeled *Giardia* cysts were then spiked on a glass slide and sealed with a coverslip for luminescence imaging analysis. Under the 980 nm laser excitation, *Giardia* cysts labeled by modified $NaYF_4$:Yb,Tm and $NaYF_4$:Yb,Er UCNPs emit the bright upconversion luminescence in blue and green, respectively, indicating the successful labeling (Fig. 6.7c). They are highly distinguishable in the background-free condition due to the unique upconversion process excited by NIR laser. This resulted in the signal-to-background ratio of over 40:1, analyzed by intensity profiles of luminescence mode images.

The negative control experiment was carried out by incubating ABP-UCNPs with *Giardia* cysts without the addition of G203 antibody. The result shown in Fig. 6.8 indicated that there was no non-specific binding.

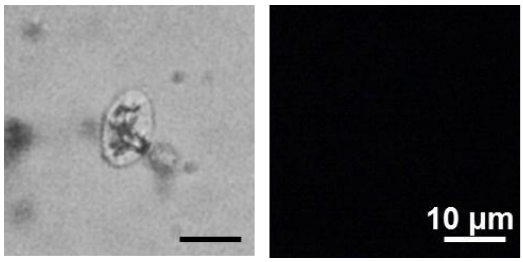

Figure 6.8. The negative control result: Transmission (left) and luminescence (right) microscopy images of the *Giardia* cysts incubated with ABP-UCNPs in the absence of G203 antibody. Image exposure time: 60 ms.

The remarkable photostability of G203-ABP-UCNPs labeled *Giardia* cysts was observed. Labeled *Giardia* cysts emit non-blinking non-bleaching upconversion luminescence under a continuous 980 nm NIR laser illumination for 4 hrs, as shown in typical snapshot images (Fig. 6.9). These phenomena are attributed to highly doped emitters (hundreds to thousands of Ln^{3+} ions) in individual UCNPs. This property suggests advanced imaging applications for long-time track and/or *in situ* studies.

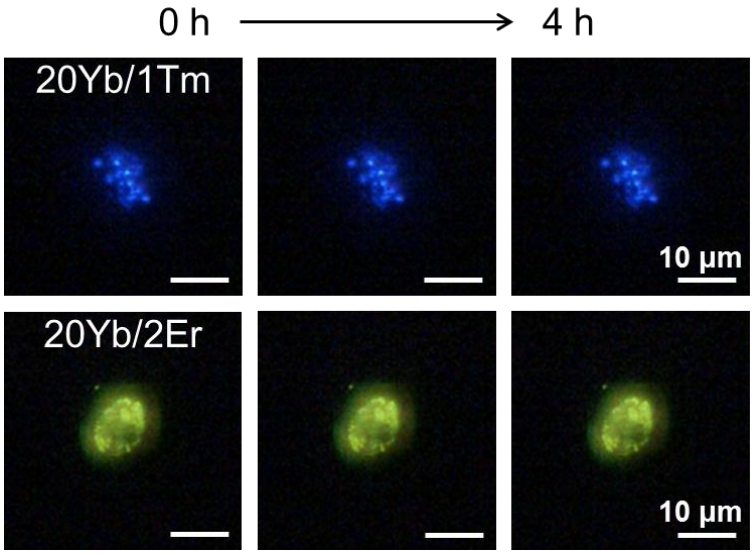

Figure 6.9. Time-lapse images of G203-ABP-UCNPs labeled *Giardia* cysts under a continuous illumination by 980 nm NIR laser for 4 hrs. Image exposure time: 60 ms.

G203-ABP-UCNPs with different lifetimes can be directly used as lifetime multiplexing bioprobes for the rapid and simultaneous detection of multiple analytes. The ease of the conjugation process by the ABP linker (as a universal approach) allows to simply conjugate G203 to different lifetimes encoded UCNPs with a silica shell to label different populations of *Giardia* cysts. As shown in Fig. 6.10, ~150 labeled cysts were imaged on each sample slide and their lifetime properties acquired by TR-OSAM were plotted as histograms in blue ($NaYF_4$:Tm1%,Yb20% and $NaYF_4$:Tm4%,Yb20%) and in green ($NaYF_4$:Er,Yb), respectively. This highly symmetric lifetime distribution fits well with Gaussian statistics. The analysis of histogram bins suggested that relatively uniform τ (lifetime) values distributed across each population of cysts with the corresponding narrow CV: 10% for 4 mol% Tm^{3+} labeled cysts at the mean lifetime of 39 μs, and only 7% for 1 mol% Tm^{3+} labeled ones at the mean lifetime of 150 μs. Narrow CVs at well separated lifetime channels enable two populations of cysts to be clearly distinguished though they emit the same color at blue (Fig. 6.10b). The lifetime-based characteristic is independent of luminescence intensities, suggesting superior advantages of the optical coding in temporal domain for cells labeling.

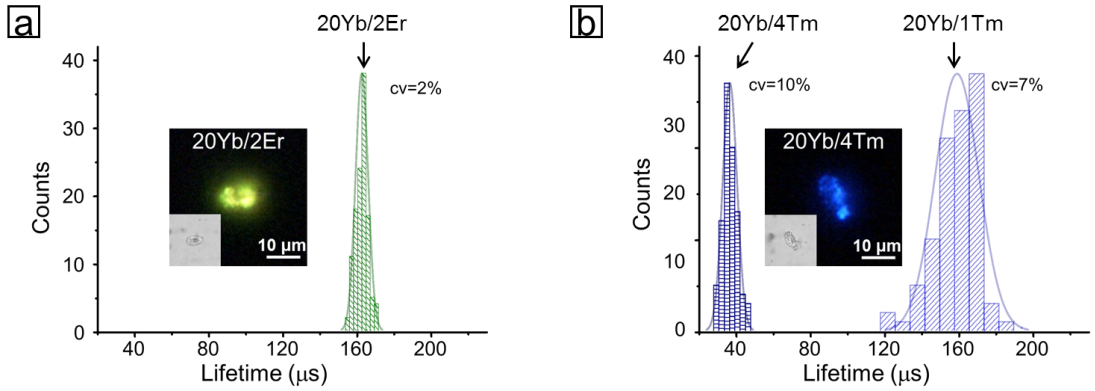

Figure 6.10. Lifetime histograms and representing imaging results for *Giardia* cysts labeled by various G203-ABP-UCNPs with different lifetimes, (a) $NaYF_4$:20%Yb,2%Er UCNPs, and (b) $NaYF_4$:20%Yb,1%Tm and $NaYF_4$:20%Yb,4%Tm UCNPs, respectively.

6.3 Conjugation experiment II: COOH-UCNPs + streptavidin + antibodies

Experimental Design:

In this design, we investigate the protocol of indirectly conjugating UCNPs to biotinylated antibodies *via* the streptavidin (SA)-biotin interaction. As illustrated in Fig. 6.11, UCNPs are surface functionalized to bear functional carboxyl groups (-COOH) *via* the hydrophobic-hydrophobic interaction between OA ligands and PEG phospholipids with carboxylate groups, so that an EDC/sulfo-NHS-mediated coupling reaction can be used to conjugate SA and then recognize biotinylated antibodies for the immunofluorescence staining.

To minimize the non-specific binding and aggregations resulted from centrifugal washing steps, we immobilized *Giardia* cysts on a coverslip, followed by binding reactions with biotinylated antibodies and the subsequent incubation with SA-conjugated UCNPs. We documented this standard immunofluorescence staining protocol as below:

Experimental Procedure:

1. Encapsulation of UCNPs by PEG-phospholipids

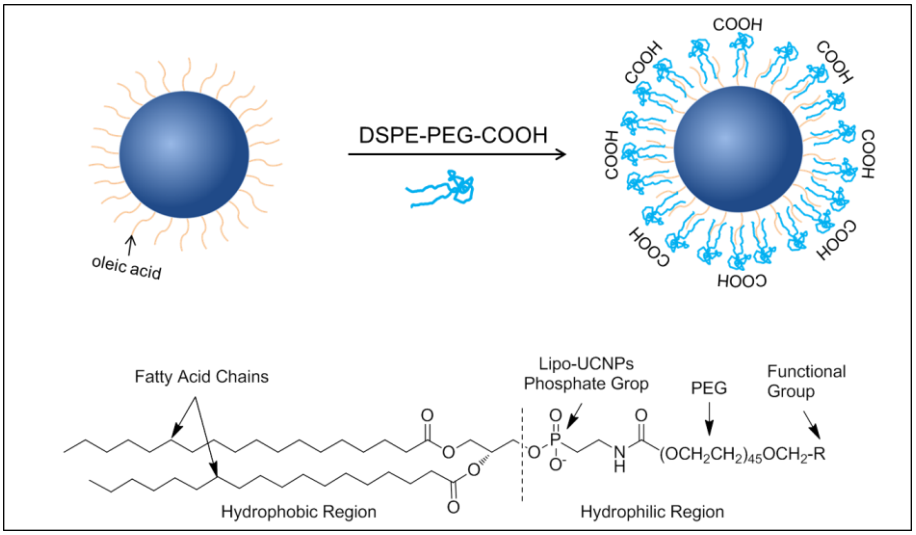

Figure 6.11. Illustration of the hydrophobic-hydrophobic interaction to prepare water-dispersible and COOH-functionalized UCNPs by inserting a monolayer of PEG-phospholipids onto OA-capped UCNPs. The molecular structure of the designed phospholipid 1,2-distearoyl-*sn*-glycero-3-phosphoethanolamine-N-[carboxy(polyethylene glycol)-2000] (DSPE-PEG-COOH) is shown at the bottom.

The Fig. 6.11 describes the principle of encapsulating OA-capped UCNPs by PEG-phospholipids. The designed phospholipid contains four segments: two fatty acid chains, a phosphate group, a PEG segment, and a functional -COOH group for surface engineering. The hydrophobic-hydrophobic interaction can be driven by the strong van der Waals force between the hydrophobic tail of phospholipids and primary OA ligands on UCNPs, to form a double layer of polymers. Fatty acid chains of phospholipids are embedded into OA ligands on UCNPs, while the hydrophilic segment points out toward the aqueous environment. Thus, UCNPs can become water dispersible and encapsulated by an inert, nontoxic, and nonimmunogenic hydrophilic polymer. In fact, on the basis of such interaction, various functional groups (not shown here), e.g. amine, maleimide, biotin, and folate acid, at the end of the PEG segment can be designed to modify UCNPs, permitting to different conjugations for other biomolecules.

(1) 10 mg OA-capped UCNPs were dispersed in 1 mL of chloroform to form a transparent suspension by ultrasonication.
(2) 10 mg DSPE-PEG-COOH phospholipids in 2 mL chloroform were then added.

The quantity of PEG phospholipids can be increased to obtain denser -COOH groups on UCNPs.

(3) The chloroform was slowly evaporated at room temperature with gentle stirring for two days, and there formed a film of UCNPs.

(4) The film of UCNPs was further heated at 75 °C for 15 mins to completely remove chloroform.

(5) The dried film was then hydrated with MilliQ water to disperse UCNPs into water under vigorous ultrasonication.

(6) Excessive lipids were removed from DSPE-PEG-COOH functionalized UCNPs by the repeated ultracentrifugation (14,000 rpm for 15 mins × 2 times).

(7) After filtration (such as 0.65 μm centrifugal filter) to remove large aggregates, resulting UCNPs in PBS buffer were monodisperse as shown in Fig. 6.12. DSPE-PEG-COOH functionalized UCNPs were stored at 4 °C for further use.

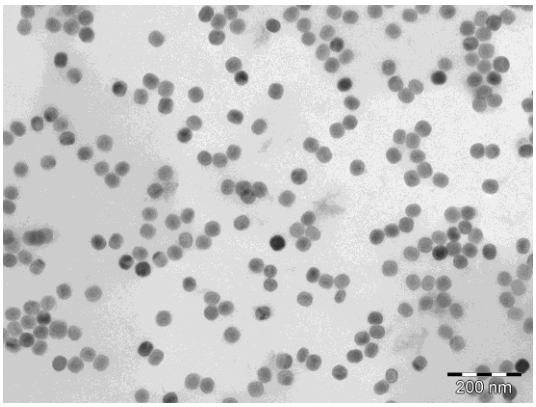

Figure 6.12. TEM image of PEG-phospholipids functionalized UCNPs in PBS buffer.

2. Preparation of SA conjugated UCNPs

The conjugation of -COOH groups to SA is based on the conventional EDC/NHS reaction between -COOH groups on UCNPs and amino groups ($-NH_2$) of SA. Details of the protocol are described as follows:

(1) 1 mg DSPE-PEG-COOH functionalized UCNPs were suspended into 2 mL activation buffer (50 mM MES buffer, pH 6.0). The stirring or gentle ultrasonication was applied to increase the dispersion of UCNPs.

(2) 1 mg EDC and 4 mg Sulfo-NHS were dissolved in MES buffer.

Equilibrate EDC (-20 ˚C) and Sulfo-NHS (4˚C) to room temperature in a desiccator to avoid condensation. EDC and Sulfo-NHS like being dissolved immediately before use to facilitate the faster dissolution.

(3) The mixture of above solutions reacted for 4 hrs at room temperature.

(4) EDC/Sulfo-NHS activated UCNPs were centrifugally washed by three times to remove excess reagents before resuspension into 1 mL coupling buffer (0.1 M PB buffer, pH 7.2).

(5) 0.5 mg activated UCNPs were mixed thoroughly with 3.0 mg SA in 1 mL coupling buffer, and the mixture was incubated at 4 ˚C for 48 hrs.

(6) Add 4 mg of *L*-lysine to neutralize any unreacted Sulfo-NHS for 30 mins at room temperature.

(7) Resulting SA conjugated UCNPs (SA-UCNPs) were pelleted by centrifuge with the supernatant discarded. The suspension of SA-UCNPs conjugates was stored at 2-8 ˚C in 100 μL 1:10 coupling buffer, forming ~10 mg/mL.

3. Immunofluorescence staining of *Giardia* cysts.

The immunofluorescence staining was carried out on the poly-*L*-lysine modified coverslips which can immobilize *Giardia* cysts.

(1) Coverslips need thorough cleaning before poly-*L*-lysine coating.

(i) Put coverslips into 1M HCl solution in a glass container in the hood. A Teflon coverslip rack can be used if many coverslips to be cleaned, so that coverslips are not stacked on one the other and evenly washed in the acid.

(ii) Coverslips were immersed in acid from 4 hrs to overnight with occasion swirling.

(iii) Coverslips were washed liberally with deionized water to ensure no residual acid solution.

(iv) Coverslips were rinsed with absolute ethanol for quick drying.

(2) The poly-*L*-lysine were coated onto coverslips following standard steps:

(i) The poly-*L*-lysine (500 μg/mL) was added to coat the surface of coverslips. The amount of poly-*L*-lysine could be 4~8 μg/cm^2.

(ii) Incubation was carried out at least for 2 hrs with agitation.

(iii) Aspirate poly-*L*-lysine solution and rinse thoroughly coverslips with deionized water.

(iv) Get each coverslip to dry at least 1 hr. Coverslips should be sterilized by UV irradiation, particularly important for cells culture.

(3) 5 μL *Giardia* cysts in suspension were directly placed on the poly-*L*-lysine coated coverslip. Cysts will be randomly distributed on the coverslip for 90 mins.

The Cytospin technique can be used to facilitate the attachment of cells on the coverslip. The microscope can also be used to confirm the cell attachment. More detailed protocols can be found from:

http://www.ihcworld.com/_protocols/histology/cytospin.htm.

(4) As-prepared cysts on the coverslip were rinsed with 100 μL PBS (10 mM) twice followed by 0.05% Tween 20 in PBS (v/v) for 5 mins. The buffer on coverslips was aspirated as much as possible with the residual liquid further wicked by a small wedge of filter paper, but cysts should be still kept in wet for immunofluorescence reaction.

(5) To supress the possible non-specific binding, 100 μL blocking buffer (5% BSA in PBS, 0.05% Tween 20) is necessary to cover cysts in the humidified chamber and incubated at room temperature for 30 mins.

5 % normal goat serum should be used for stringent block.

(6) 30 μL of primary antibody G203 solution (0.44 mg/mL in buffer) was added onto the coverslip for 60 mins in the humidified chamber at room temperature, followed by washing with PBS to remove unbound antibodies.

The antibody solution was short spun with a centrifuge before use. As the most important part of immunofluorescence staining, it is ideal to have the primary antibody with good affinity and excellent specificity.

Optimal dilutions and incubation times need to be determined empirically. The amount of primary antibody used here was certainly more than enough, so further dilutions and optimizations are needed to achieve better staining images and cost reduction.

(7) 30 μL of goat anti-mouse biotinylated secondary antibody in blocking buffer were added on each coverslip for 60 mins incubation, and washed as above. The incubation was kept in the humidified chamber.

Antibodies solution was short spun by centrifuge before use. A 1:10 dilution of biotin-conjugated secondary antibodies was used here. Optimal conditions should be empirically determined. Normally recommended concentrations of secondary antibody range from 1:200-1:500 dilutions.

(8) In the end, we applied 50 μL of SA-UCNPs (~1mg/mL) to stain cysts for 2 hrs at room temperature.

(9) Coverslips were washed in the same way for antibody. To completely wash out the remaining salt on the coverslip, coverslips were dip into deionized water several times. Then, extra liquid was wicked by a KimWipe.

(10) A drop of mounting medium (5-10 μL, 20% glycerol, 10% Mowiol 4-88, and 70% Tris-HCl buffer) was placed onto a clean microscope slide. Turn the stained coverslip with cell-side down and slowly put onto mounting medium from one edge. The mounted microscope slide was stored in fridge to solidify for 1-2 hrs.

To evaluate the indirect conjugation protocol, labelled *Giardia* cysts fixed on glass slides were scanned and imaged by TR-OSAM. As shown in Fig. 6.13 and Fig. 5.5, labelled *Giardia* cysts emit strong blue colour without background interference under a 980 nm NIR laser excitation. Our heavily doped UCNPs emit ultra-bright upconversion luminescence, so that it only requires as short as 0.1 s exposure time to capture these *Giardia* cysts by a standard CCD camera. The TR-OSAM allows the rapid scanning to pinpoint areas of interest on the slide and the visual inspection after locating positions, which can eliminate false positive events as well as differentiate both doublet (two cysts in close proximity) and triplet (three cysts in close proximity) events. These results demonstrate compelling advantages of heavily doped UCNPs as a bright, photostable and background-free bioprobe for immunofluorescence staining and imaging, as well as ideal for the rare-event cells detection and quantification. This developed conjugation and labelling method based on solid support here can minimize both aggregations and non-specific binding towards high-quality immunofluorescence imaging, since centrifugal-free washing steps have been applied. The method also can be used for

detection and quantification of the specific antigens on the cysts surface in early diagnosis.

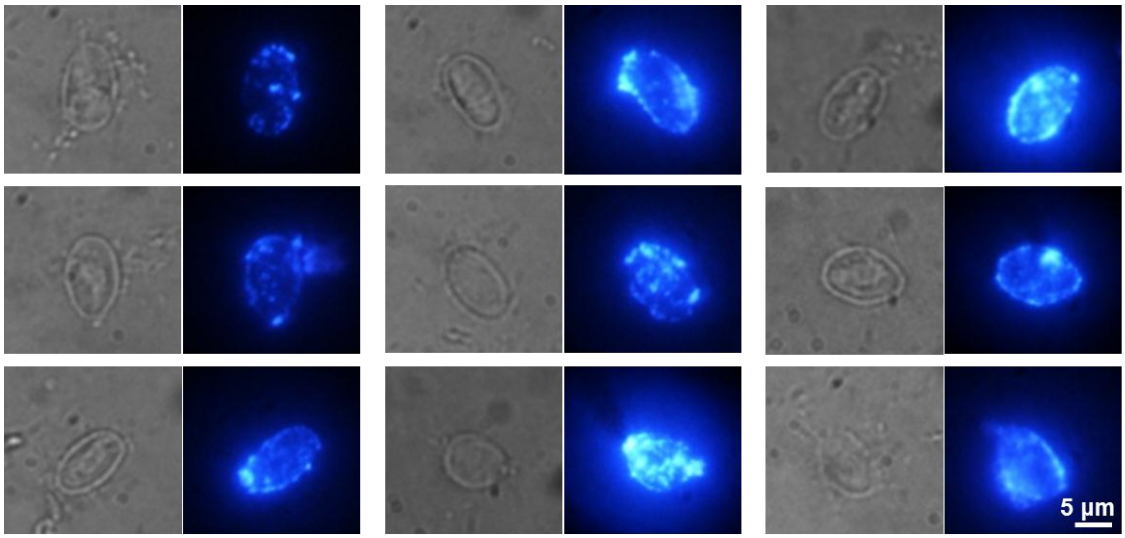

Figure 6.13. Labelled *Giardia* images under the bright filed (left) and luminescence (right) mode by TR-OSAM.

6.4 Discussion

Reviewing two developed labeling protocols in this chapter, we summarized pros and cons of each conjugation approach, and proposed the viable solution to the nano-/bio-interface of UCNPs for efficient immunofluorescence staining with specific biological samples.

The protocol of silica-coated UCNPs → ABP linker → primary antibody has shown a variety of advantages: The universal nature of the ABP linker can facilely conjugate silica-coated UCNPs with specific biomolecules, thus representing a versatile bioconjugation method. It is a simple and straightforward protocol, helpful to reduce laborious procedures since it bypasses the EDC/sulfo-NHS reaction, streptavidin-biotin conjugation and the use of secondary antibody. The ABP linker itself is quite robust and stable and can survive from the ultrasonication treatment. Though it needs post work of coating silica layer, the microemulsion technique has been fairly matured for many years to generate a uniform and nanoscale layer of silica on nanoparticles, which can easily translate into modifying UCNPs. The extent of the enlarged particle size owing to

the additional silica shell deposition can be eased by controlling the silica layer thinner than 5 nm. Such size control is critical to biological applications requiring small sized bioprobes. To prevent the aggregation caused by the hydrolysis of silica surface, it is recommended to endow the silica layer with positive or negative charged groups (e.g. -NH2 or -COOH), which repel particles from being aggregated. It is should be noted that the introduction of supplementary charged groups would not affect the ABP linker's binding activities.

In our experiments, we observed the generation of aggregates during centrifugal washing. This suggests the need of optimizing the amount and ratios of used reagents, such as UCNPs, the ABP linker, and primary antibody as well as appropriate binding and washing buffers. Developing new labeling procedures that avoid the use of high-speed centrifugal washing for purifying functionalized UCNPs is preferable, otherwise aggregates will be inevitably caused. For example, it is worth to incorporate ultrasmall magnetic nanoparticles (sub-5 nm) within the silica shell, so that the magnetic separation approach can be used instead of centrifugation.

The protocol based on OA-capped UCNPs → amphiphilic PEG phospholipids with -COOH groups → EDC/sulfo-NHS → SA → biotinylated secondary antibody, is common method for bio-/nano-conjugation since both the EDC/sulfo-NHS coupling reaction and the following conjugation of activated UCNPs with SA are standardized. In view of the high affinity of SA-biotin, SA-UCNPs can be widely applied to label biological samples bearing with biotinylated antibodies, but the prerequisite is to functionalize UCNPs with -COOH groups and then activate functionalized UCNPs by EDC/sulfo-NHS before linking with SA. We have functionalized –COOH groups to UCNPs by embedding amphiphilic polymer phospholipids DSPE-PEG-COOH into OA-capped UCNPs through the hydrophobic-hydrophobic interaction. However, the double layer of polymer ligands composed of OA and DSPE-PEG-COOH can lead to long hydrocarbon chains, which will favor the crosstalk occurring between any two modified UCNPs, forming undesirable aggregates in the end.

To minimize the chance of crosstalk, it is provoked to directly replace OA ligands by a hydrophilic organic reagent *via* the ligand exchange reaction. Instead of embedding

amphiphilic ligands to form the second layer polymer on UCNPs, the ligand exchange reaction allows to reserve one layer ligand structure without extending the length of hydrocarbon chains. OA ligands capping make UCNPs hydrophobic as Ln^{3+} ions are coordinated by -COOH groups of OA and the hydrophobic end -CH_3 of OA points outwards, hence we should use either multi-chelated ligands or an excess of single-chelated ligands but yielding higher coordination coefficient with Ln^{3+} ions than that of OA ligands to realize OA ligands exchange and obtain -COOH groups functionalized UCNPs. To date, PEG diacid (Boyer, Manseau et al. 2009, Cao, Tong et al. 2012), PAA (Liu, Tu et al. 2010, Jeong, Won et al. 2011, Zhao, Kutikov et al. 2013), and citric acid (Wu, Han et al. 2009) have been demonstrated to enable the replacement of OA ligands and remain the good colloidal stability in aqueous surroundings and bioactive moieties. On the basis of the working principle, the ligand exchange reaction is simple and straightforward, and has negligible effects on the morphology, crystallization, and luminescence efficiency of UCNPs. The ligand exchange reaction approach, not yet carried out in this thesis, is worthwhile to be examined in future to solve the currently disturbing crosstalk problem.

Additionally, the SA-biotin conjugation route relies on the delicate operation and requires series of empirical optimization for each reaction step. The conjugation of large proteins, such as SA size ~5 nm, that increase the diameter of final bioactive UCNPs, can make constraints to some biological applications where small sized bioprobes are necessitated. The conjugation of large proteins, e.g., SA and antibodies, will create the increased space in between bioprobes and targeted biomolecules, which would limit large proteins conjugated bioprobes for the subcellular localization of an antigen.

6.5 Conclusions

In this chapter, we exploit two different protocols to functionalize UCNPs and conjugate them with specific antibodies for immunofluorescence staining. For the first protocol, we successfully demonstrated that the universal ABP linker directly linking the silica shell of UCNPs and primary antibody can significantly ease labeling procedures. As an alternative protocol in Chapter 6, we have shown that -COOH groups

modified UCNPs indirectly conjugated to SA then to biotinylated antibodies can recognize targeted antigens as well. Both approaches can be used to label cells of interest either in the suspension or on the solid support, such as coverslip, for the immunofluorescence staining. All results suggest functionalized UCNPs are a suitable bioprobe for the ultrasensitive detection and precise quantification of specific antigens of biological samples, particularly important for early diagnosis and prognosis applications. Despite these progresses, more work is urged to develop a “smart” nano-/bio-interface, which can circumvent the aggregation and non-specific binding of UCNPs, optimize the antibody binding orientation, and avoid the antibody denaturing.

Chapter 7: Conclusions and Perspectives

7.1 Summary

In the thesis, we investigated two vital topics of UCNPs — optical multiplexing expansion and upconversion brightness enhancement. A series of outstanding advantages of UCNPs have inspired many promising applications in bioimaging, biosensing and biomedical fields. However, translating the active research of UCNPs into practical applications is being exposed to challenges of the limited multiplexing identity and inefficient upconversion luminescence. To this end, we have introduced the lifetime multiplexing concept to greatly expand current spectral multiplexing channels by tuning the respective lifetime of upconversion emission bands. Furthermore, we significantly enhanced the upconversion brightness *via* breaking down the long-standing concentration quenching problem by virtue of high excitation irradiance. On top of these discoveries, we have explored new avenues arising from the ability of manipulating single UCNPs and evaluated their performances in different applications.

Key results of my PhD work can be summarized below:

1) We comprehensively investigated as-prepared different-sized $NaYF_4$:Er,Yb UCNPs in both spectral and temporal domains, respectively. We observed the higher ratio of red-to-green emissions and the shorter lifetime of UCNPs when the particle size decreases. We confirmed that four nonradiative mechanisms lead to the size-dependent upconversion luminescence (spectrum and lifetime) with the support of a core-shell physical model. By the experimental and theoretical analysis of two groups of UCNPs with the particle size in a range of 20 nm~45 nm and 6 nm~15 nm, we interpreted the weight of four nonradiative mechanisms for the size-dependent upconversion luminescence and determined the dominance of the surface defect density in nonradiative decays for smaller UCNPs (<15 nm). We found the role of the UCNPs size in tuning the

upconversion lifetime as a new route, laying the foundation to apply different-sized UCNPs for the lifetime multiplexing.

2) We have demonstrated the lifetime multiplexing concept in the upconversion luminescence. We discovered three methods — the size-dependent nonradiative quenching, the concentration-dependent energy transfer, and the distance-dependent FRET, to precisely control micro-/milli-second upconversion decays. As the lifetime coding is independent from the spectral characteristic, we can create hundreds of multiplexing channels in the temporal domain by combining distinguished lifetimes of respective emissions (for each colour). This work dramatically expands the portfolio of the optical multiplexing capacity, and provides opportunities for lifetime-encoded suspension arrays that permits high-throughput screening complexities in life sciences and medicine.
3) We have significantly enhanced the upconversion luminescence under the sufficient excitation irradiance by unlocking previous dark activators. We presented the evidence that using relatively high-irradiance excitation on UCNPs can break through the long-standing concentration quenching limitation, allowing to enrich the effective activator from a few hundred to tens of thousands in single UCNPs. We demonstrated that the different excitation irradiance level results in different optimal activator concentrations of UCNPs. Thanks to the improved upconversion signal of activator-enriched UCNPs, we can remotely track single UCNPs in the fibre dip sensor (over three orders of magnitude more sensitive than commercial QDs). This work strengthens the in-depth understanding of the Ln^{3+}-doped upconversion luminescence, lays new platforms for exploring upconversion nanomaterials, and promotes applications of UCNPs from ultrasensitive detection, imaging, to security printing.
4) We have rendered originally hydrophobic UCNPs with the hydrophilic surface function by two chemical approaches. In the first approach, we used the ABP linker to directly conjugate silica-coated UCNPs with primary antibodies, such as G203, without the involvement of secondary antibodies. This direct conjugation method can ease the labelling procedure and serves as a prompt and new protocol for the immunolabeling and multiplexing detection. For the second protocol, we used the hydrophobic-hydrophobic interaction to functionalize

UCNPs with -COOH groups that can be indirectly linked with biotinylated antibodies immobilized on cells. This function enables surface-functionalized UCNPs to recognize targeting antigens and therefore label cells of interest either in the suspension or on solid supports, e.g., the coverslip. The success of immunofluorescence staining and imaging confirmed our functionalized UCNPs as a suitable bioprobe for the ultrasensitive detection and precise quantification of specific antigens on cells, promising for the early diagnosis and prognosis.

7.2 Future Scope

The thesis has explored solutions against existing limitations and certain void fields in the upconversion luminescence. These achievements suggest many straightforward opportunities for the upconversion luminescence in the fundamental science and practical applications, which are worthwhile to probe.

Optical multiplexing channels can be further radically expanded by designing a **Spectral-Temporal-Spatial** three-dimentional fluorescent bioprobe to endow the extreme multiplexing capacity and sensitivity. Channels in the spectral domain can be increased by introducing other Ln^{3+} ions, such as Eu^{3+}, Tb^{3+}, Dy^{3+}, and Sm^{3+}. More lifetime identities in the temporal domain will be differentiated through engineering nanostructures of UCNPs, like the shell layer, size and shape of nanocrystals. Spatial-dimension channels will be conceived by embedding controllable amounts of UCNPs in microspheres to generate luminescent intensity-distinguished properties. With different colours, lifetimes, and intensities of UCNPs as identities, the great wealth library of the optical multiplexing coding could be available for highly sensitive and simultaneous analysis of multiple targets in a single test.

The **optimal concentration** in the upconversion luminescence should be re-identified under different excitation conditions and locked down for specific applications. For common binary systems, it is important to explore the power-dependent optimal concentration threshold in Yb-Er and Yb-Ho systems, since their energy levels may lead to different behaviors as observed in Yb-Tm dopants. For emerging ternary systems, introduced extra type of Ln^{3+} ions, e.g. Nd^{3+} as a sensitizer to influence the upconversion luminescence, could regain new balanced optimal concentrations in UCNPs for varying excitation irradiances. Moreover, it is largely unknown optimal concentrations of modified binary (Yb-Er, Yb-Tm and Yb-Ho) and ternary (Yb-Er-Nd, Yb-Tm-Nd and Yb-Ho-Nd) systems where their nanostructures have grown the additional inert/active shell layer or enabled the SPR construction for the signal amplification. In addition, refining the excitation irradiance level and form (pulse or CW) illuminated on biological samples cannot be neglected when searching brightest UCNPs. The damage threshold and effects of different excitations (irradiance level

and/or laser form) on biological samples in various environments should be in parallel studied. We may need to trade off the upconversion brightness achieved under high excitation irradiance to protect biological samples of interest. We believe the proposed comprehensive study is essential to deeply understand and apply the upconversion luminescence.

The proof-of-concept demonstration of UCNPs in life sciences has necessitated the suitable **nano-/bio-interface chemistry**. Firstly, we will diagnose a group of functional groups, such as peptides, proteins or oligonucleotides, for covalent or noncovalent binding UCNPs with biomolecules to recognize several functional groups with the high site-specific conjugation coefficient. Subsequently, these selected functional groups will be further filtered to far supress or avoid the aggregation or precipitation of functionalized UCNPs in relevant aqueous solutions *in vitro*, on solid supports like microarrays, in cells or *in vivo*. Thirdly, we will optimize the orientation of antibodies conjugated with UCNPs to facilitate the binding with targeted antigens for the improved biolabelling efficiency. This three-step process could be beneficial to figure out a road map of the **nano-/bio-interface chemistry** for UCNPs, pinpointing the preferred functionalization route for specific applications, ranging from microarray technology to fluorescence in situ hybridization to *in vivo* imaging.

References

Afshar V, S., Y. Ruan, S. C. Warren-Smith and T. M. Monro (2008). "Enhanced fluorescence sensing using microstructured optical fibers: a comparison of forward and backward collection modes." Optics letters 33(13): 1473-1475.

Afshar V, S., S. C. Warren-Smith and T. M. Monro (2007). "Enhancement of fluorescence-based sensing using microstructured optical fibres." Optics Express 15(26): 17891-17901.

Balboni, I., S. M. Chan, M. Kattah, J. D. Tenenbaum, A. J. Butte and P. J. Utz (2006). Multiplexed protein array platforms for analysis of autoimmune diseases. Annual Review of Immunology. 24: 391-418.

Ballou, B., B. C. Lagerholm, L. A. Ernst, M. P. Bruchez and A. S. Waggoner (2004). "Noninvasive imaging of quantum dots in mice." Bioconjugate chemistry 15(1): 79-86.

Bartel, D. P. (2004). "MicroRNAs: Genomics, biogenesis, mechanism, and function." Cell 116(2): 281-297.

Bendall, S. C., E. F. Simonds, P. Qiu, E.-a. D. Amir, P. O. Krutzik, R. Finck, R. V. Bruggner, R. Melamed, A. Trejo, O. I. Ornatsky, R. S. Balderas, S. K. Plevritis, K. Sachs, D. Pe'er, S. D. Tanner and G. P. Nolan (2011). "Single-cell mass cytometry of differential immune and drug responses across a human hematopoietic continuum." Science 332(6030): 687-696.

Boyer, J. C. and F. C. J. M. van Veggel (2010). "Absolute quantum yield measurements of colloidal NaYF4: Er3+, Yb3+ upconverting nanoparticles." Nanoscale 2(8): 1417-1419.

Braeckmans, K., S. C. De Smedt, C. Roelant, M. Leblans, R. Pauwels and J. Demeester (2003). "Encoding microcarriers by spatial selective photobleaching." Nature Materials 2(3): 169-173.

Brokmann, X., J.-P. Hermier, G. Messin, P. Desbiolles, J.-P. Bouchaud and M. Dahan (2003). "Statistical aging and nonergodicity in the fluorescence of single nanocrystals." Physical review letters 90(12): 120601.

Bruchez, M., M. Moronne, P. Gin, S. Weiss and A. P. Alivisatos (1998). "Semiconductor nanocrystals as fluorescent biological labels." Science 281(5385): 2013-2016.

Bunzli, J. C. G. (2010). "Lanthanide Luminescence for Biomedical Analyses and Imaging." Chemical Reviews 110(5): 2729-2755.

Cao, Y. W. C., R. C. Jin and C. A. Mirkin (2002). "Nanoparticles with Raman spectroscopic fingerprints for DNA and RNA detection." Science 297(5586): 1536-1540.

Chen, G., J. Shen, T. Y. Ohulchanskyy, N. J. Patel, A. Kutikov, Z. Li, J. Song, R. K. Pandey, H. Ågren and P. N. Prasad (2012). "(α-NaYbF4: Tm3+)/CaF2 Core/Shell Nanoparticles with Efficient Near-Infrared to Near-Infrared Upconversion for High-Contrast Deep Tissue Bioimaging." ACS nano 6(9): 8280-8287.

Cheng, L., K. Yang, S. Zhang, M. Shao, S. Lee and Z. Liu (2010). "Highly-sensitive multiplexed in vivo imaging using PEGylated upconversion nanoparticles." Nano Research 3(10): 722-732.

Cohen, B. E. (2010). "Biological imaging: Beyond fluorescence." Nature 467(7314): 407-408.

Cunin, F., T. A. Schmedake, J. R. Link, Y. Y. Li, J. Koh, S. N. Bhatia and M. J. Sailor (2002). "Biomolecular screening with encoded porous-silicon photonic crystals." Nature Materials 1(1): 39-41.

Curley, P., A. Ferguson, J. White and W. Amos (1992). "Application of a femtosecond self-sustaining mode-locked Ti: sapphire laser to the field of laser scanning confocal microscopy." Optical and quantum electronics 24(8): 851-859.

Deniz, E., S. Sortino and F. M. Raymo (2010). "Fluorescence Switching with a Photochromic Auxochrome." Journal of Physical Chemistry Letters 1(24): 3506-3509.

Denk, W., J. H. Strickler and W. W. Webb (1990). "Two-photon laser scanning fluorescence microscopy." Science 248(4951): 73-76.

Deschenes, L. A. and D. A. Vanden Bout (2002). "Single molecule photobleaching: increasing photon yield and survival time through suppression of two-step photolysis." Chemical physics letters 365(5): 387-395.

Diamente, P. R., M. Raudsepp and F. C. J. M. van Veggel (2007). "Dispersible Tm3+-Doped Nanoparticles that Exhibit Strong 1.47 μm Photoluminescence." Advanced Functional Materials 17(3): 363-368.

Dieke, G. H. and H. Crosswhite (1963). "The spectra of the doubly and triply ionized rare earths." Applied Optics 2(7): 675-686.

Dong, B., S. Xu, J. Sun, S. Bi, D. Li, X. Bai, Y. Wang, L. Wang and H. Song (2011). "Multifunctional NaYF4: Yb3+, Er3+@ Ag core/shell nanocomposites: integration of upconversion imaging and photothermal therapy." Journal of Materials Chemistry 21(17): 6193-6200.

Donnert, G., J. Keller, R. Medda, M. A. Andrei, S. O. Rizzoli, R. Luhrmann, R. Jahn, C. Eggeling and S. W. Hell (2006). "Macromolecular-scale resolution in biological fluorescence microscopy." Proceedings of the National Academy of Sciences of the United States of America 103(31): 11440-11445.

Ebendorff-Heidepriem, H. and T. M. Monro (2007). "Extrusion of complex preforms for microstructured optical fibers." Optics Express 15(23): 15086-15092.

Ebendorff-Heidepriem, H., S. C. Warren-Smith and T. M. Monro (2009). "Suspended nanowires: fabrication, design and characterization of fibers with nanoscale cores." Optics Express 17(4): 2646-2657.

Ferrari, B. C., K. Stoner and P. L. Bergquist (2006). "Applying fluorescence based technology to the recovery and isolation of Cryptosporidium and Giardia from industrial wastewater streams." Water Research 40(3): 541-548.

Fisher, W., W. Partridge, C. Dees and E. Wachter (1997). "Simultaneous Two‐Photon Activation of Type‐I Photodynamic Therapy Agents." Photochemistry and photobiology 66(2): 141-155.

Fodor, S. P. A., J. L. Read, M. C. Pirrung, L. Stryer, A. T. Lu and D. Solas (1991). "Light-directed spatially addressable parallel chemical synthesis." Science (Washington D C) 251(4995): 767-773.

Fulton, R. J., R. L. McDade, P. L. Smith, L. J. Kienker and J. R. Kettman (1997). "Advanced multiplexed analysis with the FlowMetrix(TM) system." Clinical Chemistry 43(9): 1749-1756.

Gai, S., P. Yang, C. Li, W. Wang, Y. Dai, N. Niu and J. Lin (2010). "Synthesis of Magnetic, Up‐Conversion Luminescent, and Mesoporous Core–Shell‐Structured Nanocomposites as Drug Carriers." Advanced Functional Materials 20(7): 1166-1172.

Gao, X., Y. Cui, R. M. Levenson, L. W. Chung and S. Nie (2004). "In vivo cancer targeting and imaging with semiconductor quantum dots." Nature biotechnology 22(8): 969-976.

Grant, A. J., F. J. Morgan, T. J. McKinley, G. L. Foster, D. J. Maskell and P. Mastroeni (2012). "Attenuated Salmonella Typhimurium lacking the pathogenicity island-2 type 3 secretion system grow to high bacterial numbers inside phagocytes in mice." PLoS pathogens 8(12): e1003070.

Guo, Y., M. Kumar and P. Zhang (2007). "Nanoparticle-Based Photosensitizers under CW Infrared Excitation." Chemistry of Materials 19(25): 6071-6072.

Han, M. Y., X. H. Gao, J. Z. Su and S. Nie (2001). "Quantum-dot-tagged microbeads for multiplexed optical coding of biomolecules." Nature Biotechnology 19(7): 631-635.

Heer, S., K. Kömpe, H. U. Güdel and M. Haase (2004). "Highly Efficient Multicolour Upconversion Emission in Transparent Colloids of Lanthanide ‐ Doped NaYF4 Nanocrystals." Advanced Materials 16(23 ‐ 24): 2102-2105.

Hennink, E. J., R. deHaas, N. P. Verwoerd and H. J. Tanke (1996). "Evaluation of a time-resolved fluorescence microscope using a phosphorescent Pt-porphine model system." Cytometry 24(4): 312-320.

Heyduk, T. and E. Heyduk (2001). "Luminescence energy transfer with lanthanide chelates: Interpretation of sensitized acceptor decay amplitudes." Analytical Biochemistry 289(1): 60-67.

Idris, N. M., M. K. Gnanasammandhan, J. Zhang, P. C. Ho, R. Mahendran and Y. Zhang (2012). "In vivo photodynamic therapy using upconversion nanoparticles as remote-controlled nanotransducers." Nature Medicine.

Idris, N. M., Z. Li, L. Ye, E. K. Wei Sim, R. Mahendran, P. C.-L. Ho and Y. Zhang (2009). "Tracking transplanted cells in live animal using upconversion fluorescent nanoparticles." Biomaterials 30(28): 5104-5113.

Jiang, S., Y. Zhang, K. M. Lim, E. K. Sim and L. Ye (2009). "NIR-to-visible upconversion nanoparticles for fluorescent labeling and targeted delivery of siRNA." Nanotechnology 20(15): 155101.

Kurner, J. M., I. Klimant, C. Krause, E. Pringsheim and O. S. Wolfbeis (2001). "A new type of phosphorescent nanospheres for use in advanced time-resolved multiplexed bioassays." Analytical Biochemistry 297(1): 32-41.

Lander, E. S., L. M. Linton, B. Birren, C. Nusbaum, M. C. Zody, J. Baldwin, K. Devon, K. Dewar, M. Doyle, W. FitzHugh, R. Funke, D. Gage, K. Harris, A. Heaford, J. Howland, L. Kann, J. Lehoczky, R. LeVine, P. McEwan, K. McKernan, J.

Meldrim, J. P. Mesirov, C. Miranda, W. Morris, J. Naylor, C. Raymond, M. Rosetti, R. Santos, A. Sheridan, C. Sougnez, N. Stange-Thomann, N. Stojanovic, A. Subramanian, D. Wyman, J. Rogers, J. Sulston, R. Ainscough, S. Beck, D. Bentley, J. Burton, C. Clee, N. Carter, A. Coulson, R. Deadman, P. Deloukas, A. Dunham, I. Dunham, R. Durbin, L. French, D. Grafham, S. Gregory, T. Hubbard, S. Humphray, A. Hunt, M. Jones, C. Lloyd, A. McMurray, L. Matthews, S. Mercer, S. Milne, J. C. Mullikin, A. Mungall, R. Plumb, M. Ross, R. Shownkeen, S. Sims, R. H. Waterston, R. K. Wilson, L. W. Hillier, J. D. McPherson, M. A. Marra, E. R. Mardis, L. A. Fulton, A. T. Chinwalla, K. H. Pepin, W. R. Gish, S. L. Chissoe, M. C. Wendl, K. D. Delehaunty, T. L. Miner, A. Delehaunty, J. B. Kramer, L. L. Cook, R. S. Fulton, D. L. Johnson, P. J. Minx, S. W. Clifton, T. Hawkins, E. Branscomb, P. Predki, P. Richardson, S. Wenning, T. Slezak, N. Doggett, J. F. Cheng, A. Olsen, S. Lucas, C. Elkin, E. Uberbacher, M. Frazier, R. A. Gibbs, D. M. Muzny, S. E. Scherer, J. B. Bouck, E. J. Sodergren, K. C. Worley, C. M. Rives, J. H. Gorrell, M. L. Metzker, S. L. Naylor, R. S. Kucherlapati, D. L. Nelson, G. M. Weinstock, Y. Sakaki, A. Fujiyama, M. Hattori, T. Yada, A. Toyoda, T. Itoh, C. Kawagoe, H. Watanabe, Y. Totoki, T. Taylor, J. Weissenbach, R. Heilig, W. Saurin, F. Artiguenave, P. Brottier, T. Bruls, E. Pelletier, C. Robert, P. Wincker, A. Rosenthal, M. Platzer, G. Nyakatura, S. Taudien, A. Rump, H. M. Yang, J. Yu, J. Wang, G. Y. Huang, J. Gu, L. Hood, L. Rowen, A. Madan, S. Z. Qin, R. W. Davis, N. A. Federspiel, A. P. Abola, M. J. Proctor, R. M. Myers, J. Schmutz, M. Dickson, J. Grimwood, D. R. Cox, M. V. Olson, R. Kaul, N. Shimizu, K. Kawasaki, S. Minoshima, G. A. Evans, M. Athanasiou, R. Schultz, B. A. Roe, F. Chen, H. Q. Pan, J. Ramser, H. Lehrach, R. Reinhardt, W. R. McCombie, M. de la Bastide, N. Dedhia, H. Blocker, K. Hornischer, G. Nordsiek, R. Agarwala, L. Aravind, J. A. Bailey, A. Bateman, S. Batzoglou, E. Birney, P. Bork, D. G. Brown, C. B. Burge, L. Cerutti, H. C. Chen, D. Church, M. Clamp, R. R. Copley, T. Doerks, S. R. Eddy, E. E. Eichler, T. S. Furey, J. Galagan, J. G. R. Gilbert, C. Harmon, Y. Hayashizaki, D. Haussler, H. Hermjakob, K. Hokamp, W. H. Jang, L. S. Johnson, T. A. Jones, S. Kasif, A. Kaspryzk, S. Kennedy, W. J. Kent, P. Kitts, E. V. Koonin, I. Korf, D. Kulp, D. Lancet, T. M. Lowe, A. McLysaght, T.

Mikkelsen, J. V. Moran, N. Mulder, V. J. Pollara, C. P. Ponting, G. Schuler, J. R. Schultz, G. Slater, A. F. A. Smit, E. Stupka, J. Szustakowki, D. Thierry-Mieg, J. Thierry-Mieg, L. Wagner, J. Wallis, R. Wheeler, A. Williams, Y. I. Wolf, K. H. Wolfe, S. P. Yang, R. F. Yeh, F. Collins, M. S. Guyer, J. Peterson, A. Felsenfeld, K. A. Wetterstrand, A. Patrinos, M. J. Morgan and C. Int Human Genome Sequencing (2001). "Initial sequencing and analysis of the human genome." Nature 409(6822): 860-921.

Larson, D. R., W. R. Zipfel, R. M. Williams, S. W. Clark, M. P. Bruchez, F. W. Wise and W. W. Webb (2003). "Water-soluble quantum dots for multiphoton fluorescence imaging in vivo." Science 300(5624): 1434-1436.

Lee, H., J. Kim, H. Kim and S. Kwon (2010). "Colour-barcoded magnetic microparticles for multiplexed bioassays." Nature Materials 9(9): 745-749.

Li, L.-L., P. Wu, K. Hwang and Y. Lu (2013). "An Exceptionally Simple Strategy for DNA-Functionalized Up-Conversion Nanoparticles as Biocompatible Agents for Nanoassembly, DNA Delivery, and Imaging." Journal of the American Chemical Society 135(7): 2411-2414.

Li, L. L., R. Zhang, L. Yin, K. Zheng, W. Qin, P. R. Selvin and Y. Lu (2012). "Biomimetic surface engineering of lanthanide-doped upconversion nanoparticles as versatile bioprobes." Angew Chem Int Ed Engl 51(25): 6121-6125.

Li, Y., E. C. Y. Liu, N. Pickett, P. J. Skabara, S. S. Cummins, S. Ryley, A. J. Sutherland and P. O'Brien (2005). "Synthesis and characterization of CdS quantum dots in polystyrene microbeads." Journal of Materials Chemistry 15(12): 1238-1243.

Li, Y. G., Y. T. H. Cu and D. Luo (2005). "Multiplexed detection of pathogen DNA with DNA-based fluorescence nanobarcodes." Nature Biotechnology 23(7): 885-889.Lidke, D. S., P. Nagy, R. Heintzmann, D. J. Arndt-Jovin, J. N. Post, H. E. Grecco, E. A. Jares-Erijman and T. M. Jovin (2004). "Quantum dot ligands provide new insights into erbB/HER receptor–mediated signal transduction." Nature biotechnology 22(2): 198-203.

Lippincott-Schwartz, J., N. Altan-Bonnet and G. H. Patterson (2003). "Photobleaching and photoactivation: following protein dynamics in living cells." Nature cell biology: S7-14.

Liu, C., Z. Gao, J. Zeng, Y. Hou, F. Fang, Y. Li, R. Qiao, L. Shen, H. Lei and W. Yang (2013). "Magnetic/upconversion fluorescent NaGdF4: Yb, Er Nanoparticle-Based Dual-Modal molecular probes for imaging tiny tumors in vivo." ACS nano 7(8): 7227-7240.

Liu, J., W. Bu, L. Pan and J. Shi (2013). "NIR - Triggered Anticancer Drug Delivery by Upconverting Nanoparticles with Integrated Azobenzene - Modified Mesoporous Silica." Angewandte Chemie International Edition.

Liu, Q., Y. Sun, T. Yang, W. Feng, C. Li and F. Li (2011). "Sub-10 nm Hexagonal Lanthanide-Doped NaLuF4 Upconversion Nanocrystals for Sensitive Bioimaging in Vivo." Journal of the American Chemical Society 133(43): 17122-17125.

Lu, Y., D. Jin, R. C. Leif, W. Deng, J. A. Piper, J. Yuan, Y. Duan and Y. Huo (2011). "Automated detection of rare - event pathogens through time - gated luminescence scanning microscopy." Cytometry Part A 79(5): 349-355.

Lu, Y., P. Xi, J. A. Piper, Y. Huo and D. Jin (2012). "Time-gated orthogonal scanning automated microscopy (OSAM) for high-speed cell detection and analysis." Sci Rep 2: 837.

Mandecki, W., B. Ardelt, T. Coradetti, H. Davidowitz, J. A. Flint, Z. L. Huang, W. M. Kopacka, X. Lin, Z. Y. Wang and Z. Darzynkiewicz (2006). "Microtransponders, the miniature RFID electronic chips, as platforms for cell growth in cytotoxicity assays." Cytometry Part A 69A(11): 1097-1105.

Michalet, X., F. Pinaud, T. D. Lacoste, M. Dahan, M. P. Bruchez, A. P. Alivisatos and S. Weiss (2001). "Properties of fluorescent semiconductor nanocrystals and their application to biological labeling." Single Molecules 2(4): 261-276.

Nicewarner-Pena, S. R., R. G. Freeman, B. D. Reiss, L. He, D. J. Pena, I. D. Walton, R. Cromer, C. D. Keating and M. J. Natan (2001). "Submicrometer metallic barcodes." Science 294(5540): 137-141.

Nicholson, J. K. and J. C. Lindon (2008). "Systems biology - Metabonomics." Nature 455(7216): 1054-1056.

Nirmal, M., B. Dabbousi, M. Bawendi, J. Macklin, J. Trautman, T. Harris and L. Brus (1996). "Fluorescence intermittency in single cadmium selenide nanocrystals." Nature 383(6603): 802-804.

Nuriya, M., J. Jiang, B. Nemet, K. B. Eisenthal and R. Yuste (2006). "Imaging membrane potential in dendritic spines." Proceedings of the National Academy of Sciences of the United States of America 103(3): 786-790.

Ostrowski, A. D., E. M. Chan, D. J. Gargas, E. M. Katz, G. Han, P. J. Schuck, D. J. Milliron and B. E. Cohen (2012). "Controlled Synthesis and Single-Particle Imaging of Bright, Sub-10 nm Lanthanide-Doped Upconverting Nanocrystals." ACS nano 6(3): 2686-2692.

Pantazis, P., J. Maloney, D. Wu and S. E. Fraser (2010). "Second harmonic generating (SHG) nanoprobes for in vivo imaging." Proceedings of the National Academy of Sciences 107(33): 14535-14540.

Pathak, S., S.-K. Choi, N. Arnheim and M. E. Thompson (2001). "Hydroxylated quantum dots as luminescent probes for in situ hybridization." Journal of the American Chemical Society 123(17): 4103-4104.

Pawson, T. and P. Nash (2003). "Assembly of cell regulatory systems through protein interaction domains." Science 300(5618): 445-452.

Pregibon, D. C., M. Toner and P. S. Doyle (2007). "Multifunctional encoded particles for high-throughput biomolecule analysis." Science 315(5817): 1393-1396.

Qian, L. P., L. H. Zhou, H.-P. Too and G.-M. Chow (2011). "Gold decorated NaYF4: Yb, Er/NaYF4/silica (core/shell/shell) upconversion nanoparticles for

photothermal destruction of BE (2)-C neuroblastoma cells." Journal of Nanoparticle Research 13(2): 499-510.

Rajapakse, H. E., N. Gahlaut, S. Mohandessi, D. Yu, J. R. Turner and L. W. Miller (2010). "Time-resolved luminescence resonance energy transfer imaging of protein-protein interactions in living cells." Proceedings of the National Academy of Sciences of the United States of America 107(31): 13582-13587.

Resch-Genger, U., M. Grabolle, S. Cavaliere-Jaricot, R. Nitschke and T. Nann (2008). "Quantum dots versus organic dyes as fluorescent labels." Nature methods 5(9): 763-775.

Sako, Y. (2006). "Imaging single molecules in living cells for systems biology." Molecular Systems Biology 2.

Salafsky, J. S. and B. Cohen (2008). "A second-harmonic-active unnatural amino acid as a structural probe of biomolecules on surfaces." The Journal of Physical Chemistry B 112(47): 15103-15107.

Scharenberg, C. W., M. A. Harkey and B. Torok-Storb (2002). "The ABCG2 transporter is an efficient Hoechst 33342 efflux pump and is preferentially expressed by immature human hematopoietic progenitors." Blood 99(2): 507-512.

Schena, M., D. Shalon, R. W. Davis and P. O. Brown (1995). "QUANTITATIVE MONITORING OF GENE-EXPRESSION PATTERNS WITH A COMPLEMENTARY-DNA MICROARRAY." Science 270(5235): 467-470.

Selvin, P. R. (2002). "Principles and biophysical applications of lanthanide-based probes." Annual Review of Biophysics and Biomolecular Structure 31: 275-302.

Selvin, P. R., T. M. Rana and J. E. Hearst (1994). "Luminescence resonance energy transfer." Journal of the American Chemical Society 116(13): 6029-6030.

Shan, G., R. Weissleder and S. A. Hilderbrand (2013). "Upconverting Organic Dye Doped Core-Shell Nano-Composites for Dual-Modality NIR Imaging and Photo-Thermal Therapy." Theranostics 3(4): 267.

Shan, J., S. J. Budijono, G. Hu, N. Yao, Y. Kang, Y. Ju and R. K. Prud'homme (2011). "Pegylated Composite Nanoparticles Containing Upconverting Phosphors and meso‐Tetraphenyl porphine (TPP) for Photodynamic Therapy." Advanced Functional Materials 21(13): 2488-2495.

Smolorz, S., F. Wise and N. Borrelli (1999). "Measurement of the nonlinear optical response of optical fiber materials by use of spectrally resolved two-beam coupling." Optics letters 24(16): 1103-1105.

Sommerdijk, J. L. and A. Bril (1974). "Phosphors for the conversion of infrared radiation into visible light." Philips Tech. Rev. 34: 1-32.

Song, Z., Y. G. Anissimov, J. Zhao, A. V. Nechaev, A. Nadort, D. Jin, T. W. Prow, M. S. Roberts and A. V. Zvyagin (2013). "Background free imaging of upconversion nanoparticle distribution in human skin." Journal of biomedical optics 18(6): 061215-061215.

Southern, E. M. (1996). "DNA chips: Analysing sequence by hybridization to oligonucleotides on a large scale." Trends in Genetics 12(3): 110-115.

Sukhanova, A., J. Devy, L. Venteo, H. Kaplan, M. Artemyev, V. Oleinikov, D. Klinov, M. Pluot, J. H. Cohen and I. Nabiev (2004). "Biocompatible fluorescent nanocrystals for immunolabeling of membrane proteins and cells." Analytical biochemistry 324(1): 60-67.

Sun, Y., M. Yu, S. Liang, Y. Zhang, C. Li, T. Mou, W. Yang, X. Zhang, B. Li and C. Huang (2011). "Fluorine-18 labeled rare-earth nanoparticles for positron emission tomography (PET) imaging of sentinel lymph node." Biomaterials 32(11): 2999-3007.

Thomson, J. M., J. Parker, C. M. Perou and S. M. Hammond (2004). "A custom microarray platform for analysis of microRNA gene expression." Nature Methods 1(1): 47-53.

Trau, M. and B. J. Battersby (2001). "Novel colloidal materials for high-throughput screening applications in drug discovery and genomics." Advanced Materials 13(12-13): 975-+.

van de Rijke, F., H. Zijlmans, S. Li, T. Vail, A. K. Raap, R. S. Niedbala and H. J. Tanke (2001). "Up-converting phosphor reporters for nucleic acid microarrays." Nature biotechnology 19(3): 273-276.

van 't Veer, L. J. and R. Bernards (2008). "Enabling personalized cancer medicine through analysis of gene-expression patterns." Nature 452(7187): 564-570.

Visscher, K., G. Brakenhoff and T. Visser (1994). "Fluorescence saturation in confocal microscopy." Journal of Microscopy 175(2): 162-165.

Wang, C., L. Cheng, Y. Liu, X. Wang, X. Ma, Z. Deng, Y. Li and Z. Liu (2013). "Imaging ‐ Guided pH ‐ Sensitive Photodynamic Therapy Using Charge Reversible Upconversion Nanoparticles under Near ‐ Infrared Light." Advanced Functional Materials.

Wang, D. N., S. Y. Liu, B. J. Trummer, C. Deng and A. L. Wang (2002). "Carbohydrate microarrays for the recognition of cross-reactive molecular markers of microbes and host cells." Nature Biotechnology 20(3): 275-281.

Wang, D. Y., A. L. Rogach and F. Caruso (2002). "Semiconductor quantum dot-labeled microsphere bioconjugates prepared by stepwise self-assembly." Nano Letters 2(8): 857-861.

Wang, F., R. R. Deng, J. Wang, Q. X. Wang, Y. Han, H. M. Zhu, X. Y. Chen and X. G. Liu (2011). "Tuning upconversion through energy migration in core-shell nanoparticles." Nature Materials 10(12): 968-973.

Wang, F., Y. Han, C. S. Lim, Y. Lu, J. Wang, J. Xu, H. Chen, C. Zhang, M. Hong and X. Liu (2010). "Simultaneous phase and size control of upconversion nanocrystals through lanthanide doping." Nature 463(7284): 1061-1065.

Wang, F. and X. G. Liu (2008). "Upconversion multicolor fine-tuning: Visible to near-infrared emission from lanthanide-doped NaYF4 nanoparticles." Journal of the American Chemical Society 130(17): 5642-+.

Wang, H. J., R. Shrestha and Y. Zhang (2013). "Encapsulation of Photosensitizers and Upconversion Nanocrystals in Lipid Micelles for Photodynamic Therapy." Particle & Particle Systems Characterization.

Weijer, C. J. (2003). "Visualizing signals moving in cells." Science 300(5616): 96-100.

Widengren, J. and R. Rigler (1996). "Mechanisms of photobleaching investigated by fluorescence correlation spectroscopy." Bioimaging 4(3): 149-157.

Wilson, R., A. R. Cossins and D. G. Spiller (2006). "Encoded Microcarriers For High‐Throughput Multiplexed Detection." Angewandte Chemie International Edition 45(37): 6104-6117.

Won, S., H.-D. Kim, J.-Y. Kim, B.-C. Lee, S. Chang and C.-S. Park (2010). "Movements of Individual BK< sub> Ca</sub> Channels in Live Cell Membrane Monitored by Site-Specific Labeling Using Quantum Dots." Biophysical journal 99(9): 2853-2862.

Wu, S. W., G. Han, D. J. Milliron, S. Aloni, V. Altoe, D. V. Talapin, B. E. Cohen and P. J. Schuck (2009). "Non-blinking and photostable upconverted luminescence from single lanthanide-doped nanocrystals." Proceedings of the National Academy of Sciences of the United States of America 106(27): 10917-10921.

Wu, X., H. Liu, J. Liu, K. N. Haley, J. A. Treadway, J. P. Larson, N. Ge, F. Peale and M. P. Bruchez (2002). "Immunofluorescent labeling of cancer marker Her2 and other cellular targets with semiconductor quantum dots." Nature biotechnology 21(1): 41-46.

Xiao, M. and P. R. Selvin (2001). "Quantum yields of luminescent lanthanide chelates and far-red dyes measured by resonance energy transfer." Journal of the American Chemical Society 123(29): 7067-7073.

Xiao, Y. and P. E. Barker (2004). "Semiconductor nanocrystal probes for human metaphase chromosomes." Nucleic Acids Research 32(3): e28-e28.

Xie, X. and X. Liu (2012). "Photonics: Upconversion goes broadband." Nature Materials 11(10): 842-843.

Yang, X. T. and Y. Zhang (2004). "Encapsulation of quantum nanodots in polystyrene and silica micro-/nanoparticles." Langmuir 20(14): 6071-6073.

Ye, Z. Q., M. Q. Tan, G. L. Wang and J. L. Yuan (2004). "Preparation, characterization, and time-resolved fluorometric application of silica-coated terbium(ill) fluorescent nanoparticles." Analytical Chemistry 76(3): 513-518.

Zhang, C., Y. Yuan, S. Zhang, Y. Wang and Z. Liu (2011). "Biosensing Platform Based on Fluorescence Resonance Energy Transfer from Upconverting Nanocrystals to Graphene Oxide." Angewandte Chemie International Edition 50(30): 6851-6854.

Zhang, F., Q. Shi, Y. Zhang, Y. Shi, K. Ding, D. Zhao and G. D. Stucky (2011). "Fluorescence Upconversion Microbarcodes for Multiplexed Biological Detection: Nucleic Acid Encoding." Advanced Materials 23(33): 3775-3779.

Zhang, H., Y. Li, I. A. Ivanov, Y. Qu, Y. Huang and X. Duan (2010). "Plasmonic modulation of the upconversion fluorescence in NaYF4: Yb/Tm hexaplate nanocrystals using gold nanoparticles or nanoshells." Angewandte Chemie 122(16): 2927-2930.

Zhang, H., Y. Li, Y. Lin, Y. Huang and X. Duan (2011). "Composition tuning the upconversion emission in NaYF4:Yb/Tm hexaplate nanocrystals." Nanoscale 3(3).

Zhang, L., A. McKay and D. Jin (2013). "High-throughput 3-dimensional time-resolved spectroscopy: simultaneous characterisation of luminescence properties in spectral and temporal domains." RSC Adv. 3(23): 8670-8673.

Zhang, P., W. Steelant, M. Kumar and M. Scholfield (2007). "Versatile photosensitizers for photodynamic therapy at infrared excitation." Journal of the American Chemical Society 129(15): 4526-4527.

Zhu, X., J. Zhou, M. Chen, M. Shi, W. Feng and F. Li (2012). "Core–shell Fe< sub> 3</sub> O< sub> 4</sub>@ NaLuF< sub> 4</sub>: Yb, Er/Tm nanostructure for MRI, CT and upconversion luminescence tri-modality imaging." Biomaterials 33(18): 4618-4627.

Zijlmans, H., J. Bonnet, J. Burton, K. Kardos, T. Vail, R. Niedbala and H. Tanke (1999). "Detection of cell and tissue surface antigens using up-converting phosphors: a new reporter technology." Analytical biochemistry 267(1): 30-36.

Zou, W. Q., C. Visser, J. A. Maduro, M. S. Pshenichnikov and J. C. Hummelen (2012). "Broadband dye-sensitized upconversion of near-infrared light." Nature Photonics 6(8): 560-564.